NUMERICAL MODELLING OF HIGH-FREQUENCY GROUND-PENETRATING RADAR ANTENNAS

CRAIG WARREN

Doctor of Philosophy

The University of Edinburgh

2009

A mind is like a parachute. It doesnt work if it's not open.

— Frank Zappa

DECLARATION

I hereby declare that this thesis and the work reported herein was composed and originated entirely by myself, under the supervision of Dr. Antonios Giannopoulos in the School of Engineering at The University of Edinburgh.

The following conference and journal publications are as a result of the research conducted for this thesis, which has not been submitted for any other degree or professional qualification.

- C. Warren and A. Giannopoulos. Optimising models of commercial GPR antennas. In *Proceedings of the 5th International Workshop on Advanced Ground Penetrating Radar*, 2009.
- C. Warren and A. Giannopoulos. Simulating Commercial GPR antennas: How close can we get? In *Proceedings of the 12th International Conference on Ground Penetrating Radar*, 2008.
- M. Gordon, C. Warren, and A. Giannopoulos. Experimental and Computational Modelling of GPR Signals within Natural Stone Sett Construction. In *Proceedings of the 12th International Conference on Structural Faults and Repair*, 2008.
- C. Warren and A. Giannopoulos. Numerical modelling of commercial GPR antennas. In *Proceedings of the 21st SAGEEP Symposium on the Application of Geophysics to Engineering and Environmental Problems*, 2008. Invited paper.
- C. Warren and A. Giannopoulos. Numerical modelling of commercial GPR antennas. In *Proceedings of the 13th European Meeting of Environmental and Engineering Geophysics of the Near Surface Geoscience Division of EAGE*, 2007.

Edinburgh, 2009

Craig Warren

ABSTRACT

Ground-Penetrating Radar (GPR) is a non-destructive electromagnetic investigative tool used in many applications across the fields of engineering and geophysics. The propagation of electromagnetic waves in lossy materials is complex and over the past 20 years, the computational modelling of GPR has developed to improve our understanding of this phenomenon.

This research focuses on the development of accurate numerical models of widely-used, high-frequency commercial GPR antennas. High-frequency, high-resolution GPR antennas are mainly used in civil engineering for the evaluation of structural features in concrete i. e., the location of rebars, conduits, voids and cracking. These types of target are typically located close to the surface and their responses can be coupled with the direct wave of the antenna. Most numerical simulations of GPR only include a simple excitation model, such as an infinitesimal dipole, which does not represent the actual antenna. By omitting the real antenna from the model, simulations cannot accurately replicate the amplitudes and waveshapes of real GPR responses.

Numerical models of a 1.5 GHz Geophysical Survey Systems, Inc. (GSSI) antenna and a 1.2 GHz MALÅ GeoScience (MALÅ) antenna have been developed. The geometry of antennas is often complex with many fine features that must be captured in the numerical models. To visualise this level of detail in 3D, software was developed to link Paraview—an open source visualisation application which uses the Visualisation Toolkit (VTK)—with GprMax3D—electromagnetic simulation software based on the Finite-Difference Time-Domain (FDTD) method. Certain component values from the real antennas that were required for the models could not be readily determined due to commercial sensitivity. Values for these unknown parameters were found by implementing an optimisation technique known as Taguchi's method. The metric used to initially assess the accuracy of the antenna models was a cross-corellation of the crosstalk responses from the models with the crosstalk responses measured from the real antennas. A 98 % match between modelled and real crosstalk responses was achieved.

Further validation of the antenna models was undertaken using a series of laboratory experiments where oil-in-water (O/W) emulsions were created to simulate the electrical properties of real materials. The emulsions provided homogeneous liquids with controllable permittivity and conductivity and enabled different types of targets, typically encountered with GPR, to be tested.

The laboratory setup was replicated in simulations which included the antenna models and an excellent agreement was shown between the measured and modelled data. The models reproduced both the amplitude and waveshape of the real responses whilst B-scans showed that the models were also accurately capturing effects, such as masking, present in the real data. It was shown that to achieve this accuracy, the real permittivity and conductivity profiles of materials must be correctly modelled.

The validated antenna models were then used to investigate the radiation dynamics of GPR antennas. It was found that the shape and directivity of theoretically predicted far-field radiation patterns differ significantly from real antenna patterns. Being able to understand and visualise in 3D the antenna patterns of real GPR antennas, over realistic materials containing typical targets, is extremely important for antenna design and also from a practical user perspective.

ACKNOWLEDGMENTS

I would like to acknowledge my supervisor, Doctor Antonios Giannopoulos, for his continual support throughout the duration of my studies. His encouragement, guidance, and passion for the subject were invaluable.

I would like to thank my second supervisor, Professor Michael C. Forde, for his support and guidance. Quite often a five minute chat turned into an hour-long discussion, but I always came away with much useful advice.

I would like to thank my friends and colleagues in The Institute for Infrastructure and Environment, of whom there are too many to mention specifically, for making it such a pleasant and stimulating environment to work in. Specific mention to the *11 am coffee-goers* and the irreverent chat (important networking) that always took place.

I would also like to acknowledge my office-mates over the years Ria Diamanti, Francis Drossaert, Robert De Bold, and Scott Rodgers for their companionship, and their understanding answers to my many stupid questions.

My apologies to Clare Baird and Bryony Davidson who were continually subjected to my *important* whinging.

I owe sincere thanks to Holly Smith for her love, support and encouragement, without which I would not have found the motivation to complete this work.

Finally, and most importantly, I would like to thank my parents, John and Sheila, for their understanding, love and support throughout my university career. I would also like to thank my brother, Simon, for unwittingly ensuring I never lost touch with the real world!

CONTENTS

LIST OF FIGURES

LIST OF TABLES

ACRONYMS

ABC	Absorbing Boundary Condition
ADC	Analogue-to-Digital converter
ADE	Auxiliary Differential Equation
ADI	Alternating-Direction Implicit
AMD	Advanced Micro Devices
ANN	Artificial Neural Network
BHS	Bruggeman-Hanai-Sen
CEM	Computational Electromagnetics
CFL	Courant-Friedrichs-Lewy
CFS	Complex Frequency Shifted
CFRP	Carbon Fibre Reinforced Polymer
CMP	Common Mid-Point
CO	Common Offset
CP	Contour Path
CPML	Convolutional Perfectly Matched Layer
CPU	Central Processing Unit
CRIM	Complex Refractive Index Model
DC	Direct Current
DMI	Distance Measurement Instrument
EMF	Electromotive Force
FDTD	Finite-Difference Time-Domain
FEM	Finite Element Method
FFT	Fast Fourier Transform

FVTD Finite-Volume Time-Domain

GA Genetic Algorithm

GFRP Glass Fibre Reinforced Polymer

GPML Generalised Perfectly Matched Layer

GPR Ground-Penetrating Radar

GSSI Geophysical Survey Systems, Inc.

HDPE High-Density Polyethylene

LD Level Difference

MALÅ MALÅ GeoScience

MoM Method of Moments

O/W oil-in-water

OA Orthogonal Array

PCB Printed Circuit Board

PEC Perfect Electric Conductor

PML Perfectly Matched Layer

PSD Power Spectral Density

PSO Particle Swarm Optimisation

RAM Random-Access Memory

RIPML Recursive Integration Perfectly Matched Layer

RSS Residual Sum of Squares

SA Simulated Annealing

SGE Sun Grid Engine

SMT Surface Mount Technology

TLM Transmission Line Method

UPML Uniaxial Perfectly Matched Layer

VTK Visualisation Toolkit

W/O water-in-oil

WARR Wide-Angle Reflection-Refraction

XML Extensible Markup Language

1 INTRODUCTION

1.1 MOTIVATION AND AIMS FOR THE RESEARCH

Ground-Penetrating Radar (GPR) is a non-destructive electromagnetic investigative tool used in many diverse applications across the fields of engineering and geophysics. These applications can range from, the investigation of glacial deposits tens of metres below the subsurface, to the location of rebars, a few millimetres in diameter, embedded in concrete. This wide range of spatial scales is often coupled with naturally occurring or man-made material heterogeneities, which result in many difficult operating environments for GPR. In turn, data sets obtained with GPR from these environments are complex, application-specific, and require extensive experience to accurately interpret. The core difficulty with the interpretation of such data is that the prediction and understanding of the propagation of electromagnetic waves in heterogeneous environments, itself, presents a challenging problem. The investigation of this problem is the primary motivation for the computational modelling of GPR.

The numerical modelling of GPR has developed over the past 20 years, or so. A typical GPR numerical simulation should include, at some degree of detail, a model of the source or antenna, a model of subsurface or structure, and models of the targets. The research described in this thesis is focused primarily on high-frequency GPR used in civil engineering for the evaluation of structural features in concrete i. e., the location of rebars, conduits, voids and cracking. These types of target are typically located close to the surface, in materials with high velocities of propagation, and hence target responses can be coupled with the direct wave of the antenna. Unfortunately, most numerical simulations of GPR only include a simple excitation model such as an infinitesimal dipole which does not represent the real antenna used in practice. By omitting the real antenna from the model two major problems are encountered: firstly, the simulations cannot accurately replicate the amplitudes and waveshapes of real responses; and secondly, the simulations cannot replicate the interaction between target responses and the direct wave of a real antenna.

The main aim of this research was to advance the state of computational modelling of GPR by creating models of widely-used commercial GPR antennas. This would enable direct comparisons of real and modelled amplitude

and waveshape information from typical GPR targets, and lead to a better understanding and interpretation of real GPR data.

1.1.1 *Objectives*

The specific objectives for this research are summarised as follows:

- Investigate and develop the necessary computational tools (software and hardware) to facilitate the 3D numerical modelling of Ground-Penetrating Radar (GPR) antennas.
- Create accurate 3D Finite-Difference Time-Domain (FDTD) models of widely-used high-frequency commercial GPR antennas.
- Validate the antenna models using real data from actual GPR systems. A comprehensive validation should include a range of different targets and environments typically encountered in high-frequency GPR surveys.
- Use the antenna models to investigate the amplitude and waveshape information of target responses.
- Use the antenna models to analyse the radiation dynamics of the antennas in typical GPR environments.

1.2 OVERVIEW OF THE THESIS

At the beginning of each individual chapter an overview of the chapter is presented and at the end of each chapter a summary of the main points and conclusions from that chapter is given. The following paragraphs are intended to provide a brief overall view of the structure and content of the entire thesis.

Chapter 2 introduces GPR by presenting some history and typical applications. The focus of the chapter is on the basic principles of operation of GPR in terms of the propagation of electromagnetic waves in different materials. The components of an actual GPR system are identified and the importance of the antennas to the performance of a GPR system is discussed.

Chapter 3 focuses on the FDTD method as a numerical modelling technique for GPR simulations. The chapter begins the discretisation of Maxwell's curl equations and a description of the Yee algorithm. The importance of correctly modelling the constitutive relations is discussed, and the advantages and disadvantages of the FDTD method are analysed.

Chapter 4 presents a review of research into the numerical modelling of GPR, with specific focus on the modelling of GPR antennas.

Chapter 5 discusses the development of the computational tools used to create models of GPR antennas.

Chapter 6 describes the initial development of models of two commercial GPR antennas. The process used to create the models, including how the geometry and electrical characteristics of each antenna was determined and how these physical features were described in the models, is discussed. Initial validations of the models using their cross-talk responses are shown, and the chapter concludes with a sensitivity analysis of unknown parameters in the models.

Chapter 7 describes an optimisation technique used to find optimum values for the unknown parameters in the antenna models. The results of the optimisation are presented in terms of improved modelled cross-talk responses.

Chapter 8 focuses on further validation of the antenna models through a series of experiments using emulsions to simulate the electrical properties of real materials. The experimental setups are replicated in numerical models, which include the optimised antenna models, and the modelled responses are then compared with data collected from the experiments using real GPR systems.

Chapter 9 presents an application of the validated antenna models. The models are used to investigate the radiation dynamics of the antennas. Radiation patterns in free-space, and over lossless and low-loss half-spaces, are studied. In addition, time domain snapshots of current flow on the surface of the antenna bowties, as well as time domain snapshots of the field propagation, are analysed.

Finally, Chapter 10 summarises the conclusions from each chapter and provides recommendations for further research.

2

THE PRINCIPLES AND PRACTICE OF GROUND-PENETRATING RADAR

This chapter introduces the theoretical principles of the operation of GPR along with the practical features of GPR systems. The chapter begins with a brief summary of the history of GPR and an overview of applications. The basic principles of the propagation of electromagnetic waves are then described along with the constitutive parameters of typical materials encountered with GPR. The transmitter and receiver antennas are highlighted as key to the performance of GPR systems, with frequency and resolution discussed. Finally, surveying methods, data processing and interpretation methods are reviewed.

2.1 HISTORY AND APPLICATIONS

GPR is part of a family of non-destructive electromagnetic techniques used for investigating objects buried beneath the subsurface or located within a visually opaque structure. The objectives and principles of operation of GPR are similar to conventional radar but applied to subsurface features. The development of conventional radar—an acronym for radio detection and ranging— was rapidly accelerated around the time of World War II, principally through the need to locate enemy aircraft. This advancement in radar technology was subsequently transferred to civil applications, and it was in the post-war period that there were reported attempts of measuring subsurface features with radio waves (El-Said, 1956). However, these were not the first attempts at such work, as a patent which appeared in 1910 by Leimbach and Lowy (Daniels, 2004) revealed similar efforts. Throughout the 1960s and early 1970s researchers used radio waves to probe ice and other favourable geological materials. With a better understanding of the electrical properties of geological materials, and advances in technology, commercial GPR systems from the likes of GSSI, MALÅ, and Sensors and Software Inc. were developed. Annan (2002) provides a comprehensive breakdown of the history of GPR through the decades from both a commercial and research perspective.

Currently, GPR has many well-developed applications in archetypal fields such as civil engineering and geophysics, as well as emerging uses in less obvious areas. The following list is an overview of some of these applications.

- Infrastructure assessment
  - Concrete inspection: location of rebars, conduits, post-tension cables, and voids
  - Road inspection: determination of layer thicknesses
  - Railway inspection: location and assessment of condition of track ballast
- Buried utilities: Mapping and location of pipes, cables, and voids
- Mining and quarrying: Mineral exploration, mine safety
- Ice and snow: ice profiling and glaciology studies
- Archaeology: Mapping, exploration, and excavation planning
- Geotechnical and environmental: Groundwater mapping, contaminated land assessment, and bedrock profiling
- Military and security: Location of landmines, detection of human bodies and location of hidden tunnels

The types of targets and features investigated in these applications can vary in size and depth from targets a few centimetres in diameter buried just below the subsurface, to the profiling of geological materials hundreds of metres deep. The near-surface applications are typically those associated with civil engineering i. e., concrete inspection, and the location of buried utilities. The wide range of applications coupled with the continual development of GPR systems technology means there are many diverse areas of research linked to GPR. Daniels (2004) states that GPR,

> ...embraces a range of specialisations such as electromagnetic propagation in lossy media, ultra-wideband antenna technology and radar systems design, discriminant waveform signal and image processing.

2.2 WAVE PROPAGATION

The basic premise of GPR is the propagation of electromagnetic waves in different materials. In this section, the theory of the propagation of electromagnetic waves, material properties and the constitutive relations are introduced and discussed within the context of GPR. In Chapter 3 these topics are then further developed with the introduction of Maxwell's equations and the FDTD method.

GPR uses electromagnetic fields to investigate lossy dielectric materials and detect structural features as well as changes in material properties. This is

commonly achieved using reflection measurements, but transmission measurements can also be used e. g., in borehole applications. GPR operates over a finite frequency range in the microwave region of the electromagnetic spectrum, from approximately 1 MHz to 5 GHz. The transmitted signal travels through a material and is scattered and/or reflected by changes in the electrical properties of the material.

2.2.1 *Material characterisation*

Materials are characterised as *dielectrics*, *magnetics*, or *conductors* depending on whether *polarisation*, *magnetisation*, or *conduction* is the predominant phenomenon (Balanis, 1989).

Dielectrics

Dielectric materials (insulators) contain bound positive and negative charges that are not free to travel. However, when an external electric field is applied, the centroids of these charges can shift slightly in position creating numerous electric dipoles. There are three mechanisms that produce electric polarisation in dielectrics: dipole polarisation, ionic polarisation, and electronic polarisation. For GPR frequencies, dipole polarisation is the predominant mechanism where the dipoles in the material align with an applied electric field. Such materials are known as *polar*, and water is a typical example.

The free-space relationship between an applied electric field and the electric flux density is given by one of the constitutive relations (2.1). In this thesis the notation $\vec{E} = \vec{E}(x, y, z; t)$ is used to denote a field quantity that is a function of space and time.

$$\vec{D} = \epsilon_0 \vec{E}, \tag{2.1}$$

where:

$\vec{D}$ = electric flux density (C/m^2)

ϵ_0 = permittivity of free-space (8.854×10^{-12} F/m)

$\vec{E}$ = electric field intensity (V/m)

The electric polarisation in a dielectric changes this relationship and a polarisation vector is added (2.2).

$$\begin{aligned} \vec{D} &= \epsilon_0 \vec{E} + \vec{P}, \\ \Leftrightarrow \vec{D} &= \epsilon_0 \vec{E} + \epsilon_0 \chi_e \vec{E}, \\ \Leftrightarrow \vec{D} &= \epsilon_0 (1 + \chi_e) \vec{E}, \\ \Leftrightarrow \vec{D} &= \epsilon_s \vec{E}, \end{aligned} \tag{2.2}$$

where:

$\vec{P}$ = electric polarisation (C/m^2)

χ_e = electric susceptibility (dimensionless)

ϵ_s = static permittivity (F/m)

The static permittivity is usually given as a dimensionless relative value called the relative static permittivity ϵ_r or dielectric constant (2.3).

$$\epsilon_r = \frac{\epsilon_s}{\epsilon_0} \tag{2.3}$$

The relative static permittivity of a dielectric indicates the relative charge storage capacity of the material.

Magnetics

Magnetic materials can exhibit magnetic polarisation when subjected to a magnetic field. In a similar manner to the electric flux density in a dielectric material, the free-space relationship between an applied magnetic field and the magnetic flux density is given by one of the constitutive relations (2.4).

$$\vec{B} = \mu_0 \vec{H}, \tag{2.4}$$

where:

$\vec{B}$ = magnetic flux density (Wb/m^2)

μ_0 = permeability of free-space ($4\pi \times 10^{-7}$ H/m)

$\vec{H}$ = magnetic field intensity (A/m)

Most materials encountered with GPR have a permeability close to free-space and are, therefore, assumed non-magnetic, which is the case for all the materials used in this research. However, when materials contain more than 10–20% by volume of magnetic minerals (magnetite, hematite, or maghemite), e. g. iron-rich sand, rusting steel rebars, their permeability must be considered (Goodwin and Cassidy, 2008).

Conductors

Conductors are materials where the predominant characteristic is the motion of electric charges and the creation of current flow. In a conductor there are a large number of free electrons which drift randomly producing a net zero current. When an electric field is applied the electrons still move randomly but drift in the negative direction of the electric field producing a conduction current in the conductor. The conductivity, σ, of a conductor characterises the free electron conductive properties. The conductivity can be used to relate the electric field intensity to the conduction current density and is given by one of the constitutive relations (2.5) which is the generalised case of the circuit relation known as Ohm's Law.

$$\vec{J}_c = \sigma \vec{E}, \tag{2.5}$$

where:

$\vec{J}_c$ = conduction current density (A/m^2)

σ = electric conductivity (S/m)

$\vec{E}$ = electric field intensity (V/m)

Permittivity, permeability, and conductivity are known as the constitutive parameters and have so far been assumed to be scalar quantities. In Chapter 3 it is shown that the constitutive parameters can be tensors, and one of their important dependancies is frequency.

2.2.2 *Wave velocity and attenuation*

The velocity and attenuation of electromagnetic waves propagating through a material are determined by the material properties permittivity, permeability, and conductivity. For GPR the permittivity and conductivity have the most significant impact. The velocity v (m/s) of an electromagnetic wave in a material

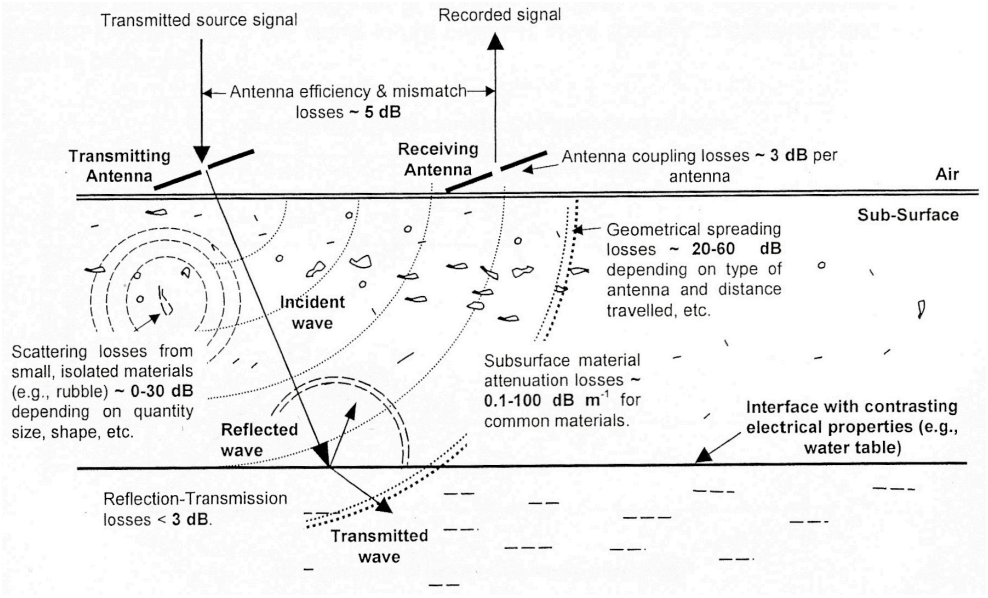

Figure 1: GPR signal attenuation paths (Cassidy, 2008)

is given by (2.6), which is developed from the solution of a uniform plane wave propagating in a lossy material (Balanis, 1989).

$$v = c\left(\frac{\mu_r \epsilon_r}{2}\left(\sqrt{1+\left(\frac{\sigma}{\omega}\right)^2}+1\right)\right)^{-\frac{1}{2}}, \tag{2.6}$$

where:

c = velocity of light in free-space $(299,792,458\ m/s)$

μ_r = relative permeability (dimensionless)

ω = angular frequency (rad/s)

For materials with negligible conductivity, and a permeability close to that of free-space, the equation for the velocity (2.6) simplifies, and the velocity can be calculated using only the permittivity of the material.

The depth of penetration or range of a GPR system is primarily governed by the attenuation of the transmitted wave as it travels from transmitter to receiver. The attenuation[1] α (dB/m) of electromagnetic waves in a material is

1 The attenuation coefficient is often expressed in Nepers-per-metre (Np/m) but decibels-per-metre (dB/m) is a much more practical unit for GPR.

given by (2.7), which is again developed from the solution of a uniform plane wave propagating in a lossy material (Balanis, 1989).

$$\alpha = 8.686\omega \sqrt{\frac{\mu_0 \mu_r \epsilon_0 \epsilon_r}{2} \left(\sqrt{1 + \left(\frac{\sigma}{\epsilon_0 \epsilon_r \omega} \right)^2} - 1 \right)} \tag{2.7}$$

From (2.7) it is clear that higher frequencies will suffer more attenuation that lower frequency waves. The ratio $\frac{\sigma}{\epsilon_0 \epsilon_r \omega}$ is called the loss tangent and determines whether a material is low-loss, indicated by a loss tangent of less than one.

The attenuation of electromagnetic waves in a material is one of the contributors to the *total path loss* which is given by (2.8) (Daniels, 2004). Figure 1 provides a graphical view of the loss mechanisms that contribute to the *total path loss*.

$$L_T = L_e + L_m + L_{t1} + L_{t2} + L_{t3} + L_s + L_a + L_{sc}, \tag{2.8}$$

where:

L_e = antenna radiation efficiency (dB)

L_m = antenna reflection (mismatch) efficiency (dB)

L_{t1} = transmission from air to material 1 (dB)

L_{t2} = transmission from material 1 to material 2 (dB)

L_{t3} = retransmission from material 1 to air (dB)

L_s = spreading loss (dB)

$L_a = \alpha$ = material attenuation (dB)

L_{sc} = scattering loss (dB)

L_e is a loss associated with the antenna radiation efficiency which is a measure of the conduction and dielectric losses in the antenna. The antenna radiation efficiency e_{cd}, given by (2.9), is defined as a ratio of the power delivered to the

antenna radiation resistance and power delivered to the antenna loss resistance.

$$e_{cd} = \frac{R_r}{R_r + R_L}, \tag{2.9}$$

where:

R_r = antenna radiation resistance (Ω)

R_L = antenna loss resistance (Ω)

The other antenna loss term L_m is due to reflections from a mismatch of impedances between the transmission lines feeding the antennas and the antenna elements.

The transmission and retransmission losses L_{t1}, L_{t2} and L_{t3} occur because the electromagnetic wave impinges upon interfaces of materials with contrasting electrical properties. The amount of energy reflected or transmitted is related to the reflection coefficient which is given by (2.10) for normal incident reflections[2].

$$R = \frac{Z_2 - Z_1}{Z_2 + Z_1}, \tag{2.10}$$

where:

Z_1 = intrinsic impedance of material 1 (Ω)

Z_2 = intrinsic impedance of material 2 (Ω)

The largest contributors to the total path loss are the last three losses in (2.8). The material attenuation L_a has been discussed and was given by (2.7). The spreading loss L_s is the amount of energy an electromagnetic wave looses as it travels outwards through the subsurface. L_s is a function of the type of antenna and the distance to the target.

The scattering loss L_{sc} can be explained by firstly considering the mechanism of scattering from a typical target. Scattering can occur from the target or feature of interest, as well as from other features of no interest. When an incident electromagnetic field encounters a target, a secondary scattered field propagates outward from the target. The larger the fraction of power that the target extracts from the incident field, the more detectable it is to GPR. The

2 The angle at which the minimum reflection coefficient occurs is known as Brewster's angle (Encyclopaedia Britannica, 2009).

relationship between the power in the incident field P_i and the power in the field scattered by the target is given by (2.11).

$$P_s = \xi A_e P_i, \tag{2.11}$$

where:

P_s = power of the scattered field (W)

P_i = power of the incident field (W)

ξ = power fraction, $0 \leqslant \xi \leqslant 1$ (m^{-2})

A_e = effective cross section (m^2)

The term ξA_e in (2.11) is known as the scattering cross section for the target. Annan (2005) reports on work originally by Mie, which investigated the scattering behaviour of a Perfect Electric Conductor (PEC) sphere of arbitrary dimension using sinusoidal excitation. When the dimensions of such a target are small compared to the excitation wavelength the response is called the Rayleigh response. When the dimensions of the target approach the excitation wavelength the response is called the Mie or resonant response. Finally, as the dimensions of the target become much larger than the excitation wavelength the response is called the optical response, and the scattering cross section becomes equal to the geometric cross section of the target. The Rayleigh region is of most interest to GPR, where $\xi A_e \propto f^4$ and hence a small increase in excitation frequency can result in a much more detectable target.

Scattering from objects of no interest can create problems in achieving a clear response from the target of interest. With GPR the electromagnetic waves are typically transmitted through complicated materials which have many small scale features with contrasting electrical properties. These features return weak, undetectable responses but extract energy from the electromagnetic waves. This energy is scattered or absorbed and is quantified by the scattering loss L_{sc} and known as clutter.

Having discussed the constitutive parameters and their effects on wave velocity and attenuation, Table 1 gives some typical values of permittivity, conductivity, and attenuation for common materials encountered with GPR. Velocities are typically quoted in metres-per-nanosecond (m/ns), and in this case the attenuation values are at a frequency of 1 GHz.

MATERIAL	ϵ_r	v (m/ns)	σ (mS/m)	α (dB/m)
Air	1	0.3	0	0
Clay (dry)	2-20	0.07-0.21	1-100	1-36
Clay (wet)	15-40	0.05-0.08	100-1000	42-252
Concrete (dry)	4-10	0.09-0.15	1-10	<1-5
Concrete (wet)	10-20	0.07-0.09	10-100	5-36
Fresh water	81	0.03	0.1-10	<1
Fresh water ice	3-4	0.15-0.17	1	<1
Granite (dry)	5-8	0.11-0.13	0.001-0.00001	<1-5
Granite (wet)	5-15	0.08-0.13	1-10	<1-4
Limestone (dry)	4-8	0.11-0.15	0.001-0.0000001	<1
Limestone (wet)	6-15	0.08-0.12	10-100	6-42
Sand (dry)	4-6	0.12-0.15	0.001-1	<1
Sand (wet)	10-30	0.05-0.09	0.1-10	<1-3
Sea water	81	0.03	4000	>600
Sea water ice	4-8	0.11-0.15	10-100	8-57
Soil (average)	16	0.08	5	2

Table 1: Typical material properties of common materials encountered with GPR (Cassidy, 2008)

2.2.3 *Mixtures of materials*

The materials encountered with GPR are rarely homogeneous and usually a mixture of many other materials or components. To determine GPR responses for such materials it is necessary to understand, at a macroscopic level, the electrical properties of mixtures of materials. The Topp equation (Topp et al., 1980), given by (2.12), is an empirical relationship that can be used to calculate bulk permittivity and conductivity values from volumetric water content.

$$\epsilon' = 3.03 + 9.3\ \theta_v + 146\ \theta_v^2 - 76.6\ \theta_v^3, \tag{2.12}$$

where:

ϵ' = apparent relative bulk permittivity

θ_v = volumetric water content

The Topp equation assumes a value of 3–4 for the relative permittivity at zero water content, and also assumes negligible conductivity.

Another commonly used mixing model is the Complex Refractive Index Model (CRIM) (Wharton et al., 1980), given by (2.13), which weights the relative permittivity based on the volume fraction and the square root of the complex permittivity of the material.

$$\epsilon_{mix} = \left(\sum_{i=1}^{N} \theta_i \sqrt{\epsilon_i} \right)^2, \tag{2.13}$$

where:

ϵ_{mix} = complex relative bulk permittivity

ϵ_i = complex relative permittivity of the ith component

θ_i = volume fraction of the ith component

The Bruggeman-Hanai-Sen (BHS) model (Hanai et al., 1960) is another mixing relationship which uses effective media theory to derive composite material properties from the constituents. The BHS model is further described in Chapter 8 where it is utilised for determining the permittivity and conductivity of emulsions composed of oil and water.

Figure 2: Annotated photograph of a typical GPR system (Geophysical Survey Systems, Inc., 2001)

2.3 GPR SYSTEMS

A typical GPR system consists of a control and display unit, and transmitting and receiving antennas as shown in Figure 2. The majority of GPR systems are based on an impulse time domain waveform where a broadband pulse is generated and transmitted via the transmitter antenna into the material to be investigated. The receiver antenna is then used to detect reflected signals which are then displayed on the control and display unit.

The antennas are key components of a GPR system and the most commonly used antenna is the bowtie dipole for ground-coupled applications. Horn antennas are also sometimes used for air-coupled applications. The transmitter and receiver antennas are usually of identical type and can be housed in the same enclosure or separately.

Figure 3 shows the signal paths for a configuration with separable transmitter and receiver antennas above a buried target. In the air, a spherical wave composed of the incident and reflected waves propagates upwards. In the ground, the transmitted signal is composed of two parts: a spherical body ground wave, and a planar wavefront travelling at the critical angle which links the spherical air wave and spherical ground wave. The first signal recorded by the receiver is usually the largest in amplitude and is called the direct wave. It is composed of the direct air wave and the direct ground or evanescent wave

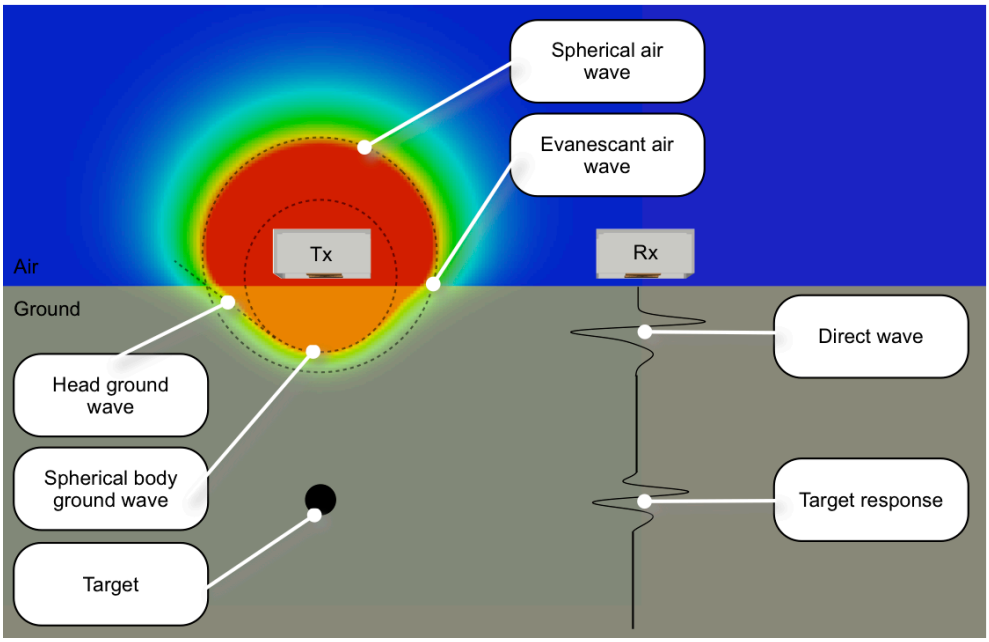

Figure 3: Wave propagation and received responses

which propagates along the air-ground interface. The reflection from the buried target or interface occurs later in received response and has a smaller amplitude due to the total path attenuation.

The resolution of a GPR system is a critical parameter as it determines how accurately targets can be located, and how much geometrical detail can be extracted. The overall resolution of the system is given by a vertical or depth resolution, and a horizontal or lateral resolution. To separately distinguish two identical targets it is widely recognised that their reflected pulses must be separated by half of their pulse width, where the pulse width is specified as the width of half the peak amplitude. Figure 4 shows two identical targets separated vertically by a distance Δr, and the same targets separated horizontally by a distance Δl.

For the vertical resolution the time difference Δt between the targets must be greater than half of the pulse width W. The travel time for the first target is given by (2.14), the travel time to the second target is given by (2.15), and hence the time difference can be calculated (2.16).

$$t_1 = \frac{2d}{v}, \tag{2.14}$$

$$t_2 = \frac{2d + 2\Delta r}{v}, \tag{2.15}$$

$$\Rightarrow \Delta t = \frac{2\Delta r}{v} \tag{2.16}$$

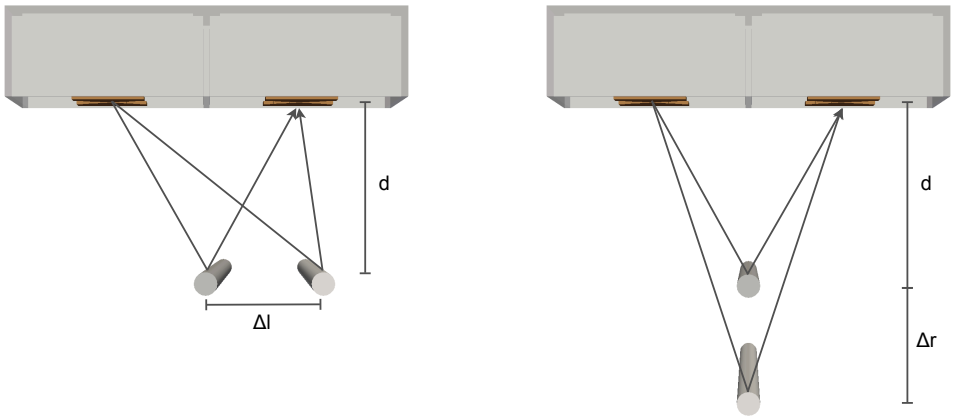

Figure 4: Horizontal and vertical resolution of a GPR system

This leads to a minimum vertical spacing of Δr given by (2.17).

$$\frac{W}{2} = \frac{2\Delta r}{v},$$

$$\Leftrightarrow \Delta r \geqslant \frac{vW}{4} \tag{2.17}$$

The vertical resolution is, therefore, a function of the pulse width and hence the frequency of the transmitted pulse as well as the velocity of the material.

For the horizontal resolution, the travel-time to first target is given by (2.18), the travel time to the second target is given by (2.19), and when Δl is small compared to d (which is generally the case in practice), the time difference is given by (2.20).

$$t_1 = \frac{2d}{v}, \tag{2.18}$$

$$t_2 = \frac{2\left(\sqrt{d^2 + \Delta l^2} - d\right)}{v}, \tag{2.19}$$

$$\Rightarrow \Delta t \approx \frac{\Delta l^2}{vd} \tag{2.20}$$

This leads to a horizontal resolution is given by (2.21).

$$\Delta l \geqslant \sqrt{\frac{vdW}{2}} \tag{2.21}$$

The horizontal resolution is a function of the pulse width, velocity, and the distance of the targets from the antennas.

2.4 DATA COLLECTION AND PROCESSING

There are a number of different surveying methods and antenna orientations that can be used when carrying out GPR surveys. Each can be exploited to enhance the responses of certain types and orientations of features and targets.

The three common GPR surveying methods—Common Offset (CO) reflection, Common Mid-Point (CMP) reflection, and Wide-Angle Reflection-Refraction (WARR)—are shown in Figure 5. For each method a single survey line will produce a sectional B-scan image and a number of parallel survey lines can be processed to produce a 3D image. With the CMP reflection method, the transmitter and receiver separation is increased about a common mid-point on the survey line. This method is typically used to give a velocity depth profile for a material about a common point. With the WARR method, the transmitter antenna is fixed and the receiver antenna is moved along the survey line. The CO reflection method is used most in practice as commercial GPR systems typically have transmitter and receiver antennas housed in the same enclosure.

The transmitter and receiver antennas can also be used in different orientations as shown in Figure 6. Altering the orientation of the antennas can significantly enhance responses from certain types of targets because the radiation patterns of typical GPR antennas are not omnidirectional. This means the antennas radiate or receive electromagnetic waves more effectively in some directions than others. The broadside and end-fire orientations tend to be used for detecting targets oriented parallel to the antenna axis e. g., pipes and elongated features. The cross polarised orientation has been used for crack detection on airport runways (Birtwisle and Utsi, 2008) and is generally used for detecting randomly orientated objects (Cassidy, 2008). Chapter 9 presents a detailed look at the radiation patterns of the real GPR antennas modelled in this thesis.

The interpretation of GPR data can be significantly improved by the use of basic onsite data processing as well as more advanced offsite post-processing. It is important to realise that if processing techniques are not applied carefully, important features can be removed from the data and worse, spurious features may be introduced into the data. Many of the techniques used for processing GPR data have evolved from well-established seismic data processing methods, a comprehensive treatment of which can be found in Yilmaz (2001). The following techniques would be considered basic processing methods which would typically be applied to the GPR data in real-time onsite, using software built into the GPR system control and display unit. The order that the processing techniques are described is the order that they would be typically applied. The data used to demonstrate the processing techniques is from a concrete slab containing

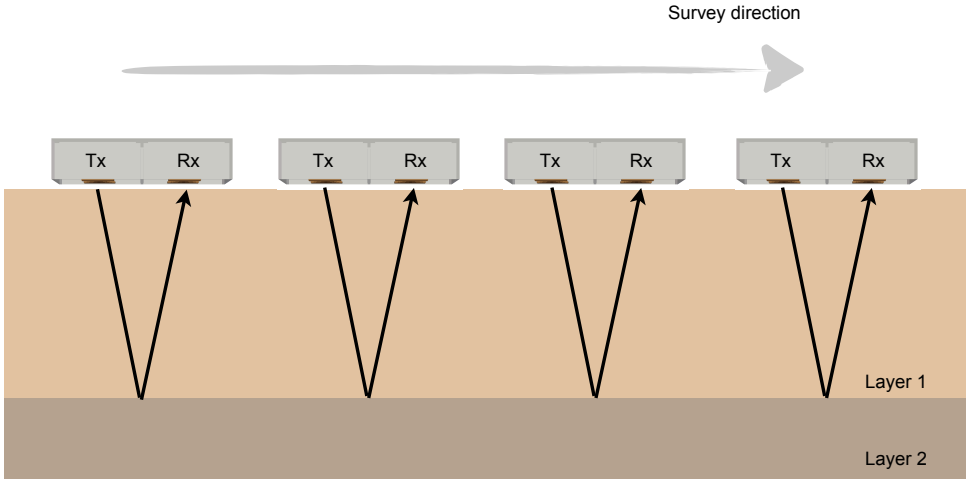

(a) Common Offset (CO) reflection

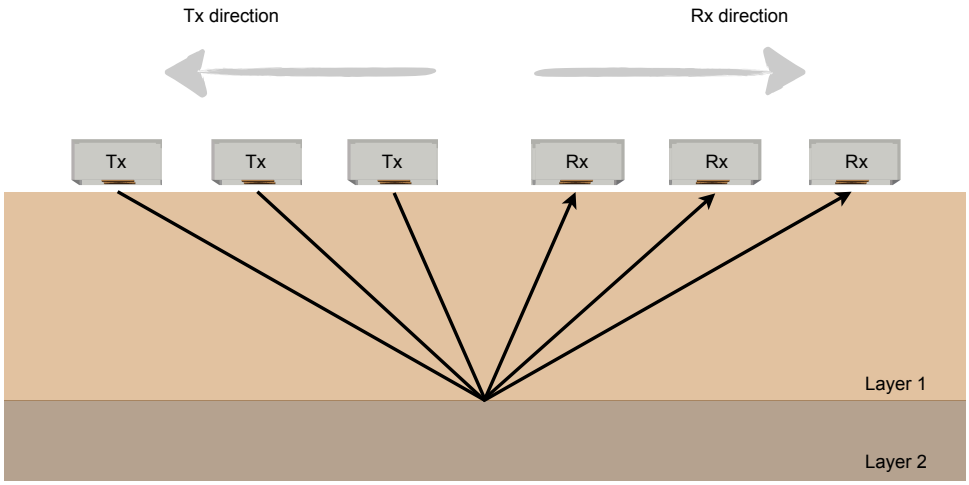

(b) Common Mid-Point (CMP) reflection

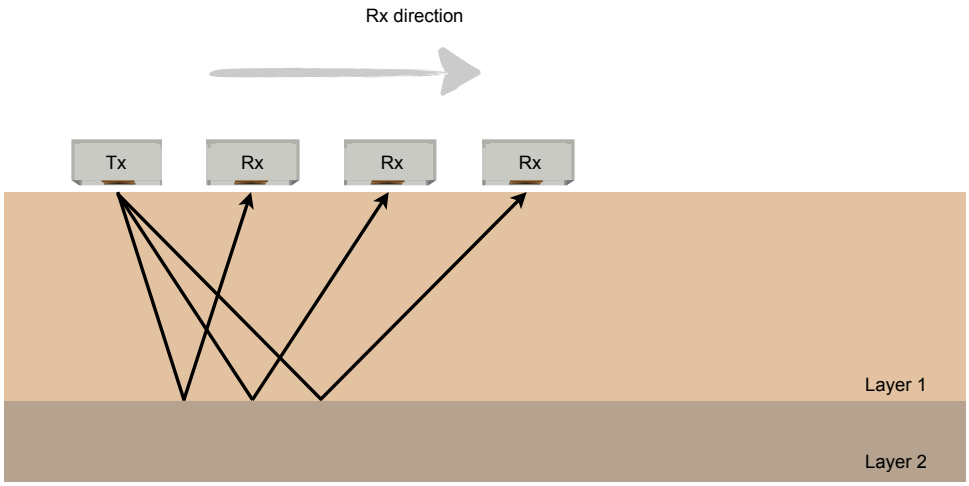

(c) Wide-Angle Reflection-Refraction (WARR)

Figure 5: Surveying methods

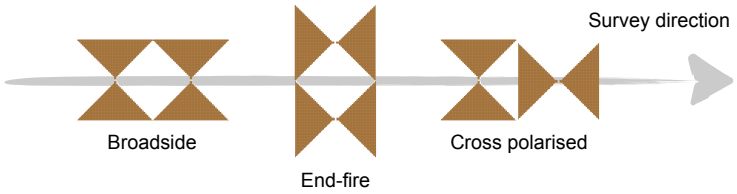

Figure 6: Transmitter and receiver antenna orientations

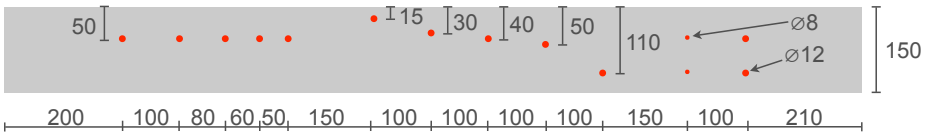

Figure 7: Location of rebars in concrete slab (all dimensions in mm)

steel rebars at various horizontal and vertical spacings, as shown in Figure 7. A GSSI 2.6 GHz antenna was used in all the examples.

Averaging/stacking

Averaging, or stacking is used to reduce random noise by averaging several A-scans together.

Time-zero correction

Time-zero correction is the process of adjusting the response so that time-zero corresponds to the reflection from the surface of the ground or structure that the antenna is in contact with. A correct time-zero adjustment is critical for accurate depth determination, especially for near-surface targets. Yelf (2004) demonstrated that because the direct wave from the antenna is affected by the material the antenna is in contact with, the time-zero correction is material dependent. Figure 8 shows an example of a B-scan before and after time-zero processing.

Time-varying gain

It has been shown that electromagnetic waves can be rapidly attenuated as they propagate through different materials. The response from a target can therefore be much smaller in amplitude than the direct wave. To clearly display both these responses a time varying gain function is typically applied to the data. The early time part of the data that contains the direct wave may have some attenuation applied and the late time response from a target may have

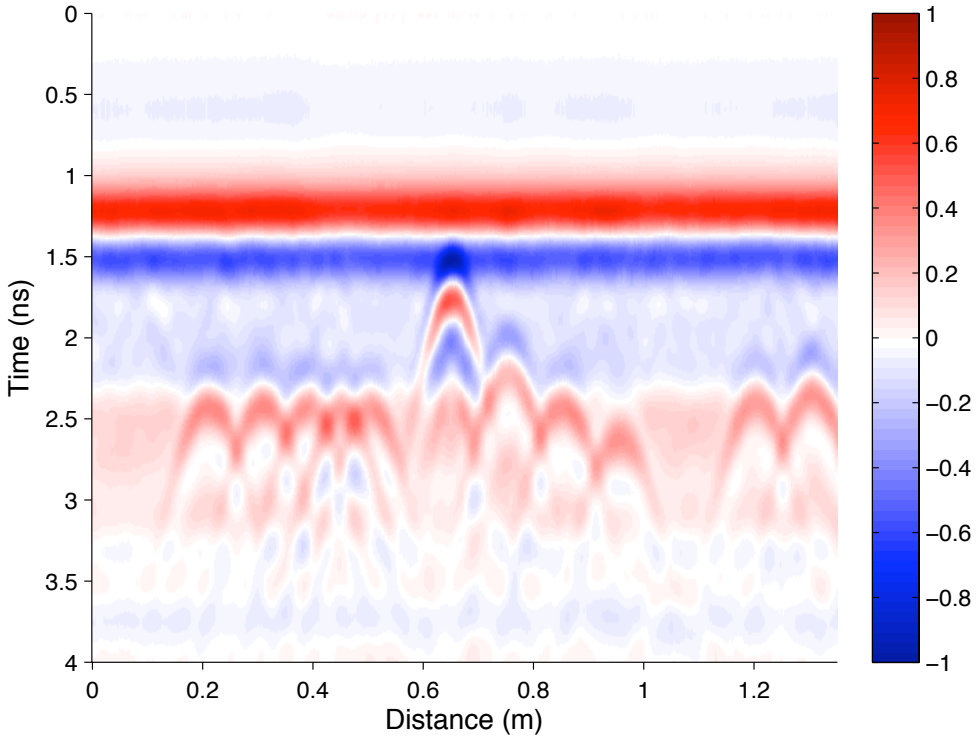

(a) Before time-zero correction

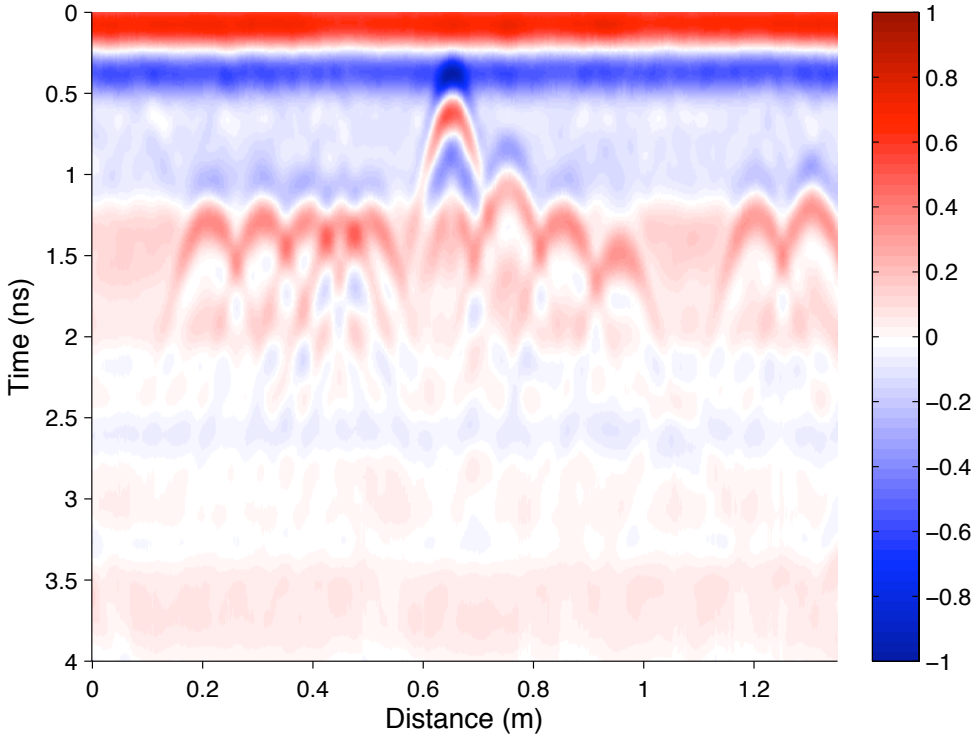

(b) After time-zero correction

Figure 8: B-scan: Time-zero correction

some gain applied. Figure 9 shows an example of a B-scan with insufficient and excessive gain applied.

Mean value/background removal

Mean value, or background removal is a type of spatial filtering used to reduce clutter and remove the direct wave from the response. It should be used carefully where features of interest are planar interfaces, as these responses can be removed by this type of filtering (Daniels, 2004). Figure 10 shows an example of a B-scan before and after background removal.

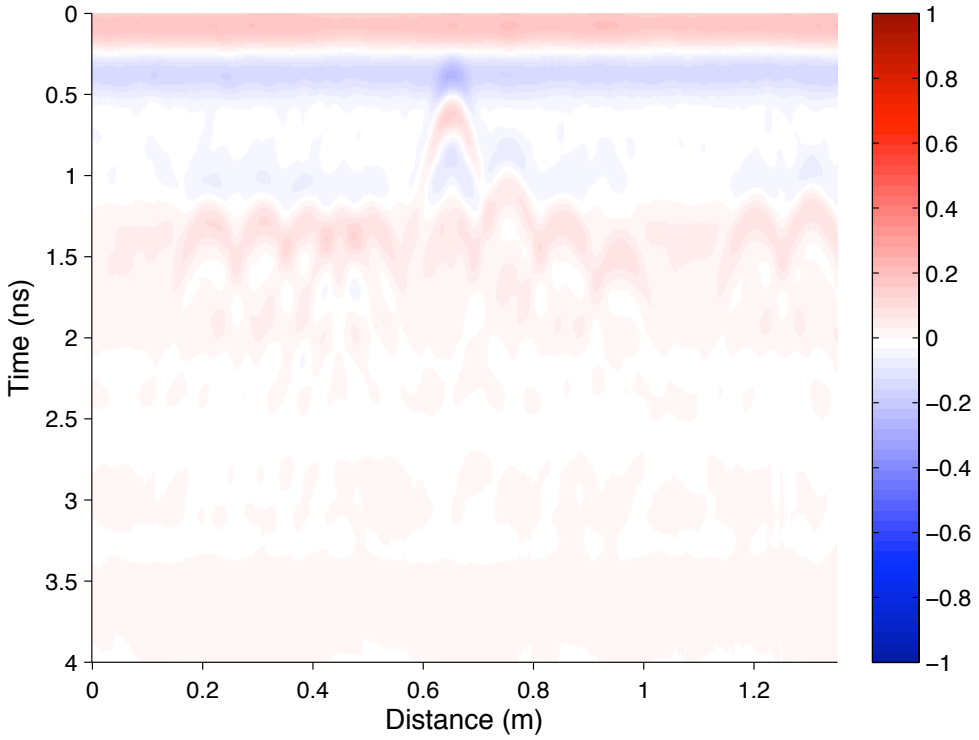

(a) Insufficient gain

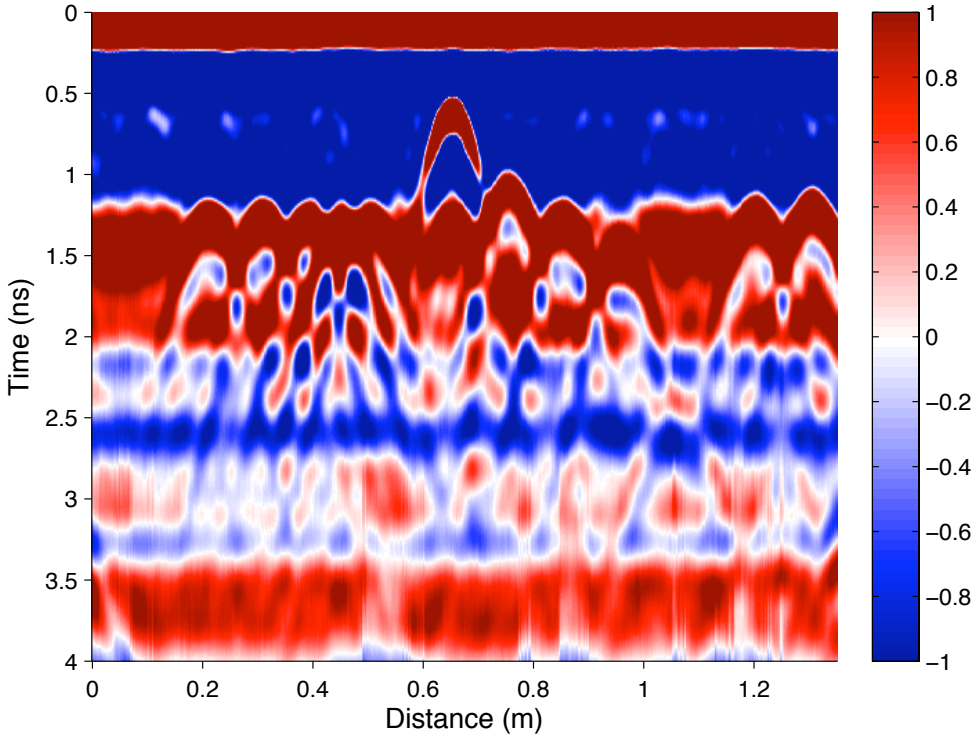

(b) Excessive gain

Figure 9: B-scan: Application of time-varying gain

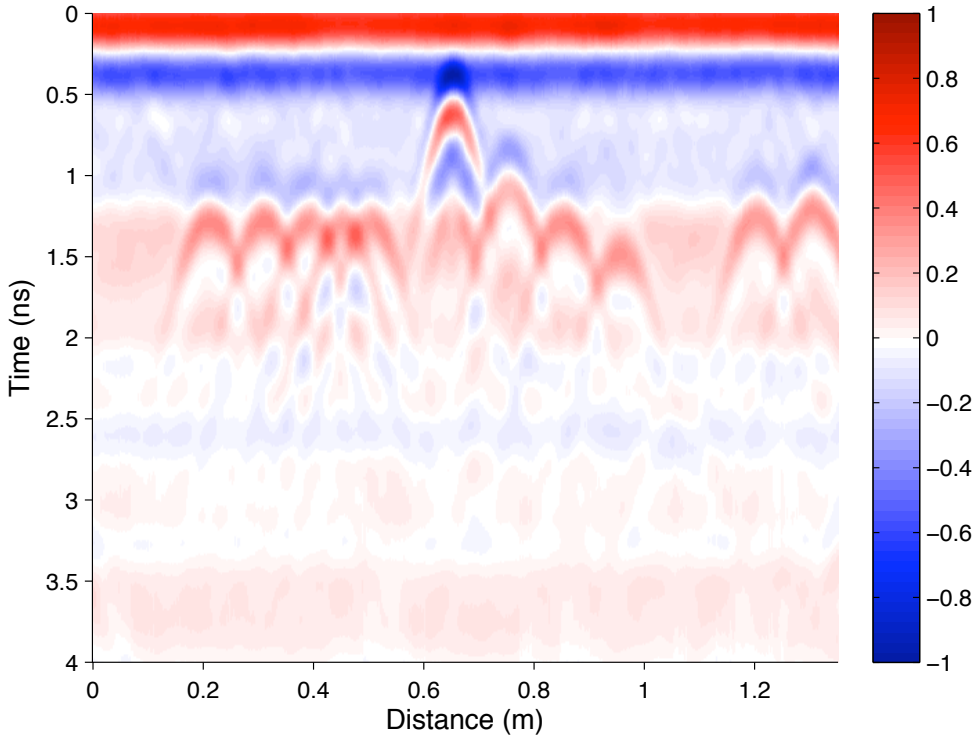

(a) Before background removal

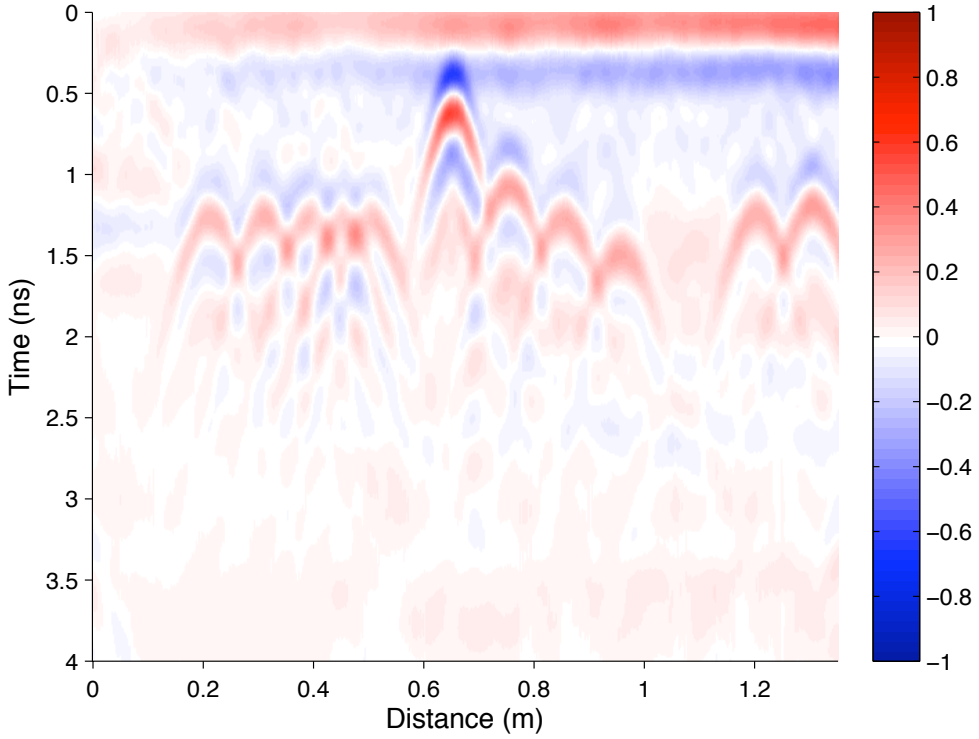

(b) After background removal

Figure 10: B-scan: Mean value/background removal

Filtering

Frequency filtering is a common signal processing technique and when correctly applied can greatly enhance features in GPR data. Typically, simple low and high-pass filters are used and can be applied vertically to each A-scan or horizontally across a B-scan. A *dewow* high-pass filter is commonly applied to remove very low frequency components which can be associated with antenna tilt and inductive phenomena (Annan, 2005). Similarly, a low-pass filter can be applied to reduce high-frequency noise.

More advanced processing techniques can be applied after a GPR survey using dedicated signal processing software. Deconvolution and migration are two examples of such techniques which are briefly described here. The reader is once again referred to Yilmaz (2001) for a full treatment of the subject.

The response recorded by a GPR system can be considered the output of a series of filters fed by the transmitted pulse. The aim of deconvolution, or wavelet optimisation, is to reverse some of this filtering process by deconvolving out the antenna response and, thus, increasing the temporal resolution of the data.

Migration is an imaging technique used to reconstruct the radar reflectivity distribution of the subsurface. It requires knowledge of the velocity structure of the subsurface. Assuming the correct velocity, the migration of a hyperbola (the response from a cylindrical target) results in the hyperbola being collapsed into a shape which approximates the geometrical representation of a cylinder. Figure 11 demonstrates the migration of several rebars using a Kirchhoff migration technique (Yilmaz, 2001).

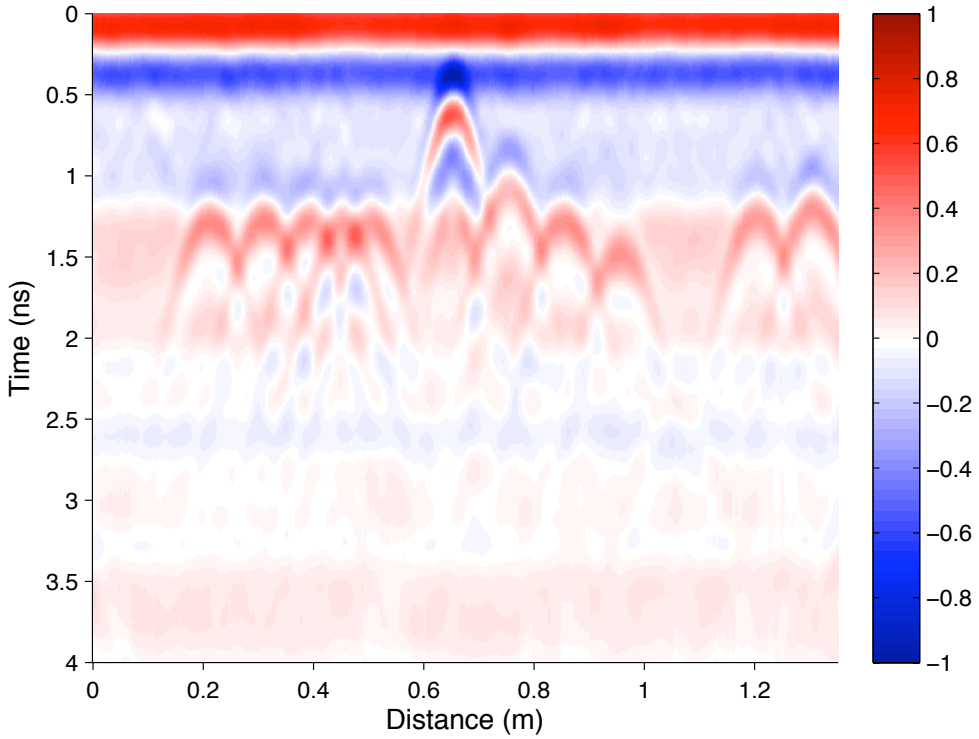

(a) Before migration

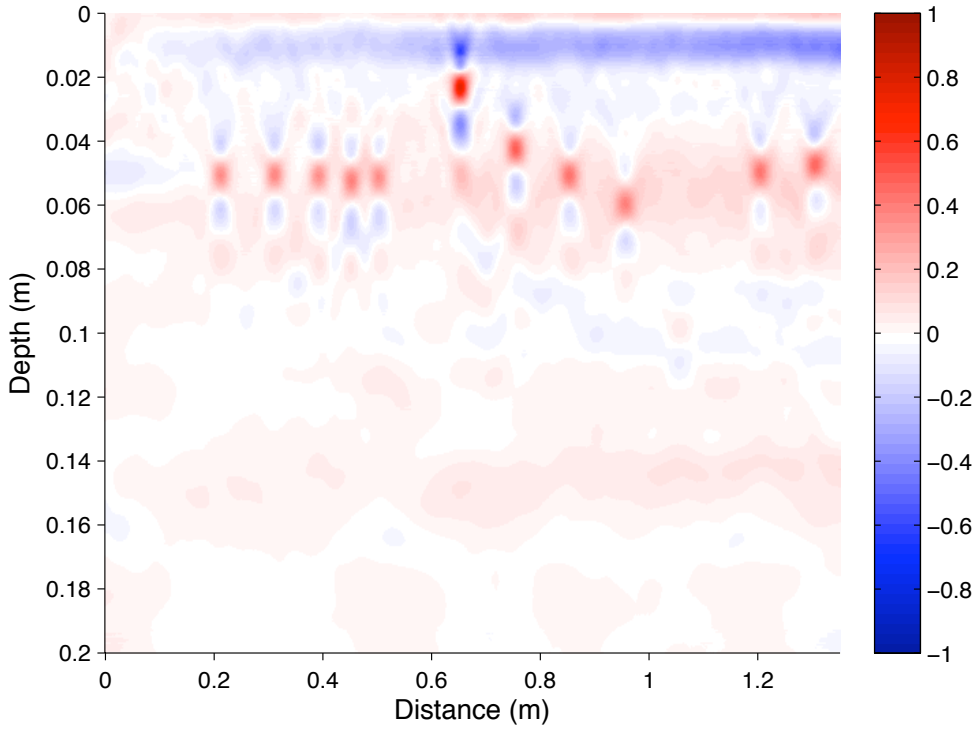

(b) After migration

Figure 11: B-scan: Migration processing

2.5 SUMMARY

GPR is a non-destructive electromagnetic technique used to detect objects buried beneath the subsurface or in a visually opaque material. The aim of this chapter was to describe the governing principles of the operation of GPR and give an overview of the wide ranging applications of GPR. GPR is mainly used in the fields of engineering and geophysics, where the engineering applications tend to be near-surface detection and identification of targets, and the geophysical applications are often much deeper probing of the earth. There are a wide range of diverse areas of research linked to GPR, e. g., electromagnetic propagation in lossy materials, ultra-wideband antenna technology and signal and image processing.

The suitability and success of GPR in a specific environment is largely dependent on the material properties of permittivity, permeability, and conductivity. These parameters control the velocity and attenuation of the electromagnetic waves and, hence, determine the potential penetration depth and resolution. Velocity and attenuation are also influenced by the frequency of the electromagnetic waves.

The GPR transmitter and receiver antennas are critical components to the overall performance of a GPR system. It is crucial to use a GPR system with a frequency of operation suitable for the environment so that the required depth and resolution of the target can be achieved. As GPR antennas are directional, it is important to use an orientation suitable for the target to be detected.

Despite sophisticated processing algorithms, the interpretation of GPR data is still application specific and highly dependent on the skill, experience and knowledge of the individual user. This is one of the key arguments for developing accurate numerical models. Numerical modelling can feed useful developments into all of the fields of research linked to GPR.

3

MAXWELL'S EQUATIONS AND THE FDTD METHOD

This chapter begins with an overview of the laws governing electromagnetic field theory. Material properties, the constitutive relations and, specifically, dispersion are then discussed. The FDTD method and Yee's algorithm are then described along with the general advantages and disadvantages of the FDTD method as a Computational Electromagnetics (CEM) technique. Lastly, numerical dispersion, errors, stability considerations and absorbing boundaries associated with the FDTD method are analysed.

3.1 MAXWELL'S EQUATIONS

Electromagnetic field theory is governed by a set of basic laws which were written in their final form by Scottish physicist and mathematician, James Clerk Maxwell. These laws were formulated from a series of experiments carried out in the nineteenth century by scientists including: Ampere, Faraday, Gauss, Lenz, Coulomb, and Volta. Most texts on the subject of electromagnetics begin with a comprehensive description of these laws which are commonly referred to as *Maxwell's equations*. As such, the following is a concise study of Maxwell's equations within the context of GPR modelling and the FDTD method, a more in-depth treatment is provided in Balanis (1989), Kraus (1991), or Taflove and Hagness (2005).

Maxwell's equations can be formulated in either the time or frequency domain. The frequency domain formulation provides a single harmomic solution and must, therefore, be repeated for all frequencies of interest. Whereas the time-domain representation, which is the basis of the FDTD method, generates a time sequence which can be Fourier transformed to provide a single solution for all frequencies of interest. This is well suited to GPR problems which typically involve an impulse excitation.

Maxwell's equations can be given in both integral and differential form. In this study a description of each equation is followed intuitively by the integral form. The differential form of each equation is also given as it is this form that leads to the derivation of the FDTD method.

3.1.1 *Gauss's Law for electric fields*

Gauss's Law for electric fields states that the total electric flux leaving a closed surface is proportional to the charge enclosed by the surface, which is given by (3.1).

$$\iint \vec{D} \cdot \vec{ds} = \iiint \rho dv \tag{3.1a}$$

$$\nabla \cdot \vec{D} = \rho \tag{3.1b}$$

where:

$\vec{D}$ = electric flux density (C/m^2)

$\vec{ds}$ = vector magnitude and direction of infinitesimal surface area (m^2)

ρ = charge density (C/m^3)

dv = infinitesimal volume (m^3)

3.1.2 *Gauss's Law for magnetic fields*

Gauss's law for magnetic fields states that the total magnetic flux leaving a closed surface must equal zero, which is given by (3.2).

$$\iint \vec{B} \cdot \vec{ds} = 0 \tag{3.2a}$$

$$\nabla \cdot \vec{B} = 0 \tag{3.2b}$$

where:

$\vec{B}$ = magetic flux density (Wb/m^2)

The important difference between the electric and magnetic laws is that no Gaussian surface can contain an isolated magnetic charge – magnetic charges can only exist in pairs.

3.1.3 *Ampere's Law*

Ampere's Law relates the integrated magnetic field around a closed loop to the electric field passing through the loop, which is given by (3.3).

$$\oint \vec{H} \cdot \vec{dl} = \iint \left(\vec{J}_S + \vec{J}_C + \frac{\partial \vec{D}}{\partial t} \right) \cdot \vec{ds} \tag{3.3a}$$

$$\nabla \times \vec{H} = \vec{J}_S + \vec{J}_C + \frac{\partial \vec{D}}{\partial t} \tag{3.3b}$$

where:

$\vec{H}$ = magnetic field (A/m)

$\vec{J}_S$ = impressed (source) electric current density (A/m^2)

$\vec{J}_C$ = electric conduction current density (A/m^2)

$\frac{\partial \vec{D}}{\partial t}$ = electric displacement current density (A/m^2)

The electric displacement current density represents the displacement of charges, whereas the electric conduction current density represents the flow of electrons.

3.1.4 *Faraday's Law*

Faraday's Law relates the rate of change of magnetic flux through a closed loop to the Electromotive Force (EMF) around the loop, which is given by (3.4).

$$\oint \vec{E} \cdot \vec{dl} = -\iint \left(\vec{M}_S + \frac{\partial \vec{B}}{\partial t} \right) \cdot \vec{ds} \tag{3.4a}$$

$$\nabla \times \vec{E} = -\vec{M}_S - \frac{\partial \vec{B}}{\partial t} \tag{3.4b}$$

where:

$\vec{M}_S$ = impressed (source) magnetic current density (A/m^2)

$\frac{\partial \vec{B}}{\partial t}$ = magnetic displacement current density (A/m^2)

The impressed magnetic current density $\vec{M}_S$ is not a physically realisable quantity, but was introduced to balance Ampere's and Faraday's Laws (Balanis, 1989).

3.1.5 *Constitutive relations*

The constitutive relations quantify the physical properties of materials by providing a macroscopic description of how their charged particles respond *en masse* to the application of electromagnetic fields. The constitutive relations were introduced in Chapter 2 as scalar quantities but are given in (3.5) in there full tensor form.

$$\vec{J}_C = \bar{\bar{\sigma}} * \vec{E} \tag{3.5a}$$

$$\vec{D} = \bar{\bar{\epsilon}} * \vec{E} \tag{3.5b}$$

$$\vec{B} = \bar{\bar{\mu}} * \vec{H} \tag{3.5c}$$

where a star $*$ denotes convolution and a double bar $\bar{\bar{}}$ denotes a tensor quantity. In general, the constitutive parameters can each be a function of: the position within a material (*homogeneity*); the direction of an applied field (*isotropy*); the strength of an applied field (*linearity*); and frequency (*dispersivity*). Most materials are linear, homogeneous, and isotropic, hence the constitutive parameters reduce to scalar quantities. However, the property of dispersion, which describes the condition when the wavelength λ of a propagating wave varies with frequency f, cannot be disregarded.

The *dispersion equation*s for complex permittivity and complex conductivity are given by (3.6).

$$\tilde{\epsilon} = \epsilon' - j\epsilon'' \tag{3.6a}$$

$$\tilde{\sigma} = \sigma' - j\sigma'' \tag{3.6b}$$

where a tilde $\tilde{}$ denotes a frequency domain quantity. The dispersion equations can then be substituted into the phasor form of Ampere's Law (3.3b) yielding (3.7).

$$\nabla \times \tilde{H} = \tilde{J}_S + (\sigma' - j\sigma'')\tilde{E} + j\omega(\epsilon' - j\epsilon'')\tilde{E} \tag{3.7}$$

from which:

$$\sigma' - j\sigma'' + j\omega(\epsilon' - j\epsilon'') \equiv \sigma_e + j\omega\epsilon_e$$

where:

ϵ_e = real effective permittivity

σ_e = real effective conductivity

Thus, the real effective permittivity and conductivity are defined by (3.8).

$$\epsilon_e = \epsilon' - \frac{\sigma''}{\omega} \tag{3.8a}$$

$$\sigma_e = \sigma' + \omega\epsilon'' \tag{3.8b}$$

When measurements are made on a conducting dielectric it is these effective constitutive parameters that are measured and their real and imaginary components cannot be separated.

The dispersion of the relative permittivity of many materials may be described using relations such as the well-known *Debye equation* (Debye, 1929) given by (3.9).

$$\begin{aligned} \tilde{\epsilon_r} &= \epsilon'_r - j\epsilon''_r, \\ \Leftrightarrow \tilde{\epsilon_r} &= \epsilon'_{r\infty} + \frac{\epsilon'_{rs} - \epsilon'_{r\infty}}{1 + j\omega\tau_e}, \end{aligned} \tag{3.9}$$

where:

ϵ'_{rs} = static relative permittivity (dimensionless)

$\epsilon'_{r\infty}$ = relative permittivity at a theoretical infinite frequency (dimensionless)

τ_e = relaxation time (s)

Figure 12 shows the complex relative permittivity $\tilde{\epsilon_r}$ obtained from the Debye equation used to represent the dispersive properties of pure water. It can be seen that for the frequencies of interest for GPR work, which extend to approximately 5 GHz and are highlighted in grey, the real part of the permittivity is approximately constant but the imaginary part rises monotonically.

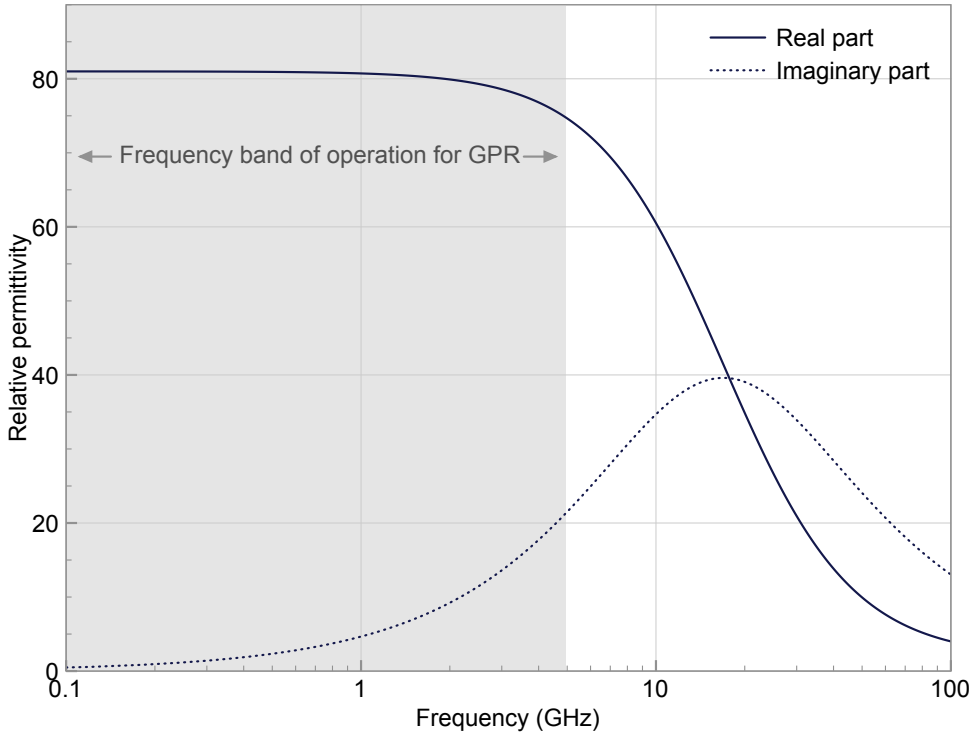

Figure 12: Debye relation for the complex permittivity of water

3.1.6 *Maxwell's curl equations*

It can be shown that Gauss's relations are implicitly enforced by Ampere's and Faraday's Laws, assuming sources and fields are initially set to zero (Taflove and Hagness, 2005). The differential form of Ampere's and Faraday's Laws is commonly used for solving boundary-value electromagnetic problems. The constitutive equations can be substituted into Ampere's and Faraday's Laws and subsequently rearranged to give Maxwells' curl equations:

$$\frac{\partial \vec{E}}{\partial t} = \frac{1}{\epsilon}(\nabla \times \vec{H} - \vec{J}_S - \sigma \vec{E}) \tag{3.10}$$

$$\frac{\partial \vec{H}}{\partial t} = \frac{1}{\mu}(-\nabla \times \vec{E} - \vec{M}_S - \sigma^* \vec{H}) \tag{3.11}$$

where:

$\sigma^* =$ equivalent magnetic loss (Ω/m)

In turn, (3.10) and (3.11) can be decomposed into six coupled, scalar partial differential equations given by (3.12) and (3.13), which are the basis for the development of the FDTD method.

$$\frac{\partial E_x}{\partial t} = \frac{1}{\epsilon}\left(\frac{\partial H_z}{\partial y} - \frac{\partial H_y}{\partial z} - J_{Sx} - \sigma E_x\right) \tag{3.12a}$$

$$\frac{\partial E_y}{\partial t} = \frac{1}{\epsilon}\left(\frac{\partial H_x}{\partial z} - \frac{\partial H_z}{\partial x} - J_{Sy} - \sigma E_y\right) \tag{3.12b}$$

$$\frac{\partial E_z}{\partial t} = \frac{1}{\epsilon}\left(\frac{\partial H_y}{\partial x} - \frac{\partial H_x}{\partial y} - J_{Sz} - \sigma E_z\right) \tag{3.12c}$$

$$\frac{\partial H_x}{\partial t} = \frac{1}{\mu}\left(\frac{\partial E_y}{\partial z} - \frac{\partial E_z}{\partial y} - M_{Sx} - \sigma^* H_x\right) \tag{3.13a}$$

$$\frac{\partial H_y}{\partial t} = \frac{1}{\mu}\left(\frac{\partial E_z}{\partial x} - \frac{\partial E_x}{\partial z} - M_{Sy} - \sigma^* H_y\right) \tag{3.13b}$$

$$\frac{\partial H_z}{\partial t} = \frac{1}{\mu}\left(\frac{\partial E_x}{\partial y} - \frac{\partial E_y}{\partial x} - M_{Sz} - \sigma^* H_z\right) \tag{3.13c}$$

3.2 THE FINITE-DIFFERENCE TIME-DOMAIN METHOD AND THE YEE ALGORITHM

The FDTD method is part of a larger group of techniques in CEM used for solving Maxwell's equations. These methods fall into two main categories — differential and integral equation solvers — which can be implemented in the time or frequency domain. The differential solvers include: FDTD, Finite-Volume Time-Domain (FVTD), Finite Element Method (FEM), and Transmission Line Method (TLM). The integral equation methods, which are commonly referred to as the Method of Moments (MoM), are derived from solutions of the integral form of Maxwell's equations. All of the different techniques present compromises between computational efficiency, stability, and the ability to model complex geometries. In this research, the FDTD method was chosen for the numerical modelling work. There were several important reasons for using the FDTD method: it has inherent simplicity, efficiency and conditional stability; due to popularisation, it has become a mature and well-researched technique; there was access to existing well-developed and validated software (Giannopoulos, 2005).

In 1966, Yee developed what transpired to be a seminal algorithm for discretising Maxwell's curl equations (Yee, 1966) and this became the basis

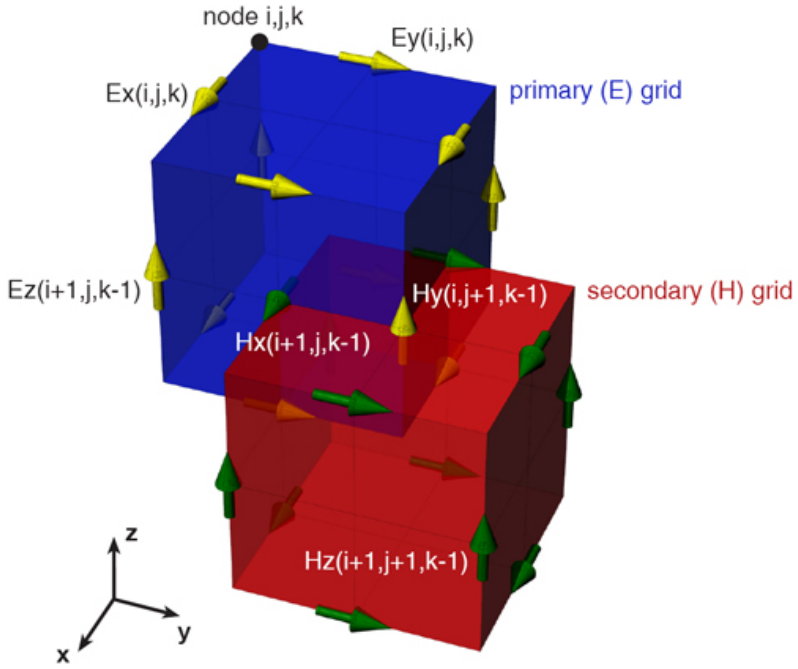

Figure 13: The 3D Yee cell (Schmid and Partner Engineering AG (SPEAG), 2009)

for the FDTD method. Yee's algorithm solves for both electric and magnetic fields using second-order accurate, central-difference approximations to the partial spatial and temporal derivatives of (3.12) and (3.13). A grid of cubic cells is used to discretise 3D space. In a Yee cell, each E-field component is surrounded by four circulating H-field components and *vice versa*, as shown in Figure 13. This arrangement means that the E-field and H-field components are staggered in space by half a cell. The E-field and H-field components are also staggered in time. A *leapfrog* time-stepping method is used to update the fields: firstly the E-field components are updated using previously calculated H-field components; the H-field components are then updated using previously calculated E-field components; and then the time-step is advanced and the process repeated. Figure 14 shows a 1D example (propagation in the x-direction) of the staggered E-field (red circles) and H-field (green triangles) components and the leapfrogging update sequence. At the current time-step (shown by the dotted grey line) the H_y components at time $n + \frac{1}{2}$ are about to be calculated using the previously updated E_z components. When all the H_y components have been updated the time line advances half a time-step and the E_z components at time $n + 1$ are updated using the previously updated H_y components, and so the sequence continues until the end of the prescribed time.

An example of applying Yee's algorithm to the E_x field component (3.12a) is given in (3.14). The notation $u(i\Delta x, j\Delta y, k\Delta z, n\Delta t) = u^n_{i,j,k}$ is used where

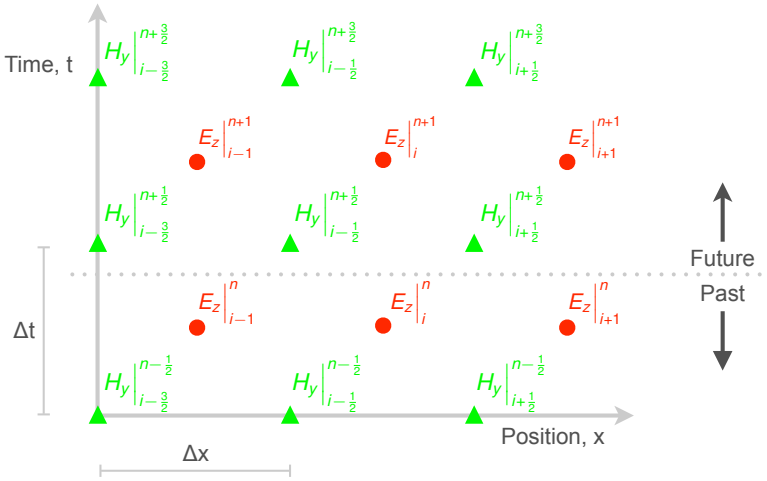

Figure 14: Leapfrogging of E-field and H-field components in space and time for 1D

Δx,Δy, and Δz are the grid spacing increments, Δt is the time increment, and n is an integer.

$$\begin{aligned}\frac{E_x\Big|_{i,j+\frac{1}{2},k+\frac{1}{2}}^{n+\frac{1}{2}} - E_x\Big|_{i,j+\frac{1}{2},k+\frac{1}{2}}^{n-\frac{1}{2}}}{\Delta t} &= \left(\frac{1}{\epsilon_{i,j+\frac{1}{2},k+\frac{1}{2}}}\right)\frac{H_z\Big|_{i,j+1,k+\frac{1}{2}}^{n} - H_z\Big|_{i,j,k+\frac{1}{2}}^{n}}{\Delta y} \\ &- \left(\frac{1}{\epsilon_{i,j+\frac{1}{2},k+\frac{1}{2}}}\right)\frac{H_y\Big|_{i,j+\frac{1}{2},k+1}^{n} - H_y\Big|_{i,j+\frac{1}{2},k}^{n}}{\Delta z} \\ &- \left(\frac{1}{\epsilon_{i,j+\frac{1}{2},k+\frac{1}{2}}}\right) J_{Sx}\Big|_{i,j+\frac{1}{2},k+\frac{1}{2}}^{n} \\ &- \left(\frac{1}{\epsilon_{i,j+\frac{1}{2},k+\frac{1}{2}}}\right)\sigma_{i,j+\frac{1}{2},k+\frac{1}{2}} E_x\Big|_{i,j+\frac{1}{2},k+\frac{1}{2}}^{n}\end{aligned} \tag{3.14}$$

A potential problem exists with the right hand side of (3.14) as it contains an E_x field value which must be evaluated at time-step n. Since the only stored value of E_x is at $n-\frac{1}{2}$, a *semi-implicit approximation* given by (3.15) (Taflove and Hagness, 2005) is used.

$$E_x\Big|_{i,j+\frac{1}{2},k+\frac{1}{2}}^{n} = \frac{E_x\Big|_{i,j+\frac{1}{2},k+\frac{1}{2}}^{n+\frac{1}{2}} + E_x\Big|_{i,j+\frac{1}{2},k+\frac{1}{2}}^{n-\frac{1}{2}}}{2} \tag{3.15}$$

The resulting equation is then rearranged to give a typical update equation for E_x which is shown in (3.16).

$$\begin{aligned} E_x\Big|^{n+\frac{1}{2}}_{i,j+\frac{1}{2},k+\frac{1}{2}} = & \left(\frac{1 - \frac{\sigma_{i,j+\frac{1}{2},k+\frac{1}{2}} \Delta t}{2\epsilon_{i,j+\frac{1}{2},k+\frac{1}{2}}}}{1 + \frac{\sigma_{i,j+\frac{1}{2},k+\frac{1}{2}} \Delta t}{2\epsilon_{i,j+\frac{1}{2},k+\frac{1}{2}}}} \right) E_x\Big|^{n-\frac{1}{2}}_{i,j+\frac{1}{2},k+\frac{1}{2}} \\ & + \left(\frac{\frac{\Delta t}{\epsilon_{i,j+\frac{1}{2},k+\frac{1}{2}}}}{1 + \frac{\sigma_{i,j+\frac{1}{2},k+\frac{1}{2}} \Delta t}{2\epsilon_{i,j+\frac{1}{2},k+\frac{1}{2}}}} \right) \frac{H_z\Big|^{n}_{i,j+1,k+\frac{1}{2}} - H_z\Big|^{n}_{i,j,k+\frac{1}{2}}}{\Delta y} \\ & - \left(\frac{\frac{\Delta t}{\epsilon_{i,j+\frac{1}{2},k+\frac{1}{2}}}}{1 + \frac{\sigma_{i,j+\frac{1}{2},k+\frac{1}{2}} \Delta t}{2\epsilon_{i,j+\frac{1}{2},k+\frac{1}{2}}}} \right) \frac{H_y\Big|^{n}_{i,j+\frac{1}{2},k+1} - H_y\Big|^{n}_{i,j+\frac{1}{2},k}}{\Delta z} \\ & - \left(\frac{\frac{\Delta t}{\epsilon_{i,j+\frac{1}{2},k+\frac{1}{2}}}}{1 + \frac{\sigma_{i,j+\frac{1}{2},k+\frac{1}{2}} \Delta t}{2\epsilon_{i,j+\frac{1}{2},k+\frac{1}{2}}}} \right) J_{Sx}\Big|^{n}_{i,j+\frac{1}{2},k+\frac{1}{2}} \end{aligned} \tag{3.16}$$

The remaining update equations for E_y, E_z, H_x, H_y, and H_z are derived in a similar manner and are given in Appendix A.

Constitutive parameters can be specified at their corresponding electric and magnetic field component locations and, thus, the FDTD grid can be built to represent different materials. At interfaces of different materials, electric and magnetic field components can be shared between several cells. Thus, there can be potential problems as to what constitutive parameters should be used for these components. Without correction, the order in which each material is introduced into the FDTD grid will determine what constitutive parameters are applied at the interface i. e., whichever material is introduced later will take precedence. One solution is to use a *weighted-average* of constitutive parameters. The weighted-average model is obtained by applying Ampere's Law (3.3a) around each tangential electric field component at the interface. Figure 15 shows an example of an electric field component E_x that is common to four grid cells. Ampere's Law may be applied to the E_x component by performing a summation of four separate integrations within the cell, as given by (3.17).

$$\sum_{i=1}^{4} \oint_{c_i} \vec{H} \cdot \vec{dl} = \sum_{i=1}^{4} \frac{\partial}{\partial t} \iint_{s_i} \epsilon_i \vec{E} \cdot \vec{ds} + \iint_{s_i} \sigma_i \vec{E} \cdot \vec{ds} \tag{3.17}$$

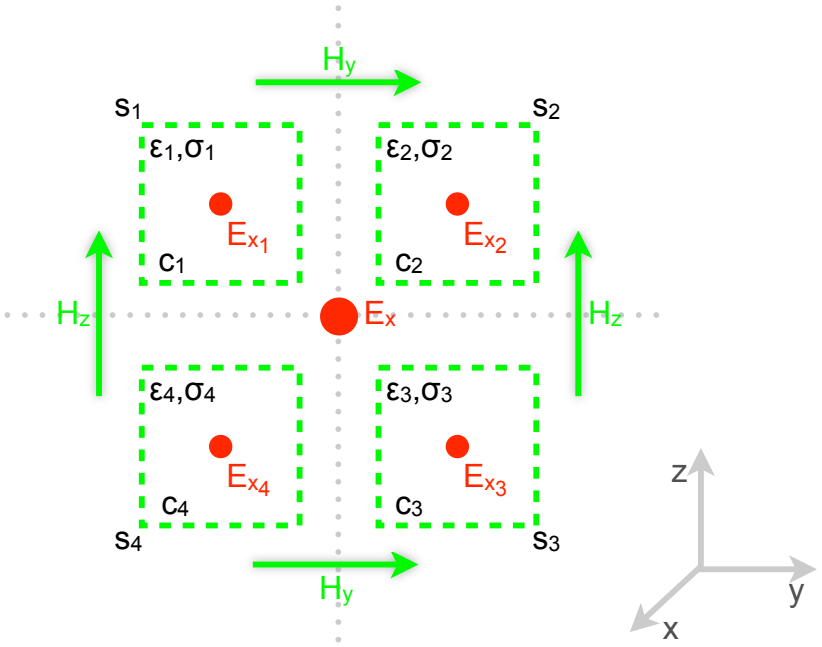

Figure 15: Weighted-average model for permittivity and conductivity at a material interface

where:

c_i = contour of patch (m)

s_i = surface area of patch (m^2)

Using (3.17), and the fact that the tangential electric field must be continuous at the interface, yields average values for the permittivity and conductivity (3.18) which can be used in the standard FDTD update equations.

$$\epsilon_{av} = \frac{\sum_{i=1}^{4} \epsilon_i s_i}{s} \tag{3.18a}$$

$$\sigma_{av} = \frac{\sum_{i=1}^{4} \sigma_i s_i}{s} \tag{3.18b}$$

where:

s = total surface area of all patches (m^2)

3.2.1 *Stability, numerical dispersion, and errors*

The FDTD method is a conditionally stable explicit numerical technique, where the stability is governed by the Courant-Friedrichs-Lewy (CFL) condition (3.19). To ensure stability, the CFL condition states that the time-step Δt used is limited by the cell size Δx, Δy, Δz chosen and the maximum velocity of propagation, which in most cases will be the speed of light in free-space c.

$$\Delta t \leqslant \frac{1}{c\sqrt{\frac{1}{(\Delta x)^2} + \frac{1}{(\Delta y)^2} + \frac{1}{(\Delta z)^2}}} \tag{3.19}$$

The CFL condition is an important limitation of the FDTD method. A simulation containing fine geometrical features or short electromagnetic wavelengths, that must be adequately resolved by using a fine spatial discretisation, will result in a very small time-step and, hence, long simulation times.

Dispersion can occur in physical media and wave-guides, but can also be an unwanted artefact of numerical simulation. Numerical dispersion is a source of error in the FDTD method and it is important to ensure that any such numerical dispersion is minimal compared to the physical dispersion of interest. It is common to describe dispersion as the variation of wavenumber $k = \frac{2\pi}{\lambda}$ with angular frequency $\omega = 2\pi f$ and for the 1D FDTD method, is controlled by the ratio given in (3.20).

$$R = \frac{c\Delta t}{\Delta l}, \tag{3.20}$$

where Δl is the spatial discretisation. It can be shown that when $R = 1$ the numerical dispersion relation simplifies to the analytical dispersion relation $\omega = \pm ck$. This choice of Δt is called the *magic time-step* because the spatial and temporal difference approximations cancel and propagation occurs at exactly one cell per time-step. If $R \leqslant 1$ the numerical dispersion is stronger and if $R \geqslant 1$ the algorithm becomes unstable (Bondeson et al., 2005).

Dispersion analysis for the 3D FDTD method is significantly more complex than for the 1D case. If $\Delta x = \Delta y = \Delta z = \Delta l$ is used in (3.19) then by comparing with the 1D case, the time-step is reduced by a factor of $\sqrt{3}$. Therefore, the spatial discretisation error is generally larger than the temporal discretisation error, although they cancel each other to some extent. The dispersion error is often quantified as the difference between the numerical phase and group velocities, and the real velocities. A full treatment of FDTD numerical dispersion is given in Bondeson et al. (2005) and Taflove and Hagness (2005), but an accepted rule-of-thumb is that numerical dispersion can be

adequately controlled by ensuring that the wavelength of the highest frequency present in the simulation is resolved by at least twenty cells[1].

One of the biggest drawbacks of the FDTD method is its basis on a uniform Cartesian grid. This means objects with boundaries that are not aligned with the grid are approximated in a *staircase* fashion. The errors due to the staircase approximation of PEC surfaces have been analysed by Cangellaris and Wright (1991) and Holland (1993) and it was concluded that the staircase approximation introduced delays in waves that were propagating along the PEC surfaces. The propagation of higher frequencies were more affected by these delays and the delays were also increased by using coarser spatial discretisations. There are a number of solutions to mitigate the staircasing problem:

1. Use a global unstructured grid to model non-conformal objects.
2. Use a fine global grid.
3. Use fine sub-grids within the global grid.
4. Use local sub-cell methods to model non-conformal objects.

The first solution cannot be easily implemented with the FDTD method as it is essentially a FEM representation. The second solution potentially requires a large amount of computational resources. It has been shown that the use of sub-grids within a main FDTD grid can reduce computational requirements without compromising accuracy (Chevalier et al., 1997, Diamanti and Giannopoulos, 2009). However, the implementation of sub-gridding methods is significantly more onerous than that of the last solution, which is to use a local sub-cell method. There are a number of local sub-cell methods for non-conformal objects (Anderson et al., 1996, Benkler et al., 2006, Dey and Mittra, 1997, Jurgens et al., 1992, Mezzanotte et al., 1995) the simplest of which is the diagonal split-cell model, which is a subset of the general Contour Path (CP) method. The CP method is based upon the use of the integral form of Ampere's and Faraday's laws (3.3a) and (3.4a) which form orthogonal contours in the 3D FDTD grid. These contours can be locally deformed to fit non-conformal objects. In this research, the diagonal split-cell method was trialled to potentially improve the modelling of bowtie antenna elements which typically have boundaries at approximately 45° to the grid cells. The implementation and results from this study are presented in Chapter 5.

1 This results in a approximately a 1% relative error in group velocity (Bondeson et al., 2005)

3.2.2 *Absorbing boundaries*

The FDTD method is often used to model unbounded or open regions of space, and to ensure that a model closely represents this theoretically infinite real space, the computational domain must be truncated by introducing absorbing boundaries at the edges of the FDTD grid. There is a large body of continuing research into absorbing boundaries for numerical models but for the purposes of this research, only a brief overview will be given. There are two main types of Absorbing Boundary Condition (ABC), the analytical ABC, and the Perfectly Matched Layer (PML) ABC. Analytical ABCs were the first solution to closing the computational space and involved applying a differential operator to the local field at all points on the outer boundary of the domain. If properly constructed, the differential operator *annihilates* terms of the outgoing wave expansion leaving a remainder term that diminishes to zero as the inverse power of distance from the observation point to the origin (Taflove and Hagness, 2005). The most commonly used analytical ABCs are those of Higdon (1986) and Liao et al. (1984).

A more effective ABC approach is to define a boundary region (usually a few cells thick) of an artificial absorbing material that surrounds the domain. Ideally, this material is reflectionless for any angle and frequency of incident wave and is highly absorbing. This type of boundary is known as a PML ABC and was introduced by Berenger (1994). Berenger's original formulation used a field-splitting strategy that resulted in a PML that vastly out-performed previous ABC techniques. Subsequently, the PML has received much attention from researchers validating Berenger's work and trying to improve upon its performance.

The Convolutional Perfectly Matched Layer (CPML) evolved from Berenger's original split-field PML formulation and used a stretched-coordinate system to repose the split-field PML in a non-split form. The CPML used Complex Frequency Shifted (CFS) tensor coefficients to mitigate reflection errors caused by evanescent waves and late-time low frequency interactions. The original implementation of the CPML used an Auxiliary Differential Equation (ADE) formulation but Roden and Gedney (2000) proposed an improved formulation using recursive-convolution, which is now what is referred to as the CPML.

Berenger's split-field PML resulted in an artificial absorbing material, whereas Gedney (1996) applied a Uniaxial Perfectly Matched Layer (UPML) to the FDTD method that did not require field-splitting. The UPML demonstrated good performance for terminating simulations involving inhomogeneous, non-linear, and dispersive materials.

More recently a non-split Recursive Integration Perfectly Matched Layer (RIPML) was proposed for elastic wave modelling by Drossaert and Giannopoulos (2007) and applied to electromagnetic modelling by Giannopoulos (2008). The RIPML has shown modest performance improvements over the CPML whilst maintaining the same computational requirements.

3.3 SUMMARY

The aim of this chapter was to give a general overview of electromagnetic field theory in relation to GPR modelling and the FDTD method. It has been shown that Maxwell's curl equations, which are the differential forms of Ampere's and Faraday's Laws, can be discretised according to Yee's algorithm to form the basis of the FDTD method. Equations are used to update, in a leapfrog fashion, the electric and magnetic fields which are staggered in time and space on a 3D grid of Yee cells. The update equations contain material parameters — permittivity, permeability, and conductivity — from the constitutive relations that can be uniquely specified for any point in the grid. Dispersion is an important phenomenon, both in terms of being able to model physical dispersion using relations such as the Debye equation, as well as controlling numerical dispersion which is unavoidable in most 3D FDTD simulations. The stability of the FDTD method is governed by ensuring the CFL condition is satisfied. The computational domain can be truncated using a PML ABC which has been shown to effectively absorb incident waves, preventing unwanted reflections from the domain boundaries. Overall, the FDTD method is an explicit, robust and efficient CEM technique that is especially suitable for use in modelling GPR problems.

4

REVIEW OF GROUND-PENETRATING RADAR ANTENNA MODELLING

The aim of this chapter is to provide a review of the numerical modelling of GPR, with specific focus on antennas. The numerical modelling of GPR, and specifically forward models, has been an active area of research since the early 1990s, primarily due to a demand for a fuller understanding of the fundamental phenomena of GPR. In addition, the sophistication, size, and dimensionality of GPR models have accelerated rapidly over the years as computational resources have improved and become more accessible. A good GPR forward model is an extremely useful tool for furthering knowledge in many of the research areas associated with GPR. For example, a GPR forward model can be used for testing new signal and image processing techniques, and it can also be utilised for more advanced techniques such as inversion, where geometrical and electrical characteristics of structures and materials can be extracted from GPR data.

Most GPR forward simulations prior to 1991 were simple 2D models (Oristaglio and Hohmann, 1984). Moghaddam et al. (1991) was one of the first to move towards a 3D model using the FDTD method. Moghaddam et al. developed a 2.5D model that was a 2D projection of a 3D FDTD grid where all six field components were used. Sine and cosine transforms were used to reduce the 3D problem to 2D. Giannopoulos (1997) developed and compared 3D models of GPR using both TLM and FDTD methods. Responses from small localised targets were analysed using different orientations of simple Hertzian sources.

A GPR forward model can include sub-models of the GPR antennas, the subsurface or structure, and the targets. Calculating the electromagnetic fields radiated from antennas with simple geometries, such as the cylindrical monopole and the conical monopole, is a canonical antenna analysis problem that has had rigourous treatment, documented by King (1956) or Balanis (1997). These simple antennas can be analysed theoretically and were some of the first to be analysed numerically by Maloney et al. (1989) using the FDTD method. A comparison of the results from the FDTD model showed excellent agreement with accurate experimental measurements. In fact, at the time, no theoretical analyses could better the numerical results in terms of agreement with the experimental data.

Practical antennas that contain loading resistors, absorber material, shielding, and complex geometries simply cannot be analysed in the theoretical

manner used for the cylindrical and conical monopoles. However, the work of Maloney et al. (1989) demonstrated that numerical methods such as the FDTD technique could be used to calculate the electromagnetic fields radiated from such antennas. In the past twenty years, the FDTD method has been a favoured technique for the analysis of many different types of communication antennas and has been especially prominent for modelling GPR. Much of the research involving GPR antennas and forward modelling can be divided into two categories: firstly, the investigation of new antenna designs suitable for GPR, and the improvement of the classic bowtie design; and secondly, the development of forward models with realistic subsurface properties. Some studies overlap both these categories but few have directly compared modelled and measured amplitudes and wave shapes, and none have done so with GPR antennas that are widely used.

A first part of the review considers research into antenna modelling where the purpose of the modelling was to improve the performance of custom-built antenna designs. The entire review presents the most prominent numerical studies from the past decade or so.

Shlager et al. (1994) created 3D FDTD models of a resistively loaded bowtie fed through an image plane by a coaxial line. An optimised design for pulse radiation was found using a bowtie design with resistive sheet and serrated edges. Shlager et al. also investigated two important FDTD antenna modelling problems: the issue of how to model the feed region of the antenna, and the potential errors associated with staircasing. A full 3D model of the coaxial line used to feed the antenna was compared with a simple 1D transmission line model. By analysing the reflected voltage at the drive-point it was found that the results for the simple model were in good agreement with measured data (Brown and Woodward, 1952), and offered the advantage of decreased computational requirements. The staircasing of the bowtie geometry was shown to introduce additional reflections in the received response. These reflections increased in amplitude when the ratio of the largest hypotenuse of a staircased cell, divided by the minimum wavelength present in the feed pulse, became greater than 0.5.

Lestari et al. studied, both experimentally and numerically, slotted bowtie antennas (Lestari et al., 2004) and adaptive wire bowtie antennas (Lestari et al., 2005) for GPR applications. A bowtie antenna was designed using a combination of FDTD modelling and experimental work. The antenna used an absorber covering on one side and narrow slots to create resistive and capacitive loading to reduce late-time ringing. The technique was successfully applied in free-space and over lossy ground, with late-time ringing reduced to lower than -40 dB. A wire bowtie antenna was also designed that could adapt

its flare angle to different ground properties and antenna elevations. A MoM frequency domain modelling code (Lawrence Livermore Laboratory, 1981) was used for the design, following which the antenna was then built and the results confirmed experimentally.

Uduwawala and Norgren (2006) used 3D FDTD models to investigate different flare angles and lengths of a planar dipole antenna for GPR use. A Genetic Algorithm (GA) was used to find optimum values for loading resistors and the depth of the rectangular metallic shield. A UPML was used in the FDTD model to simulate the effects of using a layer of absorber in the cavities. Uduwawala and Norgren found that the classic bowtie design could not be significantly improved upon, and that using a layer of absorber in the cavities increased the direct coupling between the transmitter and the receiver.

Researchers have developed hybrid modelling methods to combine advantages and mitigate disadvantages of different techniques. Huang et al. (1999) used a simple wire dipole antenna to successfully verify the use of the Schelkunoff equivalance principle (Harrington, 1961) to hybridise the MoM and FDTD techniques.

Monorchio et al. (2004) successfully combined FEM, FDTD and time domain MoM techniques. Time domain MoM was used to model a thin-wire antenna, FEM was used for modelling curved geometries, and objects that aligned to a Cartesian grid, as well as the boundaries of the domain, were modelled using FDTD. Some late-time instabilities with this hybrid method were noted.

van Coevorden et al. (2006) used a GA to optimise the fidelity and input impedance of a thin-wire bowtie antenna. The geometry of the antenna and the position of resistive loading were adjusted to achieve broadband characteristics. The antenna was designed using both MoM and FDTD codes. It was found that the thin-wire bowtie antenna had improved fidelity and radiation efficiency when compared to a thin-wire Wu-King dipole antenna (Wu and King, 1965).

The theme throughout the second part of this review is GPR simulations that include a combination, with varying degrees of realism, of sub-models of the subsurface and the GPR antennas.

Bourgeois and Smith (1996) were probably the first to include a realistic description of a GPR antenna in their 3D FDTD model that replicated an experimental scale-model of a GPR system. Bowtie antennas were modelled with loading resistors and rectangular cavity shielding. The 1D transmission line feed model used was a continuation of work by Shlager et al. (1994). The constitutive parameters of the scale-model emulsions were simulated by fitting a Debye model. E-plane patterns were obtained for a range of antenna elevations above the surface of the emulsion, which confirmed the theory of Smith (1984) that antenna patterns become more directive as the height is

increased. Scattering responses from buried metallic and plastic pipes were modelled and showed some agreement with measured data. It was acknowledged that because the model domain was truncated using PEC boundaries, there were unwanted reflections in the modelled responses that were difficult to remove.

Roberts and Daniels (1997) created 3D FDTD models of 300 MHz unshielded bowtie antennas, which included accurate modelling of the coaxial feeding. Modelled free-space input impedances were compared to measured data (Brown and Woodward, 1952) and showed good agreement except at frequencies above 600 MHz. It was commented that by decreasing cell size from 20 mm to 10 mm the discrepancies above 600 MHz where somewhat mitigated. Roberts and Daniels then went on to compare modelled radiation patterns of a bowtie over water with measured data (Wensink et al., 1990), as well as comparing scattering responses from metallic and plastic pipes submerged in the water (Wensink et al., 1991). Roberts and Daniels notably mentioned a lack of comparison of modelled and measured amplitude data. The best agreement reached between modelled and measured data over buried targets had a peak difference of 3.3 dB.

Teixeira et al. (1998) used 3D FDTD models to investigate GPR responses on dispersive media with conductive losses. The dispersive effects of soils were modelled using a two-term Debye relation. Models were used to compare the effects of the dispersion on responses from metallic and plastic pipes. It was shown that the dispersive properties of the soils caused a degree of distortion in the responses from both pipes, but effected the response from the metallic pipe more. Teixeira et al. also extended the PML for 3D dispersive media by using a complex coordinate stretching approach. The antenna model used for these studies was a simple electric dipole.

Nishioka et al. (1999) used 3D FDTD models to study a resistively loaded bowtie antenna shielded with a rectangular metallic cavity, coated partially and fully with a frequency dependent ferrite absorber. The antenna bowties were modelled using a CP method which was shown to better match measured input impedances than the traditional staircase approximation. Fully coating the antenna cavities with the ferrite absorber had the detrimental effect of increasing the size of the backlobe of the radiation pattern i. e., radiation into the air, and also caused a distortion in the response from a buried target.

Cassidy (2001) highlighted the need for realistic models of GPR antennas to be included in simulations. Following on from the work of Bergmann et al. (1998), Cassidy developed a 3D FDTD model that was second-order accurate in time and fourth-order accurate in space $O(2,4)$, and included a description of

a pulseEKKO 1 GHz antenna[1]. The antenna description was based on limited data, but modelled results and real data from a constructed test site showed good agreement.

Lampe and Holliger (2001) created 3D FDTD models of low-frequency bowtie antennas which used Generalised Perfectly Matched Layer (GPML) (Fang and Wu, 1996) boundaries, and a sub-gridding technique (Chevalier et al., 1997). Once again, the initial validity of the model was confirmed by comparing modelled input impedances to the measured data of Brown and Woodward (1952). Antenna radiation patterns over lossless and lossy half-spaces with shielded and unshielded antennas were studied, and contrasted with results from typically assumed far-field patterns of infinitesimal dipoles. Work on these generic bowtie antenna models was further developed in Holliger et al. (2003), Lampe et al. (2003) by studying the inclusion of cavity absorbing material and loading resistors. Including these features meant more realistic antenna models but results were always compared to those of an infinitesimal dipole, and never validated against data from real antennas. Topographic roughness and subsurface heterogeneities were also investigated, and it was shown that in both cases the antenna radiation patterns were affected. Surface roughness alters the antenna height above the ground, which caused a change in the antenna radiation pattern. The subsurface heterogeneities did not affect the input impedance of the antenna, and the change in the radiation patterns was, therefore, attributed to volume scattering and attenuation. Finally, Lampe and Holliger (2005) used the same models to study the effects of Wu-King loading (Wu and King, 1965) of the bowties. It was concluded that standard Wu-King loading was impractical for most types of GPR antennas.

Uduwawala et al. (2004) used 3D FDTD models to analyse the performance of a resistively loaded bowtie antenna. The positioning and value of loading resistors, as well as bowtie flare angle and length, were investigated. It was shown that increasing the flare angle reduced clutter and increased the amplitude of target responses. Shortening the antenna length made the antenna more broadband, although reduced the amplitude of responses from targets. All observations came from modelled data, no comparisons with measured data were made.

Lee et al. (2004) designed, modelled and built a horn-fed bowtie with the aim of creating an antenna whose characteristics were less susceptible to changes in subsurface properties. The antenna was a bowtie loaded using resistive card and fed using a small dielectric filled horn curved outwards at the ends to meet the planar bowtie section.

1 Sensors and Software, Inc.

Uduwawala et al. (2005) presented research very similar to Teixeira et al. (1998) but with the inclusion of a resistively loaded bowtie antenna instead of a simple dipole, as well as surface roughness and soil heterogeneities. Like Teixeira et al., the dispersive effects of the soil were modelled using a two-term Debye relation. Comparisons of 3D FDTD models of buried metallic and plastic pipes were made, and it was shown that the surface roughness had a larger impact on the target responses than the soil heterogeneities.

Klysz et al. (2006) presented one of the first attempts to model a commercial GPR antenna. The FDTD method was used to create a 3D model of a GSSI 1.5 GHz antenna. Klysz et al. acknowledges that the constitutive parameters of the dielectric cavity absorber, and the centre frequency of the feeding pulse were unknown, and goes on to state that a Gaussian pulse with a centre frequency of 1.5 GHz was used in the model. A resistance of 80 Ω was used at the drive-point, and was determined by trial-and-error approach. Some degree of similarity was shown when modelled and measured free-space radiation patterns were compared. Measured responses from two concrete slabs of different moisture contents were compared with modelled data. Again, some similarity was shown, but the model did not include the receiver antenna, and the concrete was assumed to be a homogeneous material.

Liu et al. (2008) used a PML to represent absorber material on the shield of a monopole antenna. However, it is not stated what type of PML was used and, therefore, it is not known if the PML represented a physically realisable material. The 3D FDTD models that were created showed the effects of including shields and absorber on the response from a buried conducting target strip, and the radiation pattern of the antenna. The H-plane pattern became more directive, and the direct wave of the antenna was reduced with the inclusion of the shield and absorber material.

Pérez-Gracia et al. (2009) experimentally characterised a MALÅ 1.6 GHz antenna in air and sand. An approximate radiation pattern was experimentally determined in air by comparing footprints obtained for a range of antenna-target distances, along with profiles over a surface with a fixed surface-target distance. A more directive radiation pattern was measured in sand. Pérez-Gracia et al. found that the actual centre frequency of the 1.6 GHz antenna in sand with velocity 11 cm/ns was 1.1 GHz.

4.1 SUMMARY

The numerical modelling of GPR has grown significantly since the early 1990s, primarily through the accessibility of more powerful computational resources.

A GPR forward model can include sub-models of the antennas, the subsurface or structure, and the targets. The FDTD method has become the favoured choice for developing GPR forward models. The results from FDTD numerical modelling of the electromagnetic fields radiated by simple antennas have been compared to measurements and this has demonstrated the validity of the modelling technique. Since then, models of more complex antennas have been developed that are more representative of actual GPR antennas. Some of the results from these modelled antennas have shown agreement with measured data, but this has not been comprehensively demonstrated. The motivation for modelling such antennas has been antenna design–mostly the improvement of the classic bowtie. In parallel with the modelling of more complex antennas, has been the development of GPR models that include realistic subsurface properties. However, most of these models have not included a realistic antenna sub-model, preferring to use much simpler Hertzian dipoles as descriptions of the sources. Very few researchers have combined a realistic antenna model with a realistic subsurface model, and where this has been done, it has been with custom-built antennas that are not widely used. There is, therefore, a need to develop antenna models of realistic, widely-used antennas so that modelled responses can be directly compared with real data.

5

DEVELOPMENT OF COMPUTATIONAL TOOLS

In Chapters 6 and 7 models of two commercial GPR antennas are created, analysed and optimised. However, prior to that it is necessary to describe the development of the computational tools used to build the antenna models. This chapter begins with an outline of the process used to build the antenna models. The software used for electromagnetic simulation and geometry visualisation is described, along with the important developments and modifications made to the software to facilitate building and visualising 3D antenna models. The computational hardware resources used to run the antenna models are also described. Finally, the spatial discretisation, staircasing errors, and computational requirements of the antenna models are investigated.

5.1 SOFTWARE

Figure 16 illustrates the process used to create the antenna models. At the centre of the process is the electromagnetic simulation software (GprMax3D). Visualisation software (ParaView) is used in the pre- and post-processing stages, and MATLAB® used as the primary development environment.

5.1.1 *Electromagnetic simulation*

A key component of any GPR forward model is the electromagnetic simulation software. For this research GprMax3D, part of a suite of electromagnetic wave simulators based on the FDTD method, was used. GprMax is freely available software that was written by Giannopoulos in 1996, and has since developed into a mature application that has been successfully used by a number of researchers (Galagedara et al., 2005, Jeannin et al., 2006, Lopera and Milisavljevic, 2007, Soldovieri et al., 2007). There are a number of beneficial features to the software which will be discussed, but a major reason for using GprMax3D was that the developer was also the author's supervisor. This enabled useful insight into the core of the application, and also made it possible for the author to further develop the software to facilitate the modelling of GPR antennas.

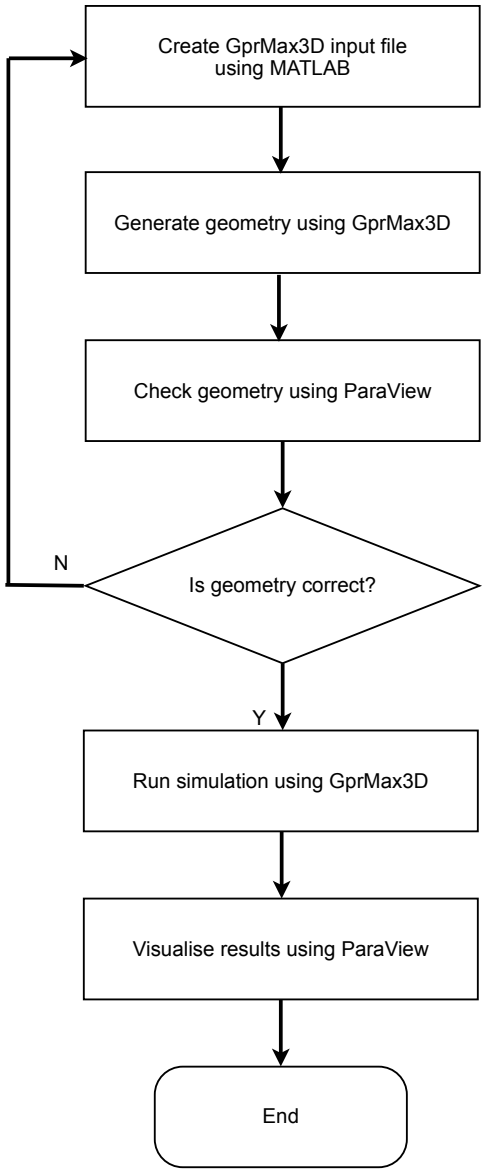

Figure 16: Flowchart of process used to create an antenna model

GprMax3D contains many features that are useful for modelling GPR antennas using the FDTD method:

- PML boundaries based on the Uniaxial Perfectly Matched Layer (UPML) that allow the computational domain to be effectively truncated. This is especially important for antenna modelling where models can be computationally expensive and, thus, a minimal, effective PML is beneficial.
- User specified excitation functions that allow custom pulse shapes with specific frequency content to be used as sources of excitation
- Voltage source, and 1D transmission line feed models
- Code parallisation using OpenMP (OpenMP.org, 2008) that allows large models to be executed on a compute cluster

MATLAB® was used for the creation of the GprMax3D input files which are based upon a series of primitives. These basic commands are used to build potentially complex objects as well as set up the general model parameters e. g., domain size, spatial discretisation, time window etc..., define materials, and specify sources and receivers. The following code is a simple example of a GprMax3D input file.

```
#title: Simple GprMax3D input file

#messages: yes
#abc_type: pml
#pml_layers: 16
#num_of_procs: 8

#domain: 0.550 0.550 0.200
#dx_dy_dz: 0.001 0.001 0.001
#time_window: 12E-9

#medium: 6.0 0.0 0.0 0.005 1.0 0.0 concrete

#box: 0.025 0.025 0.025 0.525 0.525 0.175 concrete
#cylinder: y 0.025 0.525 0.125 0.145 0.006 pec
#cylinder: y 0.025 0.525 0.225 0.125 0.006 pec
#cylinder: y 0.025 0.525 0.325 0.125 0.006 pec
#cylinder: y 0.025 0.525 0.425 0.145 0.006 pec
#geometry_vtk: 0.000 0.000 0.000 0.550 0.550 0.200 0.001
   0.001 0.001 example n

#hertzian_dipole: 1.0 1.5E+09 gaussian Tx
```

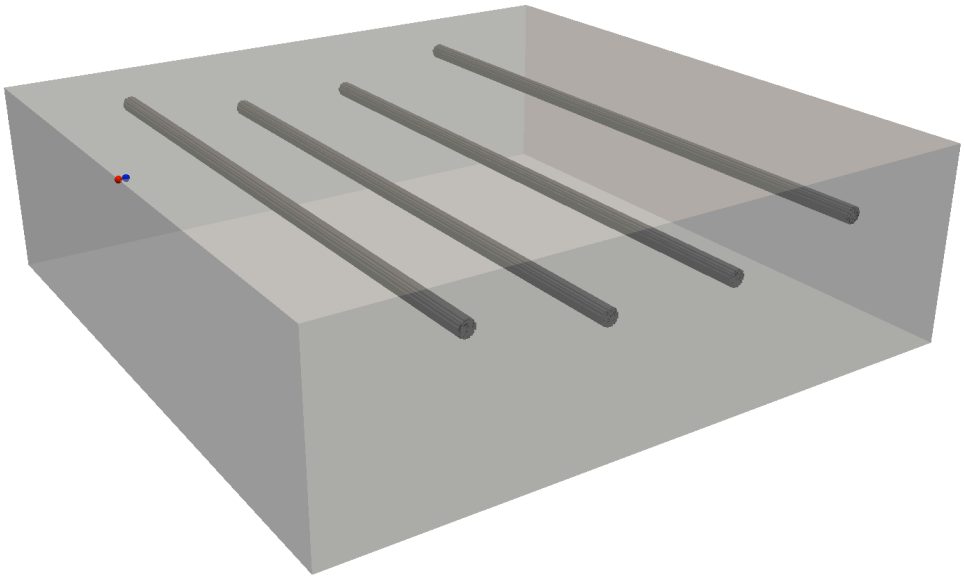

Figure 17: Visualisation of the geometry of a simple GprMax3D model (red sphere is T_x, blue sphere is R_x)

```
#analysis: 100 example.out b
#tx: y 0.025 0.250 0.175 Tx 0.0 12E-9
#rx: 0.030 0.250 0.175
#tx_steps: 0.005 0.000 0.000
#rx_steps: 0.005 0.000 0.000
#end_analysis:
```

Figure 17 shows the modelled geometry of the simple example, rendered in ParaView. The model consists of a series of rebars in a concrete slab. Although this problem could have been modelled in 2D to save computational resources, it has been modelled in 3D to illustrate the basic commands that comprise a GprMax3D input file. The model domain is 550 × 550 × 200 mm, with a spatial discretisation of $\Delta x = \Delta y = \Delta z = 1$ mm, and a 16 layer PML. A time window of 12 ns is set. In addition to the default materials *PEC* and *free_space*, *concrete* is defined as a new material with a set of constitutive parameters. The objects in the model are a box, representing the concrete slab, and PEC cylinders representing the rebars. As is typical of many GPR simulations, no physical models of the actual GPR antennas are included. Instead, a simple Hertzian dipole source (illustrated by a red point) is used to represent the transmitter antenna, and a receiver point (illustrated by a blue point) is used to represent the receiver antenna. The source and receiver are moved together in increments of 5 mm along the centre-line of the slab (perpendicular to the orientation of the rebars) for 100 analysis steps to create a B-scan.

The aforementioned example input file was generated manually using a simple text editor but for more complex geometries, such as the antenna models, MATLAB® scripts were used to generate the input files. These scripts along with the input files for the final antenna models described in Chapters 6–7 are given in Appendix B.

5.1.2 *3D visualisation*

One of the most important aspects of modelling complex antennas is the ability to visualise, preferably in 3D, the geometry including all of the fine features present. By default, GprMax3D can output a binary file containing material identifiers for each Yee cell in the FDTD grid. This file can be loaded into an application such as MATLAB® and visualised in 2D sections or as a 3D grid. There are two problems with this solution: firstly, modelling complex antennas requires setting the properties of faces and edges of cells which cannot be visualised using the default behaviour of GprMax3D and, secondly, although MATLAB® is capable of displaying 3D meshes, it was not specifically designed for this purpose and is, consequently, very slow when interactively manipulating large 3D meshes. A solution was sought that would allow the visualisation and manipulation of large and complex 3D FDTD geometry grids, whilst maintaining the open-source ethos of GprMax3D.

ParaView (Kitware Inc., 2003) is a multi-platform and open-source data-analysis and visualisation application that was developed for handling extremely large datasets. It allows these datasets to be manipulated interactively and can be run distributively on a compute cluster or standalone on a desktop computer. ParaView uses the Visualisation Toolkit (VTK) as the basis for its data-processing and rendering engine. The VTK is an open-source system for 3D computer graphics, image processing, and visualisation, and was used to link GprMax3D and ParaView.

The VTK is a large library of functions that provide high-level access to the primitives upon which the VTK format is based. In order to avoid including the entire VTK with GprMax3D, it was decided to modify the source code of GprMax3D to implement the creation of VTK geometry files at a low-level. Unfortunately, official documentation on low-level VTK file creation is sparse and incomplete (Kitware Inc., 2003). The VTK file format uses the Extensible Markup Language (XML) to define structured or unstructured grids that can contain data associated with each cell or cell vertex. Since FDTD grids are generally uniform, a structured grid definition, *ImageData*, was chosen where the points and cells that make up the grid were defined implicitly by specifying

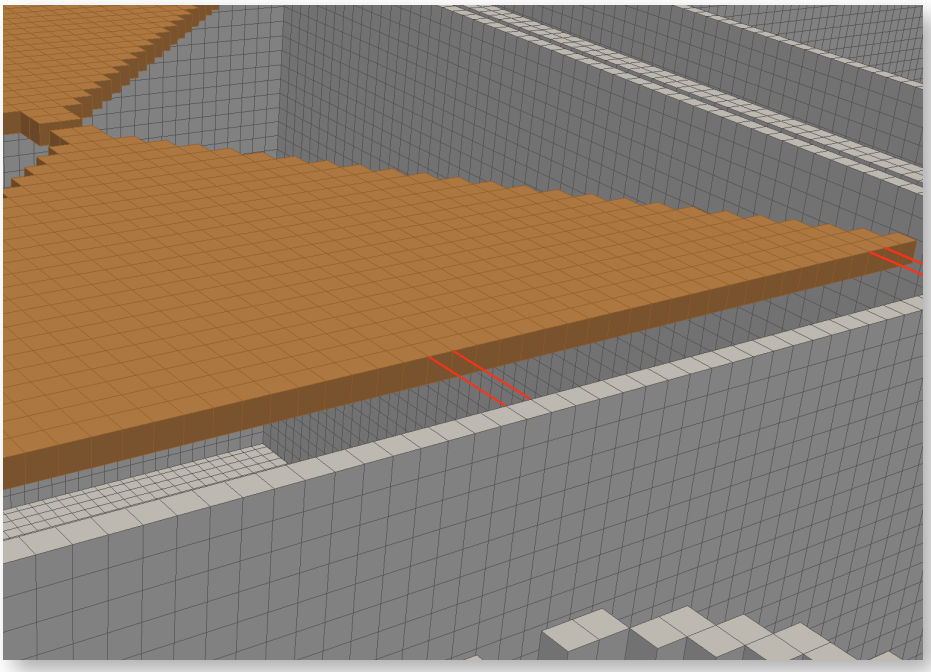

Figure 18: Visualisation of fine geometry features in FDTD mesh

an extent, origin, and spatial discretisation. The *ImageData* format was used to create a VTK file of the modelled geometry by specifying the material associated with each grid cell. However, a secondary VTK file was necessary to visualise fine geometry features where cell faces or edges had different material properties. The *PolyData* format enabled the basic building block for the grid to be a line as opposed to a cell. This allowed the creation of a VTK file, and subsequent visualisation, of specific parts of the overall FDTD grid that contained fine features. Figure 18 is an example of the two types of VTK file rendered in ParaView to allow the visualisation of geometry that includes fine features: an Surface Mount Technology (SMT) resistor is modelled by distributing its resistance over several cell edges (coloured red), and is visualised using the *PolyData* format; the remaining geometry is visualised using the *ImageData* format.

As well as allowing the visualisation of the model geometry prior to running the simulation, ParaView was used in a post-processing step to visualise and manipulate the time-dependent electromagnetic fields generated by the model.

5.2 HARDWARE

Another key aspect of developing the computational tools for antenna modelling was running the simulation software on suitable hardware. The computational requirements of the antenna models are discussed in detail in the next section, but to assess the necessary hardware resources it is necessary to mention Random-Access Memory (RAM) and Central Processing Unit (CPU) requirements. The antenna models use finely discretised 3D FDTD grids, and when they are included in a GPR simulation with structures and targets etc.., a considerable amount of RAM and CPU-time is required. These levels of computational resource are too demanding for a typical desktop computer. However, GprMax3D has been parallised using OpenMP, and a compute cluster managed by the School of Engineering was available for use, which enabled large models to execute on many CPU cores. The School of Engineering compute cluster is a Beowulf cluster (Beowulf.org, 1994) based on 2.4 GHz or 2.6 GHz Advanced Micro Devices (AMD) Opteron dual-core CPUs. Each machine node has 4 CPUs and 32 GB of RAM (8 GB of RAM per CPU). Sun Grid Engine (SGE) is used for managing jobs on the compute cluster, and bash shell scripting is the preferred method of controlling SGE job submission. The specifications of the School of Engineering compute cluster are continually evolving and thus the reader is referred to Duncan (2008) for the most up-to-date information.

The results of a test to determine the speedup obtained by running GprMax3D on the compute cluster are presented in Figure 19. Tests were completed using 1, 2, 4, 6, and 8 CPU cores, and the speedup factor was defined as the decrease in execution time relative to the execution time of the model running on a single CPU core. A typical antenna model using a domain of $284 \times 209 \times 140$ cells, a spatial discretisation of $\Delta x = \Delta y = \Delta z = 1$ mm, a time-step of $\Delta t = 1.926$ ps, and a time window of 6 ns was used for the tests. This required 600 MB of RAM. The results highlight the clear time-saving obtained from executing GprMax3D on multiple CPU cores but show that the relationship between the speedup factor and number of CPU cores is not linear.

5.3 SPATIAL DISCRETISATION, STAIRCASING, AND COMPUTATIONAL REQUIREMENTS

The FDTD technique is a volumetric method so the computational requirements are governed by the choice of spatial discretisation and the length of simulation time. If, for the same size of model domain and time window, the spatial discretisation is reduced, i. e., a smaller spatial-step is chosen, the time-step

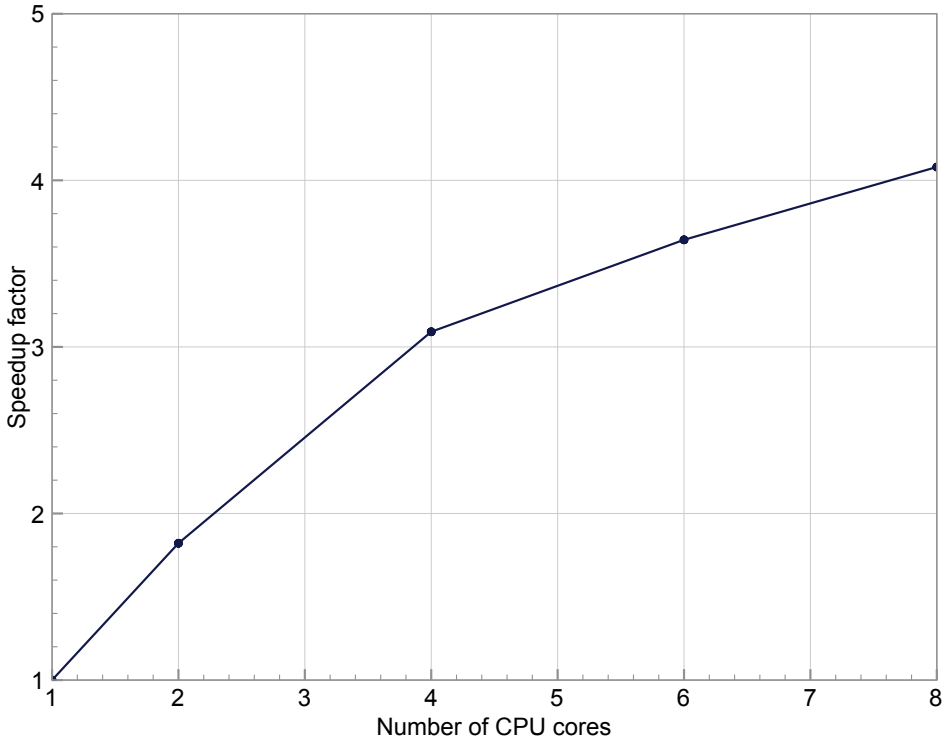

Figure 19: Speedup factor obtained executing GprMax3D on multiple CPU cores

becomes smaller because the CFL condition must be enforced and, in turn, the simulation time is increased. This increases both the amount of RAM required to hold all the quantities associated with every cell in grid as well as the amount of CPU-time required to run the simulation. Similarly, increasing the total simulation time for the model will also increase the amount of CPU-time required. A compromise must be made between the computational resources, and adequately resolving features in the model so that the simulation produces accurate results.

Two simple tests were conducted with models using five different spatial discretisations (0.5, 1, 2, 4 and 8 mm) of a PEC bowtie in free-space. The first test was designed to assess the relative computational requirements of models with different spatial discretisations. The results from the 8 mm model were used as a reference to compare the other models against. Figure 20 shows that there is a rapid increase in CPU-time and RAM requirements as the spatial-step is reduced.

The second test was designed to assess the relative accuracy of models with different spatial discretisations. Typically when staircasing approximations are studied the effects are measured by considering the input impedance of the antenna. Although the input impedance is a critical factor in the performance of the antenna, it is the measured E-field that is important for GPR. Hence, a

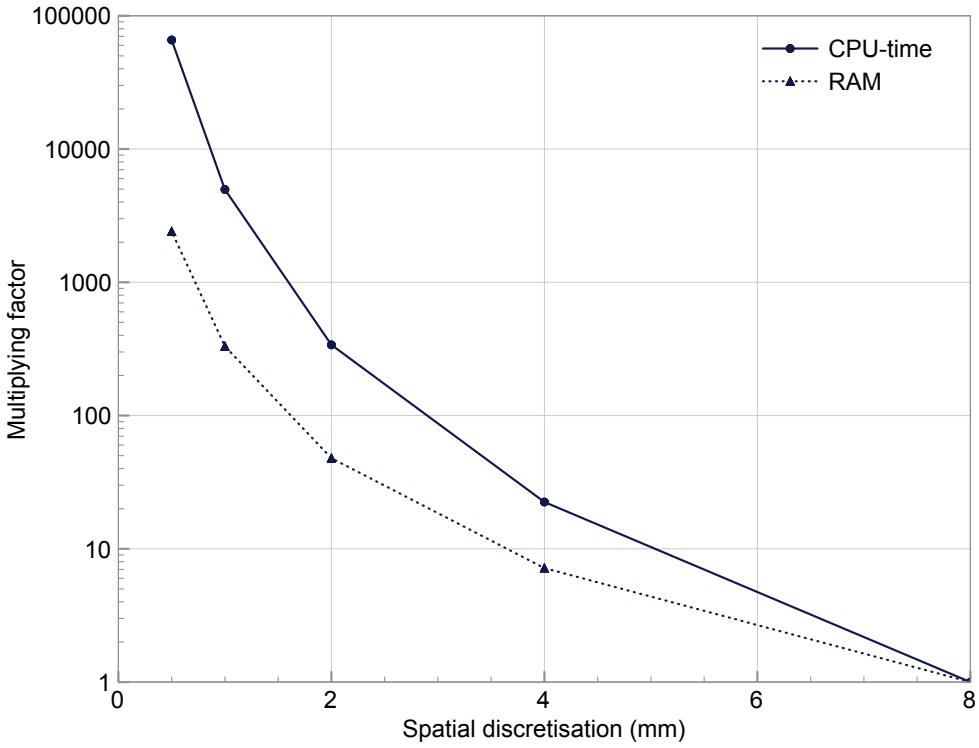

Figure 20: Relative CPU-time and RAM requirements for different model spatial discretisations

value of the E-field at the same point in each model was calculated, and the Residual Sum of Squares (RSS) given by (5.1) was computed for each model using the 8 mm model as a reference model. The sampling of each model was decimated to match the sampling of the 0.5 mm reference model.

$$\mathrm{RSS} = \sum_{i=1}^{n} (x_i - y_i)^2, \tag{5.1}$$

where:

n = total number of iterations in reference model

x = voltage of model under test (V)

y = voltage of reference model (V)

The curve labelled *standard staircasing* in Figure 21 shows that the errors increase non-linearly when the spatial-step is increased in linear increments.

The effects of staircasing approximations were studied further by investigating a simple local subcell model for PEC structures. The aim of the study was

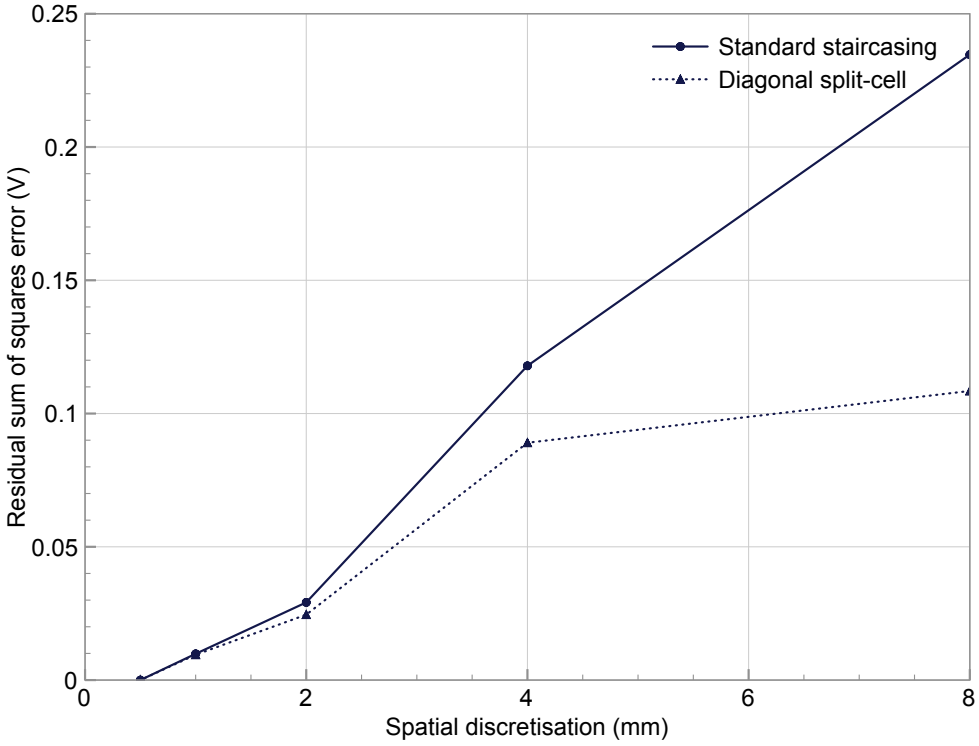

Figure 21: Residual sum of squares error for standard staircasing and diagonal split-cell models, for different model spatial discretisations

to use a simple local subcell model for the bowtie elements to determine if the accuracy of the model could be improved. The subcell model chosen was the diagonal split-cell model for PEC surfaces outlined in Taflove and Hagness (2005). In the standard FDTD model, a curved surface is approximated by a series of orthogonal E-field components located on cell edges. The split-cell model allows the standard staircase contour to be deformed to run along cell diagonals, potentially improving the modelled geometry of the PEC surface. Only the H-field components located at the centre of each split-cell require a modified FDTD update equation. The following equation (5.2) is obtained when Faraday's Law (3.4a) is applied to a split-cell.

$$\mu_0 \left(\frac{H_z\Big|_{i,j,k}^{n+\frac{1}{2}} - H_z\Big|_{i,j,k}^{n-\frac{1}{2}}}{\Delta t} \right) \cdot \left(\frac{\Delta^2}{2} \right) = \Delta \left(E_x\Big|_{i,j+\frac{1}{2},k}^{n} - E_x\Big|_{i,j-\frac{1}{2},k}^{n} \right) - \Delta \left(E_y\Big|_{i+\frac{1}{2},j,k}^{n} + E_y\Big|_{i-\frac{1}{2},j,k}^{n} \right) \tag{5.2}$$

The second term on the left-hand-side of (5.2) represents the area of the split-cell carrying the magnetic flux. Two of the electric field components on

the right-hand-side of (5.2) are inside the PEC material and can therefore be cancelled to zero. The resulting rearrangement is given by (5.3).

$$H_z\Big|_{i,j,k}^{n+\frac{1}{2}} = H_z\Big|_{i,j,k}^{n-\frac{1}{2}} + \frac{2\Delta t}{\mu_0 \Delta}\left(E_x\Big|_{i,j+\frac{1}{2},k}^{n} - E_y\Big|_{i+\frac{1}{2},j,k}^{n}\right) \tag{5.3}$$

It should be noted that the modified FDTD update equations for the H-field components are identical to the standard FDTD update equations, except that the coefficient multiplying the E-field components is doubled. This occurs because the area through which the magnetic flux flows is halved in the split-cell model. Figure 22 illustrates how the split-cell algorithm affects the boundaries of modelled materials, and highlights graphically the modified H-field components.

Mesh generation for the split-cell model is initially the same as the standard FDTD model but an additional step is necessary to determine whether there are any contiguous pairs of E-field components in a cell defined as PEC, where the remaining two components (2D case) are not PEC. If this condition is true, the cell is designated a split-cell and the H_x, H_y, or H_z component centred in that cell is updated using the appropriate form of (5.3).

The simple bowtie model used in the previous tests was analysed using the diagonal split-cell model with the previously used spatial discretisations. The RSS given by (5.1) was again used to assess the effects of the split-cell model on E-field values. Figure 21 shows the results from the split-cell model alongside the previous results using standard staircasing.

Both methods exhibit the same trend of a non-linear increase in error when the spatial-step is increased in linear increments. At a spatial discretisation of approximately 4 mm the two methods diverge significantly, and subsequently the diagonal split-cell model provides much better accuracy at a spatial discretisation of 8 mm.

It was stated in Chapter 4 that Shlager et al. (1994) had showed that the amplitude of additional reflections introduced into received responses by staircasing approximations could be controlled by ensuring that the ratio, given by (5.4), was enforced.

$$\frac{\Delta s}{\lambda} < 0.5, \tag{5.4}$$

where:

Δs = largest hypotenuse of a staircased cell mm

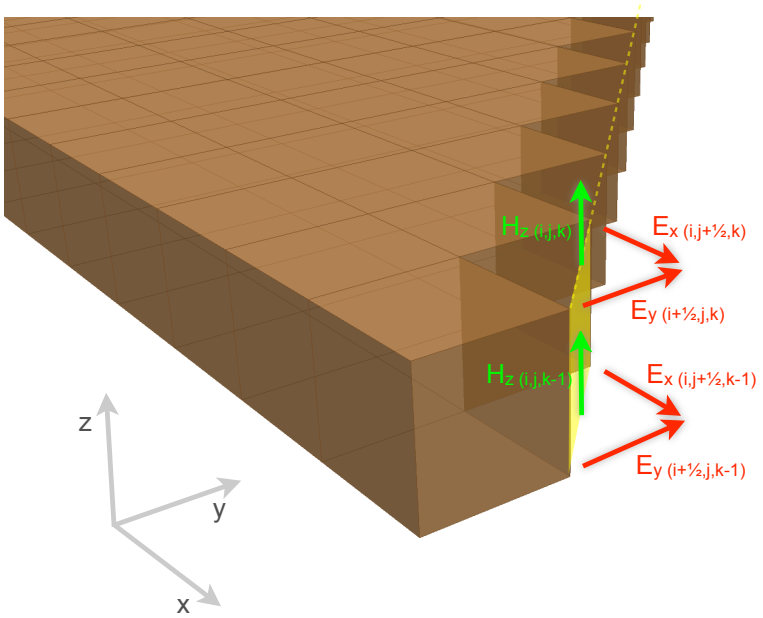

(a) 3D visualisation

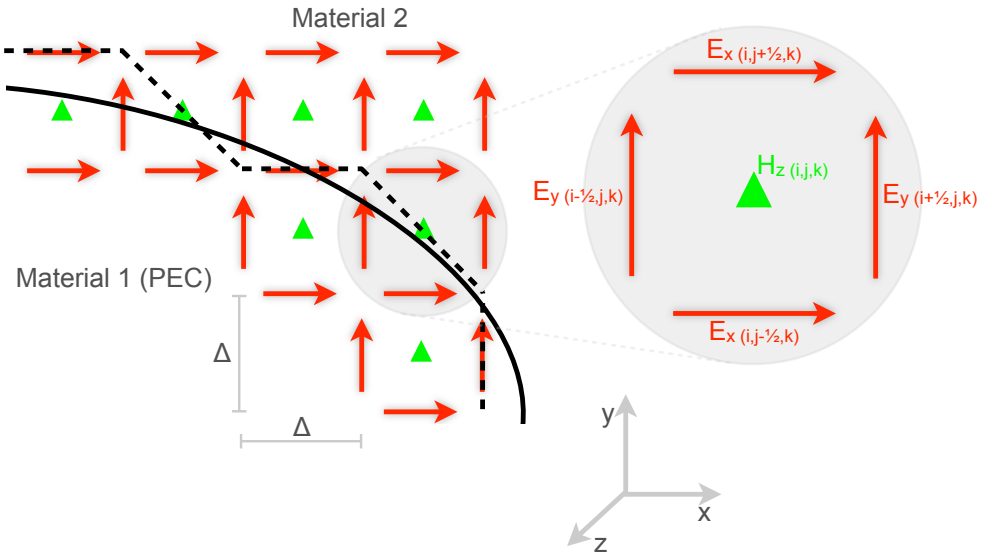

(b) 2D visualisation, highlighting a split-cell

Figure 22: Diagonal split-cell model for PEC surfaces

SPATIAL DISCRETISATION (mm)	Δs (mm)	$\frac{\Delta s}{\lambda}$
0.5	0.71	0.05
1	1.41	0.11
2	2.83	0.21
4	5.66	0.43
8	11.31	0.85

Table 2: Values for a ratio, given by Shlager et al. (1994), to control reflections in responses as a result of staircasing

To verify that (5.4) was satisfied, the maximum frequency in a feed pulse was assumed to be 2.5 GHz, yielding a minimum wavelength (occurring in water, $\epsilon_r = 81$) of 13.3 mm. Thus, a series of values of the ratio (5.4) were calculated for different spatial discretisations and are presented in Table 2. At a spatial discretisation of 8 mm the ratio is violated, which could explain why the deformed contour in the diagonal split-cell model enabled it to achieve a much better accuracy over the standard staircasing at this spatial-step.

Ultimately, a spatial-step of 1 mm was chosen for the antenna models, which was a compromise of potential accuracy and computational requirements. It was also evident that, by selecting a spatial-step of 1 mm, the smallest potential wavelength in the models (13.3 mm) was 10–20 times bigger, ensuring any numerical dispersion was adequately controlled.

5.4 SUMMARY

The aim of this chapter was to describe the software and hardware used to create the antenna models and, at the same time, discuss the computational requirements. The electromagnetic simulation software used was GprMax3D, which is based on the FDTD method, and has very useful features for antenna modelling such as PML boundaries and user specific source excitation. The visualisation of the complex 3D antenna geometries was achieved by developing code that utilised the VTK to enable GprMax3D to produce VTK geometry files. These files included all the fine features typically found in antennas and could be viewed and manipulated in ParaView, a powerful open-source visualisation application.

The models were run on a compute cluster which greatly reduced simulation times as GprMax3D had been parallelised using OpenMP and was, therefore, able to execute on multiple CPU cores.

The spatial discretisation, staircasing errors, and computational requirements of the antenna models are all closely linked. It was shown that decreasing the size of the spatial-step (8, 4, 2, 1, 0.5 mm) meant the RAM and CPU-time requirements rapidly increased. However, decreasing the spatial-step also reduced the errors associated with staircasing approximations. A diagonal split-cell local sub-model for PEC surfaces was investigated to potentially help control staircasing errors further. The split-cell model showed marginal improvements in accuracy for spatial discretisations up to of 4 mm. For spatial discretisations larger than 4 mm, the ratio given by (5.4) (Shlager et al., 1994) was not satisfied and, hence, the standard staircasing method was shown to be significantly less accurate than the diagonal split-cell model. Based on the aforementioned studies, a spatial-step of 1 mm was chosen for the antenna models, which provided a good compromise between accuracy and computational requirements, and ensured any numerical dispersion was adequately controlled.

6

INITIAL DEVELOPMENT OF ANTENNA MODELS

In this chapter, the development and preliminary validation of numerical models of two commercial GPR antennas is detailed. The chapter begins with a description of the antennas and examples of their usage in the field. This is followed by the first, and arguably most important, stage of the model creation process: determining the main components, geometry, electrical characteristics, and material properties of the real antennas. The computational tools developed in the previous chapter are then used to build the antenna models and check the modelled geometries. A preliminary validation of the models is then carried out by modelling the crosstalk responses of the antennas and comparing them with the measured crosstalk responses from the real antennas. There were certain components in the real antennas that had unknown values, due to a combination of commercial sensitivity and lack of specialist test equipment. Thus, the chapter concludes with a sensitivity study of these unknown parameters.

6.1 OVERVIEW OF THE ANTENNAS

Two of the most commonly used antennas from leading GPR system manufacturers — GSSI and MALÅ — were modelled. The 1.5 GHz (Model 5100) antenna from GSSI and the 1.2 GHz antenna from MALÅ are high-frequency, high-resolution GPR antennas. The 1.5 GHz GSSI antenna is regarded by GSSI as a legacy product having being replaced by a 1.6 GHz model of similar design. However, the 1.5 GHz antenna was an extremely popular antenna and consequently still has a large user base in industry and academia. High-frequency GPR antennas are primarily used for the evaluation of structural features in concrete: the location of rebars, conduits, and post-tensioned cables, as well as the estimation of material thickness on bridge decks and pavements. Figure 23 shows a typical example of a high-frequency GSSI antenna being used to locate features in concrete. At high frequencies, smaller targets can be more easily resolved, but the depth of penetration is compromised because high frequencies are attenuated more than low frequencies. Dependent on conditions, a typically quoted maximum depth for these types of antennas would be around 0.5 m, hence, they are most suited to the detection of near-surface targets. Both the GSSI and MALÅ antennas are based on a system configuration where the transmitter and receiver are in the same enclosure. This is a common setup for GPR

Figure 23: Photograph showing concrete evaluation using a high-frequency GSSI antenna (Geophysical Survey Systems, Inc., 2001)

systems because it is simpler for the end-user to operate than a configuration with separate transmitter and receiver units, and is cheaper to manufacture.

6.2 BUILDING THE ANTENNA MODELS

The first, and arguably most important, stage in the model creation process is to determine the geometry, electrical characteristics, and material properties of the main antenna components. Unfortunately, some of these details were either commercially sensitive or difficult to determine without specialist test equipment. Consequently the enclosures of both antennas were opened so that the main components could be studied.

6.2.1 *Fundamental components and geometry*

The geometry of the antenna components was the simplest and most readily obtainable information to input into the model. The main components of the GSSI antenna are highlighted in Figure 24 and similarly for the MALÅ antenna in Figure 25.

Both manufacturers use bowties as the transmitter (T_x) and receiver (R_x) elements in their antennas. The bowtie is a shape derived from the biconical antenna which offers many attractive electrical characteristics for a broadband

design (Balanis, 1997). Whilst the biconical antenna is often impractical to build, the bowtie is compact and cheap to produce, although it does not exhibit such broadband characteristics. The dimensions, especially the flare angle, of the bowtie are critical to the performance of the antenna (Balanis, 1997, King, 1956). The MALÅ antenna uses bowties with a flare angle of 85°, and resistive loading via discrete SMT resistors. These are attached at three locations on the open end of the bowties, and are designed to reduce unwanted resonance at the expense of a reduction in radiation efficiency. On the transmitter bowtie, 470 Ω resistors are used, and on the receiver bowtie, 150 Ω resistors. The GSSI antenna uses bowties with a flare angle of 76° and additional rectangular patches added to the open ends of the bowtie. These extensions act like straight sections of waveguide, which introduce a delay in the signal path and create destructive interference patterns that reduce unwanted resonance. In both antennas the bowties are etched from copper onto Printed Circuit Board (PCB).

The bowties are enclosed in rectangular metal boxes which act as shields and are also part of the case for the MALÅ antenna. The shields are designed primarily to prevent electromagnetic emissions from the antenna effecting surrounding electronic equipment. This is becoming an increasingly important consideration as governments restrict levels of electromagnetic emissions within the regulated spectrum used by GPR systems (Federal Communications Commission, 2002). In addition, the shape of the shielding can also be used to alter the directionality of the antenna radiation pattern. The shields, and any other metallic components in the antennas, were modelled as a PEC unless otherwise stated.

Both antennas utilise open-cell, carbon-loaded foams, which act as broadband electromagnetic absorbers to reduce unwanted resonance in the cavities behind the bowties. In the MALÅ antenna, the absorber is only used in the cavity behind the transmitter whereas in the GSSI antenna, it is used behind both the transmitter and the receiver. The permittivity and conductivity values for these absorber foams are unknown. As far as the author is aware, these foams are custom made to the manufacturers specification, details of which are commercially sensitive.

Certain components in the antenna are made from plastics: the enclosure for the GSSI antenna is polypropylene, and both antennas use High-Density Polyethylene (HDPE) for the skid plates. The skid plate is a replaceable component designed to protect the base of the antenna from damage.

Table 3 lists the properties used in the models for the known materials, i. e., the metals and plastics which have well-defined values for permittivity and conductivity. Initial values for the permittivity and conductivity of the electromagnetic absorbers were estimated using data for a typical off-the-shelf

COMPONENT	MATERIAL	ϵ_r	σ (S/m)
Bowtie	Copper	1	59.6×10^6
Skid plate	HDPE	2.35	0
PCB	Glass fibre	3	0
GSSI case	Polypropylene	2.26	0

Table 3: Permittivity and conductivity values of known materials in models (Altera Corporation, 2007, Riddle et al., 2003)

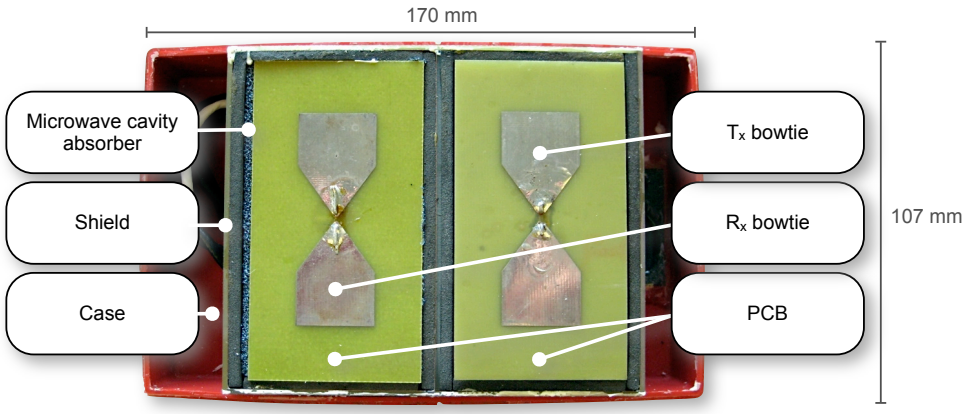

Figure 24: Annotated photograph of GSSI 1.5 GHz antenna

broadband microwave absorber (Emerson and Cuming, 1948). These initial values were refined using an iterative optimisation technique described in Chapter 7.

6.2.2 *Excitation and feeding*

The excitation of the antenna — pulse shape, frequency content, and feed method — is important for the performance of the real antenna and, hence, critical to capture in the model. The shape and frequency content of the transmitted pulses used by GSSI and MALÅ are unknown parameters, however, the antennas are of a broadband design so should, theoretically, be fed by an impulse. Since this is not physically realisable, a Gaussian shaped pulse of the form of (6.1) shown in Figure 26 was used with a centre frequency close to the manufacturers specification. This is a common choice in many GPR simulations

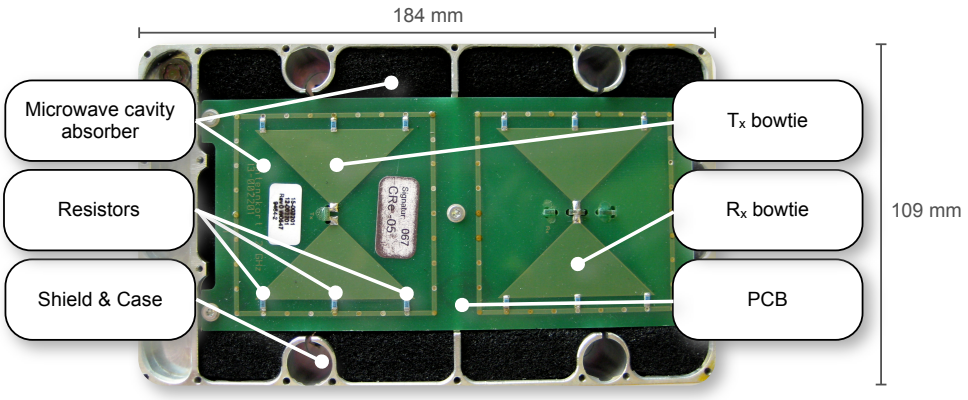

Figure 25: Annotated photograph of MALÅ 1.2 GHz antenna

(Gurel and Oguz, 2000, Lee et al., 2004, Nishioka et al., 1999, Roberts and Daniels, 1997).

$$V = e^{-2\pi^2 f^2 (t-\frac{1}{f})} \tag{6.1}$$

The transmitter and receiver bowties in the real antennas are connected to circuits that generate the transmitted pulse, and process the received signals. There are two main reasons for not modelling the physical electronic components in these circuits: firstly, the circuit design, components, and component values used are unknown; and, secondly, to accurately model components of this size would require a sub-millimetre FDTD mesh, which in turn would greatly increase the computational requirements. Therefore, a simplified feed model was sought. It was recognised by Hertel and Smith (2003) that both the geometry and type of simple feed model used could effect the impedance and admittance of the modelled antenna. Two different feed models were available in GprMax3D and, potentially, applicable: a voltage source and a 1D two-wire transmission line. In this case, both feed models could be inserted between the two arms of the transmitter bowtie (the drive-point). The tangential electric field component at the drive-point is then related to an impressed voltage (6.2).

$$V(t) = -\int_0^{l_g} \vec{E} \cdot \vec{dl}, \tag{6.2}$$

where l_g is the width of the gap. If the integral in (6.2) is converted into a summation, an update equation for the electric field component at that point in the FDTD grid can be obtained (6.3).

$$E_x\Big|_{gap}^{n} = -\frac{V}{N_g \Delta x}, \tag{6.3}$$

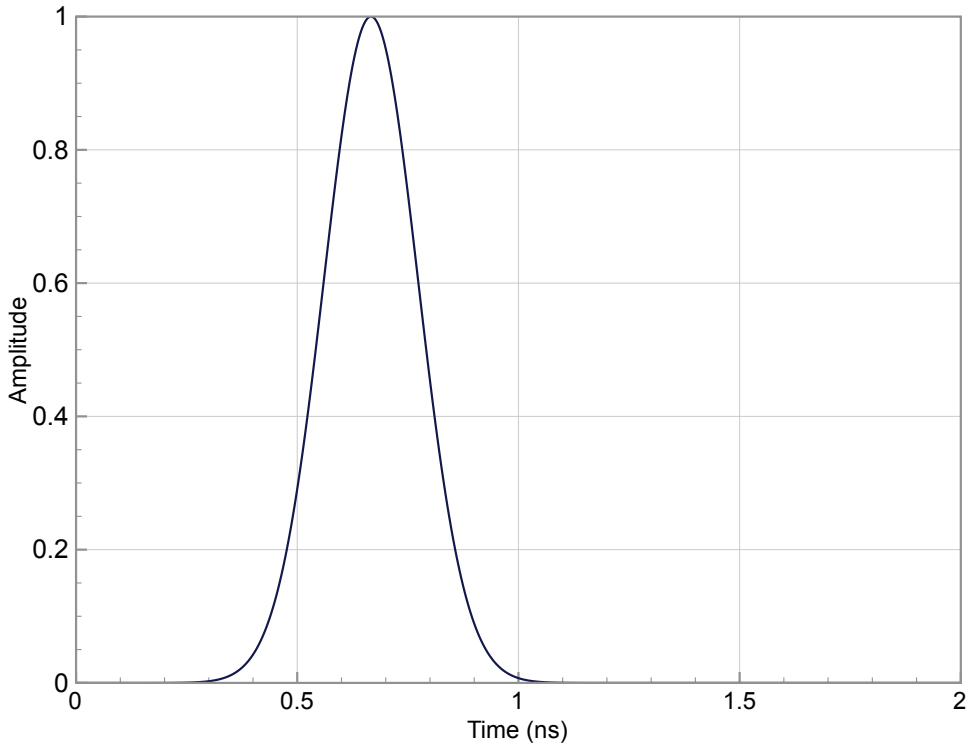

(a) Time domain response

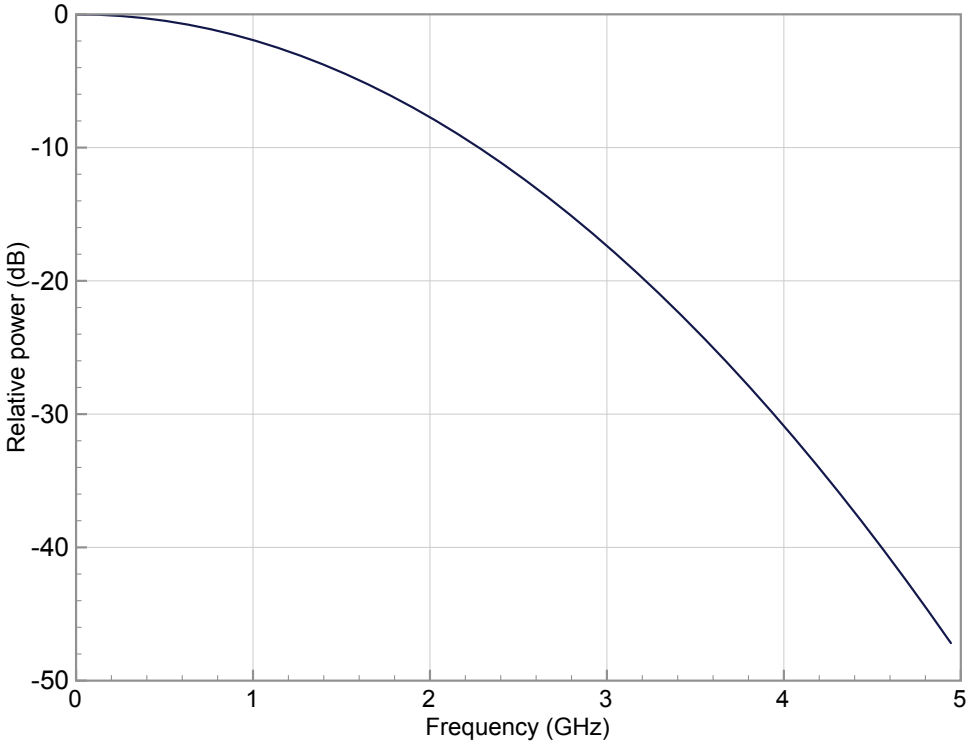

(b) Power Spectral Density (PSD)

Figure 26: Gaussian pulse with 1.5 GHz centre frequency

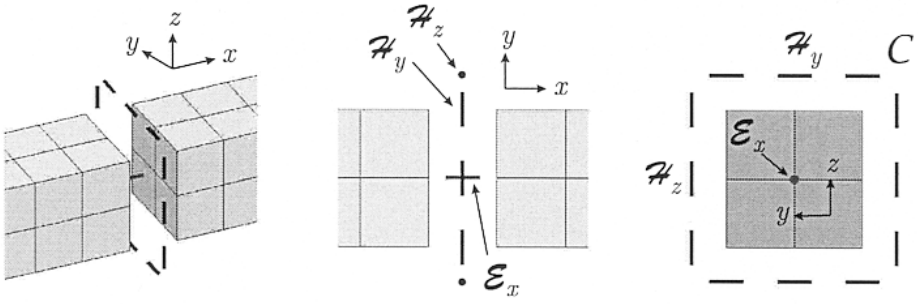

(a) Basic feed scheme: single-cell excitation

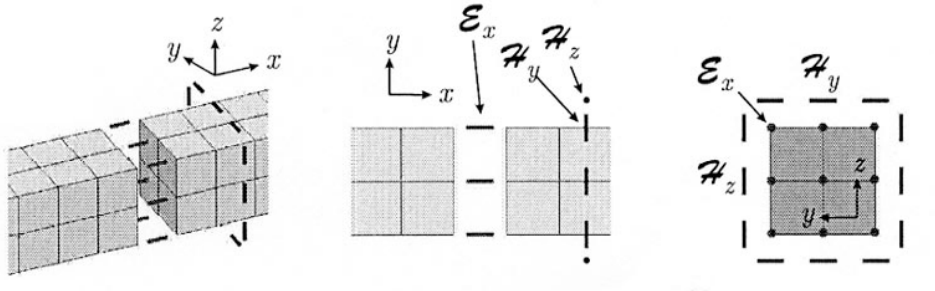

(b) Improved feed scheme: multiple-cell excitation (coarse discretisation)

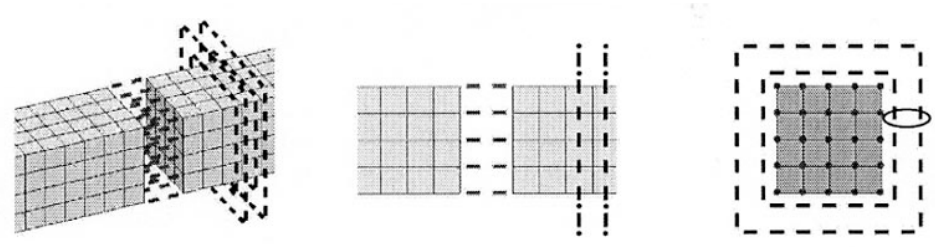

(c) Improved feed scheme: multiple-cell excitation (fine discretisation)

Figure 27: Feeding schemes showing updated field components (Hertel and Smith, 2003)

where the gap extends in the x-direction, and N_g is the number of cells within the gap. An improved feeding scheme is obtained for a multiple-cell drive-point gap if the voltage is applied uniformly, and all tangential electric field components within the gap are updated based on (6.2). Figure 27a and Figures 27b–27c show the electric field components that are updated in the basic feeding scheme, and the improved feeding scheme, respectively.

The current I at the drive-point is determined using the magnetic field (6.4).

$$I(t) = \oint_C \vec{H} \cdot \vec{ds}, \tag{6.4}$$

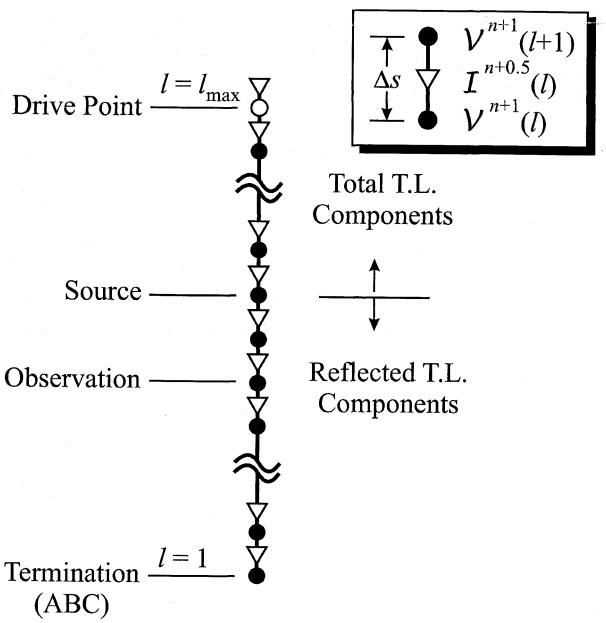

Figure 28: 1D transmission line feed model (Hertel and Smith, 2003)

Figure 27a shows that in the basic feeding scheme, the contour C is located in the drive-point gap. It has been shown when the contour is at this location the impedance of the modelled antenna does not represent the real antenna for high frequencies (Hertel and Smith, 2003). This is because the calculated current with the contour in the gap is a portion of the displacement current. When the contour encloses the antenna conductor the calculated current is only the conduction current. Figure 27b shows that in the improved feeding scheme the contour C is shifted to enclose only the antenna conductor. Figure 27c shows that for finer levels of discretisation the averaging of several contours is necessary.

In the voltage source model, the impressed voltage is forced to follow a time-domain expression e. g., a finite-duration Gaussian pulse. The voltage source may or may not include resistance, which can reduce late-time resonance in the transmitted signal, and make the source more transparent to any impinging electromagnetic waves.

In the transmission line feed model, the impressed voltage is introduced at the drive-point by virtually attaching a 1D transmission line. Figure 28 shows the staggered voltage V and current I in the transmission line. The excitation is produced by a one-way injector: an incident signal launched from the source in the transmission line towards the drive-point. The transmission line is terminated at the end furthest from the antenna by a simple ABC. The transmission line offers the advantage of being able to analyse both the incident and reflected voltages.

The receiver circuitry for both antennas was taken as a lumped resistance and modelled by specifying the corresponding conductivity of a single-cell edge in the gap between the receiver bowtie arms. The SMT resistors in the MALÅ antenna model are modelled using a similar method. The resistors used are of package size 3216 (3.2 mm × 1.6 mm), and are each modelled using two parallel lines (single-cell separation) of cell edges between the open bowtie ends and the shield (ground plane). This arrangement is highlighted in the FDTD model geometries presented in the following section. The resistance of each resistor is equally distributed by specifying the conductances of the cell edges, taking into account the two parallel current paths (6.5).

$$\sigma_{SMT} = \frac{1}{N_p} \cdot \frac{N_c}{R_{SMT}} \cdot \frac{\Delta x}{\Delta y \Delta z}, \tag{6.5}$$

where the resistor is aligned in the x direction, and where:

σ_{SMT} = conductivity of cell edge (S/m)

R_{SMT} = resistance of SMT resistor (Ω)

N_p = number of parallel current paths

N_c = number of cell edges between bowtie and shield

6.2.3 *FDTD models*

Antenna model input files for GprMax3D were created from the analysis of the physical and electrical characteristics of the real antennas. All the main components, excitation and feeding described in Section 6.2 were included in the models. Figure 29 and Figure 30 show detailed breakdowns of the FDTD meshed geometries of both antenna models. Figure 29b shows the electromagnetic absorber surrounded by a thin layer of packing foam in the cavities behind both the transmitter and receiver bowtie in the GSSI 1.5 GHz antenna. Figure 29c demonstrates how the bowtie elements are etched into the PCB, which is the case for both GSSI and MALÅ antennas. Figure 30b shows that the electromagnetic absorber is only used in the cavity behind the transmitter bowtie in the MALÅ 1.2 GHz antenna. The cell edges used to model the SMT resistors in the MALÅ antenna are highlighted in Figure 30c. The complete FDTD geometries of the two antenna models can be seen in Figure 29d and Figure 30d.

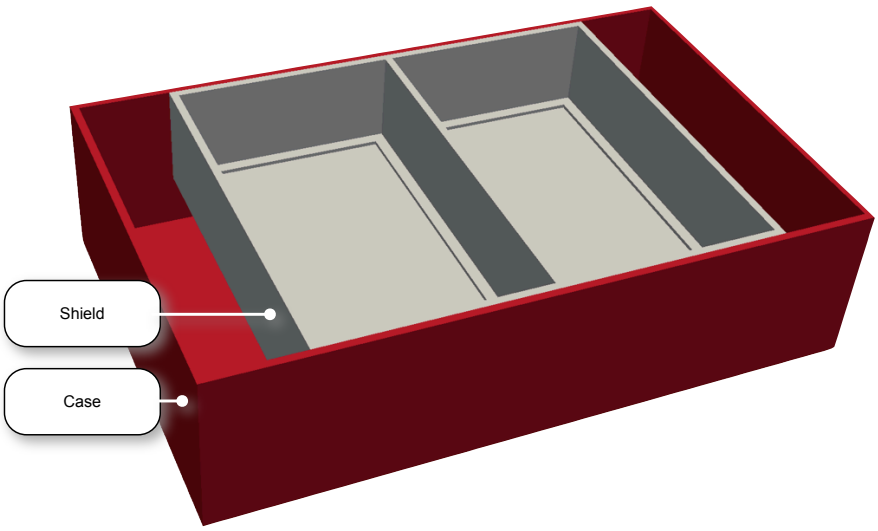

(a) Case and shielding

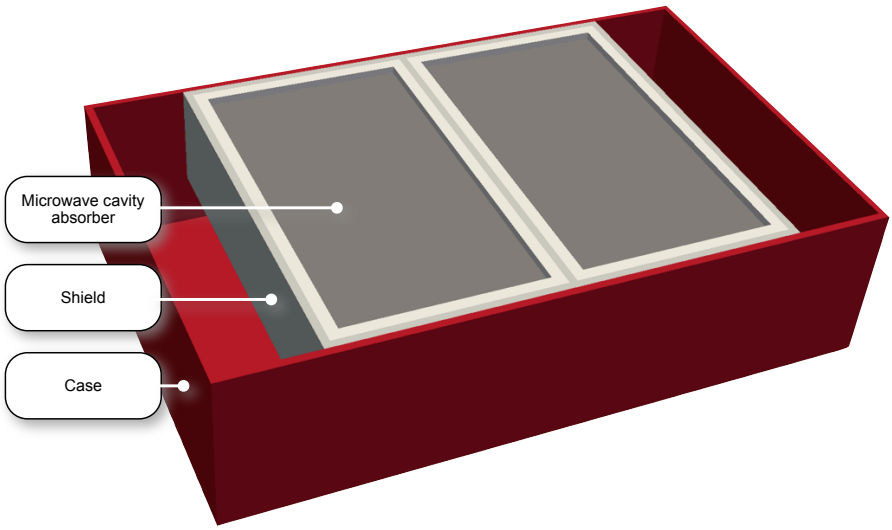

(b) Microwave cavity absorber

Figure 29: GSSI 1.5 GHz antenna: Modelled geometry (FDTD mesh)

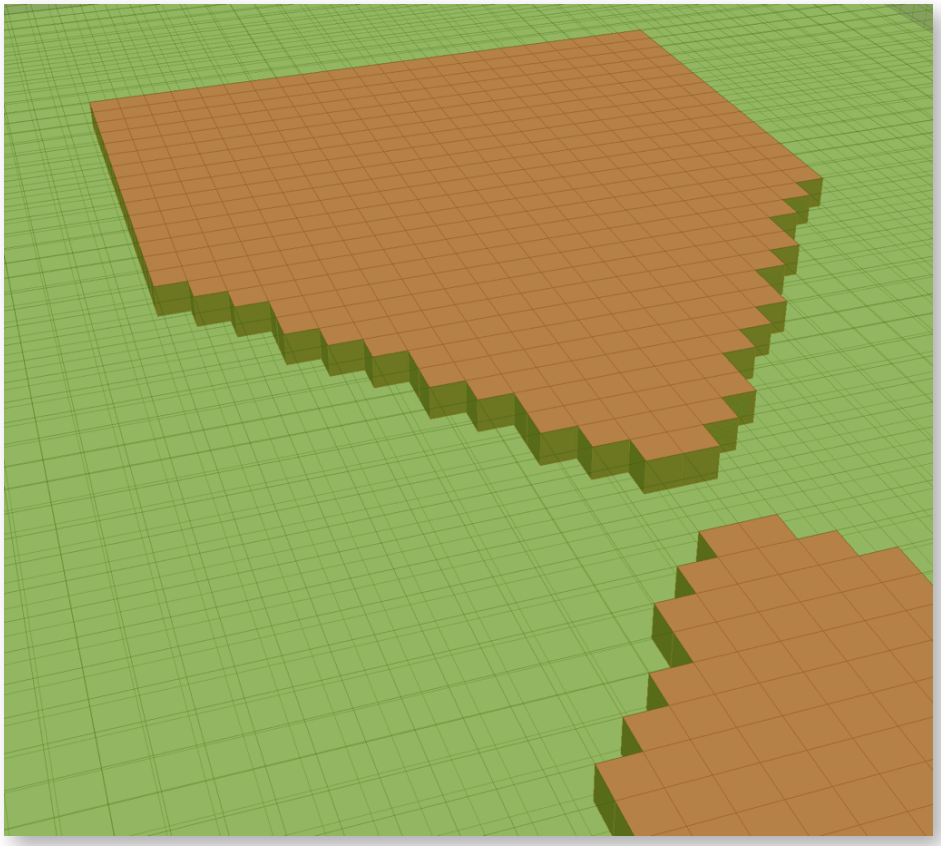

(c) Enlarged section showing bowties embedded in PCB

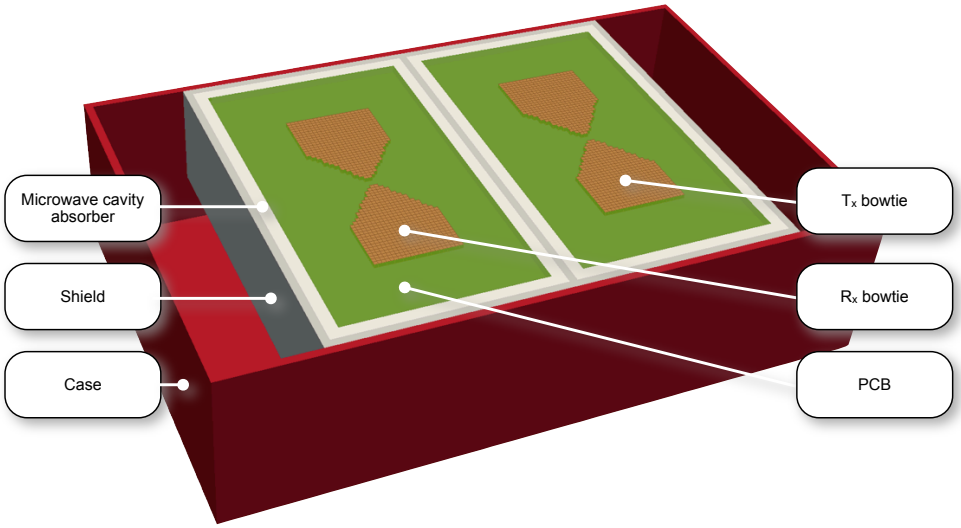

(d) All antenna components except skid

Figure 29: GSSI 1.5 GHz antenna: Modelled geometry (FDTD mesh)

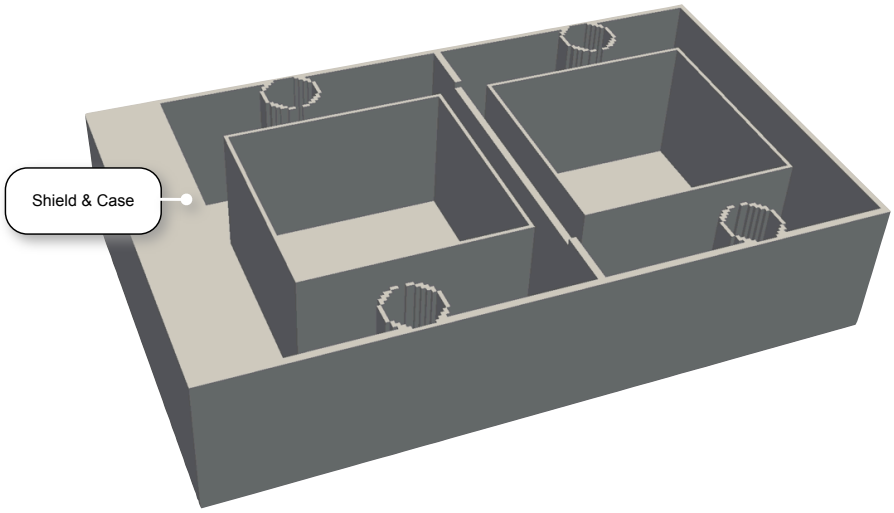

(a) Case and shielding

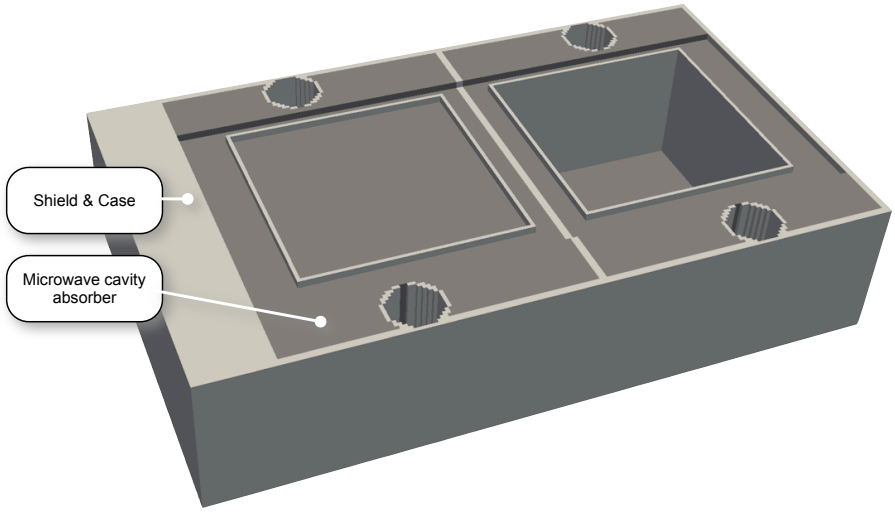

(b) Microwave cavity absorber

Figure 30: MALÅ 1.2 GHz antenna: Modelled geometry (FDTD mesh)

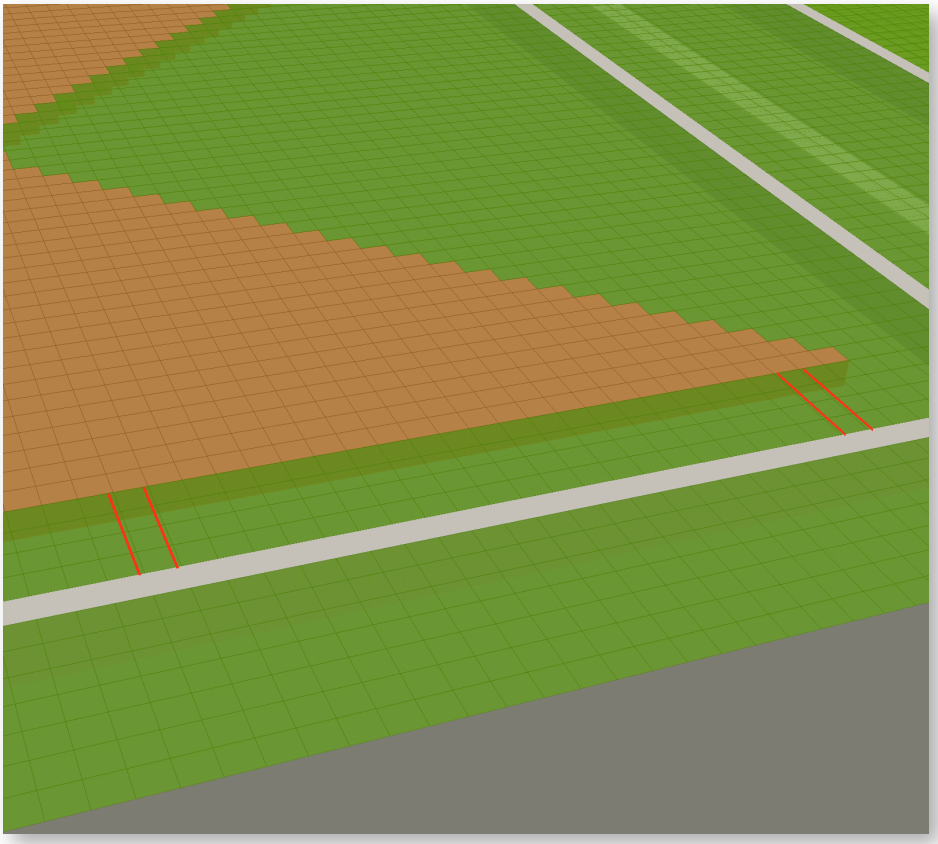

(c) Enlarged section highlighting model of SMT resistors used to load bowties

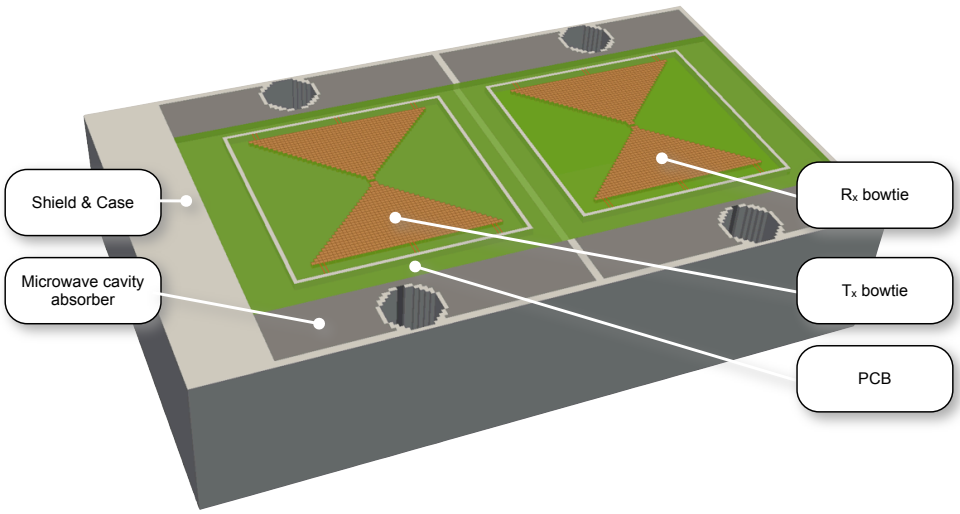

(d) All antenna components except skid

Figure 30: MALÅ 1.2 GHz antenna: Modelled geometry (FDTD mesh)

The conclusion of the study described in Chapter 5 was that all models (unless otherwise stated) should use a spatial discretisation of $\Delta x = \Delta y = \Delta z = 1$ mm and, as the CFL condition is enforced, a time-step of $\Delta t = 1.926$ ps. Since the preliminary validation required a modelled crosstalk response, the computational requirements for each antenna model could be kept to a minimium i. e., by using a well-performing PML the model domain only contained the antenna surrounded by a few cells of free-space. The domain for the GSSI antenna model was $270 \times 207 \times 143$, and for the MALÅ $284 \times 209 \times 140$, resulting in approximately 8 million cells in each model. This required 600 MB of RAM and 30 minutes run-time on 6 CPU cores for a time window of 8 ns.

6.3 PRELIMINARY MODEL VALIDATION

6.3.1 *Crosstalk*

A method of evaluating the characteristics of an antenna was required to compare the performance and accuracy of the modelled antennas to the real antennas. There are a number of fundamental parameters that describe the performance of an antenna system: radiation pattern, gain, directivity, efficiency, impedance, current distribution, and polarisation (Balanis, 1997). Any of these parameters could have been obtained straightforwardly from the antenna models. However, measuring any of these parameters from the real antennas would have required an antenna range and/or specialised test equipment, neither of which was available. A parameter that could be easily measured from the real antennas was the crosstalk response in free-space. The crosstalk response of an antenna is obtained by placing the antenna in free-space and recording the response, which will be the signal directly transmitted between transmitter and receiver. The crosstalk response may also be obtained using two identical antennas placed opposite one another, with one antenna set to transmit, and the other to receive. A crosstalk response in free-space is an important parameter to characterise the performance and behaviour of an antenna, despite free-space not being representative of materials encountered in typical GPR surveys. Ideally, the response of a real antenna should be measured over a homogeneous material with a known permittivity close to that encountered in typical GPR surveys, however, this presents practical difficulties. The crosstalk response was obtained from each real antenna by placing the antenna on a wooden tripod with the bowties facing upward. Data was recorded

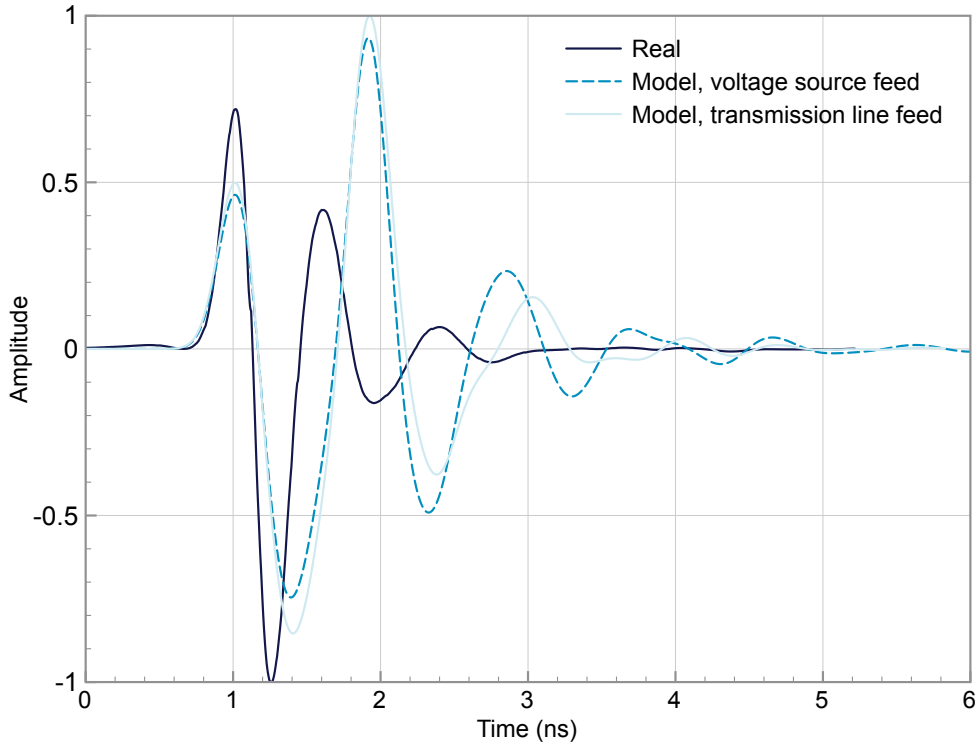

Figure 31: GSSI 1.5 GHz antenna: Preliminary model of crosstalk response compared with real crosstalk response

for a fixed length of time, and averaged to obtain the crosstalk response in free-space[1].

Figure 31 and Figure 32 show comparisons of the real and initial model crosstalk responses of the GSSI and MALÅ antennas[2]. Also shown are comparisons of the voltage source and transmission line feed models (both using a transmitter source resistance of 100 Ω). It was decided to use the voltage source feed model as it was simpler to implement and seemed to provide a marginally better match with the real crosstalk responses. The real responses follow the classic Ricker shape for the early-time part of the signal, with some additional late-time ringing in the tail. The shapes of modelled responses show similarity to the real ones but to improve them, further investigation of the values of the unknown parameters in the models and their effects on the crosstalk responses was required.

1 The crosstalk response for the GSSI 1.5 GHz antenna was recorded using the manufacturers recommended filter settings for that antenna. The MALÅ system allows user adjustable software filters to be applied, but these do not affect the recorded data.

2 The modelled responses are the E-field values at the receiver converted to voltage. All the responses have been normalised to an absolute maximum amplitude of one, and have been corrected for any DC bias present.

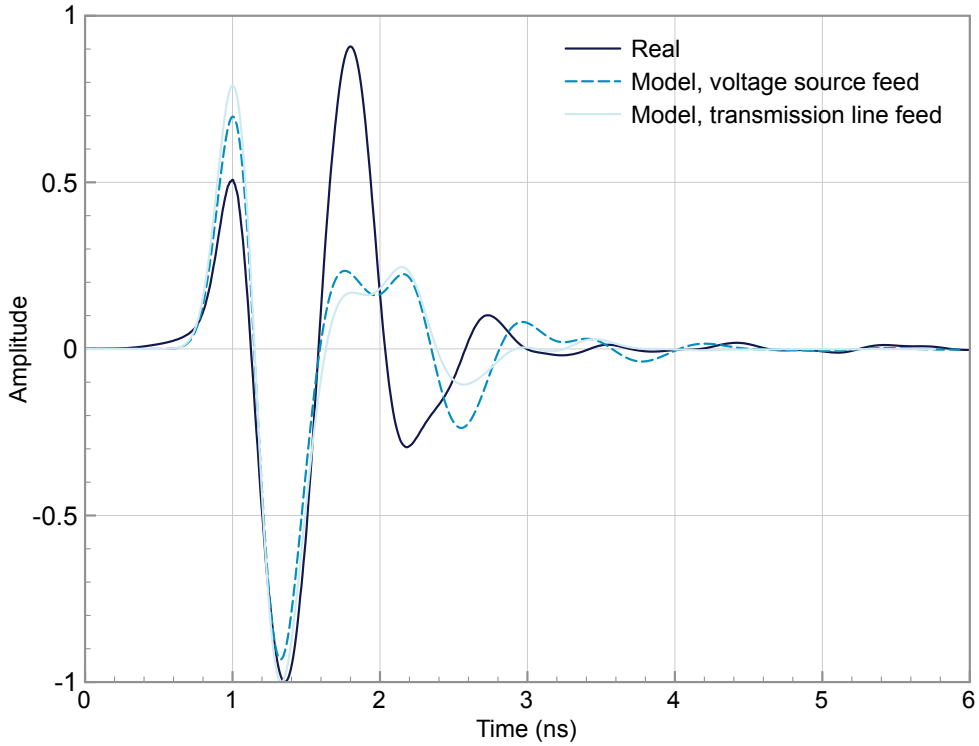

Figure 32: MALÅ 1.2 GHz antenna: Preliminary model of crosstalk response compared with real crosstalk response

6.3.2 *Sensitivity study of unknown parameters*

The unknown parameters from the real antennas, highlighted in Section 6.2 and required for the models, were:

- The centre frequency, f, and shape of the source pulse
- The resistance at the transmitter drive-point, R_{T_x}
- The resistance at the receiver, R_{R_x}
- The permittivity of the electromagnetic absorber, ϵ_r
- The conductivity of the electromagnetic absorber, σ

Ultimately, as described in Chapter 7, an optimisation technique was used to find the optimum value for each of these parameters. Initially, however, it was necessary to conduct a study to gauge the approximate effects of each parameter on the crosstalk responses. This also provided a basis for specifying an initial range for each parameter for the optimisation process.

Figures 33-37 show the effects, for a range of different values, each parameter has on the crosstalk response of each modelled antenna[3].

Figure 33 shows that varying the centre frequency of the transmitted pulse, f, over a range around the manufacturers specified centre frequency, effects both the amplitude and phase of the overall response. As f is increased the overall response becomes more compressed due to the higher frequencies present. The difference in amplitude between the responses is more significant than the phase differences, but there appears to be no consistent relationship between f and the amplitude of each peak or trough.

Figure 34 shows the change in the crosstalk response for different values of the resistance at the transmitter drive-point, R_{T_x}. As R_{T_x} is decreased more current can flow into the arms of the transmitter bowtie, more energy is transmitted and, hence, the amplitude of the received response increases.

Figure 35 shows increases in the amplitudes of the responses with increasing resistance at the receiver, R_{R_x}. This could be a result of an impedance mismatch with the receiver bowtie elements that improves as R_{R_x} is increased.

Figure 36 and Figure 37 show that the properties of the electromagnetic absorber have the largest influence on the crosstalk response of the antenna models. This is not surprising as the purpose of the absorber is to control the natural resonance of the bowties and cavities. Increasing the absorber permittivity introduces a time delay due to the decreased velocity of electromagnetic waves in the material. There is also an increase in the amplitude of the late-time part of the signal. Increasing the conductivity of the absorber decreases the amplitude of signal. This decrease in the amplitude occurs because the increase in conductivity means the signal is more quickly absorbed by the material. The increase in conductivity also introduces a slight delay in the late-time part of the signal.

3 Whilst the value of the parameter-under-test was being varied, the values for the other parameters were fixed at the median of their respective ranges.

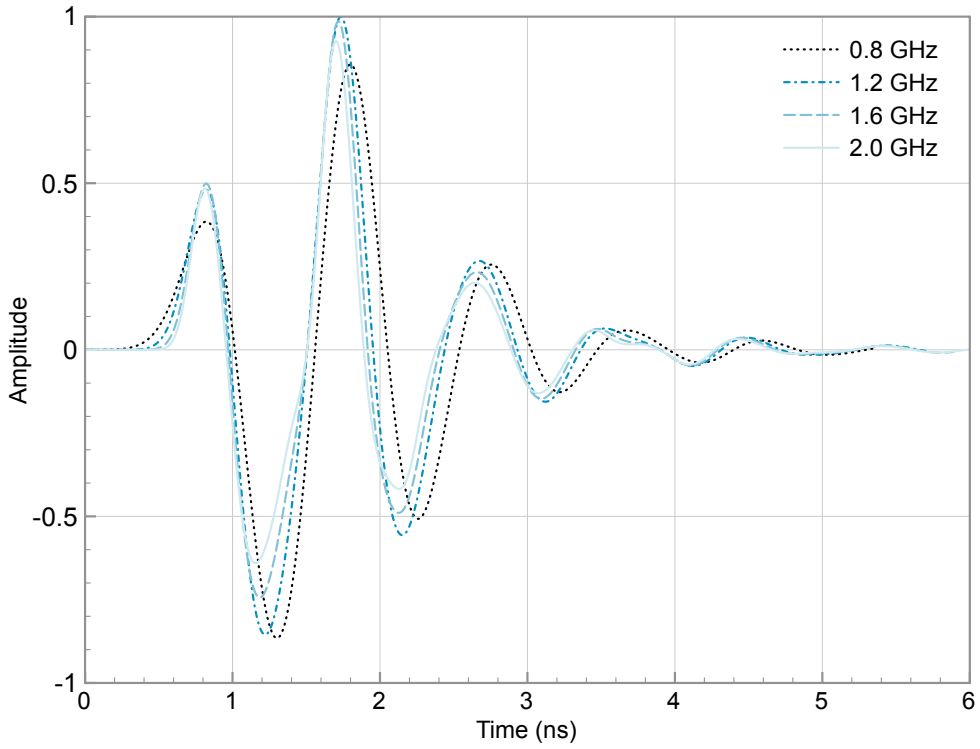

(a) GSSI 1.5 GHz antenna

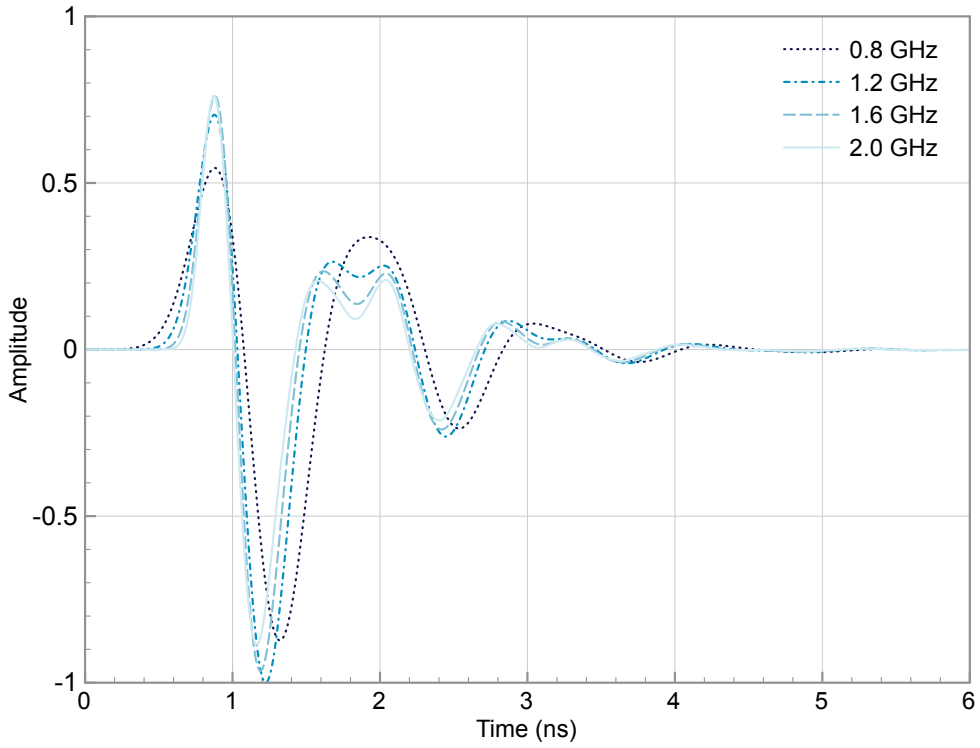

(b) MALÅ 1.2 GHz antenna

Figure 33: Modelled crosstalk responses with different values of source pulse centre frequency, f

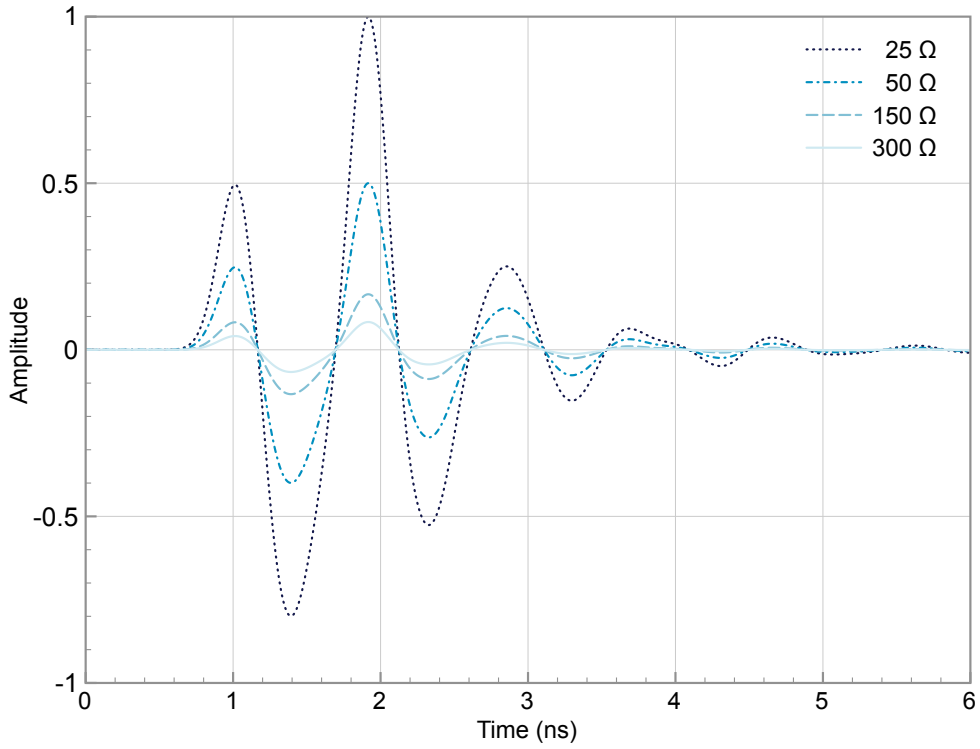

(a) GSSI 1.5 GHz antenna

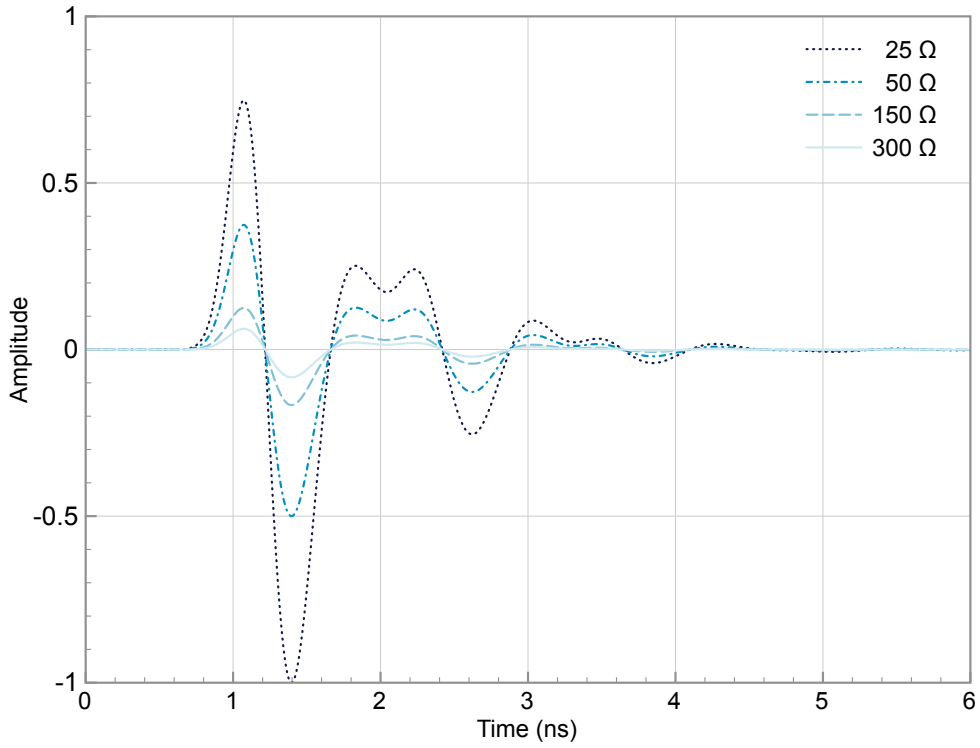

(b) MALÅ 1.2 GHz antenna

Figure 34: Modelled crosstalk responses with different values of resistance at transmitter drive-point, R_{T_x}

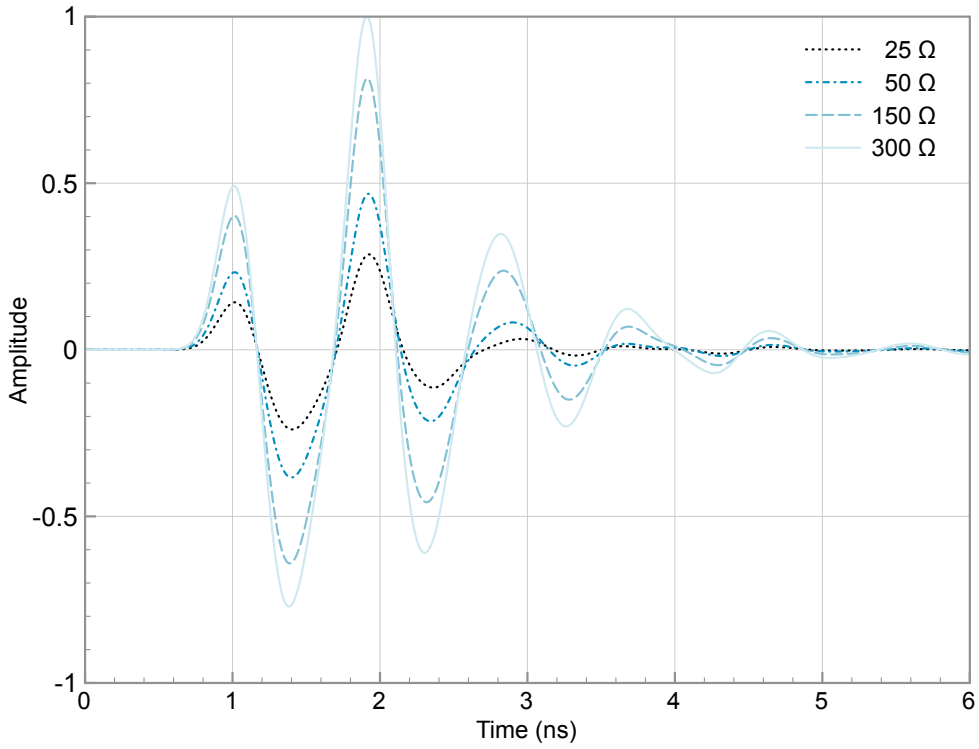

(a) GSSI 1.5 GHz antenna

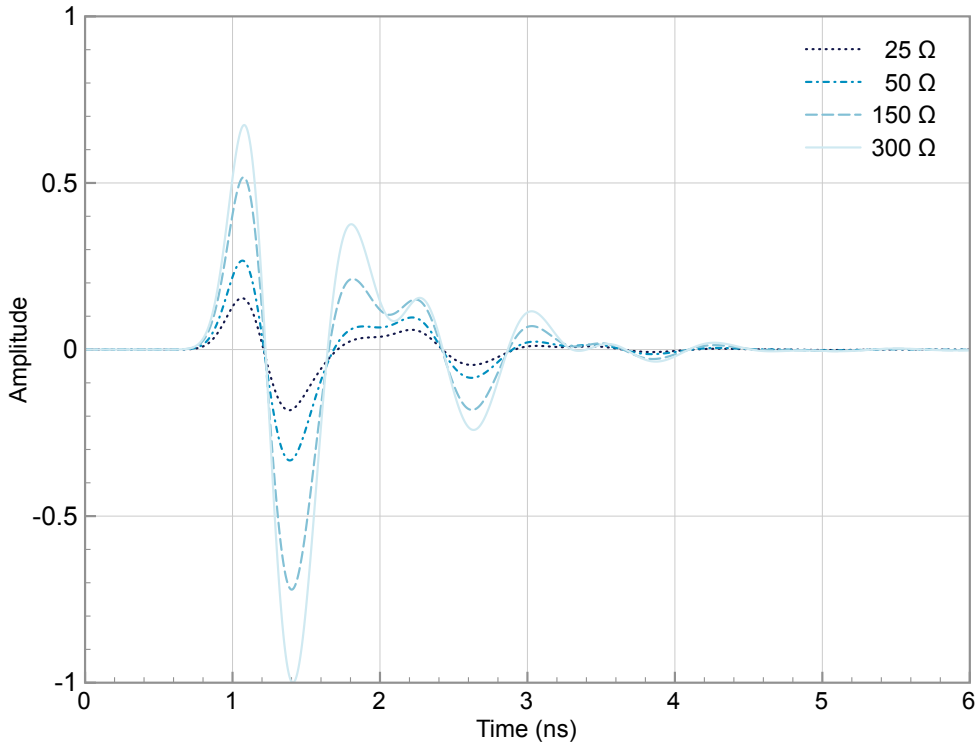

(b) MALÅ 1.2 GHz antenna

Figure 35: Modelled crosstalk responses with different values of resistance at receiver, R_{R_x}

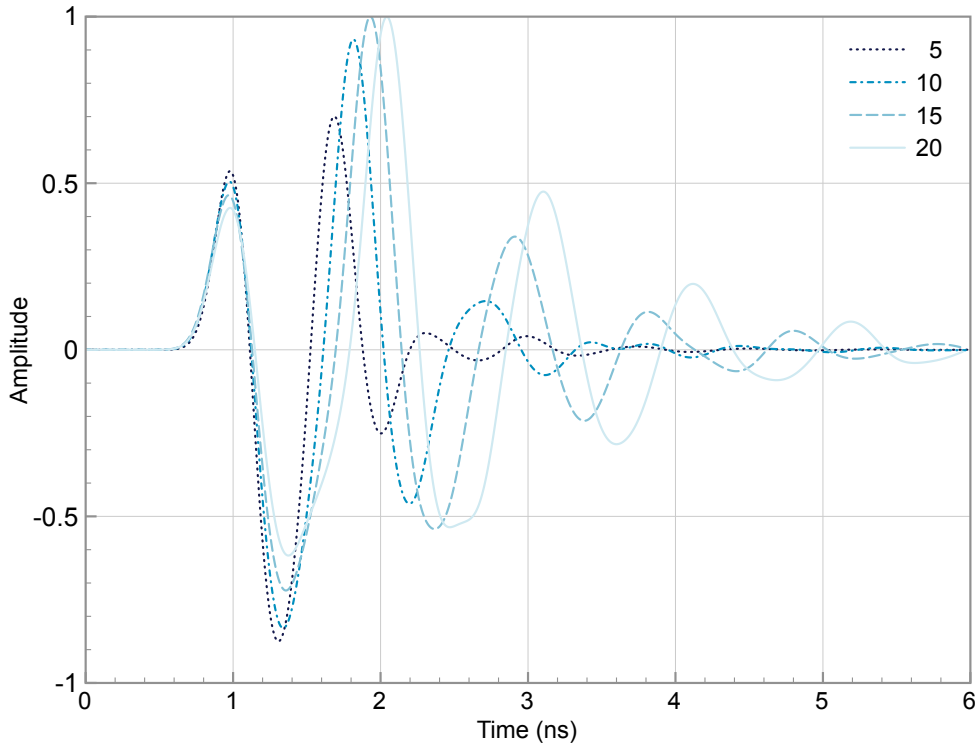

(a) GSSI 1.5 GHz antenna

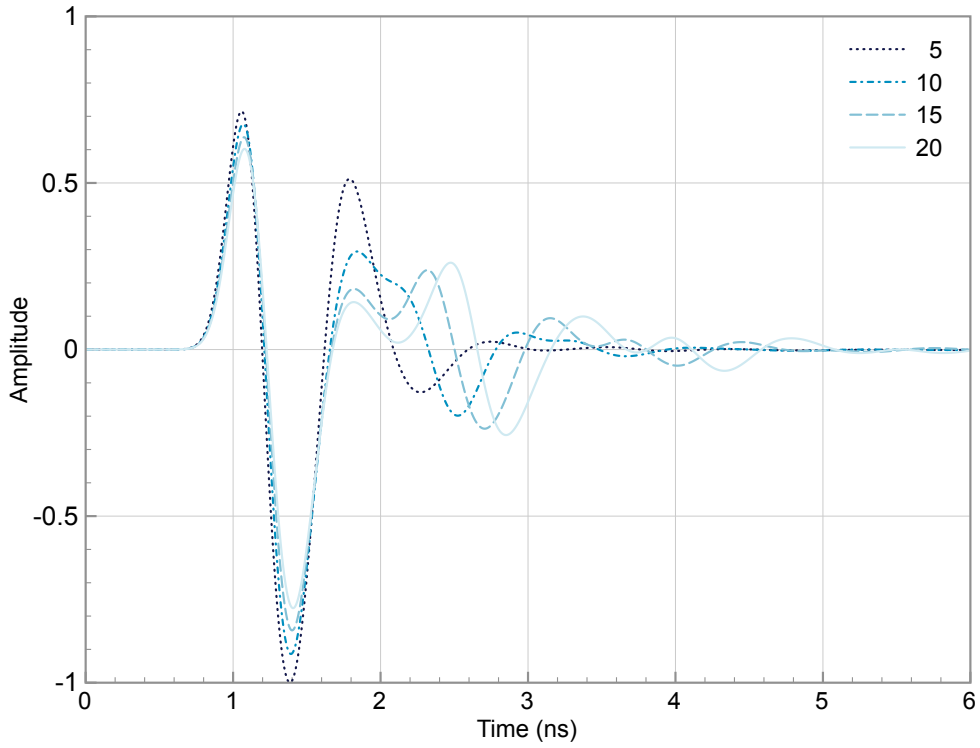

(b) MALÅ 1.2 GHz antenna

Figure 36: Modelled crosstalk responses with different values of electromagnetic absorber permittivity, ϵ_r

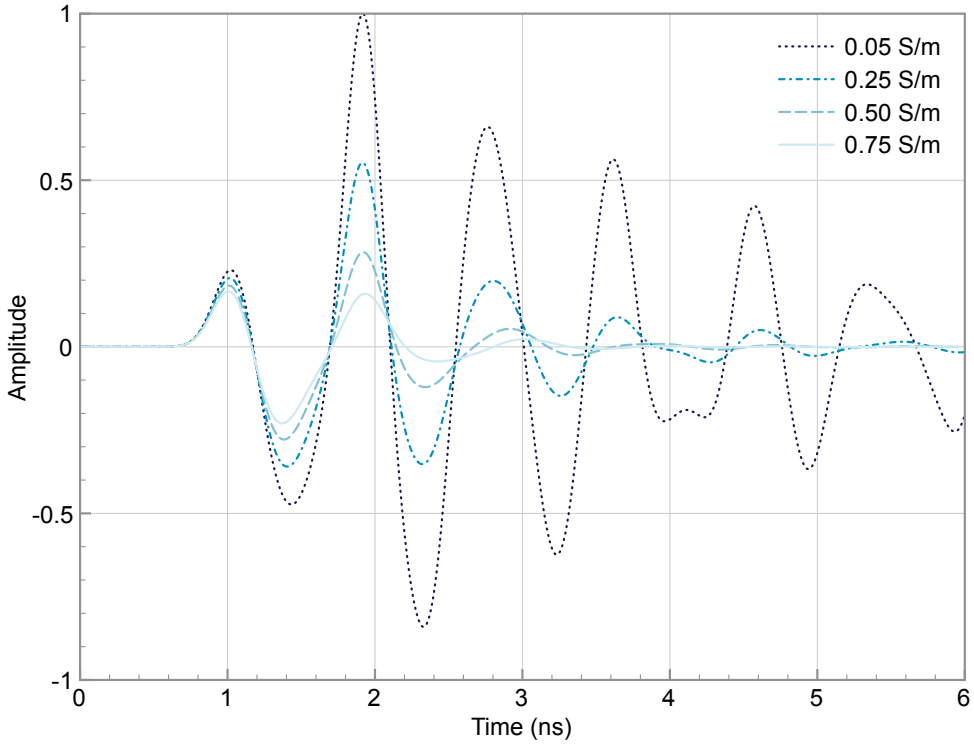

(a) GSSI 1.5 GHz antenna

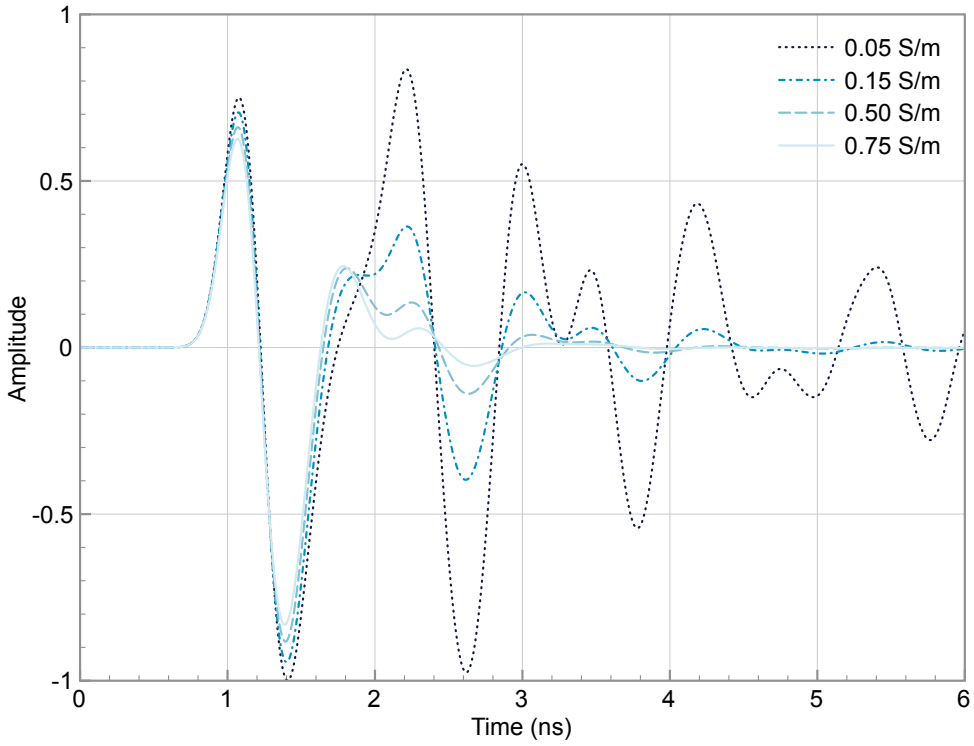

(b) MALÅ 1.2 GHz antenna

Figure 37: Modelled crosstalk responses with different values of electromagnetic absorber conductivity, σ

6.4 SUMMARY

The focus of this chapter was to detail the initial development of numerical models of two widely-used high-frequency GPR antennas. A process was established utilising GprMax3D, ParaView, and MATLAB® to build and test the models. The enclosures of real antennas were opened so that the fundamental components, geometry, and electrical characteristics could be analysed and used to create the models. The main features in the antenna models were:

- Transmitter and receiver bowties
- Electromagnetic absorber
- Bowtie loading resistors
- Shielding
- Case and skid plate
- Voltage source feed model using Gaussian shaped feed-pulse at manufacturers specified centre frequency

A number of these components had unknown values due to a combination of commercial sensitivity, and a lack of specialist test equipment. To establish the accuracy of the models, their crosstalk responses were visually compared to measured crosstalk responses from the real antennas. A sensitivity study of the unknown parameters in the models was carried out to assess the effects of each parameter on the crosstalk responses of the models. At this initial stage a range of values for each unknown parameter was defined and each range was then studied independently. The sensitivity study highlighted the permittivity and conductivity of the electromagnetic absorber as two of the most important parameters for controlling the shape (in terms of amplitude and phase) of the crosstalk response of the models. These preliminary validations of the models showed good promise, with most of the key features of the real responses captured in the models.

7

OPTIMISATION OF ANTENNA MODELS

In this chapter, the antenna models are developed further with the optimisation of the unknown parameters identified in Chapter 6. Several potential optimisation techniques are reviewed to assess their suitability to the problem. Following the selection of Taguchi's method as the preferred choice, the technique is described, and a fully automated process is developed to apply this technique to the optimisation of the unknown parameters in the models. The results of the optimisation are presented, and improved crosstalk responses of the antenna models are shown.

7.1 OPTIMISATION TECHNIQUES

Chapter 6 highlighted several unknown values for components and materials in the real antennas. It was necessary to establish values for these parameters so they could be accurately represented in the models. A sensitivity study was carried out to gauge their approximate effects on the crosstalk response of the models, but it was apparent that some method of systematic refinement of the parameter values would be required.

The goal of any optimisation is to obtain sufficient accuracy with minimum effort. The effort is usually measured as computational cost in terms of CPU run-time and memory requirements. Traditional optimisation methods such as a full factorial study, or trial-and-error approach, were considered too onerous because of the sheer number of simulations needed to achieve an optimum or satisfactory result, e. g., for a full factorial study of the GSSI antenna model, if each unknown parameter was limited to a range of twenty values then $5^{20} = 9.54 \times 10^{13}$ simulations would be required. Therefore ,several different optimisation techniques, commonly used in the field of electromagnetics, were considered:

- Artificial Neural Network (ANN)
- Genetic Algorithm (GA)
- Particle Swarm Optimisation (PSO)
- Simulated Annealing (SA)

- Taguchi's method

Table 4 shows a comparison of the characteristics of the aforementioned techniques. In general, the different methods can be divided into two categories: global and local. As the name suggests, global methods provide a global, or near global, optimum where the solutions are largely independent of the initial conditions. Global methods also offer advantages of being able to deal with non-differentiable and discontinuous functions, solutions with constrained parameters, and solutions with a large number of dimensions and many local maxima. The disadvantage of global methods is that their convergence rates can be slow. Conversely, local methods depend greatly on initial conditions and do not handle discontinuities well. For this application, a global method was especially important because the problem contained a relatively unknown solution space. In addition, a good convergence rate was also desirable. Taguchi's method has the following advantages (Weng et al., 2007a):

- Simple to implement
- Effective in reduction of experiments
- Fast convergence speed
- Global optimum results
- Independence from initial values of optimisation parameters

Taguchi's method has been used in the fields of chemical engineering, mechanical engineering, integrated chip manufacture, and power electronics (Chou, 1996, Hwang et al., 2005, Nagano et al., 2003, Wang et al., 1999), but has had only limited application in electromagnetics. Examples are the design of absorbers (Charles et al., 1999, MacDonald, 1990), linear antenna array synthesis, and the optimisation of antenna design (Weng et al., 2007b).

7.2 TAGUCHI'S METHOD

7.2.1 *The Orthogonal Array (OA)*

OAs were introduced in the 1940s, in a series of seminal papers by Rao (1946, 1947, 1949). Taguchi's method is based on the concept of the OA, which can effectively reduce the number of experiments required in a design process (Taguchi et al., 2005). They provide a systematic method to determine control parameters so that an optimal result can be found from the fewest experiments. The formal definition of an OA is given in Hedayat et al. (1999) and is summarised as follows:

METHOD	CHARACTERISTICS			
	GLOBAL OPTIMISATION	DISCONTINUOUS FUNCTION	NON-DIFFERENTIABLE FUNCTION	CONVERGENCE RATE
Gradient-based	Poor	Poor	Poor	Good
Random	Fair	Good	Good	Poor
Artificial Neural Network (ANN)	Fair	Good	Good	Good
Genetic Algorithm (GA)	Good	Good	Good	Fair
Particle Swarm Optimisation (PSO)	Good	Good	Good	Good
Simulated Annealing (SA)	Good	Good	Good	Fair
Taguchi's method	Good	Good	Good	Good

Table 4: Comparison of optimisation techniques (Weng et al., 2007a)

EXPERIMENTS	PARAMETERS		
	1	2	3
1	0	0	0
2	0	1	1
3	1	0	1
4	1	1	0

Table 5: Example of the structure of an $\mathsf{OA}(4,3,2,2)$

> Let S be a set of s levels, where the levels are values of the parameters whose effects on a response of interest are to be studied. An $\mathsf{N} \times \mathsf{k}$ array A with entries from S is said to be an *orthogonal array with* s *levels, strength* t*, and index* λ (for some t in the range $(0 \leqslant \mathsf{t} \leqslant \mathsf{k})$) if every $\mathsf{N} \times \mathsf{t}$ sub-array of A contains each t-tuple based on S exactly λ times as a row. The notation $\mathsf{OA}(\mathsf{N},\mathsf{k},\mathsf{s},\mathsf{t})$ is used to represent an OA.

A less formal definition is explained using the simple example of an $\mathsf{OA}(4,3,2,2)$ given in Table 5. There are 3 columns ($\mathsf{k}=3$) which means up to *3 different parameters* maybe studied, and there are 4 rows ($\mathsf{N}=4$) which means *4 different experiments* involving the parameters will be conducted. Since only 0's and 1's appear, this called a *2-level array* ($\mathsf{s}=2$). The levels can correspond to different parameter states, e. g. 'catalyst' or 'no catalyst', 'fast cooling' or 'slow cooling' etc., or numeric values depending on the application. The final part of the definition of the OA is the strength, and in this case the *strength is 2* ($\mathsf{t}=2$). This is the minimum number of columns that all the possible combinations of levels (7.1) will occur.

$$0\ \ 0, \qquad 0\ \ 1, \qquad 1\ \ 0, \qquad 1\ \ 1 \tag{7.1}$$

This ensures a balanced and fair comparison of levels for any parameter and any interactions of parameters. The strength of the OA should be large, but typically this is set at 2, 3 or 4 for real-world applications.

Obviously, even with a moderate number of parameters, and a small number of levels for each parameter, the number of possible combinations increases rapidly. It is, therefore, not always possible to make even one observation at each potential level combination. The purpose of the OA is to select which level combinations will be used, these are known as fractional factorial experiments.

Since the rows of an OA represent experiments — which can require, money, time, and other resources — practical constraints require minimising the

PARAMETER	SYMBOL	RANGE
Source pulse centre frequency	f	0.8–2.5 GHz
Permittivity of electromagnetic absorber	ϵ_r	1–81
Conductivity of electromagnetic absorber	σ	0.05–1 S/m
Resistance at transmitter drive-point	R_{T_x}	25–1000 Ω
Resistance at receiver	R_{R_x}	25–1000 Ω

Table 6: Initial ranges for unknown parameters in optimisation process

number of rows used. In addition, it is necessary to know the largest number of columns that can be used in the OA as this governs how many variables can be studied.

A useful property of an OA is that any $N \times k'$ sub-array of an existing $OA(N, k, s, t)$ is still an OA with a notation of $OA(N, k', s, t')$, where $t' = \min\{k', t\}$. In other words, if one or more columns are deleted from the OA the result is still an OA but with a smaller number of parameters.

The method of construction of OAs is outside the scope of this research, and is comprehensively dealt with by Hedayat et al. (1999). Many OAs with different parameters, levels, and strengths have been developed and archived in OA databases and libraries. The OAs used in this research are taken from the online library (Sloane, 2009).

7.2.2 *Developing an implementation process*

An iterative implementation of Taguchi's optimisation method was used and is shown in Figure 38. In the following subsections, a description of the various stages and their implementations is given.

Stage 1a: Select an OA

Since Taguchi's method is founded on the basis of OAs, the first stage of the process was to select an OA. This is largely governed by the number of parameters to optimise, which for both antenna models was five. The closest available OA from Sloane (2009) was an $OA(18, 7, 3, 2)$, which was then reduced to an $OA(18, 5, 3, 2)$. After selection of an OA for each model, an initial range for each parameter had to be determined. The results of the sensitivity study presented in Chapter 6 were reviewed and suitable ranges were chosen, which are given in Table 6.

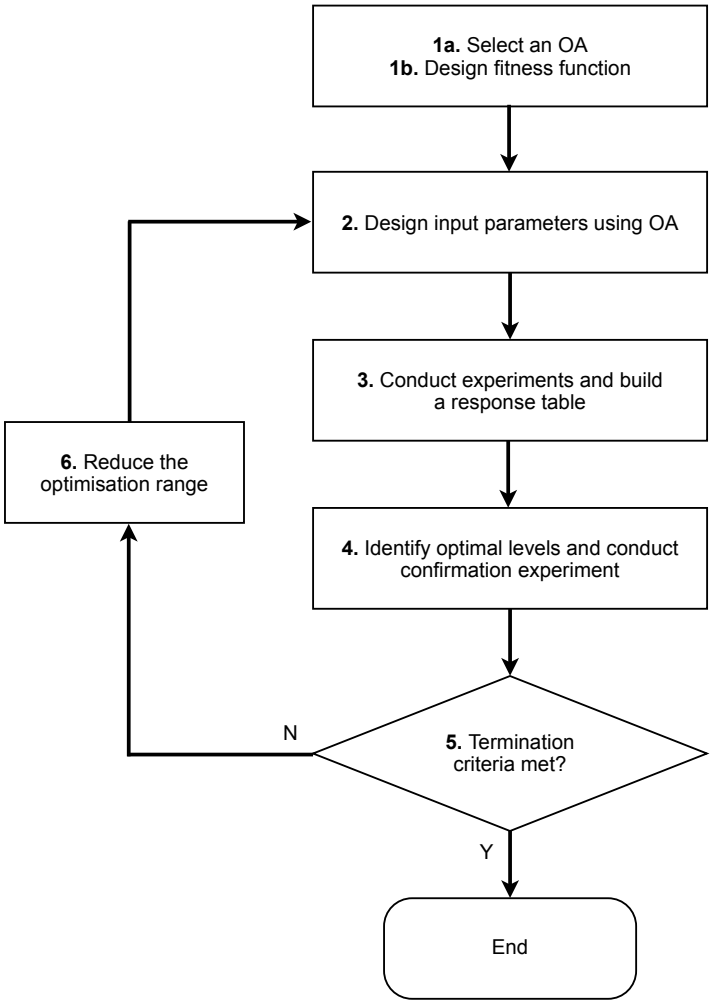

Figure 38: Process of implementing Taguchi's method (Weng et al., 2007b)

Stage 1b: Design fitness function

The second step of the problem initialisation phase is to design a fitness function to measure the outcome of an experiment and compare it to the optimisation goal. For both the antenna models, the optimisation goal was to accurately model the crosstalk response of the real antennas. The metric chosen to compare the real and modelled crosstalk responses was the sample cross-correlation given by 7.2. The cross-correlation measures the similarity of the two waveforms as a function of the time-lag applied to one of them.

$$\hat{R}_{xy}[m] = \begin{cases} \sum_{n=0}^{N-m-1} x_{n+m} y_n^* & m \geqslant 0 \\ \\ \hat{R}_{yx}^*[-m] & m < 0 \end{cases}, \tag{7.2}$$

where x and y are length N vectors, a star * denotes a conjugate operation, and a hat $\hat{}$ denotes an estimated quantity. The real and modelled signals were the same length in time but contained a different numbers of samples and, hence, had a different sample spacing. In the modelled signals, the sample spacing, and thus number of samples per scan, was fixed by the CFL condition. In the real signals, the number of samples per scan was controlled by the resolution of the Analogue-to-Digital converter (ADC) used in the GPR system hardware and, hence, this set the sample spacing. The GSSI system allows some control of the number of samples per scan (512, 1024, 2048, 4096 etc...), but in the MALÅ system this is fixed at 1024. For the cross-correlation of (7.2) to be applied the signals required to be the same length and have the same sample spacing. Therefore, for both antenna models the signal with the larger number of samples per scan (which was always the modelled signal) was resampled to the same rate as the real signal before the normalised cross-correlation was applied. The higher the value obtained from the cross-correlation, the better the indicated match between the modelled and the real responses.

Coupled to the design of the fitness function is the selection of termination criteria. Two criteria were used to terminate the optimisation process: the first was to specify a target value for the cross-correlation, initially set at 0.99 i. e., a 99% match between the modelled and real crosstalk responses; and the second criterion was to limit the number of iterations of the process, initially set to 20 iterations. These values for were determined from initial optimisation trials.

Stages 2 and 6: Input parameter levels

After the problem initialisation phase, stages 2–6 form an iterative loop as shown in Figure 38. This process is almost identical for both antenna models,

so the general procedure will be discussed and differences between the two models highlighted.

For each iteration, the range and, hence, levels for each parameter must be determined. For the first iteration, the range for each parameter is the initially specified optimisation range. In subsequent iterations, the range and corresponding values for the levels are determined by the algorithm. For the first iteration, the value for level 2 is set to the centre of the optimisation range, and values for levels 1 and 3 are calculated by adding or subtracting a variable called Level Difference (LD). The LD is calculated using (7.3).

$$\mathsf{LD}_{\mathsf{i}} = \frac{max - min}{number\ of\ levels + 1}, \tag{7.3}$$

where *min* and *max* are the lower and upper bounds of the optimisation range. The three levels are, therefore, uniformly distributed over the optimisation range. Assuming the termination criteria have not been met, the optimal values from the previous iteration are used as the central values (level 2) for the next iteration. Additionally, to reduce the optimisation range for a converged result, the level difference is multiplied with a reduced function as shown in (7.4).

$$\mathsf{LD}_{\mathsf{i}+1} = \mathsf{rr} \cdot \mathsf{LD}_{\mathsf{i}} \tag{7.4}$$

The value of rr is usually assumed to be a constant between 0.5 and 1, with values closer to one resulting in a slower convergence. A check is used to ensure that if the LD_{i} is large, and the central value is close to the upper or lower optimisation bounds, the values for levels 1 or 3 will not lie outside these bounds. If this happens, then the values for levels 1 or 3 adopt the boundary value directly.

Stages 3–5: Experiments, response table, confirmation, and termination

Once all the values for the input parameters were determined, the experiments were run. A fitness value for each experiment, based on the cross-correlation, was then calculated and these values were then used to build a response table. The response table is used to find the optimum level of each parameter for that iteration. The optimised level is determined by calculating the mean of the fitness values for each of the 3 levels for each parameter. The highest fitness value is then chosen, and that level becomes the optimised level of that parameter for that iteration. A confirmation experiment is then conducted with the optimised values, and the fitness value from it becomes the overall fitness value for that iteration. At this point, the termination criteria are checked and if necessary further iterations commence.

Automation of the process

The ultimate goal of implementing Taguchi's method was to develop a fully automated optimisation process for the unknown parameters in the antenna models. In Chapter 6 the run-time for a crosstalk antenna model was given as approximately 30 mins on 6 CPU cores. The OA used for both antenna models required 18 experiments (or models to be run) per iteration. Therefore, there was a need not only to automate the process, but also to run as many of the experiments (within the current iteration) as possible in parallel. The compute cluster described in Chapter 5 provided the necessary hardware, and a series of shell scripts were written combining shell programming, the Sun Grid Engine (SGE), MATLAB® and GprMax3D. These scripts can be found in Appendix C and are summarised as follows. Three shell scripts were used: a master job control script, a parallel execution script, and a script to assess fitness of an experiment and check the termination criteria. The master script submitted both the other scripts using the SGE, but would hold the fitness script until all the experiments that were being executed in parallel had completed. The fitness script would then execute and complete the following: compute the fitness of each experiment, build a response table, run a confirmation experiment, compute the fitness of the confirmation experiment and, lastly, check the termination criteria. The fitness script would then resubmit the master job control script if further iterations were necessary.

7.3 OPTIMISED CROSSTALK RESPONSES

The fully automated optimisation process was used to optimise the unknown parameters in the models and, therefore, match the modelled crosstalk responses to the real ones. Figure 39 shows the final modelled crosstalk response from the GSSI antenna and, similarly, Figure 40 shows that for the MALÅ antenna. The convergence history for the cross-correlation of the optimised models can be seen in Figure 41. The optimisation process was halted after 20 iterations by which point a 98% match for both antenna models had been achieved.

Figure 42 shows the convergence histories of the unknown parameters, and Tables 7 and 8 give the final optimised values of the parameters for the GSSI and MALÅ antenna models respectively. For the GSSI antenna model, the optimised value of the source pulse centre frequency was found to be 1.71 GHz, which is 14% higher than the manufacturer quoted centre frequency of 1.5 GHz. For the MALÅ antenna model, the optimised value of the source pulse centre frequency was found to be 978 MHz, which is 18.5% lower than the manufacturer quoted centre frequency of 1.2 GHz. These differences could be

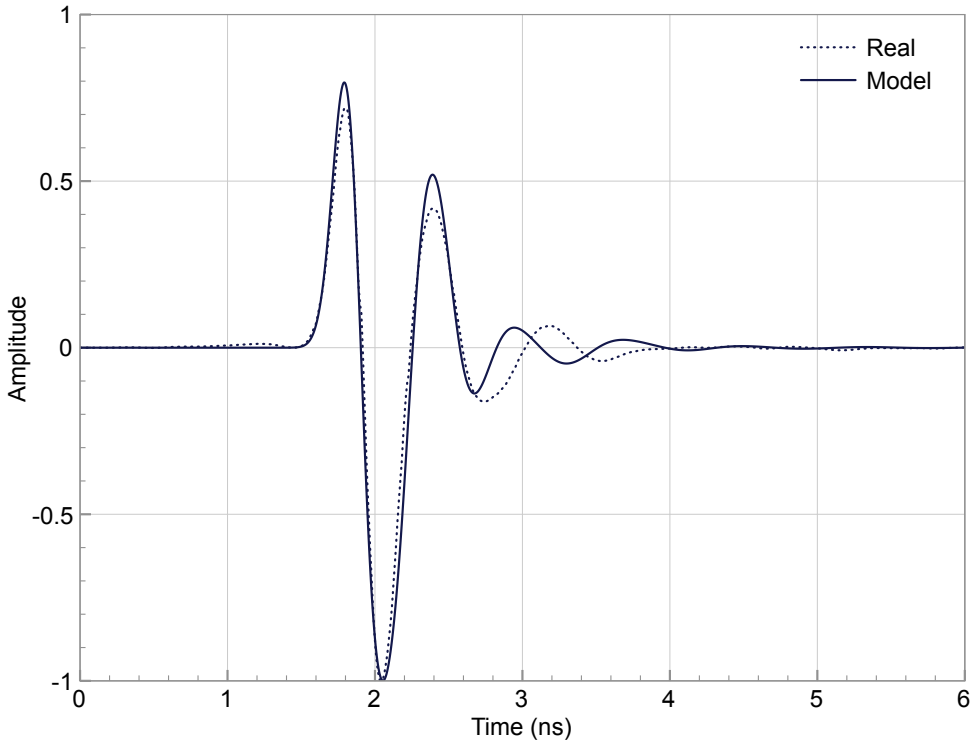

Figure 39: GSSI 1.5 GHz antenna: Optimised model of crosstalk response compared with real crosstalk response

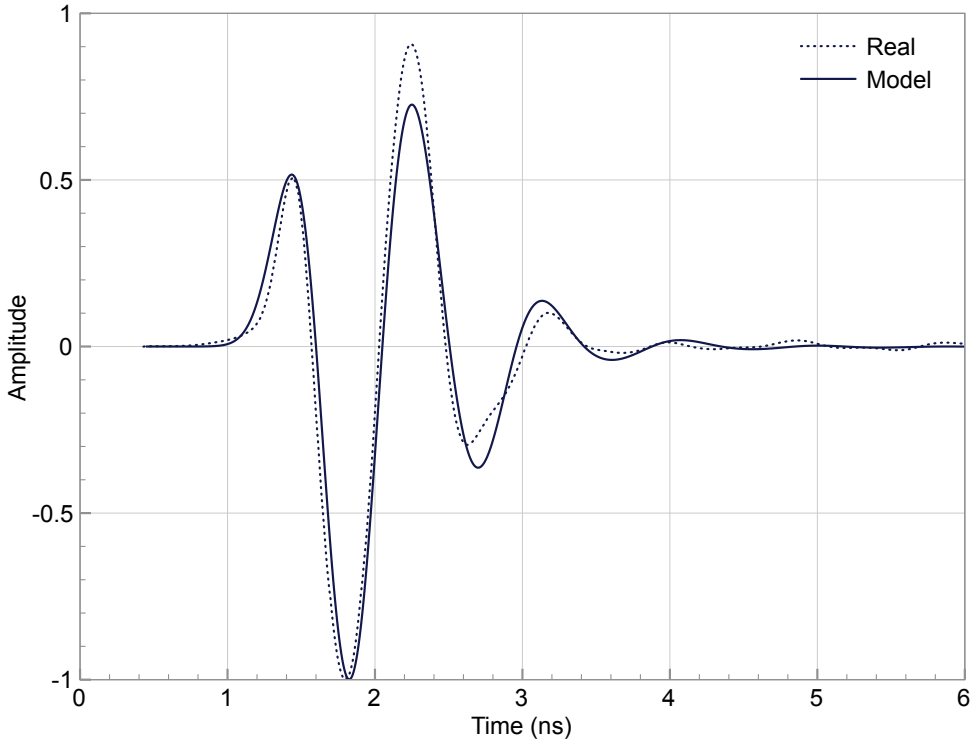

Figure 40: MALÅ 1.2 GHz antenna: Optimised model of crosstalk response compared with real crosstalk response

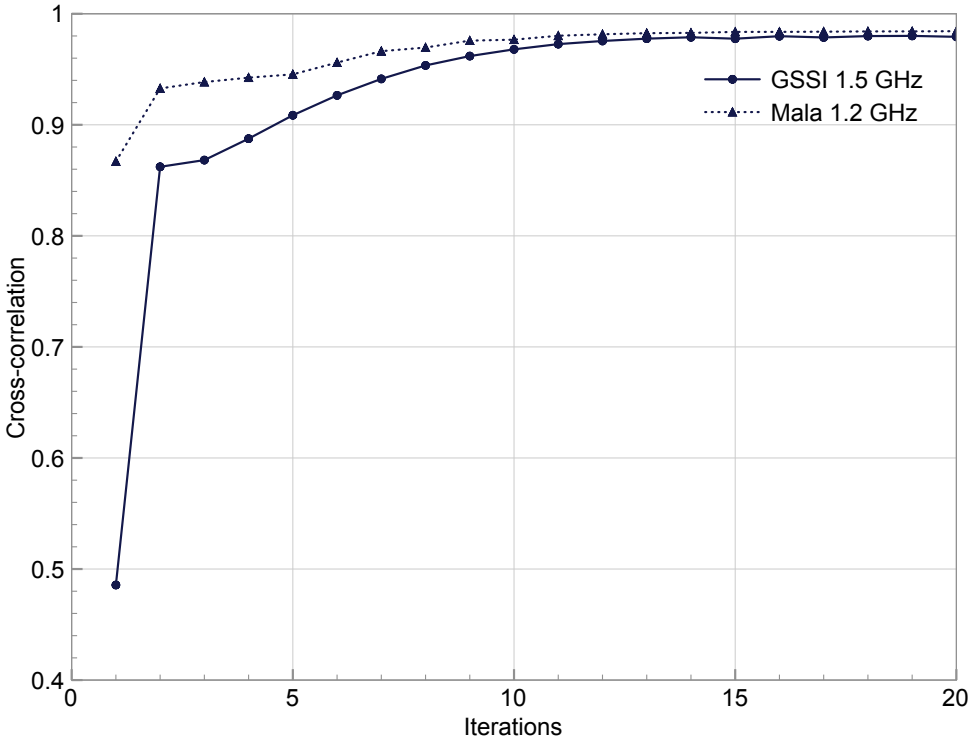

Figure 41: Convergence history of cross-corellation for antenna model optimisations

attributed to the manufacturers using source pulse shapes that are dissimilar to the assumed Gaussian shape used in the models. The optimised values of the permittivities and conductivities of the electromagnetic absorbers used in both antenna models are consistent with typical broadband microwave absorber foam (Emerson and Cuming, 1948). The optimised value of the resistance at the receiver in both antenna models is $\approx 900\ \Omega$, which suggests the receiver circuitry in both antennas is placing a similar resistive loading on the receiver bowties. There is a clear difference between the resistance at the drive-point of each antenna model. For the GSSI antenna model, the resistance at the drive-point converged to an optimised value of $4\ \Omega$, yet for the MALÅ antenna model the resistance at the drive-point hit, after 6 iterations, the upper bound of the parameter range, which was $1000\ \Omega$. Further studies into this anomaly were made by increasing the value of this upper bound. However, it was found that the value of the resistance at the drive-point continued to hit the upper bound, and no improvement in the cross-correlation value of real and modelled crosstalk was obtained.

Although there was no test equipment available to measure the input impedances of the real antennas, the modelled input impedance and admittance for both antennas were calculated and are shown in Figures 43–44. It is a useful indicator of the characteristics expected from a broadband antenna. The input

PARAMETER	SYMBOL	VALUE
Source pulse centre frequency	f	1.71 GHz
Permittivity of electromagnetic absorber	ϵ_r	1.58
Conductivity of electromagnetic absorber	σ	0.428 S/m
Resistance at transmitter drive-point	T_x	4 Ω
Resistance at receiver	R_x	925 Ω

Table 7: GSSI 1.5 GHz antenna: Final values of optimised model parameters

PARAMETER	SYMBOL	VALUE
Source pulse centre frequency	f	978 MHz
Permittivity of electromagnetic absorber	ϵ_r	6.49
Conductivity of electromagnetic absorber	σ	0.252 S/m
Resistance at transmitter drive-point	T_x	1000 Ω
Resistance at receiver	R_x	891 Ω

Table 8: MALÅ 1.2 GHz antenna: Final values of optimised model parameters

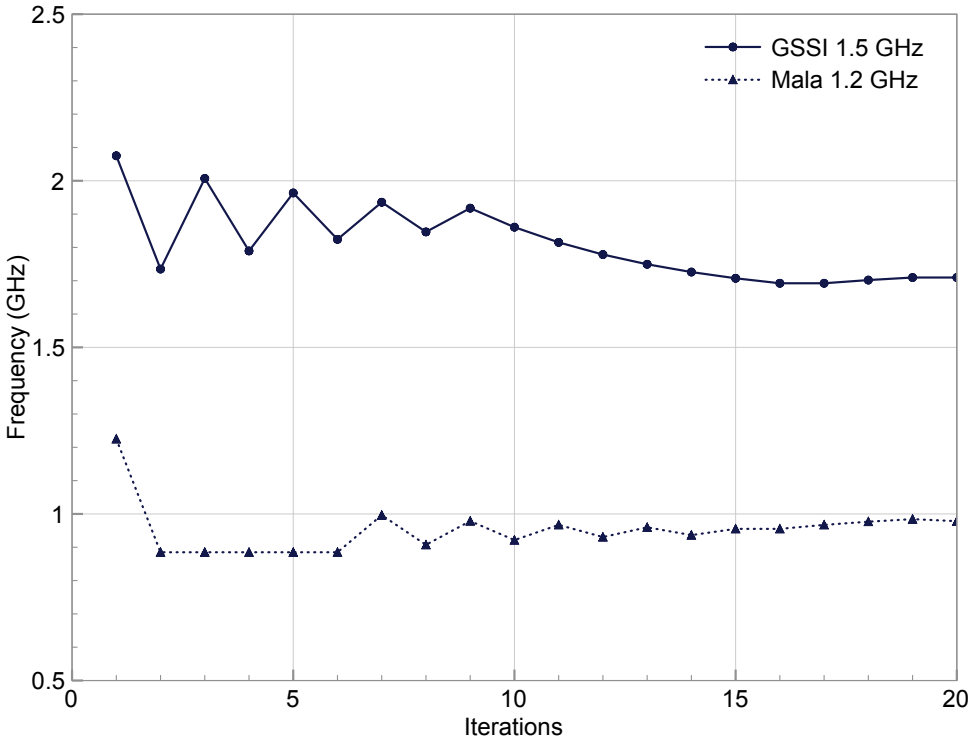

(a) Source pulse centre frequency

Figure 42: Convergence history of unknown parameters for antenna models

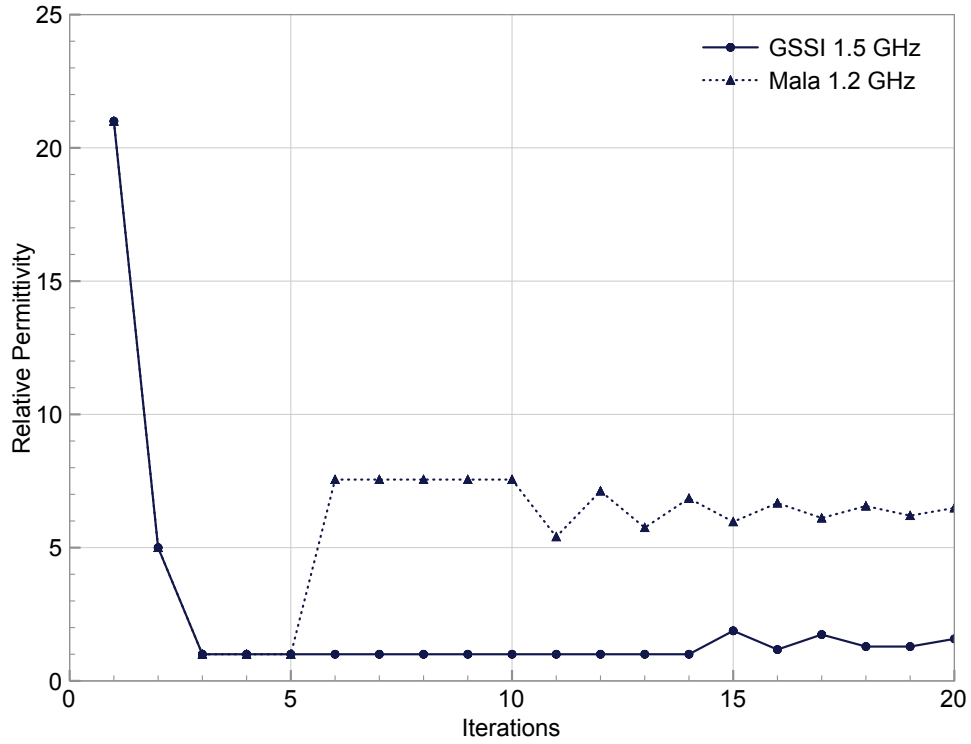

(b) Permittivities of electromagnetic absorbers

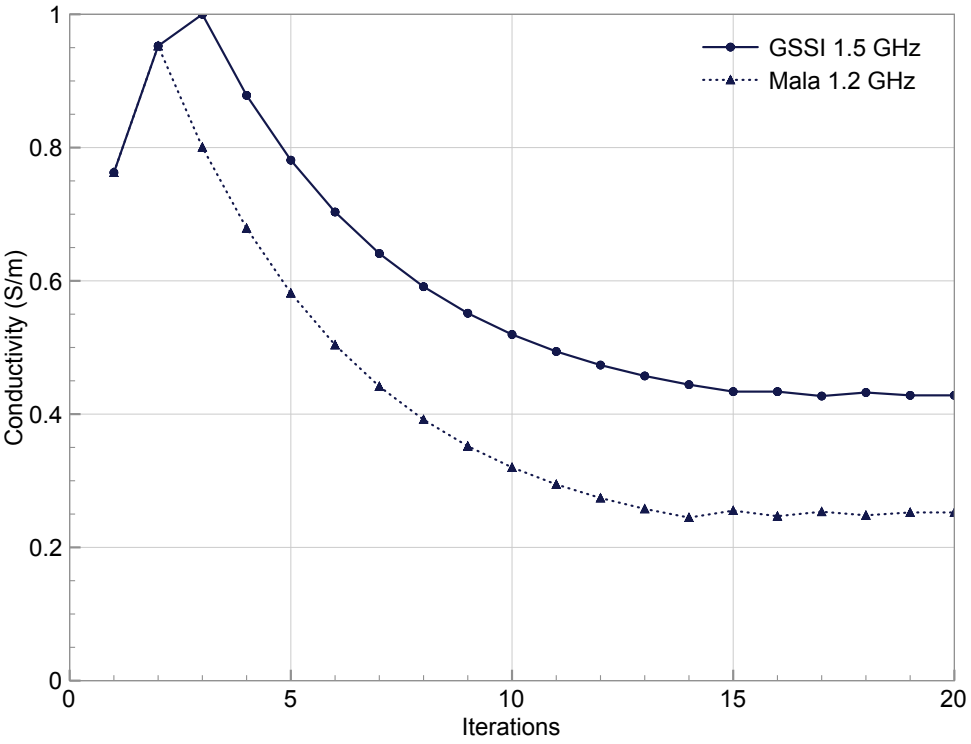

(c) Conductivities of electromagnetic absorbers

Figure 42: Convergence history of unknown parameters for antenna models

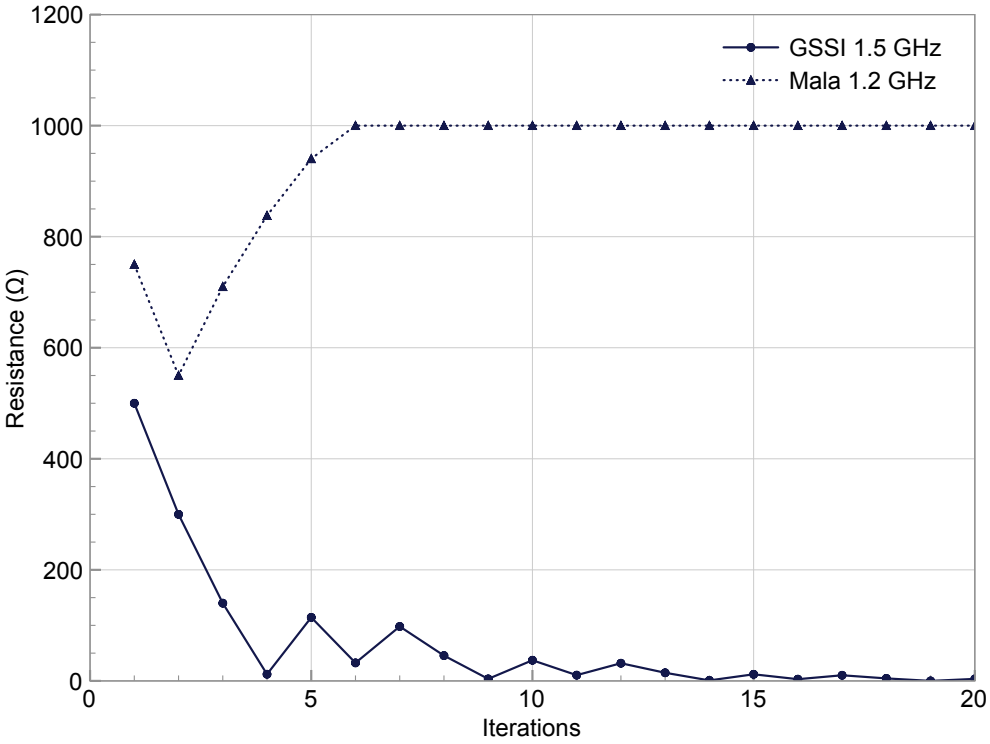

(d) Resistance at transmitter drive-point

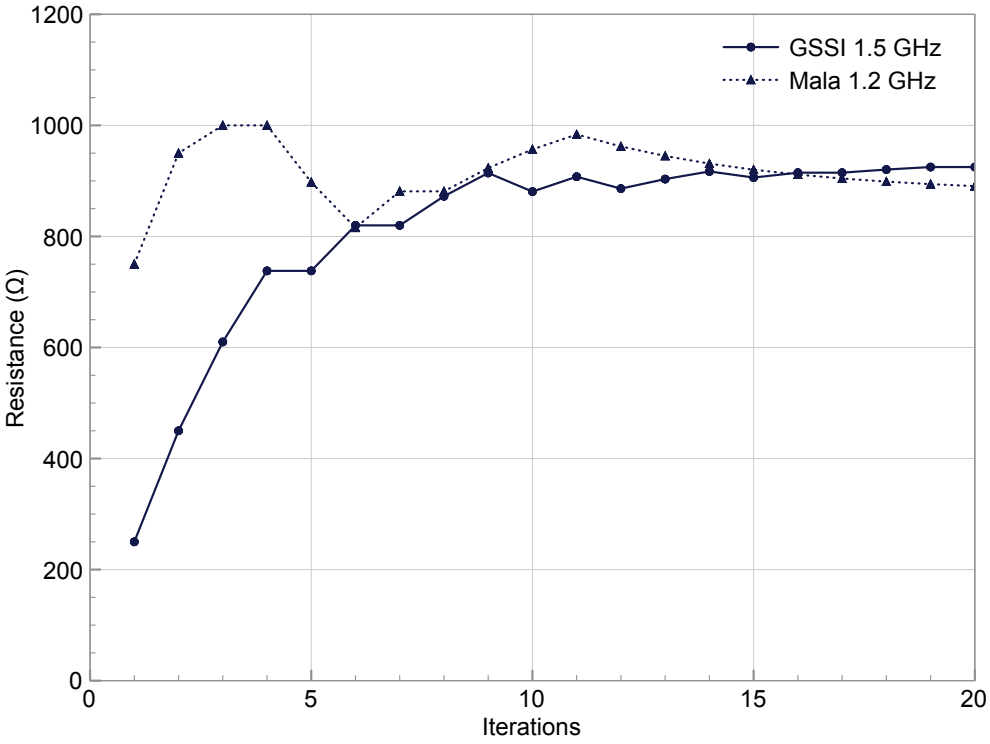

(e) Resistance at receiver

Figure 42: Convergence history of unknown parameters for antenna models

impedance (self-impedance in this case) of a modelled antenna was calculated by applying Ohm's Law to Fast Fourier Transform (FFT)s of the feed pulse voltage and current at the drive-point of the antenna. The magnitude of the real part of the impedance was taken to obtain the resistance, and the magnitude of the imaginary part for the reactance. The inverse of each gave the conductance and susceptance, respectively. The GSSI antenna model exhibits a typically (for a broadband bowtie antenna) flat input resistance of $\approx 100\ \Omega$ over its frequency band of operation i. e., 1–5 GHz. The MALÅ antenna model exhibits a similar broad and flat input resistance but it increases rapidly beyond 3 GHz. This increase in resistance could be attributed to dispersion in the resistance of the SMT loading resistors, used in the MALÅ antenna, at high frequencies.

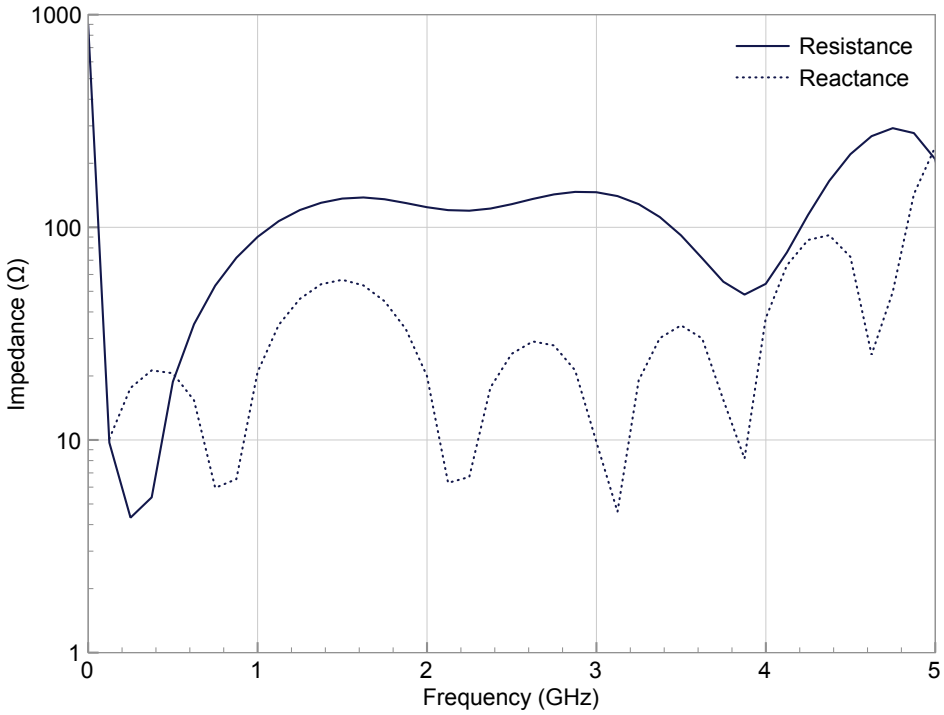

(a) Self-impedance

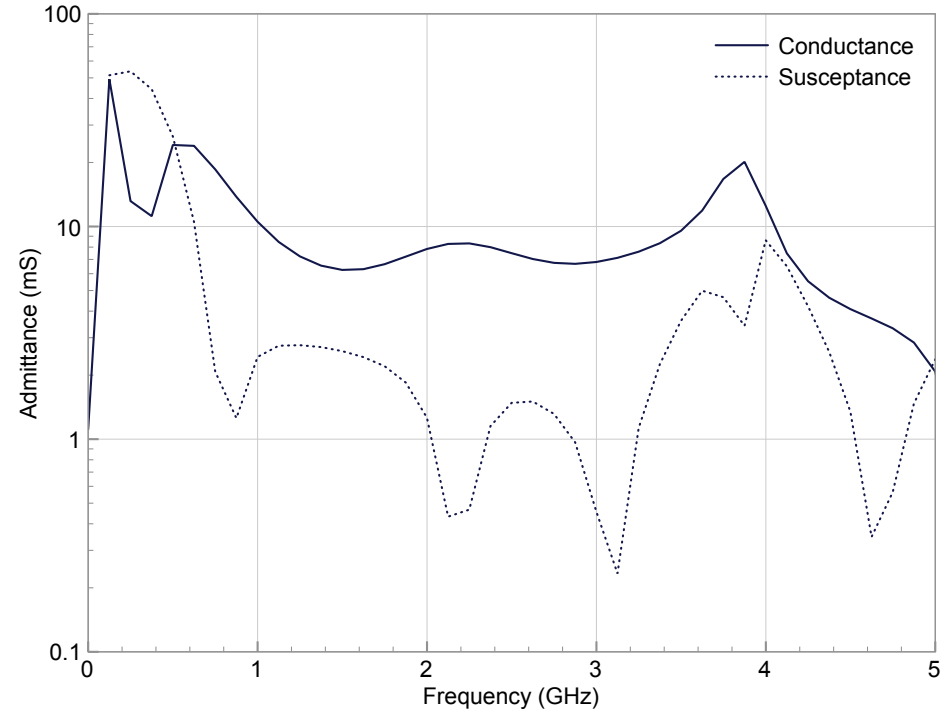

(b) Self-admittance

Figure 43: GSSI 1.5 GHz antenna: Optimised model self-impedance and self-admittance

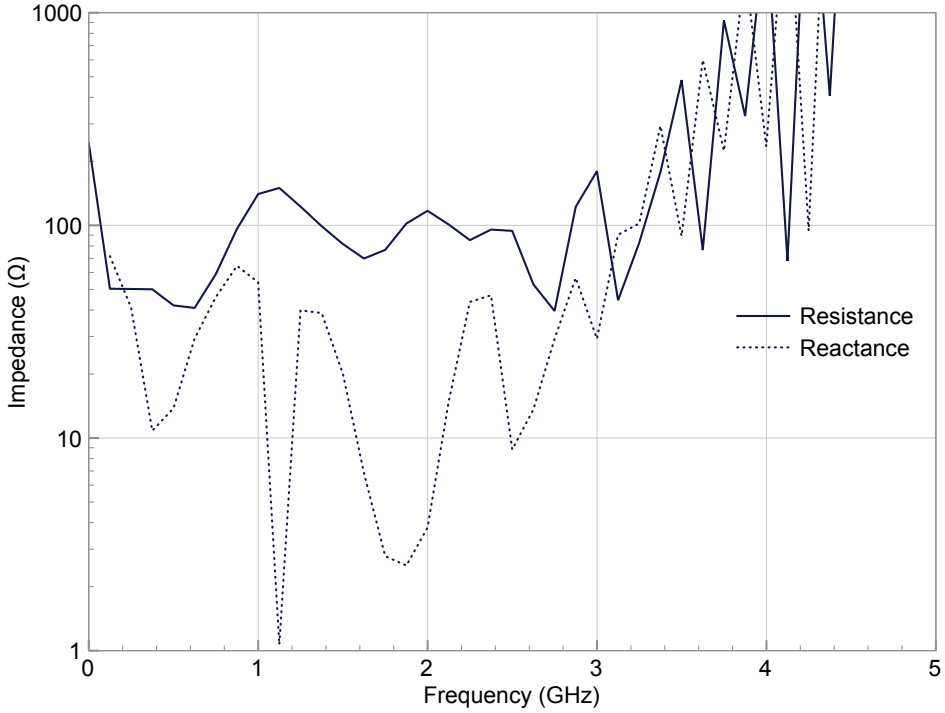

(a) Self-impedance

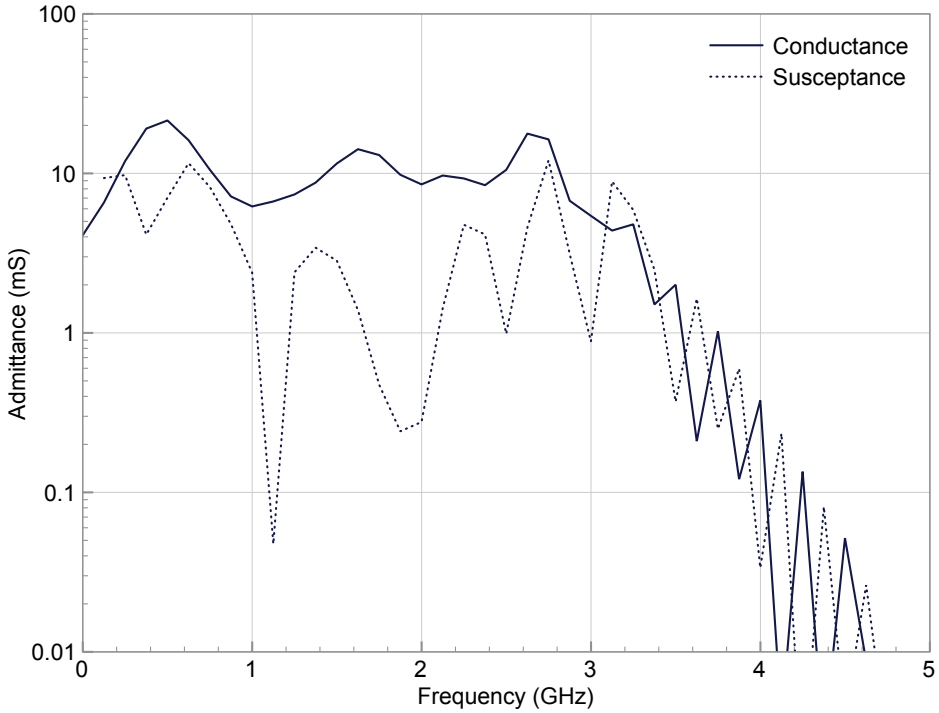

(b) Self-admittance

Figure 44: MALÅ 1.2 GHz antenna: Optimised model self-impedance and self-admittance

7.4 SUMMARY

The aim of this chapter was to describe the significant improvements made to the antenna models through the optimisation of several unknown parameters identified and initially studied in Chapter 6. Taguchi's method was identified as a global optimisation technique with a good convergence rate that was suitable for this problem. The basis of Taguchi's method is the OA which is used to effectively reduce the number of experiments (models) required to achieve an optimum result. A fully automated implementation of Taguchi's method has been developed using GprMax3D, ParaView, MATLAB® and the compute cluster. Optimised values for the unknown parameters yielded excellent matches between the modelled and real crosstalk responses for each antenna. The GSSI antenna model achieved a 98% cross-correlation match and the MALÅ also a 98% match. Both of these results were obtained within 20 iterations of the process, which indicates the method has a good convergence rate. Finally, the input impedances (self-impedances) of the antenna models were calculated and shown to exhibit flat responses over the bandwidth of operation, typical of broadband antennas.

8

VALIDATION OF ANTENNA MODELS THROUGH LABORATORY EXPERIMENTS

In Chapters 6 and 7 the antenna models were developed, optimised, and then validated by comparing their crosstalk responses to those from the real antennas. In this chapter, a more comprehensive validation of the antenna models is presented. A series of laboratory experiments were designed using emulsions to simulate the electrical properties of materials typically investigated using GPR. The emulsions presented homogeneous liquids in which targets such as rebars, pipes, and voids could be placed easily at known positions. Responses from a series of different target configurations in three different emulsions as well as the constituents of the emulsions were recorded using both GSSI and MALÅ systems. These experimental setups were then replicated in simulations that included the antenna models. The results from the real and modelled experiments were compared to assess the accuracy of the models. Additionally, simulations which included infinitesimal dipoles were compared with those that included the antenna models to highlight one of the key motivations for this research.

8.1 SELECTION OF A MODEL VALIDATION PROCESS

Following the initial success of validating the antenna models by comparing their crosstalk responses to those of the real antennas, a further, and more comprehensive, validation process was sought. The most obvious choice was to simulate a real GPR survey, and compare the model results to the real data. However, in most real GPR surveys it is common to encounter features such as rough surfaces, inhomogeneous and/or anisotropic materials. Although it is possible to include these attributes in the simulation, there is degree of uncertainty and, hence, approximation associated in doing so. It was, therefore, decided to design a series of laboratory experiments that would use emulsions to simulate the electrical properties of real materials. Smith and Scott (1990) investigated emulsion chemistry for the purposes of using emulsions in scale models of real GPR surveys. Bungey et al. (1993) and Infrasensec, Inc. (2003) also used emulsions to represent concrete slabs where different rebars configurations were tested, and the responses compared with data from real slabs. More recently, Buff (2006) used a similar procedure with gelatin to create a

transparent substance with similar electrical properties to a variety of soils, loams and sands. The two main advantages of using emulsions are: they are homogeneous liquids with known and adjustable electrical properties which can be definitively input into the simulations; and they enable a series of different target configurations to be easily tested. Data was recorded using both GSSI and MALÅ systems, and the antenna models were then validated by comparing the simulation results with the real data.

8.2 BASIC PROPERTIES AND THEORY OF EMULSIONS

The following two sections provide an overview of emulsions, the practical aspects involved in making them, and their electrical properties. The material is largely summarised from Smith and Scott (1990) and the reader is referred to Becher (1966) for a comprehensive study of the theory and practice of emulsion chemistry.

Emulsions are part of a general class of two phase systems known as *colloids*, specifically,

> An emulsion is a heterogeneous system, consisting of at least one immiscible liquid intimately dispersed in another in the form of droplets, whose diameters, in general, exceed 0.1μm. Such systems possess a minimal stability, which maybe accentuated by additives such as surface-agents, finely divided solids, etc... (Becher, 1966)

The most common emulsion is one where the two phases are oil and water. When the disperse phase (droplets) is oil and the continuous phase (matrix) is water, the emulsion is referred to as an *oil-in-water (O/W)* emulsion. Conversely, when the disperse phase is water and the continuous phase is oil, the emulsion is referred to as an *water-in-oil (W/O)* emulsion. All of the emulsions in this research were O/W emulsions because, as will be shown, their permittivity and conductivity profiles can be well predicted. Consequently, the focus of this section will be on O/W emulsions.

Oil and water do not readily form a stable mixture, and hence the formation of an emulsion usually requires the addition of an *emulsifier*. The molecules of an emulsifier have a hydrophilic (water-loving) group and a lipophilic (oil-loving) group, which lower the interfacial surface tension between the liquids. There are three classes of emulsifier: anionic, cationic, and nonionic. For anionic emulsifiers, anions are absorbed at the oil/water interface and cations are released into the aqueous phase. Similarly, for cationic emulsifiers, cations are absorbed at the oil/water interface and anions are released into the aqueous phase. However, for non-ionic emulsifiers few free ions are released into the

aqueous phase. The effectiveness of the emulsifier is greatly dependent on the constituents of the emulsion, and an empirical procedure is generally used to select the most effective emulsifier for a particular emulsion.

The mixing or agitation of the constituents of the emulsion is critical to the formation of a stable emulsion. A number of different methods can be used, from a simple propellor type mixer used to stir the liquids, through to the application of intense ultrasonic irradiation. It is critical to generate high shearing forces between the liquids by either passing the mixture through small orifices at high-pressure (a homogeniser), or by passing the mixture between a close-fitting stator and rotor (a colloid mill).

The stability of an emulsion is a measure of how the physical properties vary over time. The time scale may be of the order of seconds to years depending on the particular emulsion. There are two basic types of emulsion instability: creaming, and coagulation. When an emulsion is correctly formed, the droplets of the disperse phase are uniformly distributed throughout the emulsion. However, over time the droplets may drift upwards or downwards and form a layer of the disperse phase at the top or bottom of the vessel containing the emulsion. This process is known as *creaming*. The rate of creaming is governed by Stokes relation for the sedimentation rate ν of a spherical particle in a viscous liquid, given by (8.1) (Becher, 1966).

$$\nu = \frac{2gr^2(\rho_1 - \rho_2)}{9\eta_2}, \tag{8.1}$$

where r is the radius of the droplet, ρ_1 is the density of the disperse phase, ρ_2 and η_2 are the density and viscosity of the continuous phase, and g is acceleration due to gravity. For an O/W emulsion $\rho_2 > \rho_1$, ν is negative and the particles move upwards. It can be seen from (8.1) that creaming can be decreased by reducing the size (radius r) of the droplets, making the densities of the two phases nearly the same ($\rho_1 \approx \rho_2$), or increasing the viscosity (η_2) of the continuous phase. Creaming can often be reversed by simply stirring the emulsion.

Another change in the structure of the emulsion that affects the stability is the coagulation of the droplets. *Coagulation* occurs in stages: first, the droplets form aggregates in a process known as *flocculation*, and then several droplets combine to form one large droplet in a process known as *coalescence*. This process continues until the two phases form separate layers in the vessel containing the emulsion. At this point complete *demulsification* has occurred, and the emulsion must be reformed by applying the same process used to initially create it i. e., homogenisation, ultrasonic irradiation etc...

The most difficult parts of designing and making an emulsion is the selection of the constituents, especially the emulsifiers, and the choice of an appropriate method of agitation so that emulsion can achieve the desired stability.

8.3 ELECTRICAL PROPERTIES OF EMULSIONS

An emulsion can be considered a heterogeneous system consisting of two components, e. g. water and oil. The Bruggeman-Hanai-Sen (BHS) model is one of the most prominent mixing models for describing the permittivity and conductivity of such a system. The Bruggeman formula for lossless dielectrics is given by (8.2).

$$\left(\frac{\bar{\epsilon}_r - \epsilon_{r1}}{\epsilon_{r2} - \epsilon_{r1}}\right)^3 = (1 - \Phi_1)^3 \frac{\bar{\epsilon}_r}{\epsilon_{r2}}, \tag{8.2}$$

where:

$\bar{\epsilon}_r$ = average permittivity of the emulsion

ϵ_{r1} = real relative permittivity of disperse phase

ϵ_{r2} = real relative permittivity of continuous phase

Φ_1 = volume fraction of disperse phase

The average permeability of the emulsion is assumed to be $\mu = \mu_0$ as the constituents are generally non-magnetic.

Hanai showed that Bruggeman's expression can also be applied to lossy dielectrics by introducing a complex permittivity, which is given by (8.3).

$$\tilde{\xi_r} = \xi_r{}' - j\xi_r{}'' \equiv \epsilon_r - j\frac{\sigma}{\omega\epsilon_0} \tag{8.3}$$

Thus the Hanai-Bruggeman formula is given as (8.4).

$$\left(\frac{\tilde{\bar{\xi}}_r - \tilde{\xi}_{r1}}{\tilde{\xi}_{r2} - \tilde{\xi}_{r1}}\right)^3 = (1 - \Phi_1)^3 \frac{\tilde{\bar{\xi}}_r}{\tilde{\xi}_{r2}} \tag{8.4}$$

The Hanai-Bruggeman equation (8.4) can then be used to compute the electrical properties of a simple emulsion consisting of mineral oil, and a saline solution.

The mineral oil is assumed to be a lossless dielectric with a real relative permittivity which is independent of frequency and temperature, and with negligible conductivity. The saline solution has a complex permittivity described

by the Debye equation, and is also dependent on normality N and temperature T (8.5). The saline solution has a real frequency independent conductivity σ_2.

$$\tilde{\epsilon}_r(T,N) = \epsilon_{r\infty} + \frac{\epsilon_{r0}(T,N) - \epsilon_{r\infty}}{1 + j\omega\tau(T,N)} \tag{8.5}$$

It has been shown that the dispersion in the electrical properties of O/W emulsions can be described in a straightforward manner. For frequencies less than 3 GHz, the relative permittivity is approximately constant and equal to a low-frequency value, given by (8.6), which is dependent upon the temperature and normality of the saline solution, and the volume fraction of the disperse phase.

$$\bar{\epsilon}_{rLF}(T,N,\Phi_1) = \frac{1}{2}\left(3\epsilon_{r1} + (1-\Phi_1)^{\frac{3}{2}}\,(2\epsilon_{r0}(T,N) - 3\epsilon_{r1})\right) \tag{8.6}$$

The conductivity of the emulsion is given by (8.7).

$$\tilde{\bar{\sigma}} = \bar{\sigma}_{LF} + \Delta\tilde{\bar{\sigma}} \tag{8.7}$$

$\bar{\sigma}_{LF}$ is given by (8.8) and is a constant low-frequency value, which is again dependent upon the temperature and normality of the saline solution, and the volume fraction of the disperse phase.

$$\bar{\sigma}_{LF}(T,N,\Phi_1) = \sigma_2(T,N)\,(1-\Phi_1)^{\frac{3}{2}} \tag{8.8}$$

$\Delta\tilde{\bar{\sigma}}$ is given by (8.9), and contains a term which increases with the square of the frequency.

$$\Delta\tilde{\bar{\sigma}} = \frac{\epsilon_{rLF}\,(2\epsilon_{r0} + \epsilon_{r1})\,(\bar{\epsilon}_{rLF} - \epsilon_{r1})}{\epsilon_{r0}\,(2\bar{\epsilon}_{rLF} + \epsilon_{r1})\,(\epsilon_{r0} - \epsilon_{r1})}\epsilon_0\,(\epsilon_{r0} - \epsilon_{r\infty})\,\tau\omega^2 \tag{8.9}$$

For a complete derivation of these equations the reader is referred to Smith and Scott (1990).

Numerical values for the average electrical constitutive parameters $\bar{\epsilon}_r$ and $\tilde{\bar{\sigma}}$ of the emulsions can be calculated from specified ϵ_{r1}, Φ_1, the normality of the saline solution N, and temperature T, and using equations (8.6) and (8.7). However, the interdependence of each parameter can be more readily understood by studying the graphical representation shown in Figure 45, which is for $T = 23$°C (room temperature). The relative permittivity $\bar{\epsilon}_{rLF}$ is seen to depend mainly on the volume fraction of oil Φ_1, while the conductivity $\bar{\sigma}_{LF}$ depends mainly on the normality of the saline solution N. Both parameters are adjustable over wide ranges: $10 \leqslant \bar{\epsilon}_{rLF} \leqslant 80$ and 4×10^{-4} S/m $\leqslant \bar{\sigma} \leqslant 4$ S/m.

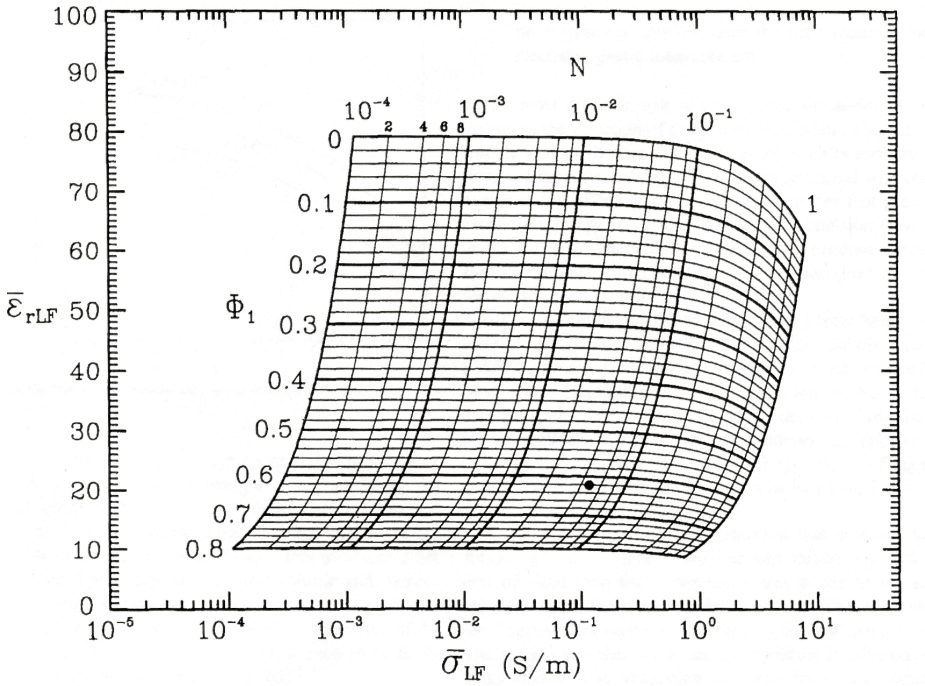

Figure 45: Volume fraction of oil, Φ_1, and normality of saline solution, N, for different permittivity, $\bar{\epsilon}_{rLF}$, and conductivity, $\bar{\sigma}_{LF}$, values of O/W emulsions (Smith and Scott, 1990)

8.4 LABORATORY EXPERIMENTS

8.4.1 *Apparatus*

The basic apparatus used for the experiments consisted of: a 50 L galvanised steel tank, a perspex rig to mount each antenna and corresponding Distance Measurement Instrument (DMI), a high-shear batch mixer, and a 25 L plastic mixing vessel. Figure 46 shows the emulsor workhead and rotor from the mixer, which combine the mixing methods of a homogeniser and a colloid mill. Figure 47 shows the tank apparatus with the antenna holder and attached GSSI DMI, which could be slid from one end of the tank to the other, allowing B-scans to be recorded. A false aluminium base was fitted to the tank that could be moved vertically in increments of 50 mm.

The design criteria for the tank were based on size and material. In previous studies by Bungey et al. (1993) and Infrasensec, Inc. (2003), emulsions were used to simulate concrete and asphalt, and the results were compared with real data taken from concrete and asphalt slabs. In these cases, the materials used for the tanks were plywood and polypropylene, both of which have a low permittivity. This was done to avoid potential unwanted reflections from the tank interfering with the responses from the emulsions and targets. However,

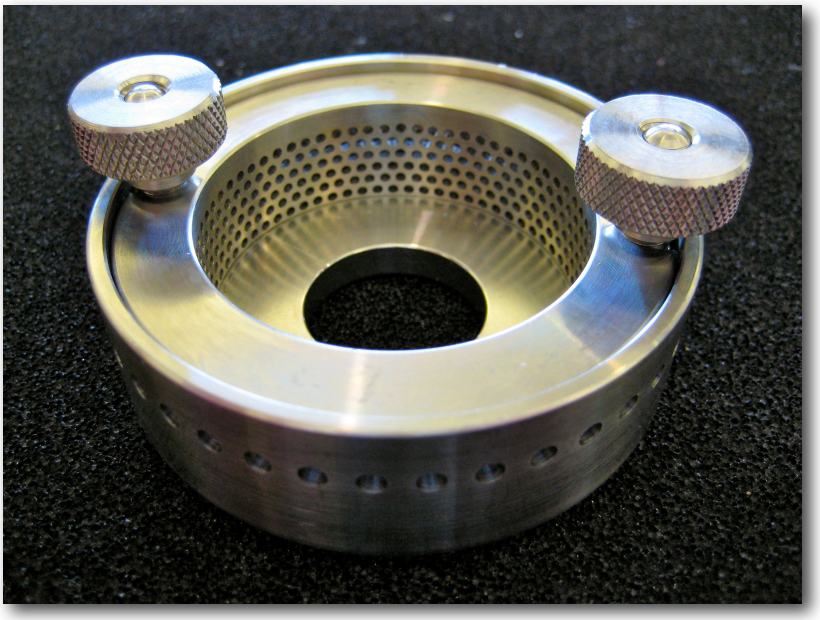

(a) Emulsor workhead

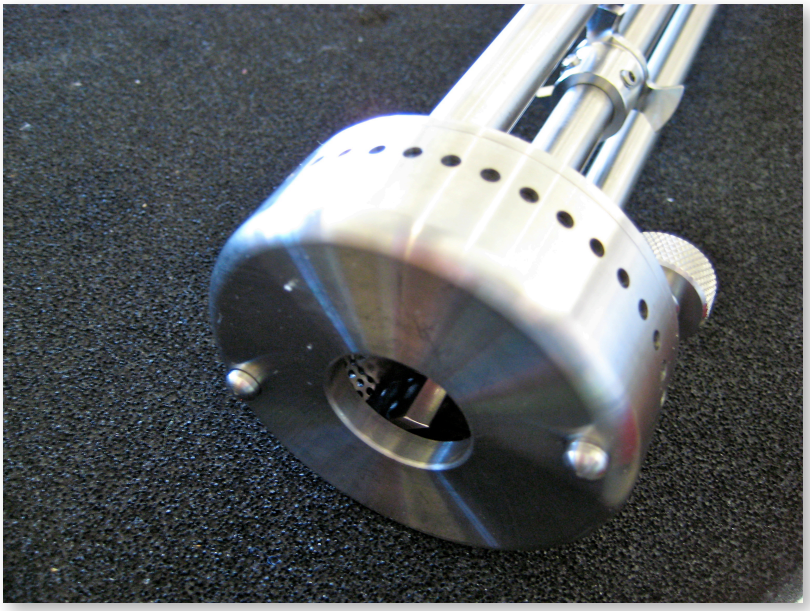

(b) Workhead (stator) fitted to rotor shaft

Figure 46: Photograph of Silverson Machines, Inc. AX3 high-shear batch mixer

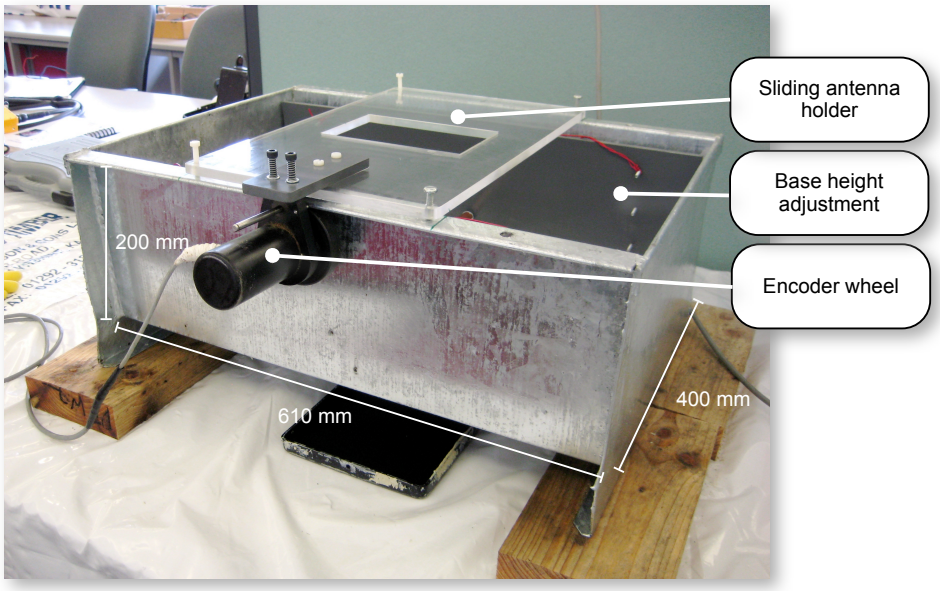

Figure 47: Annotated photograph of tank rig used for laboratory experiments

in this research, the data from the emulsions was compared with, and used to validate, the antenna models. Therefore, reflections from the tank were not as important because, as the entire tank was included in the model, they would be replicated in the simulation. Steel was chosen as the material for the tank as it provided a definitive boundary for both the experimental setup and the model. The other specifications for the tank apparatus were derived from the following criteria:

- Manageable physical size for a bench-top laboratory setup, with the benefit of minimising the computational requirements for the models;
- Ensure, where possible, the response from the base of the tank is visually separable from the direct wave of the antenna;
- Install locators on the tank base to allow consistent positioning of different targets;

A number of targets typically investigated using GPR were chosen for testing in the emulsions. Different materials and sizes of pipes and boxes, as well as a series of steel and composite rebars, which are shown in Figure 48 were tested. The specific configurations were:

- 15 mm diameter copper pipe
- 25 mm diameter plastic pipe
- 25 mm diameter, water-filled, plastic pipe

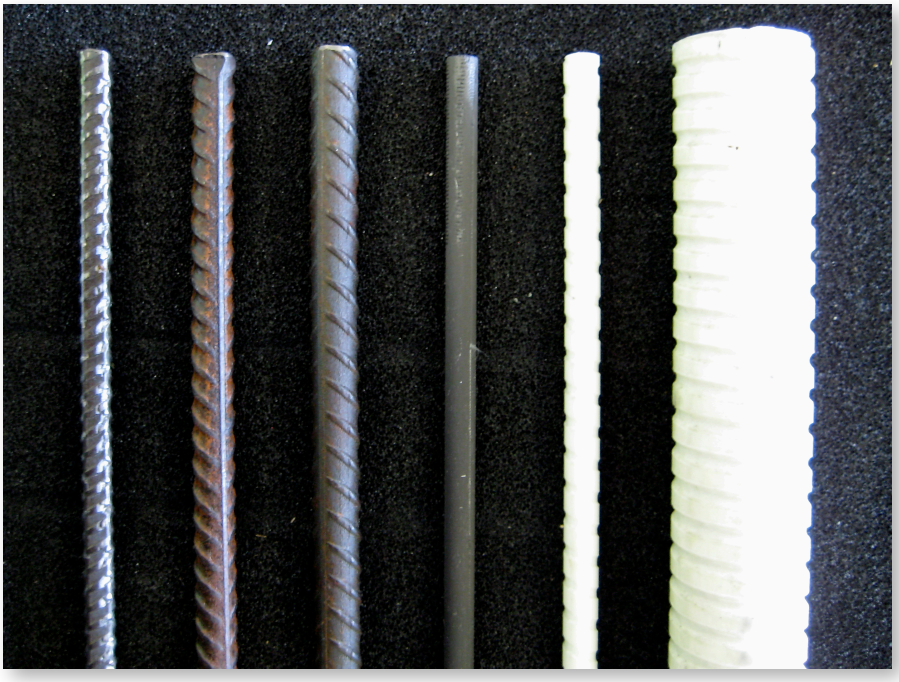

Figure 48: Photograph of steel and composite rebars: *left-to-right* 8, 10 and 12 mm diameter steel; 8 mm CFRP; 9 and 32 mm GFRP

- Copper and plastic pipes (150 mm horizontal separation)
- 120×95×55 mm metal box
- 120×100×45 mm plastic box
- 8 mm, 10 mm, and 12 mm diameter steel rebars
- 8 mm diameter Carbon Fibre Reinforced Polymer (CFRP) rebar
- 9 and 32 mm diameter Glass Fibre Reinforced Polymer (GFRP) rebars

All of the targets were tested with both GPR systems in three different emulsions as well as mineral oil and distilled water. Figure 49 shows a typical layout used for testing the pipes and rebars, i. e., target orientated perpendicular to the scan direction along the centre-line of the tank. Plastic end-plates were used to raise the pipes and rebars off the tank base.

8.4.2 *Materials*

The design and manufacture of the emulsions was based on previous research that included a comprehensive study of the emulsion chemistry (Smith and

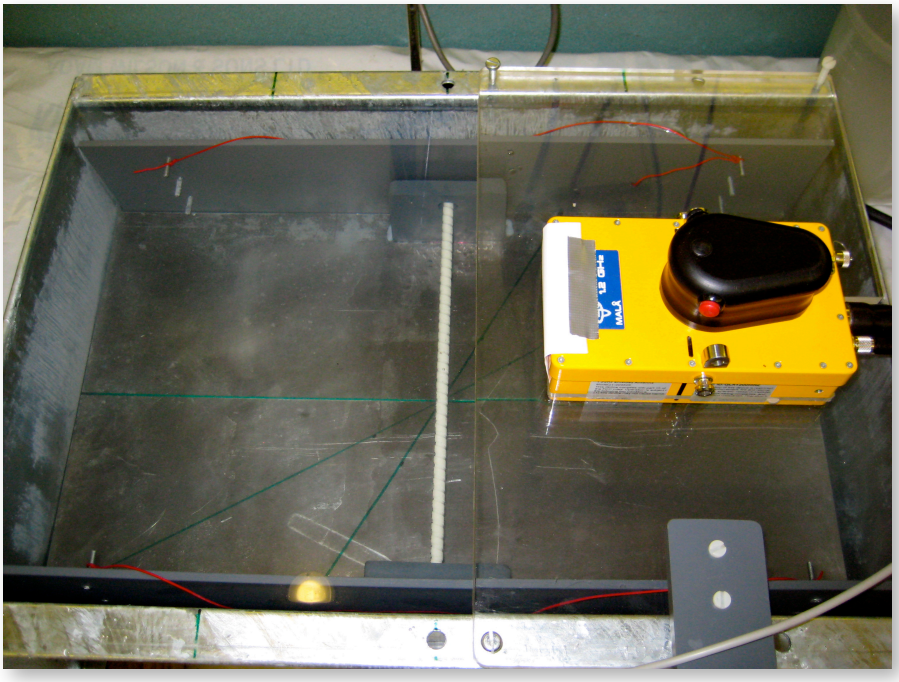

Figure 49: Photograph showing location of a 9 mm GFRP rebar in distilled water

Scott, 1990). It was decided to make three emulsions with permittivities 10, 20 and 30 spanning a wide range of common materials encountered in GPR surveys. A permittivity of 10 was the lowest attainable permittivity for an emulsion based on the design specification, and could represent curing concrete. At the other end of the scale a permittivity of around 30 could represent clayey soils or wet sand. The emulsions were designed to have negligible Direct Current (DC) conductivity but, as shown by (8.7), have a dispersive conductivity behaviour similar to many real materials.

The chemicals used were: Millube 32 – a non-additive lubricating oil[1]; emulsifiers – Tween® 20 (polyoxyethylene sorbitan monolaurate) and Span® 80 (sorbitan monooleate)[2]; and distilled water. Having specified the permittivity and conductivity of the emulsions, Figure 45 was used to obtain the required volume fraction of oil, Φ_1. Once Φ_1 was known, (8.10)–(8.13) were used to calculate the specific volumes of the oil, water and emulsifiers. Table 9 lists the volumes of each chemical used for each emulsion.

$$V_{oil} = \frac{\Phi_1 V_{tank}}{0.1\Phi_1 + 1} \tag{8.10}$$

1 Millube is a trademark of Millers Oils, Ltd.
2 Tween® and Span® are trademarks of ICI Americas, Inc.

	$\epsilon_r = 10$	$\epsilon_r = 20$	$\epsilon_r = 30$
Volume fraction of oil, Φ_1	0.8	0.64	0.5
Volume of oil, (L)	36.329	29.500	23.354
Volume of saline solution, (L)	9.082	16.594	23.354
Volume of Tween® 20, (L)	1.635	1.328	1.051
Volume of Span® 80, (L)	1.998	1.623	1.284

Table 9: Volume of constituents for O/W emulsions

$$V_{emul} = 0.1 V_{oil} \tag{8.11}$$

$$\frac{\text{Tween® 20}}{\text{Span® 80}} = \frac{4.5}{5.5} \tag{8.12}$$

$$V_{saline} = V_{tank} - V_{oil} - V_{emul} \tag{8.13}$$

8.4.3 *Methods*

To ensure the chemicals formed stable emulsions they were mixed in accordance with guidelines from the manufacturer of the mixer[3] (it is important to note that use of a high-shear mixer is essential to form stable emulsions, as a small paddle mixer was originally trialled with unsatisfactory results). The mixer could only operate on a maximum volume of approximately 25 L of the emulsion with the highest viscosity. Therefore, the process to make a sufficient volume of the emulsion to fill the steel tank was: divide total chemical volumes by two and place in mixing vessel; mix using high-shear batch mixer for 10 minutes; transfer mixture to tank; repeat mixing with remaining chemicals and add to tank; repeatedly drain off approximately 25 L batches from tank and remix to ensure a uniform stable emulsion is produced.

To verify the accuracy of the design and manufacture of the emulsions, and to provide accurate values to input into the models, it was necessary to know the permittivity of each of the emulsions, as well as the mineral oil, and the

3 Silverson Machines, Inc

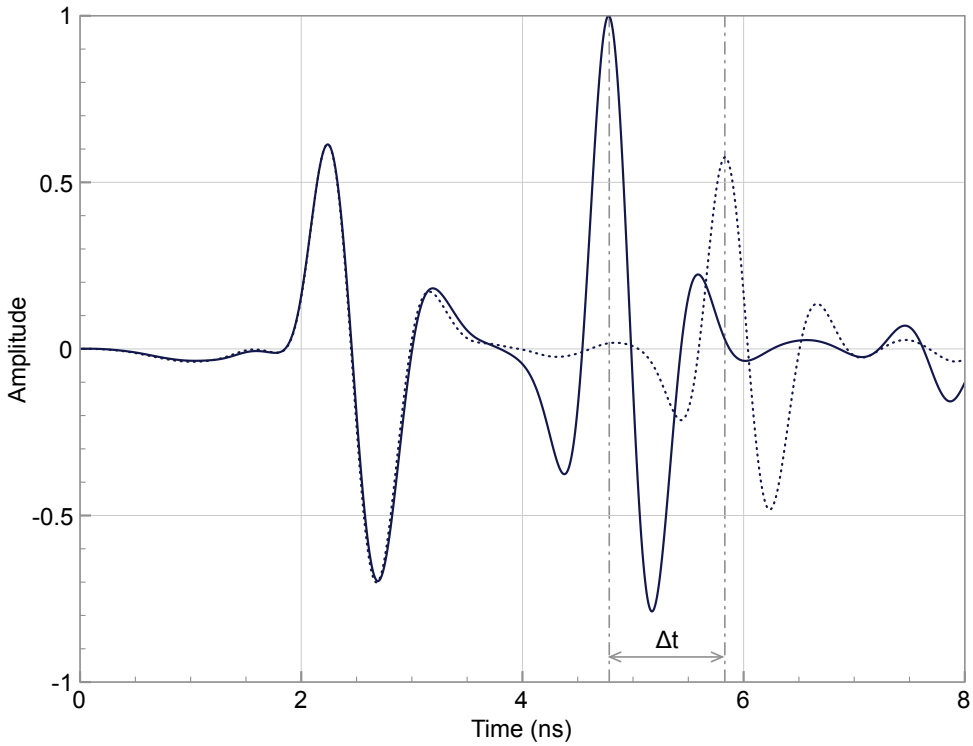

Figure 50: Example A-scans of reflections from tank base at two different base heights

distilled water. For each liquid, an A-scan was recorded with the antenna in the centre of the tank and the tank base at its lowest height. The depth of the liquid was measured at this base position. The base was then raised 50 mm and another A-scan recorded. Figure 50 shows an example of the two measurements with the time difference Δt, between corresponding points in the reflection wavelet from the base, highlighted. The distance travelled Δl was calculated using the known depth of the liquid and the separation of the transmitter and receiver elements in the antenna. The distance Δl along with time Δt was used to calculate the velocity v (8.14), and subsequently the relative permittivity of each liquid (8.15).

$$v = \frac{\Delta l}{\Delta t} \tag{8.14}$$

$$\epsilon_r = \left(\frac{c}{v}\right)^2 \tag{8.15}$$

There were two main sources of error associated with the measured permittivities: an error in the measurement of the depth of each liquid resulting in an error in Δl, and a time picking error due to the sampling of the recorded

	DESIGNED	MEASURED		
	ϵ_r	ϵ_{rmin}	ϵ_r	ϵ_{rmax}
Mineral oil	-	2.2	2.3	2.4
Emulsion 1	10.2	9.8	10.4	11.0
Emulsion 2	19.7	20.9	22.1	23.5
Emulsion 3	30.2	29.4	31.2	33.1
Distilled water	-	74.3	78.7	83.5

Table 10: Designed and measured permittivities for the emulsions and their constituents

responses resulting in an error in Δt. A ± 2 mm error was appropriated to the depth measurements, which were taken using a rule held vertically in each liquid. The time measurement error arose out of picking the same point on the reflected wavelet from the tank base in each of the two responses. The GSSI system was used for the measurements and 2048 samples per time window was set. An appropriate length of time window was chosen for each liquid and, hence, the magnitude of the time errors and, thus, the errors in the permittivity values become larger for lower velocity liquids. Table 10 lists the designed permittivities for the emulsions, along with the measured permittivities and error bounds for all the liquids. The designed and measured values of the permittivities of the emulsions show a good correspondence.

Following the permittivity measurements, the tank base was returned to its lowest height and each target configuration was tested with both the GSSI 1.5 GHz antenna and the MALÅ 1.2 GHz antenna, in all three emulsions, the mineral oil, and the distilled water. A-scans were taken by placing the antenna directly over the target placed on the centre-line of the tank, and recording data for a fixed time period. B-scans were taken by moving the antenna from one side of the tank to the other with a DMI attached. In all tests, the antennas were submerged in the liquid to the top of their skid plates ensuring no air gap existed.

8.5 NUMERICAL MODELS OF LABORATORY EXPERIMENTS

Models of the experimental setups were created in GprMax3D with ParaView utilised to visualise the geometries. The simulations included the GSSI or MALÅ antenna model developed in Chapters 6 and 7, the steel tank filled with one of the liquids, and one of the different target configurations. Figure 51 shows the meshed geometry of a typical model. The domain size was $642 \times 432 \times 267$, resulting in approximately 74 million cells, which required 5 GB of RAM.

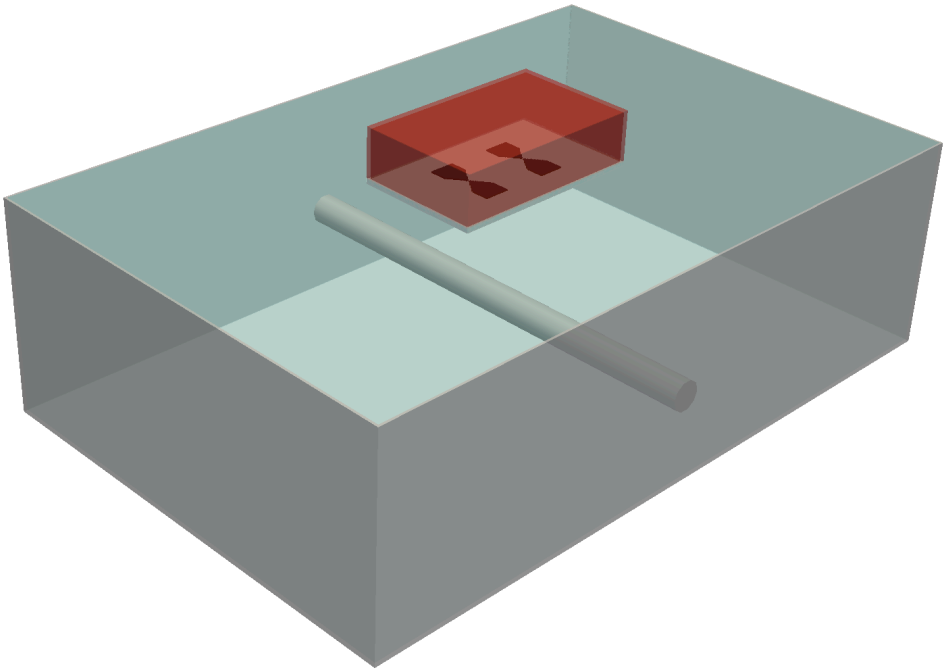

Figure 51: Modelled geometry (FDTD mesh) of emulsion tank with GSSI 1.5 GHz antenna and a typical target

The run-time for the simulations was dependent on the length of time window used, which itself was dependent on the permittivity of the liquid tested. As an example, for an emulsion with $\epsilon_r = 32$ approximately 9 hours run-time on 6 CPU cores was required to produce a single A-scan.

One of the most important aspects of the development of an accurate model was to determine the correct material parameters to input into the model. Ranges for the permittivity values of the emulsions and their constituents were established from the measurements discussed in the previous section, and are listed in Table 10. The ranges for the permittivity values of the emulsions provided a level of adjustment for the values input into the models, i. e., the permittivity values of the emulsions used in the models could be adjusted to best match the real data, within the allowable ranges.

The conductivity of the mineral oil was negligible, and the losses in the distilled water were modelled using the Debye equation repeated here for convenience.

$$\tilde{\epsilon_r} = \epsilon'_r - j\epsilon''_r,$$

$$\Leftrightarrow \tilde{\epsilon_r} = \epsilon'_{r\infty} + \frac{\epsilon'_{rs} - \epsilon'_{r\infty}}{1 + j\omega\tau_e},$$

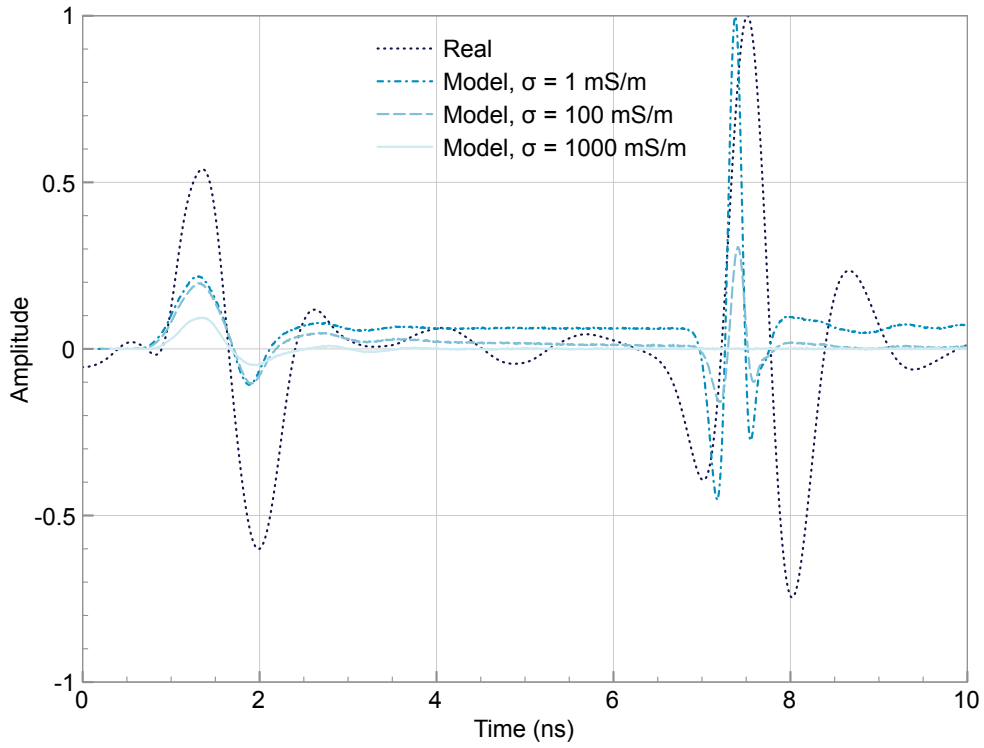

Figure 52: GSSI 1.5 GHz antenna: Modelled vs. real A-scans with different values of DC conductivity, no target in tank, and emulsion ($\epsilon_r = 32$)

where:

ϵ'_{rs} = static relative permittivity (dimensionless)

$\epsilon'_{r\infty}$ = relative permittivity at a theoretical infinite frequency (dimensionless)

τ_e = relaxation time (s)

Earlier in this chapter it was shown that the permittivities of the emulsions remained at a constant value $\bar{\epsilon}_{LF}$ over the bandwidth of interest. However, the conductivities of the emulsions were given by (8.7) involving a constant low-frequency value of conductivity $\bar{\sigma}_{LF}$ plus a term $\Delta\tilde{\bar{\sigma}}$ which increased with the square of frequency. Initially, it was decided use a simple DC value for the conductivity of the emulsions. Figure 52 shows the effects of different DC values of conductivity on the response obtained with no target in the tank and an emulsion ($\epsilon_r = 32$). It was clear from these results that the dispersion present in the conductivity of the real emulsions had a significant impact on the amplitude and shape of the responses and, therefore, must be included in the models.

	ϵ'_{rs}	$\epsilon'_{r\infty}$	τ_e (ps)
Emulsion 1	10.34	4.0	9.95
Emulsion 2	19.00	1.0	8.00
Emulsion 3	32.03	1.0	7.50

Table 11: Debye equation parameters for modelling the dispersive conductivity of the emulsions

The dispersive conductivity behaviour was modelled by fitting the Debye equation to the real conductivity profile, in a similar method to work by Bourgeois and Smith (1996). $\epsilon'_{rs} = \bar{\epsilon}_{LF}$ was used, and parameters $\epsilon'_{r\infty}$ and τ_e were adjusted to obtain a match. Figure 53a shows that the real part of the right hand side of the Debye equation stays approximately constant over the frequency bandwidth of interest. Figure 53b shows the real conductivity dispersion for each emulsion plotted against the imaginary part of the right hand side of the Debye equation with fitted parameters. An R^2 value of 0.99 was achieved for all three emulsions over the bandwidth of interest, demonstrating the goodness of the fit. Table 11 gives the adjusted values of $\epsilon'_{r\infty}$ and τ_e for the three emulsions.

Figure 54 shows the response from a tank with no target and an emulsion ($\epsilon_r = 32$), i. e. the same setup used to test the different DC conductivities, now with the fitted Debye model. A much better match is demonstrated between the real and modelled responses.

8.6 COMPARISON OF EXPERIMENTAL AND MODELLED DATA

The aim of performing a series of experiments to simulate typical materials and targets found in GPR surveys was to collect a comprehensive data-set to further validate the antenna models. However, to simulate all of the possible experimental configurations would have required more than a thousand 1000 A-scan models, consequently a subset of configurations was carefully chosen.

8.6.1 *A-scan responses*

The following analyses are visual comparisons of real and modelled responses in terms of the amplitude, phase, and shape of individual wavelets and the overall

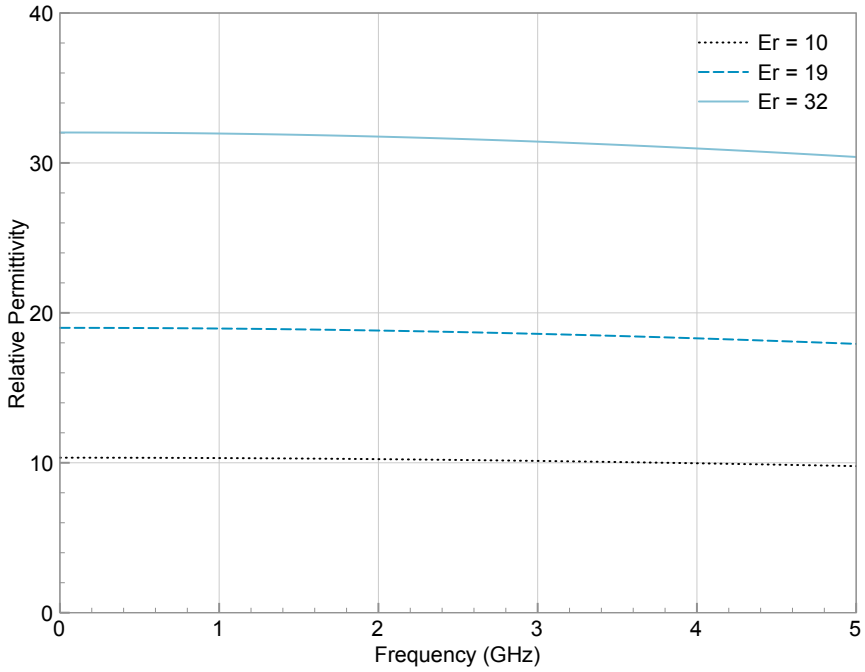

(a) Modelled relative permittivity

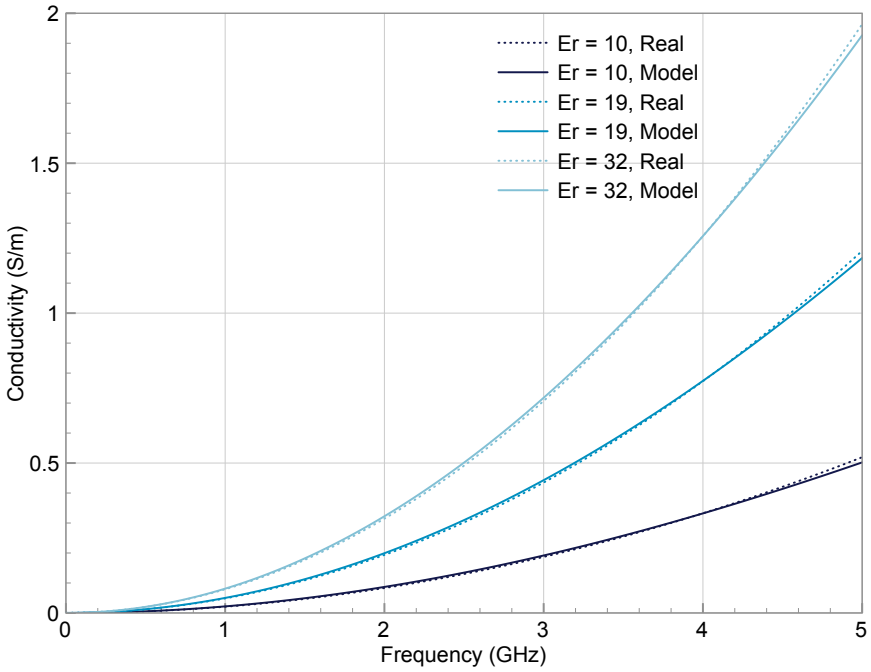

(b) Real vs. modelled conductivity

Figure 53: Variation of the constitutive parameters of the emulsions over bandwidth of interest

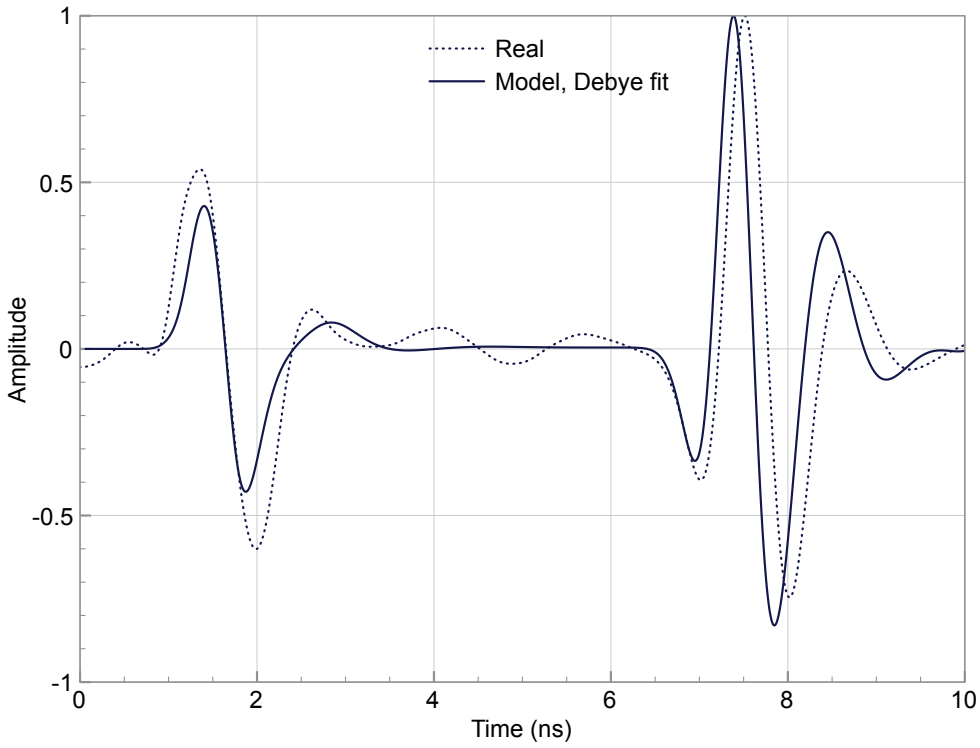

Figure 54: GSSI 1.5 GHz antenna: Modelled vs. real A-scans with Debye conductivity model, no target in tank, and emulsion ($\epsilon_r = 32$)

response[4]. No attempt is made to quantify small differences between the real and modelled responses, however any obvious differences are highlighted and their cause justified.

GSSI 1.5GHz antenna: 12 mm steel rebar in all liquids

The objective of the following series of comparisons was to study the experimental and modelled responses of a 12 mm steel rebar target in all of the different liquids with the GSSI 1.5 GHz antenna. Figures 55–59 show the real versus modelled responses in ascending order of permittivities of the liquids.

Figure 55 shows the real and modelled responses in mineral oil. The mineral oil has a low permittivity and, therefore, high velocity, which combined with the proximity of the target to the antenna, means that wavelets from the rebar and tank base overlap one another as well as the direct wave[5]. It is precisely this type of response that demonstrates the need to have an accurate antenna model in the simulation. It can be seen that the initial part of the

4 Both the real and modelled responses in all of the following subsections have been normalised to an absolute maximum amplitude of one, and have been corrected for any DC bias present. Except where otherwise stated, the responses have been aligned by their first zero crossing.

5 Reference to Figure 56, in which these wavelets are separately distinguishable and annotated, may help interpretation of Figure 55.

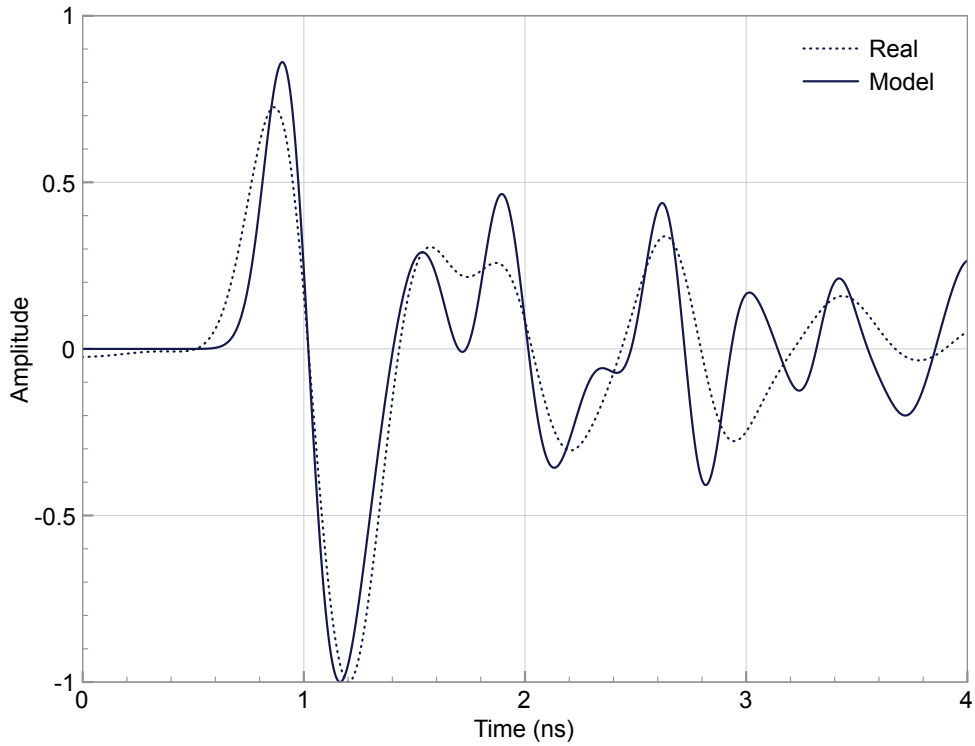

Figure 55: GSSI 1.5 GHz antenna: Modelled vs. real A-scans of a 12 mm steel rebar in mineral oil ($\epsilon_r = 2$)

direct wave is accurately represented in the model, the only minor differences being a larger first positive peak and slightly narrower wave shape. These are probably caused by differences in the real and modelled excitation pulse shape and frequency content. The typically *w-shaped* wavelets from metallic targets are difficult to separately distinguish, and the model captures this well, but contains additional ripples that are not present in the real signal.

Figure 56 shows the real and modelled responses in the first of the emulsions ($\epsilon_r = 10$). Figure 56 is annotated as an example to aid the interpretation of future Figures. The wavelets in the response that correspond to the direct wave, rebar, and base of the tank are all clearly highlighted. The direct wave is again accurately modelled exhibiting a similar set of minor differences as the mineral oil. Due to the increased permittivity, the wavelet from the steel rebar is almost separable from the direct wave and along with the wavelet from the tank base can now be easily identified. This is well predicted by the model with only minor overshoots in signal amplitude.

Figure 57 shows the real and modelled responses in the emulsion ($\epsilon_r = 19$). The model behaviour is very similar to the previous emulsion but with an even better match for the amplitudes of the wavelets from the rebar and the tank base.

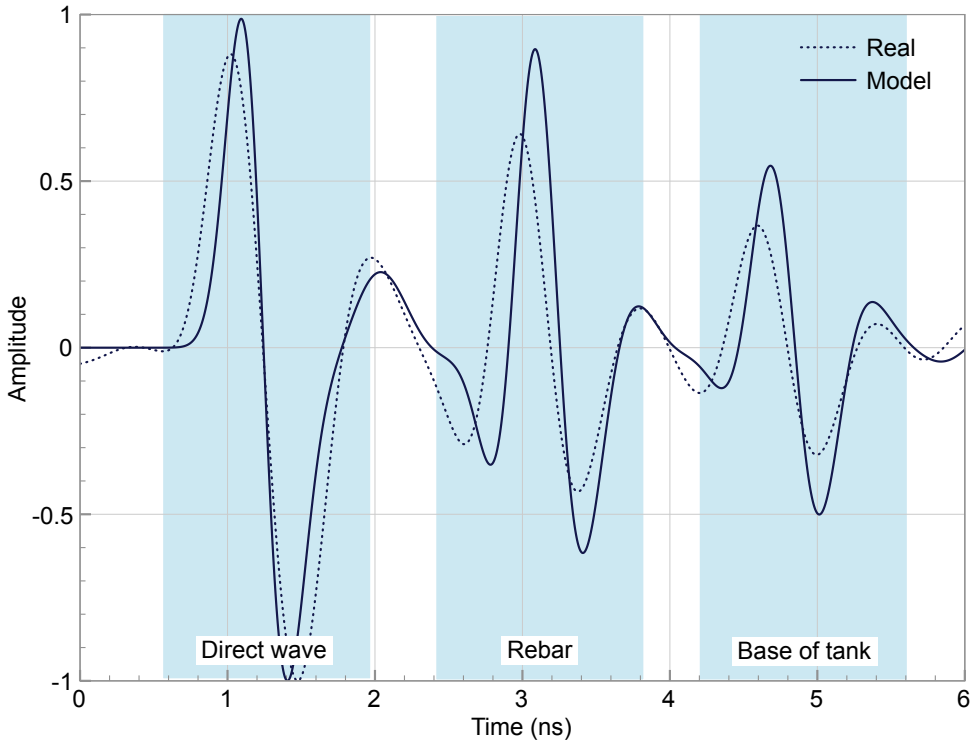

Figure 56: GSSI 1.5 GHz antenna: Modelled vs. real A-scans of a 12 mm steel rebar in emulsion ($\epsilon_r = 10$)

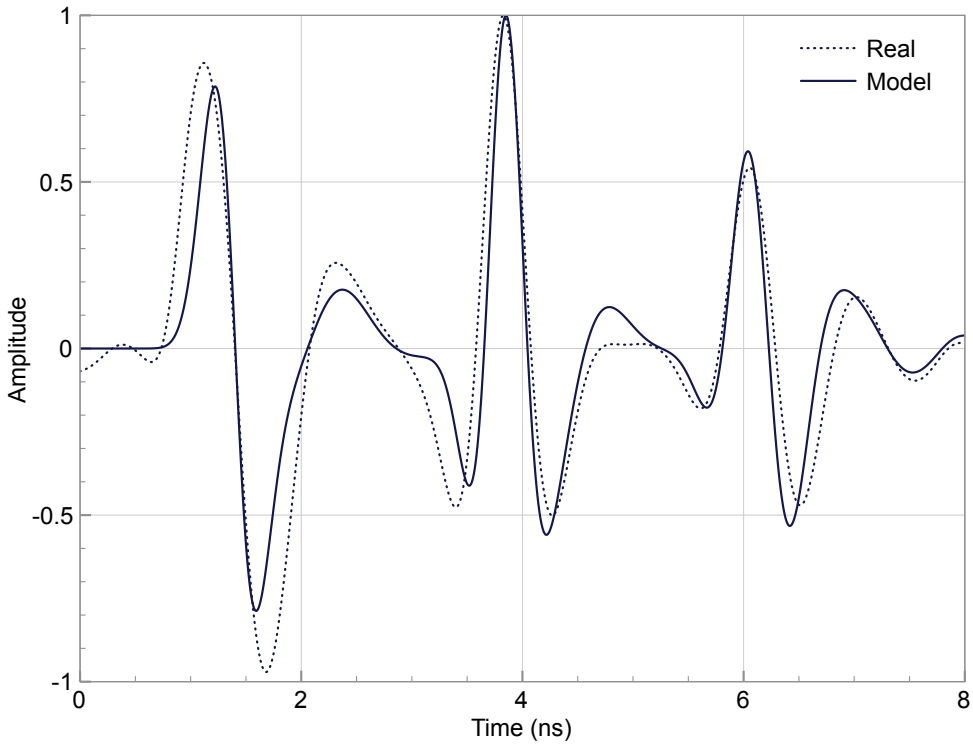

Figure 57: GSSI 1.5 GHz antenna: Modelled vs. real A-scans of a 12 mm steel rebar in emulsion ($\epsilon_r = 19$)

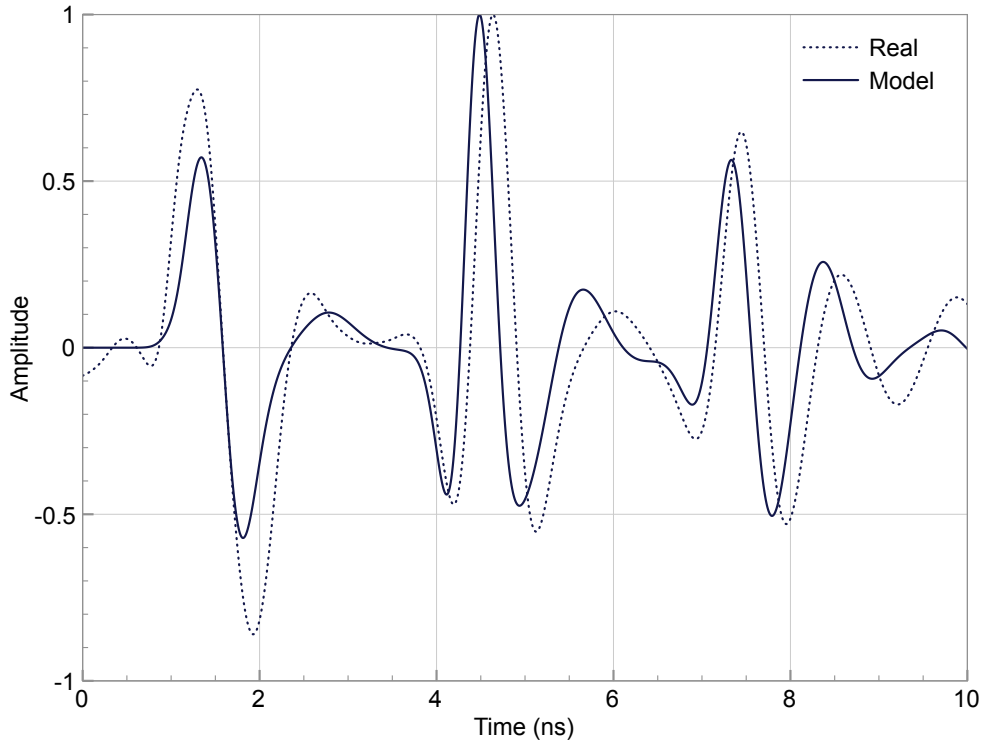

Figure 58: GSSI 1.5 GHz antenna: Modelled vs. real A-scans of a 12 mm steel rebar in emulsion ($\epsilon_r = 32$)

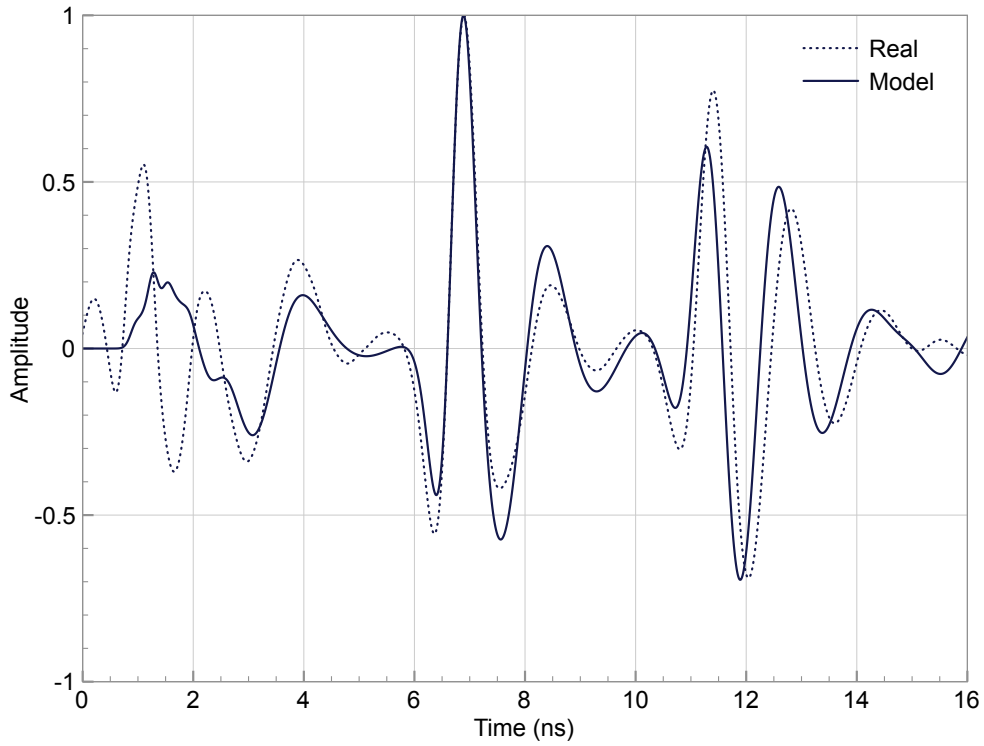

Figure 59: GSSI 1.5 GHz antenna: Modelled vs. real A-scans of a 12 mm steel rebar in distilled water ($\epsilon_r = 78$)

Figure 58 shows the real and modelled responses in the last of the emulsions ($\epsilon_r = 32$), and Figure 59 shows the real and modelled responses in the distilled water ($\epsilon_r = 78$). As the permittivity of the liquid increases, it can be observed that the model under-predicts the amplitude of the real direct wave, and in the case of the distilled water, does not well-predict the shape. This is likely attributed to fact that the unknown parameters in the antenna models were optimised based upon the crosstalk in free-space of the real antennas. As such, it can be concluded that the coupling effects between the antenna and the liquid are better optimised for lower permittivities. Despite the discrepancies in the modelled direct waves, the modelled responses from the steel rebar and tank base show excellent agreement with the real data.

GSSI 1.5GHz antenna and Hertzian dipole source: 12 mm steel rebar in mineral and distilled water

The objective of the following comparisons was to demonstrate the effects of replacing the real antenna in the model with a simple theoretical source, such as a Hertzian dipole. The modelled responses are of a 12 mm steel rebar target in mineral oil and distilled water, which shows the behaviour at two very different permittivities. Figure 60 shows that with the low permittivity of the mineral oil and the proximity of the rebar to the antenna, the simple source model does not predict any part of the real response. In Figure 61 the higher permittivity of the distilled water means that the simple source model does predict the shape of the wavelets from the rebar and the tank base but the amplitude information is incorrect. Not surprisingly the shape, amplitude and phase of the direct wave in the simple source model are very different from the real data.

GSSI 1.5GHz antenna: 8, 10, 12 mm steel rebars and a 10 mm GFRP rebar in emulsion ($\epsilon_r = 32$)

The objective of the following series of comparisons was to study the experimental and modelled responses of a series of different diameter steel and GFRP rebars in an emulsion ($\epsilon_r = 32$) with the GSSI 1.5 GHz antenna.

Figure 62 shows the modelled responses of 8, 10, 12 mm steel rebars and a 10 mm GFRP rebar in an emulsion ($\epsilon_r = 32$). The responses have been normalised as a group. It can be seen that as the diameter of the steel rebars is increased the amplitude of its wavelet increases. This is simply due to the increased target area reflecting more energy from the transmitted wave back to the receiver. The arrival times of the wavelets from the steel rebars decrease as the diameter increases, because the location of the centres of all the rebars

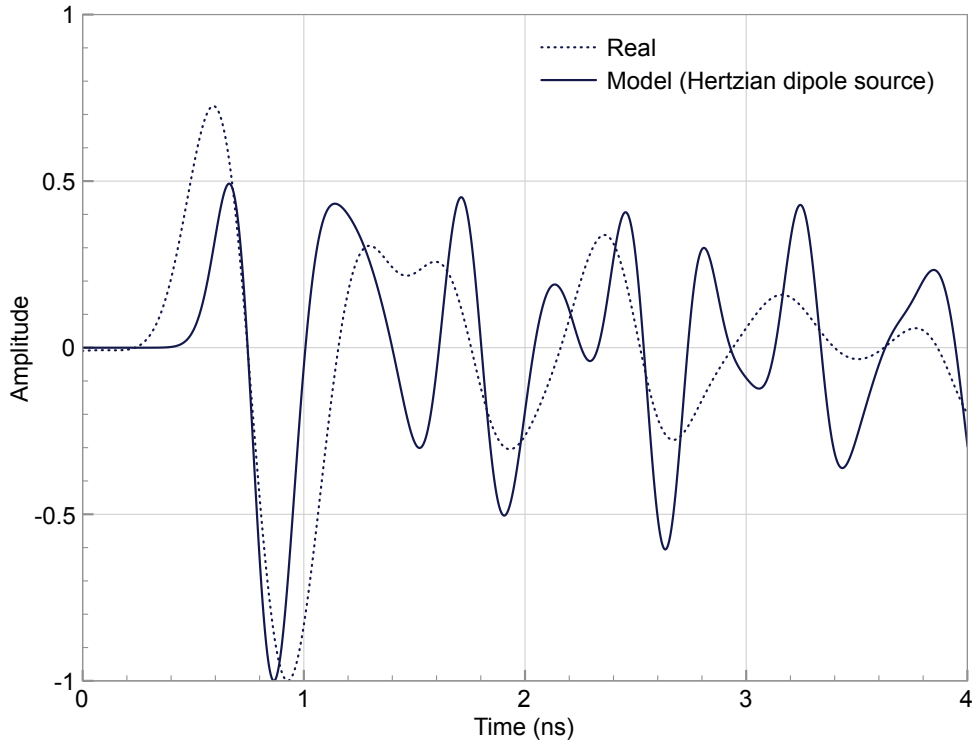

Figure 60: GSSI 1.5 GHz antenna: Modelled vs. real A-scans of a 12 mm steel rebar in mineral oil ($\epsilon_r = 2$)

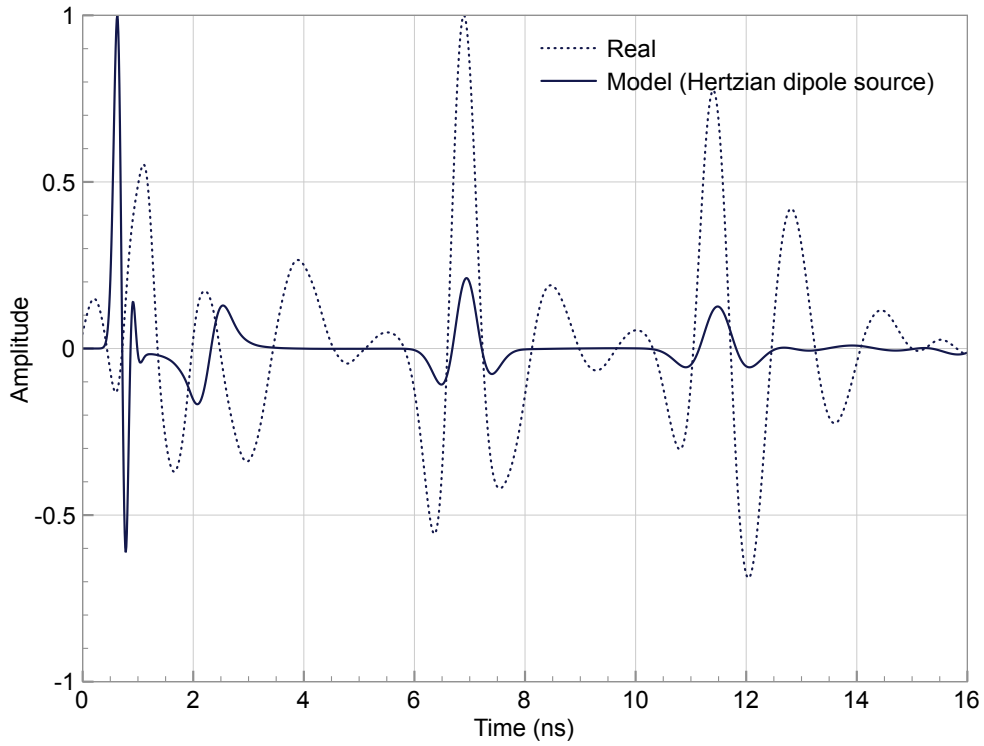

Figure 61: GSSI 1.5 GHz antenna: Modelled vs. real A-scans of a 12 mm steel rebar in distilled water ($\epsilon_r = 78$)

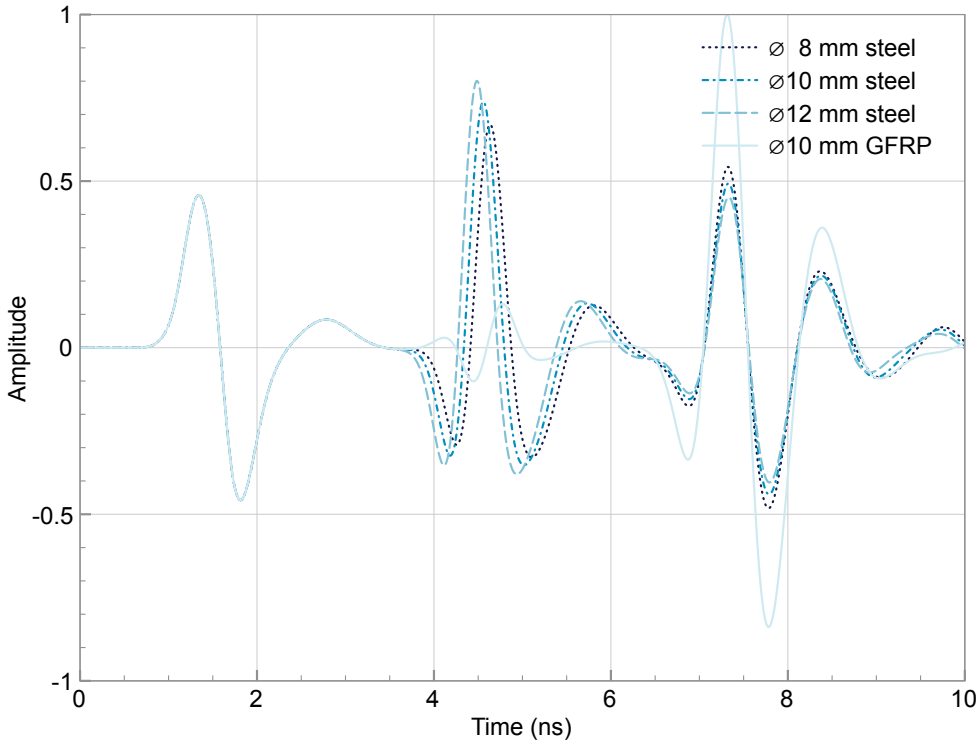

Figure 62: GSSI 1.5 GHz antenna: Modelled A-scans of 8, 10, 12 mm steel rebars and a 10 mm GFRP rebar in emulsion ($\epsilon_r = 32$)

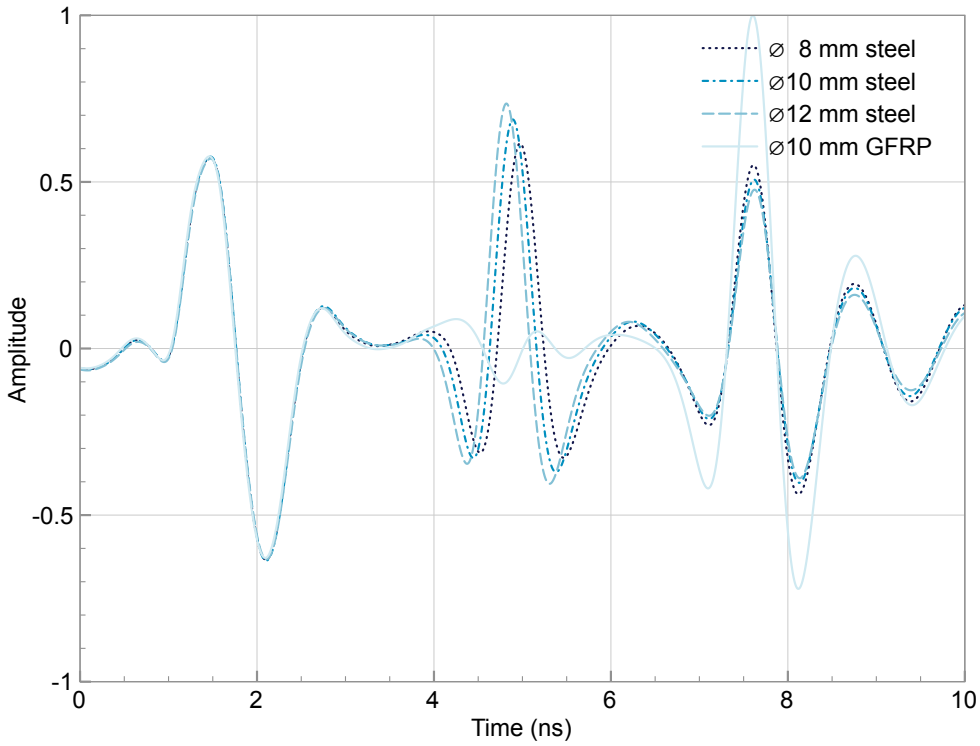

Figure 63: GSSI 1.5 GHz antenna: Real A-scans of 8, 10, 12 mm steel rebars and a 10 mm GFRP rebar in emulsion ($\epsilon_r = 32$)

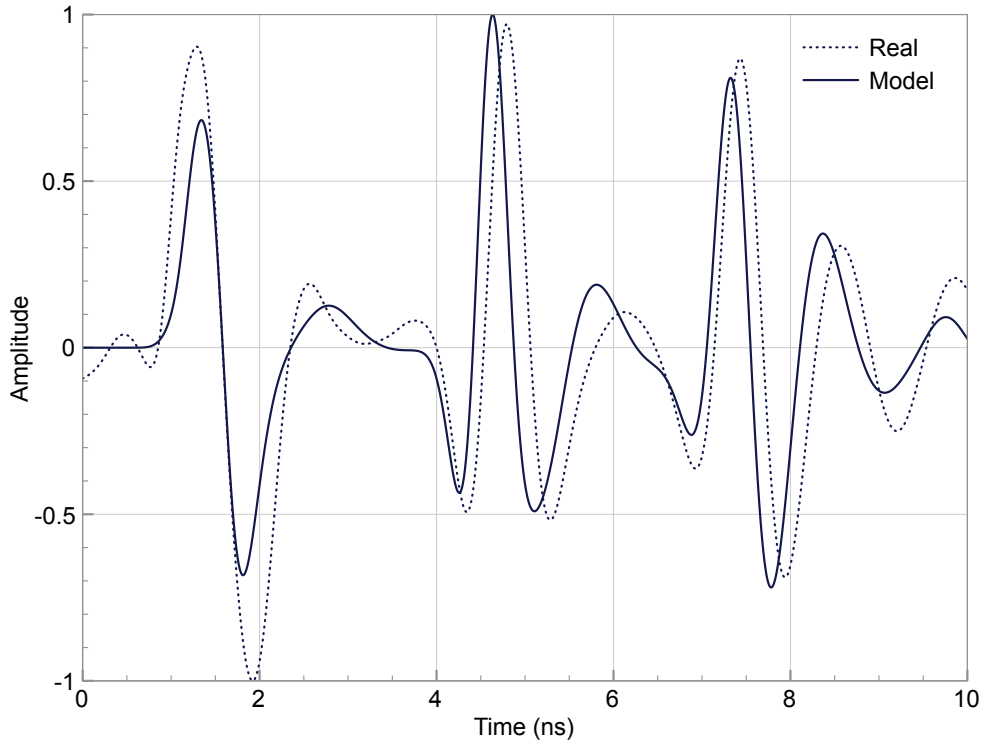

Figure 64: GSSI 1.5 GHz antenna: Modelled vs. real A-scans of a 8 mm steel rebar in emulsion ($\epsilon_r = 32$)

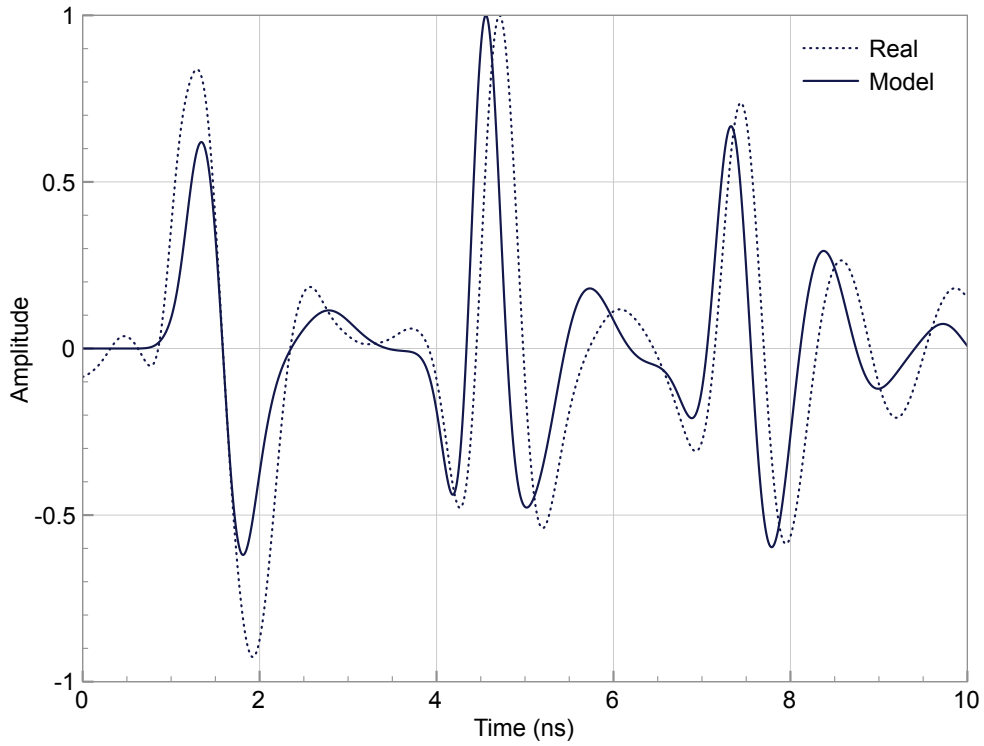

Figure 65: GSSI 1.5 GHz antenna: Modelled vs. real A-scans of a 10 mm steel rebar in emulsion ($\epsilon_r = 32$)

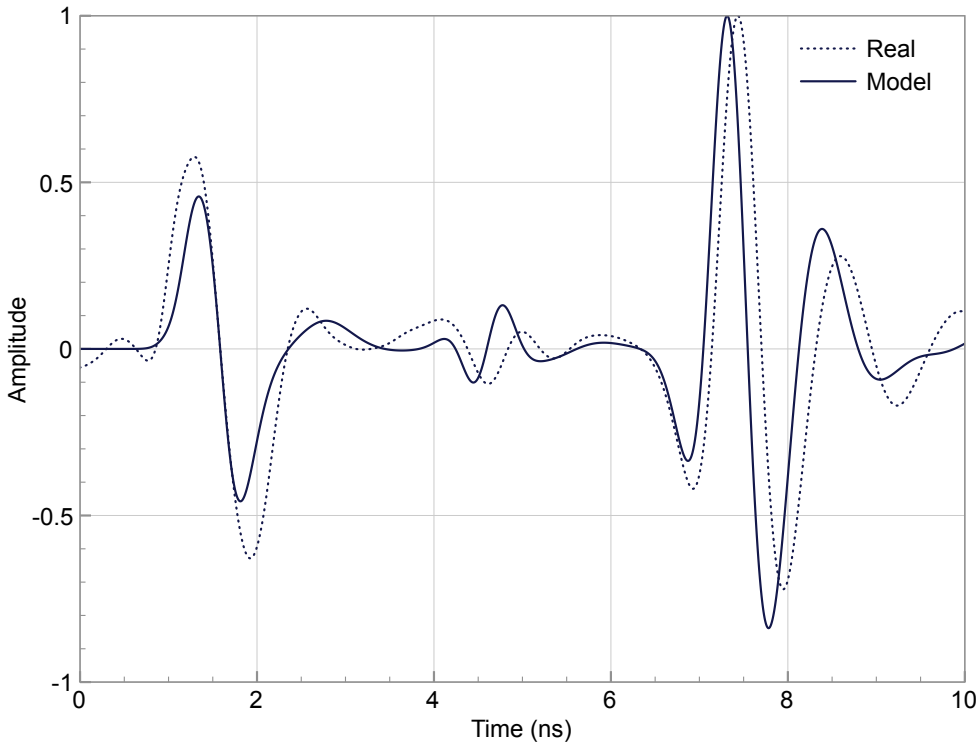

Figure 66: GSSI 1.5 GHz antenna: Modelled vs. real A-scans of a 10 mm GFRP rebar in emulsion ($\epsilon_r = 32$)

was the same and thus, the upper surface of the rebars became closer to the antenna. The wavelet from the GFRP rebar, which has a permittivity of three, has a predictably much smaller amplitude. The size and material of the rebars also influences the amplitude of the wavelets from the tank base. The larger the diameter of steel rebar the more the response from the tank base is masked and, thus, its amplitude is reduced. In the case of the GFRP rebar, the response from the metallic tank base is still much stronger than that from the GFRP despite being further from the antenna in a lossy material.

Figure 63 shows the real responses of 8, 10, 12 mm steel rebars and a 10 mm GFRP rebar in an emulsion ($\epsilon_r = 32$). The real responses follow the same behaviour seen in the corresponding models. Figures 64–66 show direct comparisons between the real and modelled responses of 8 mm and 10 mm steel rebars and a 10 mm GFRP rebar in an emulsion ($\epsilon_r = 32$). A direct comparison between the real and modelled responses of the 12 mm steel rebar in an emulsion ($\epsilon_r = 32$) was previously shown in Figure 58.

MALÅ 1.2GHz antenna: 12 mm steel rebar in all liquids

The objective of the following series of comparisons was to study the experimental and modelled responses of a 12 mm steel rebar target in all of the

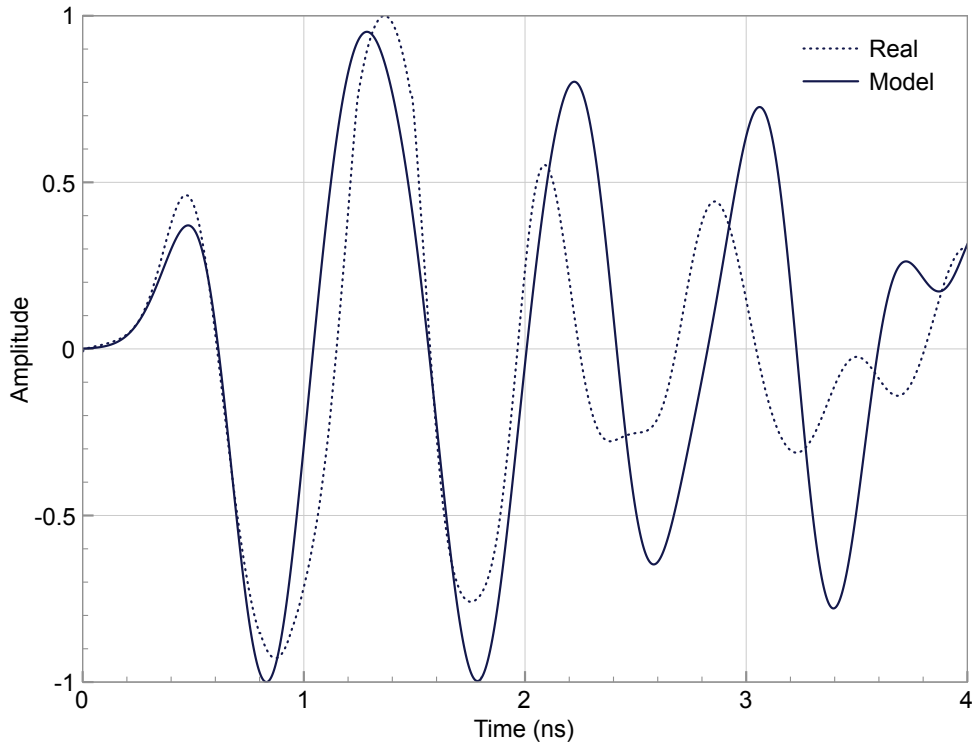

Figure 67: MALÅ 1.2 GHz antenna: Modelled vs. real A-scans of a 12 mm steel rebar in mineral oil ($\epsilon_r = 2$)

different liquids with the MALÅ 1.2 GHz antenna. Figures 67–71 show the real versus modelled responses in ascending order of permittivities of the liquids. Analysis of the responses yields the same patterns as those for the GSSI 1.5 GHz antenna. It can be observed that, in general, the match between the real and modelled responses is not as good for the MALÅ 1.2 GHz antenna as for the GSSI 1.5 GHz antenna.

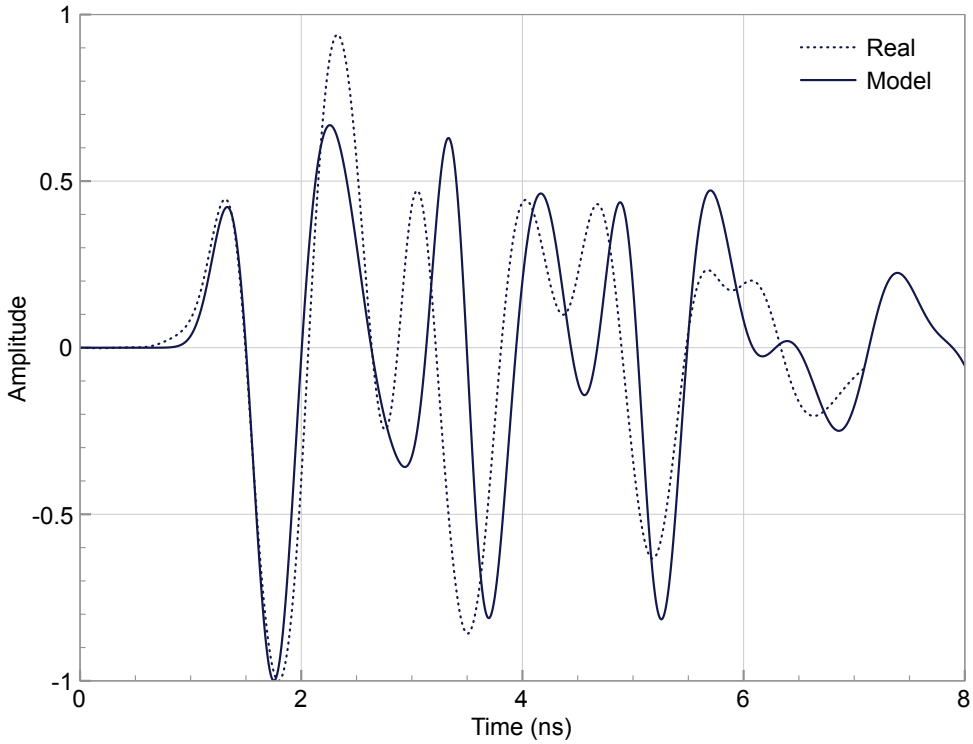

Figure 68: MALÅ 1.2 GHz antenna: Modelled vs. real A-scans of a 12 mm steel rebar in emulsion ($\epsilon_r = 10$)

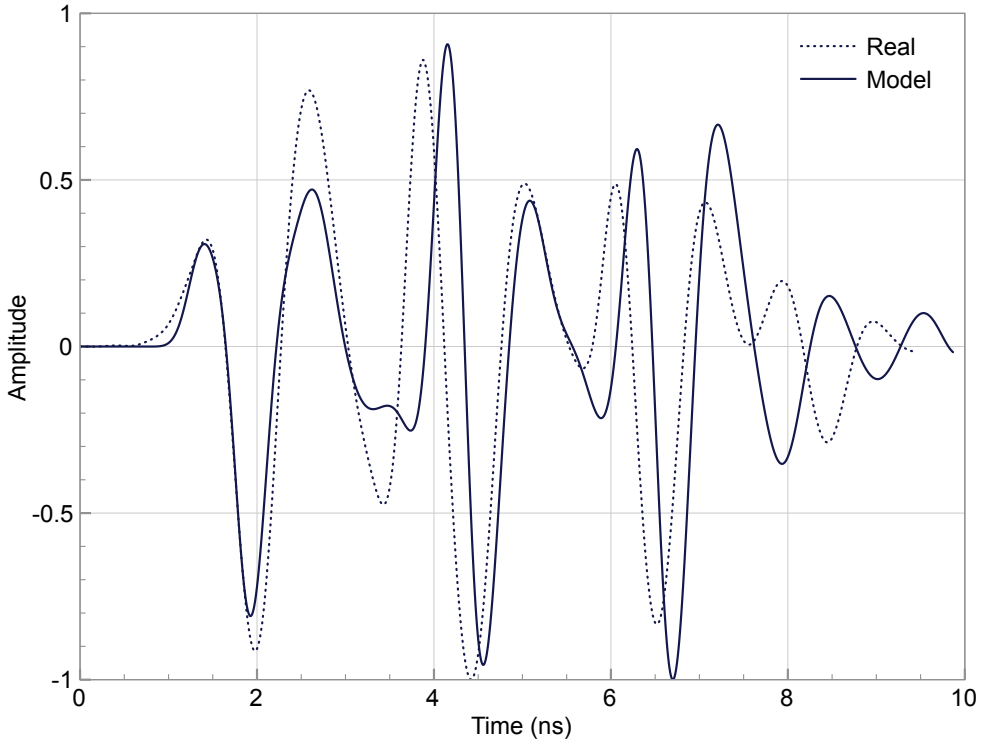

Figure 69: MALÅ 1.2 GHz antenna: Modelled vs. real A-scans of 12 mm steel rebar in emulsion ($\epsilon_r = 19$)

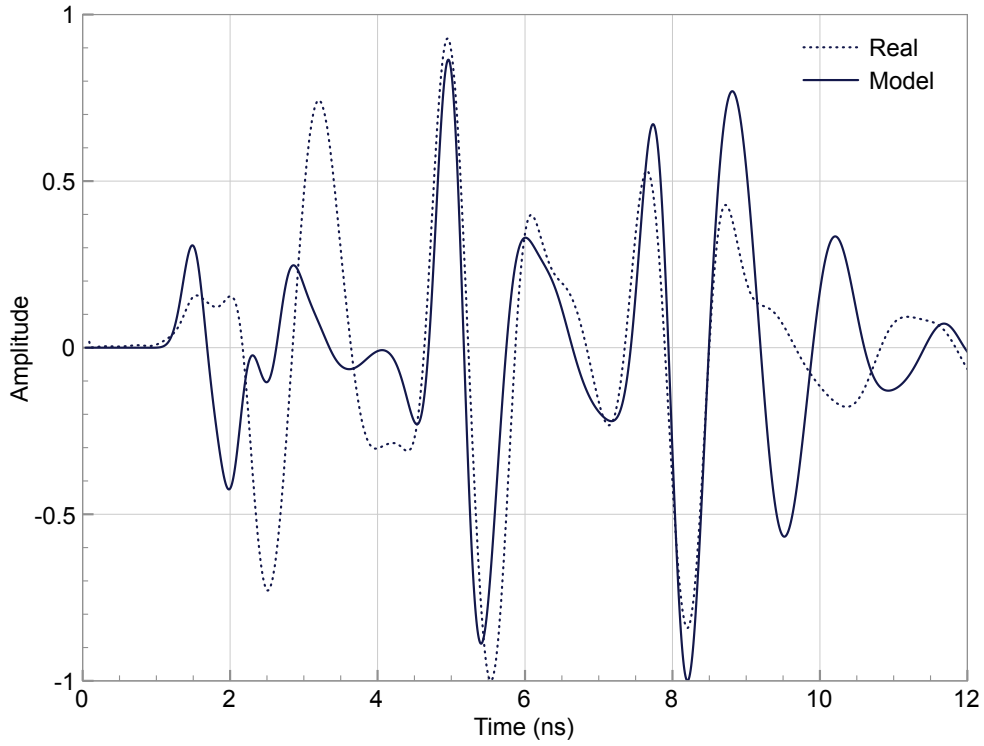

Figure 70: MALÅ 1.2 GHz antenna: Modelled vs. real A-scans of a 12 mm steel rebar in emulsion ($\epsilon_r = 32$)

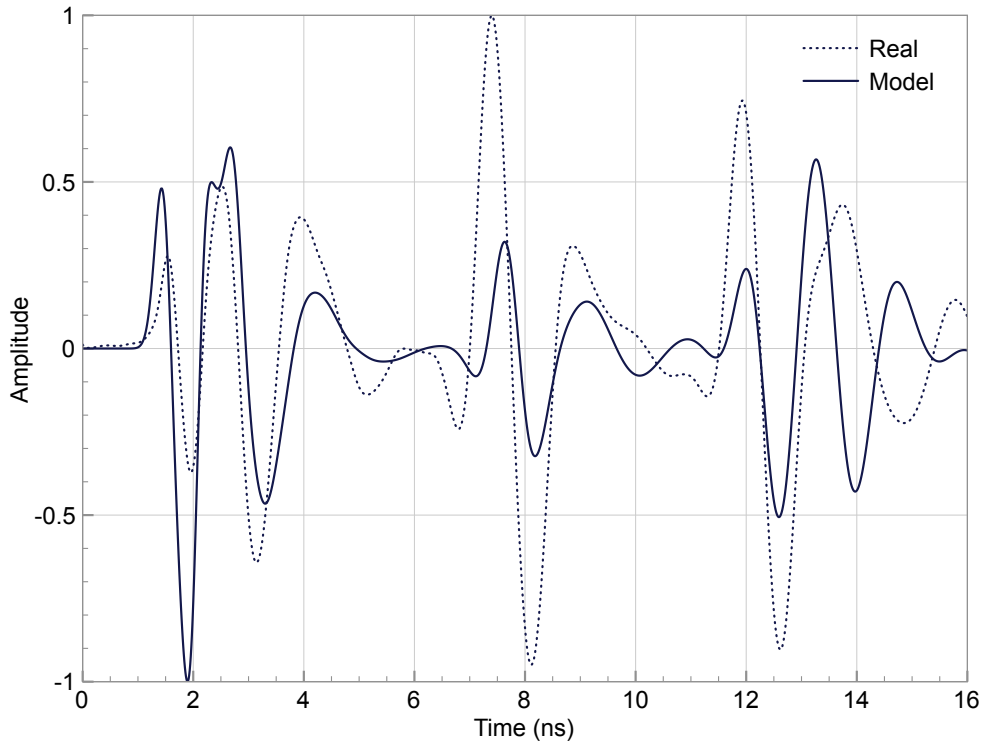

Figure 71: MALÅ 1.2 GHz antenna: Modelled vs. real A-scans of a 12 mm steel rebar in distilled water ($\epsilon_r = 78$)

8.6.2 *B-scan responses*

The accuracy of the models has been carefully analysed at a detailed level using A-scans. The general performance and accuracy of the models can also be assessed by comparing B-scans of typical GPR targets. Figures 72– 73 present B-scans from the GSSI 1.5 GHz antenna[6]. B-scans from the MALÅ 1.2 GHz antenna have not be included as the comparisons of real and modelled data were very similar to the GSSI 1.5 GHz antenna.

Figure 72 shows the real and modelled B-scans of a 12 mm steel rebar in the emulsion ($\epsilon_r = 32$). The cylindrical shape of the rebar yields a typical hyperbolic response, and the response from the tank base is clearly evident at approximately 7 ns. Under the centre of the hyperbola the response from the tank base has reduced amplitude caused by masking from the steel rebar. Reflections from the corners of tank, which appear as partial hyperbolas, can be seen at either side of the B-scan from approximately 8.5–12 ns. All of these features which are present in the real data are well predicted by the model.

Figure 73 is another example of a B-scan using emulsion ($\epsilon_r = 10$) and a rectangular metal box. The response from the metal box is much flatter than the hyperbola of the rebar, and has increased amplitude due to the lower permittivity of the emulsion. There is more masking of the response from the tank base due to the greater size of the metal box compared to the rebar. Once again, these features are clearly predicted by the model.

6 All B-scans have been adjusted so that the first zero crossing is located at 1 ns.

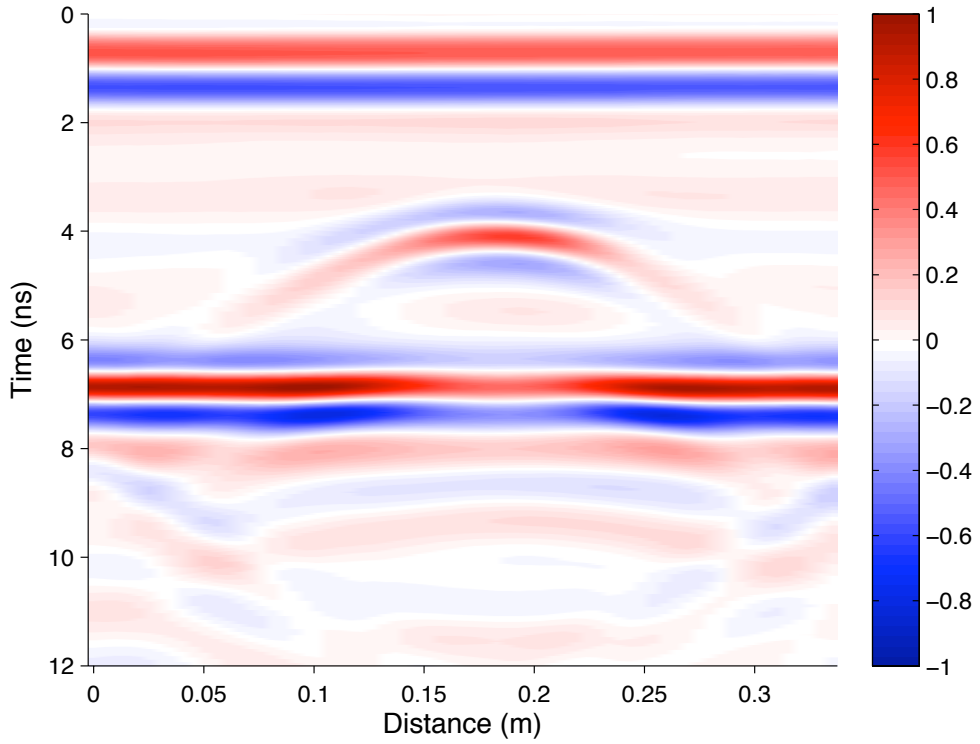

(a) Real

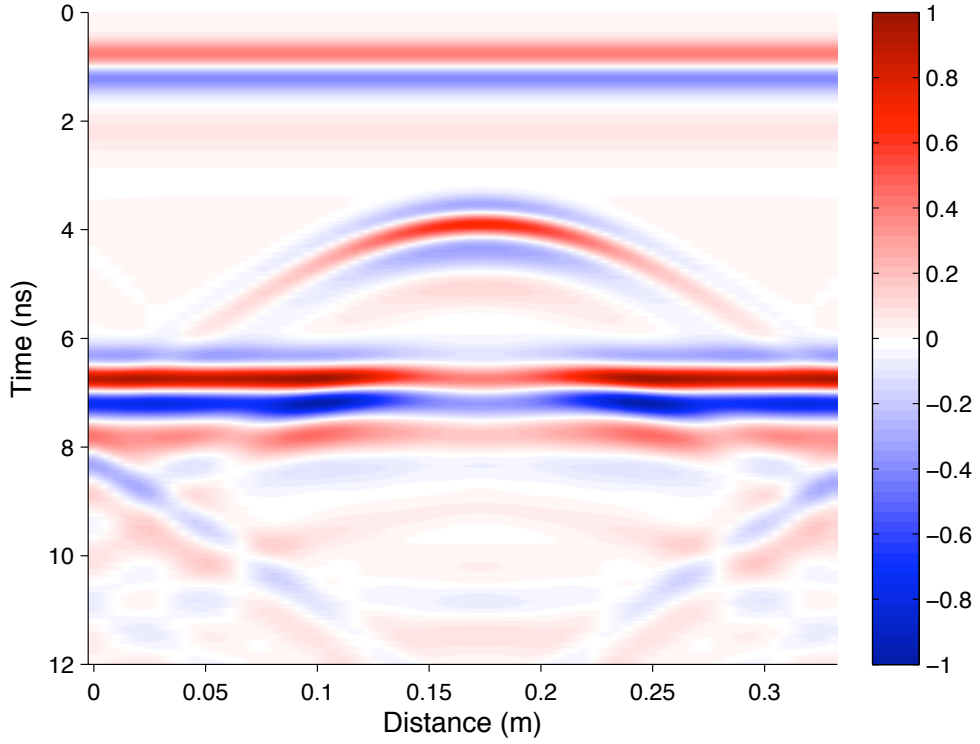

(b) Model

Figure 72: GSSI 1.5 GHz antenna: B-scans of a 12 mm steel rebar in emulsion ($\epsilon_r = 32$)

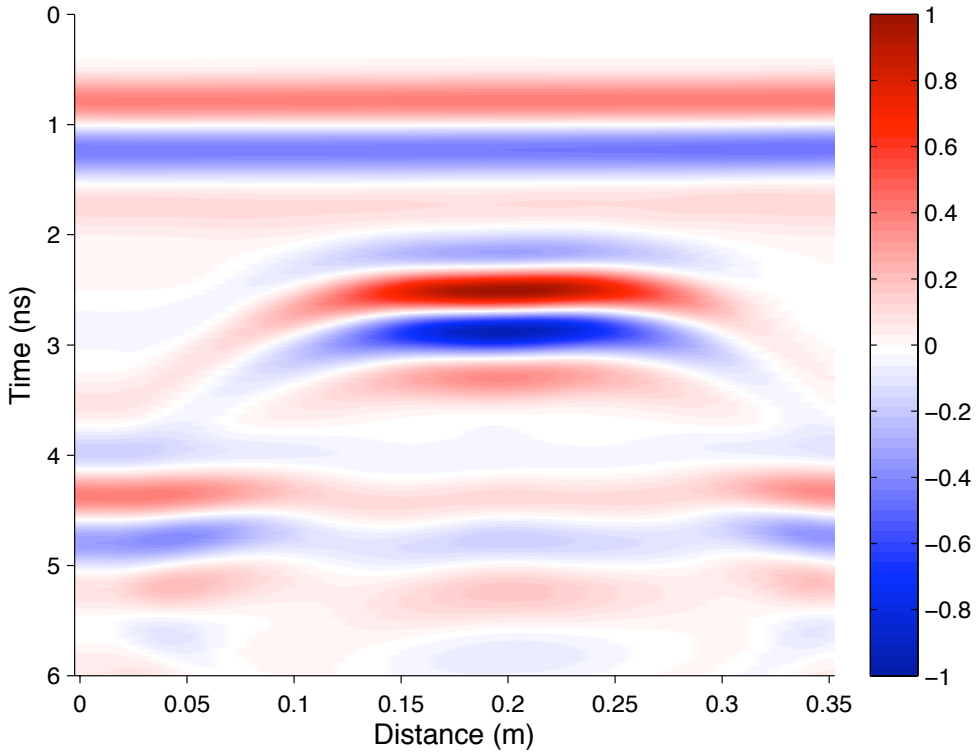

(a) Real

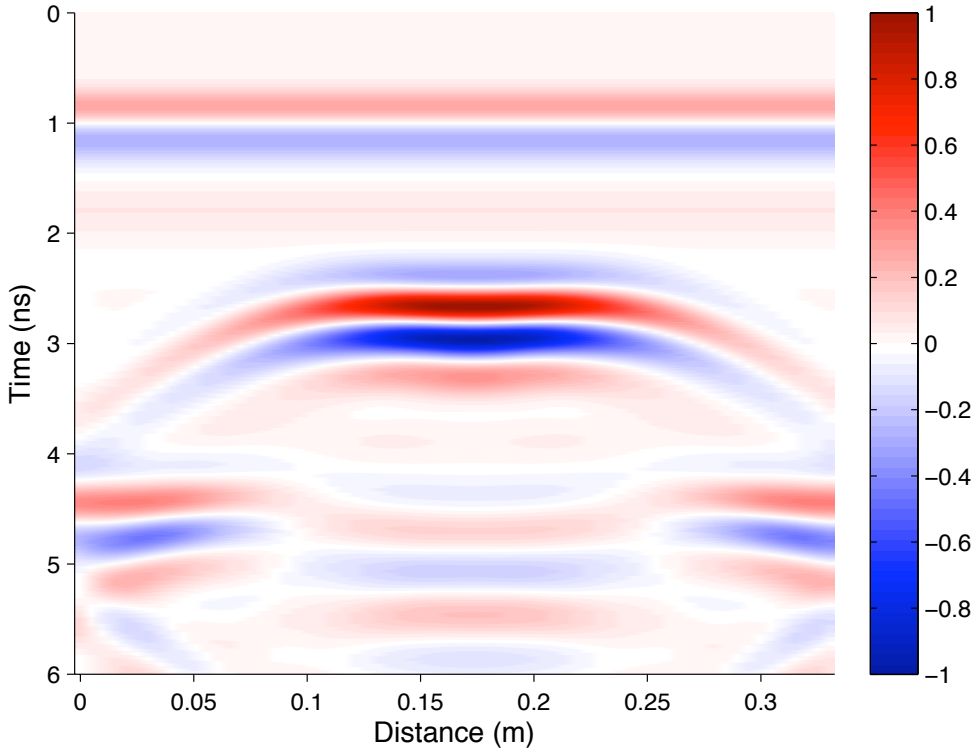

(b) Model

Figure 73: GSSI 1.5 GHz antenna: B-scans of a metal box in emulsion ($\epsilon_r = 10$)

8.7 SUMMARY

The focus of this chapter was the description of the procedure, and the analysis of the results of a comprehensive validation process used to verify the accuracy of the antenna models developed in Chapter 6 and Chapter 7. A series of O/W emulsions were designed and made to simulate the electrical properties of materials typically investigated using GPR. The two constituents of the emulsions, mineral oil ($\epsilon_r = 2$) and distilled water ($\epsilon_r = 78$), were used along with three emulsions ($\epsilon_r = 10, 19, 32$) to test a range of typical GPR targets using the GSSI 1.5 GHz antenna and MALÅ 1.2 GHz antenna. Targets included a range of cylindrical shapes in the form of steel and composite rebars of different diameters (8, 10, 12 mm), and a rectangular metallic box. The design theory and the manufacture of the emulsions were successfully verified by comparing the design permittivities to actual measurements made with the GSSI system.

Models of the experimental configurations were created in GprMax3D utilising Paraview for geometry visualisation. The constitutive parameters of each liquid were shown to be critical parameters to correctly input into the models. The permittivities of the mineral oil and emulsions had been measured, and were known to be constant over the bandwidth of interest. The permittivity and conductivity of the distilled water were modelled using the Debye equation. The design theory for the emulsions had shown the conductivity to increase with the square of the frequency, and this was replicated in the model using the Debye equation with modified $\epsilon'_{r\infty}$ and τ_e parameters.

The modelled responses were then compared with real data. By analysing A-scans of a single target configuration across all the liquids with the GSSI 1.5 GHz antenna it was shown that the modelled responses were in excellent agreement with the real data in terms of the amplitude, phase and shape of the wavelets. The importance of including an antenna model in the simulation was highlighted by analysing the responses from models where the antenna was replaced by a simple Hertzian source. In these cases, the simple source models could no longer accurately predict the amplitude or shape of the real responses, especially for low permittivity materials and near-surface targets. Responses from the different sizes of steel and composite rebars were analysed and the small differences in the phase and amplitude of the real responses were again present in the models. To get a more general assessment of the accuracy of the models, B-scans of a 12 mm steel rebar and a rectangular metal box were compared with the real data. Not only were the responses from the targets well predicted, but the masking of the signals from the tank base, and the reflections from the corners of the tank, were also replicated in the models.

A comprehensive validation of the antenna models has been carried out across a range of materials and target configurations typically investigated using GPR. The GSSI 1.5 GHz antenna and MALÅ 1.2 GHz antenna models have been shown to accurately predict not only the shape of the real responses but also, crucially, the amplitude information. This provides confidence for their use in more advanced studies.

9

RADIATION DYNAMICS OF REAL GROUND-PENETRATING RADAR ANTENNAS

This chapter focuses on the development and analysis of radiation patterns of high-frequency commercial GPR antennas. The radiation patterns were created using the antenna models that were developed, optimised, and comprehensively validated in previous chapters. In the first part of the chapter, the importance of studying the radiation patterns of antennas, with regard to their performance, is highlighted. The principal E- and H-planes are defined, along with the spherical coordinate system, and the different field regions surrounding an antenna. The free-space radiation patterns of the GSSI 1.5 GHz antenna and the MALÅ 1.2 GHz antenna are then presented and discussed. Finally, radiation patterns for both antennas over lossless and low-loss half-spaces are shown and discussed. Where possible, the modelled radiation patterns are compared with theoretical predictions and measured data.

9.1 RADIATION PATTERN THEORY

The radiation pattern of a GPR antenna is a very important parameter because it determines how well, if at all, a target can be detected. The radiation pattern of an antenna is defined in the *IEEE Standard Definitions of Terms for Antennas* (IEEE, 1983) as,

> The spatial distribution of a quantity which characterizes the electromagnetic field generated by an antenna.

Typically, a graphical representation of the received power at a constant radius, *power pattern*, or the spatial variation of the electric (or magnetic) field at a constant radius, *field pattern*, is presented. 3D antenna patterns are conventionally presented as 2D cuts of the principal E- and H-planes. The E-plane is the plane containing the E-field vector and the direction of maximum radiation. Similarly, the H-plane is the plane containing the H-field vector and the direction of maximum radiation. It is usual practice to orient the antenna so that at least one of the principal plane patterns coincides with one of the geometrical principle planes (Balanis, 1997). Figure 74 shows the system of spherical co-ordinates that are typically used to describe antenna patterns. The dipole is oriented in the x-y plane, along the y axis. An E-plane pattern

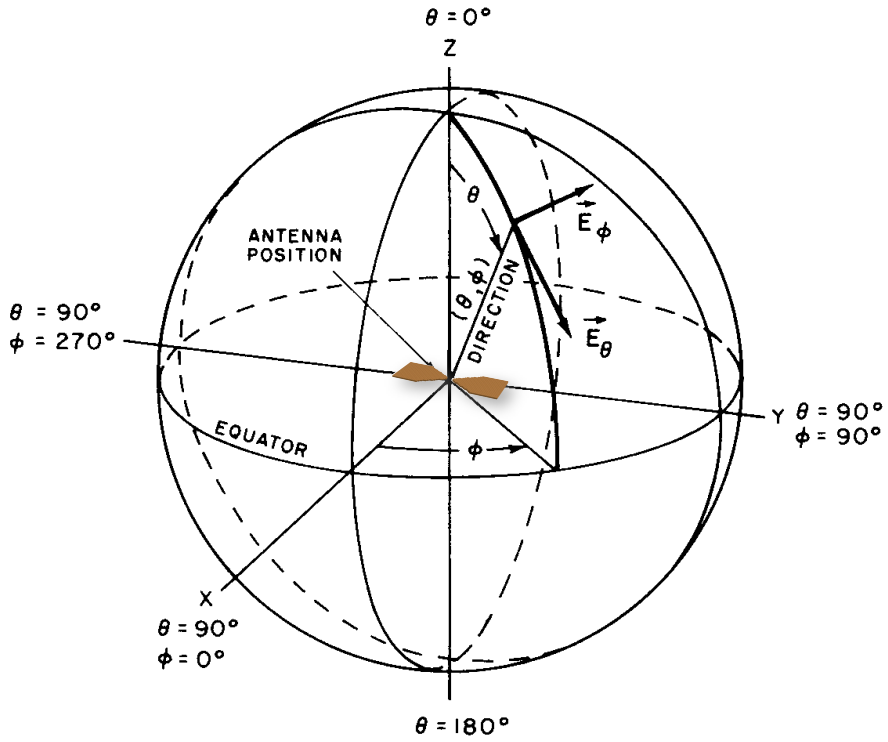

Figure 74: Spherical coordinate system geometry (adapted from (IEEE, 1979))

would be calculated from the values of $\vec{E}_\theta$ located on a circle at $\phi = 90°, 270°$. A H-plane pattern would be calculated from values of $\vec{E}_\phi$ (the perpendicular E-field component to the H-plane) located on a circle at $\phi = 0°, 360°$.

9.1.1 *Radiation lobes*

The shapes defined by radiation patterns are usually referred to as *lobes*, which can be *major* or *minor*, *side* or *back*. A major lobe is defined as the radiation lobe containing the direction of maximum radiation. A minor lobe is any lobe except the major lobe, and usually represents radiation in an undesired direction. A side lobe is a radiation lobe in any direction other than the intended lobe. Side lobes are normally the largest of the minor lobes, and it is important to minimise side lobe levels as they can result in a false target indication. A back lobe is a radiation lobe whose axis makes an angle of approximately 180° with respect to the beam of the antenna (Balanis, 1997).

9.1.2 *The critical angle*

The critical angle defines an upper limit of angles that can illuminated when a wave travels through the interface of two materials with different velocities. An

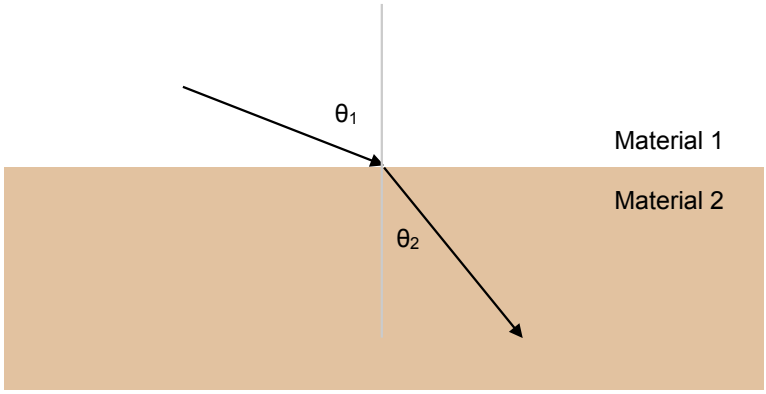

Figure 75: Waves change direction with change of material

incident wave can impinge on an interface between material 1 (which, for GPR, is usually air) and material 2 (which, for GPR, is usually the ground/structure to be investigated) at an angle given by $0° < \theta_1 < 90°$. This means the range of angles that can be illuminated in material 2 is given by (9.1) (Annan, 2005). Figure 75 shows how θ_1 and θ_2 are defined.

$$0° < \theta_2 < \arcsin\left(\frac{v_2}{v_1}\right)^{\circ}, \tag{9.1}$$

where:

$\theta_2 =$ range of illuminated angles in material 2 (°)

$v_1 =$ velocity in material 1 (m/s)

$v_2 =$ velocity in material 2 (m/s)

The maximum value of θ_2 is called the critical angle θ_c. A wave which travels horizontally in material 1 will be refracted downward at the critical angle. Angles of $\theta_2 > \theta_c$ are not mathematically possible ($\sin\theta_1 > 1$) unless angle θ_1 is a complex number. However, angles of $\theta_2 > \theta_c$ are physically possible if the horizontal phase velocity is less than the phase velocity of the material, and if the waves decay exponentially away form the material interface. Such waves are called evanescent waves and exist at the interface of different materials.

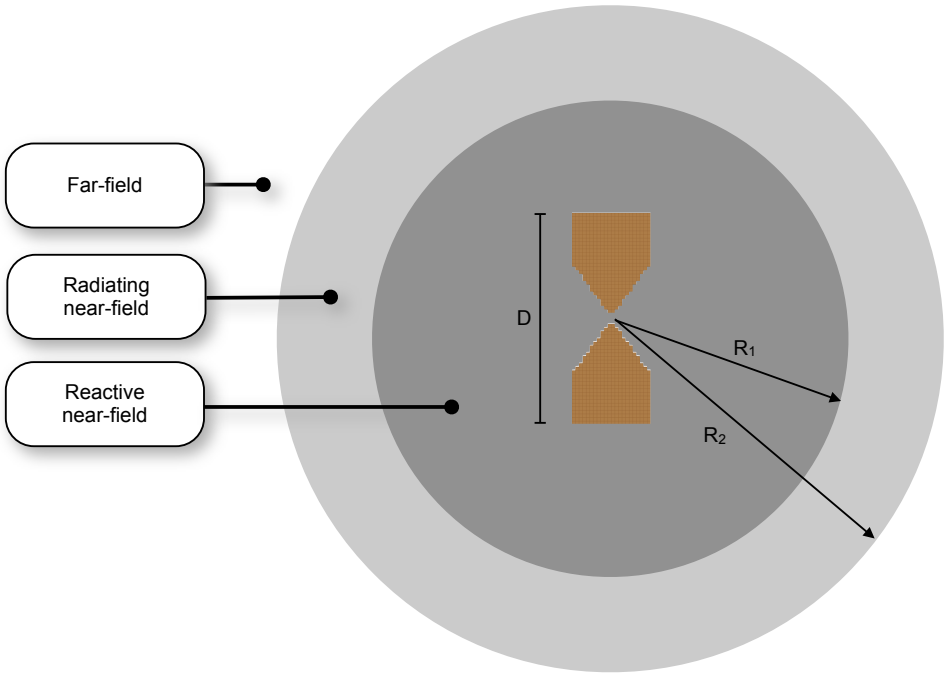

Figure 76: Field regions of an antenna

9.1.3 *Field regions*

The space surrounding an antenna is usually divided into three regions: the reactive near-field region, the radiating near-field or Fresnel region, and the far-field or Fraunhofer region. Each region is illustrated in Figure 76 and has a differently defined field structure.

The reactive near-field region extends to a radius R_1 from the antenna, given by (9.2).

$$R_1 < 0.62\sqrt{\frac{D^3}{\lambda}}, \tag{9.2}$$

where:

D = the largest dimension of the antenna (m)

λ = wavelength (m)

The Fresnel region extends from the outer boundary of the reactive near-field region to a radius R_2 from the antenna, given by (9.3).

$$R_2 < \frac{2D^2}{\lambda} \tag{9.3}$$

The far-field region extends from the outer boundary of the Fresnel region to infinity. In the far-field region, angular field distributions are assumed to be independent of the radial distance from the antenna.

9.2 GPR ANTENNA RADIATION PATTERNS

The study of antenna radiation patterns can be divided into three areas: theoretical analysis, measured data, and numerical modelling. The theoretical radiation patterns of simple antennas, such as the cylindrical monopole, can be completely predicted in free-space (King, 1956). Figure 77 shows the radiation patterns of an infinitesimal dipole in free-space. The patterns are sections of the classic *torus* shape. There are also theoretical approximations for the far-field patterns of infinitesimal dipole antennas over lossless (Engheta et al., 1982) and low-loss (Smith, 1984) half-spaces. Figure 78 shows examples of such patterns over lossless half-spaces. The patterns were calculated at a frequency of 1.71 GHz (the free-space centre frequency of the GSSI 1.5 GHz antenna model) which allows direct comparisons with modelled patterns presented later in this section. In contrast to the free-space patterns, the major and back lobes of both E-plane and H-plane patterns are reduced in amplitude, and the theoretical approximations predict sharp nulls in the major lobes around the critical angle, creating trilobate shapes.

The radiation pattern of one antenna can be measured directly with a second antenna, and this has been done in free-space for simple antennas as well as for more widely-used commercial GPR antennas (Klysz et al., 2006, Millard et al., 2002, Pérez-Gracia et al., 2009). There are also laboratory measurements of radiation patterns of simple antennas over homogeneous materials obtained directly with another antenna (Annan et al., 1975), and indirectly through the recording of responses from a simple target (Arcone, 1995). Pérez-Gracia et al. (2009) attempted to indirectly measure the radiation pattern of a MALÅ 1.6 GHz antenna using an aluminium cylinder in sand. Measuring antenna radiation patterns in free-space requires an antenna range with accurate positioning equipment, and the outcome is of limited use for GPR. To directly measure antenna radiation patterns in realistic materials, which is useful for GPR, presents many practical difficulties. This has prompted numerical simulations of GPR antenna radiation patterns.

The state of numerically derived GPR antenna radiation patterns is similar to that of measured data, and reflects the state of GPR antenna modelling in general. Radiation patterns of simple and more complex antennas have been modelled in free-space, but only radiation patterns of simple antennas

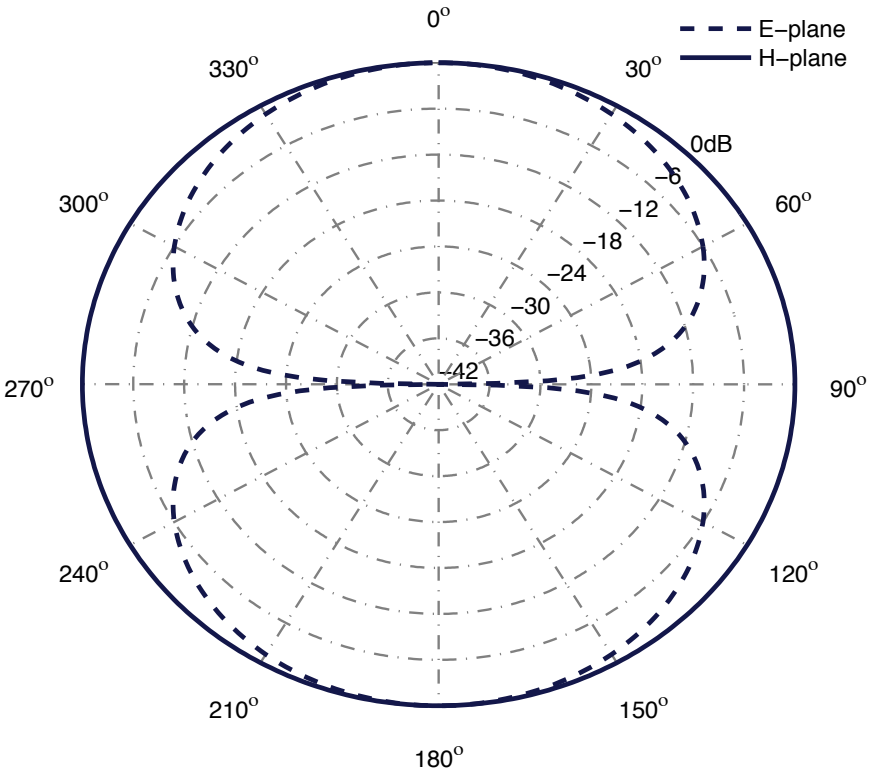

Figure 77: Radiation patterns of an infinitesimal dipole in free-space

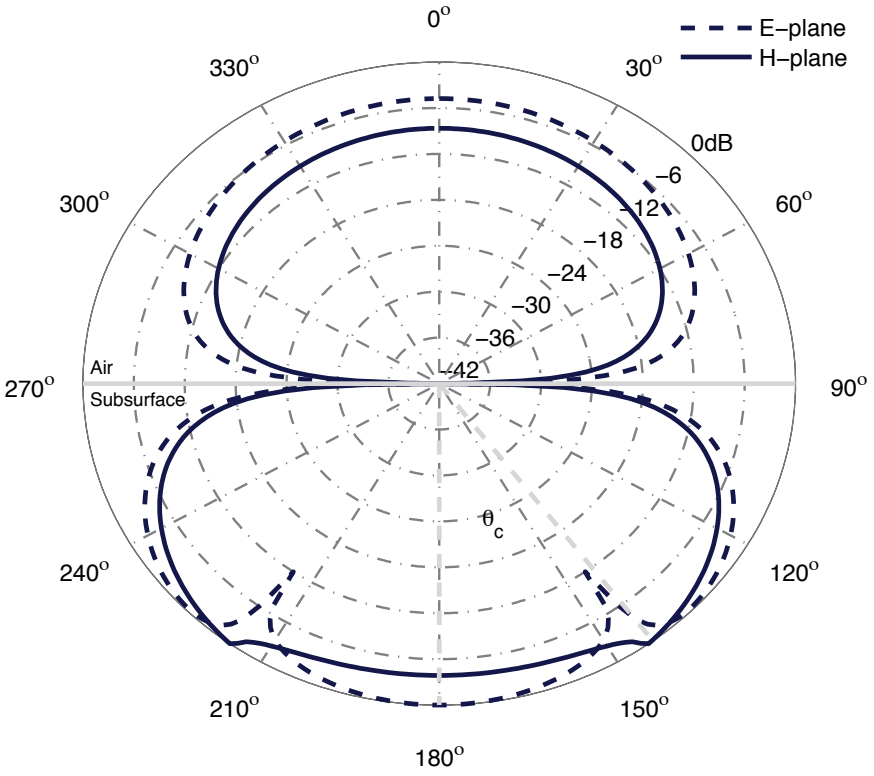

(a) $\epsilon_r = 3$, $\sigma = 0$, $\theta_c = 35°$

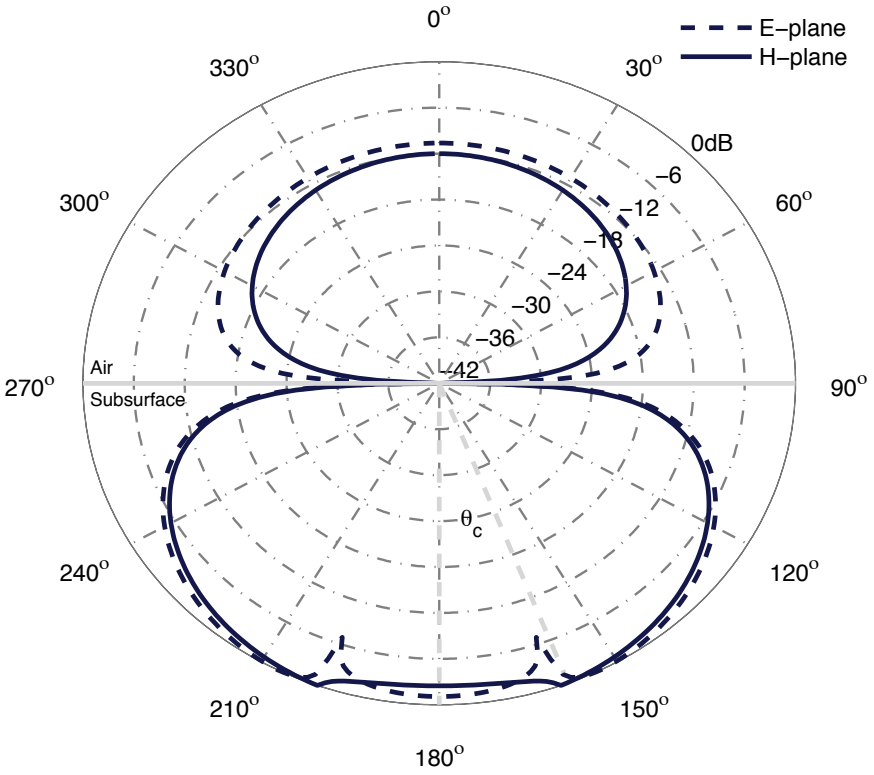

(b) $\epsilon_r = 9$, $\sigma = 0$, $\theta_c = 19°$

Figure 78: Radiation patterns of an infinitesimal dipole over lossless half-spaces

have been modelled over realistic materials. Radzevicius et al. (2003) provides a good summary of the current state of theoretical *versus* measured *versus* modelled radiation patterns of infinitesimal dipoles located over lossless and low-loss half-spaces.

The author is not aware of any currently published work that shows the radiation patterns of widely-used commercial GPR antennas in realistic environments. Such research would be extremely useful for the development of GPR antenna design and the interpretation of GPR data.

9.2.1 *Obtaining modelled antenna radiation patterns*

The antenna models optimised in Chapter 7 and validated in Chapter 8 were used as the basis to calculate the radiation patterns. For GPR, the H-plane patterns are of most interest, as it is the H-plane that is usually parallel to the survey direction. However, it is useful to visualise the E-plane as the response from a target can be influenced by out-of-plane effects.

The principal E- and H-plane patterns for each antenna model were obtained by recording the E- and H-field values at every degree on circles of radius 0.2 m, centred on the transmitter bowties of each antenna[1]. The time-domain nature of the modelling meant that one model run could provide patterns for a range of frequencies. The patterns presented were calculated at the free-space centre frequency of each antenna i. e., 1.71 GHz for the GSSI 1.5 GHz antenna model, and 978 MHz for the MALÅ 1.2 GHz antenna model. According to (9.3) a radius of 0.2 m should be in the far-field of both antennas for the frequency and constitutive parameters of the half-spaces analysed. However, measurements by Wensink et al. (1990) and simulations by Valle et al. (2001) demonstrated that far-field conditions may only start to develop at a distance of more than 30 wavelengths. Therefore, a radius of 0.2 m could be in the near-field of the antennas, but it is certainly a useful radius to analyse radiation patterns, as it is typical of the depths probed with high-frequency GPR antennas. Whether the calculated patterns are technically near-field or far-field patterns is of lesser significance than the underlying ability to study the radiation patterns of widely-used commercial GPR antennas over different half-spaces.

The E-plane patterns were calculated from the $\vec{E}_\theta$ component, which is given in Cartesian coordinates by (9.4) (Kraus, 1991).

$$\vec{E}_\theta = \vec{E}_y \frac{z}{\sqrt{y^2+z^2}} - \vec{E}_z \frac{y}{\sqrt{y^2+z^2}} \quad \text{at} \quad \phi = 90°, 270° \tag{9.4}$$

1 All the 2D patterns have been normalised to a maximum amplitude of one, and have been plotted from -42 dB to 0 dB.

Similarly, the H-plane patterns were calculated from the $\vec{E}_\phi$ component, which is the E-field component that is perpendicular to the H-plane. $\vec{E}_\phi$ is given in Cartesian coordinates by (9.5) (Kraus, 1991).

$$\vec{E}_\phi = \vec{E}_y \quad \text{at} \quad \phi = 0^\circ, 360^\circ \tag{9.5}$$

The orientation of the patterns with respect to the antenna can be visualised with reference to the spherical coordinate system shown in Figure 74.

9.2.2 *GSSI 1.5 GHz antenna radiation patterns*

Free-space

Figure 79 shows a 3D orientation of the radiation pattern of the GSSI 1.5 GHz antenna in free-space and Figure 80 presents 2D slices. A 3D radiation pattern is a powerful visualisation tool–the pattern can be easily rotated and the magnitude, detail, and spatial position of lobes and shapes readily visualised. Often what may seem like important nulls in a 2D pattern can prove to be much less significant when the pattern is viewed in 3D. Free-space radiation patterns are of little practical use for GPR, but provide a basis to compare subsequent half-space patterns. In free-space, the major lobe in the H-plane pattern is very broad, exhibits minimal directivity, and is similar to the H-plane pattern of an infinitesimal dipole in free-space. The shape of the E-plane pattern, however, is different from that of an infinitesimal dipole in free-space. It contains a broad major lobe and, due to the shielding and absorber used in the antenna, a minor back lobe.

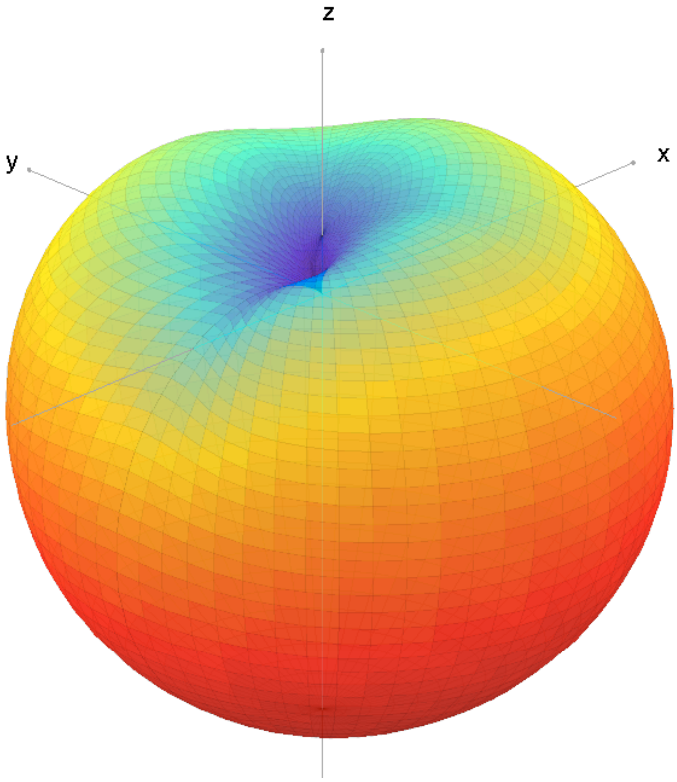

Figure 79: GSSI 1.5 GHz antenna: 3D radiation pattern in free-space

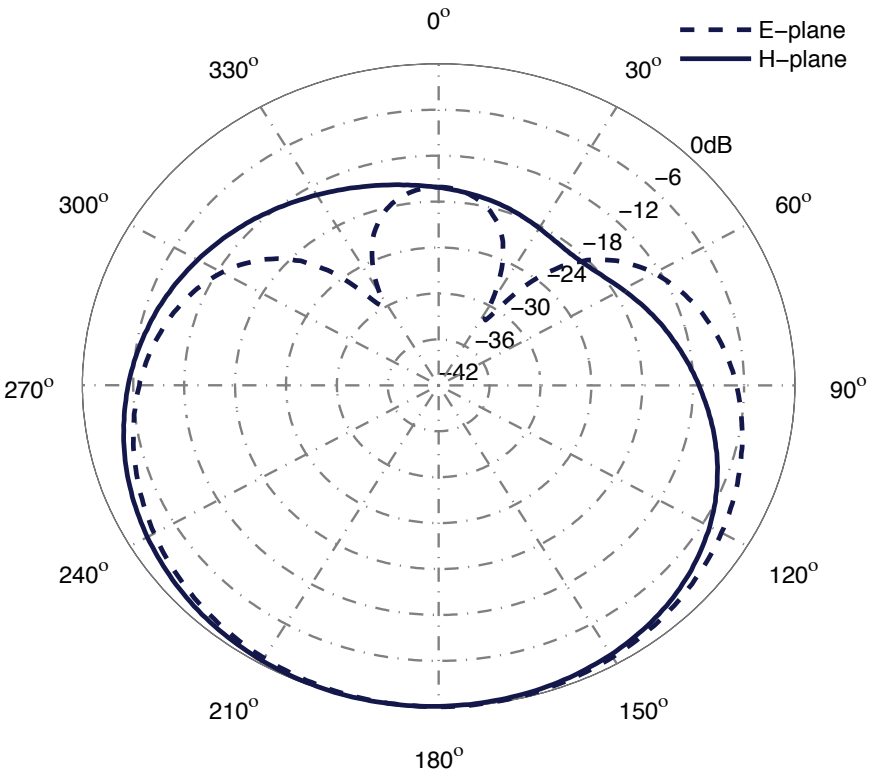

Figure 80: GSSI 1.5 GHz antenna: Radiation patterns in free-space

Lossless half-space

Figure 81a and Figure 81b present radiation patterns over lossless half-spaces of $\epsilon_r = 3$ and $\epsilon_r = 9$ respectively, and also highlight the critical angles. Presenting radiation patterns of antennas over half-spaces is most common for GPR, although half-spaces are not wholly representative of typical environments encountered with GPR. It is observed that the major lobe in the H-plane pattern is still broad, but becomes narrower and more directive as the permittivity of the half-space is increased. This is due to the reduced critical angle in the higher permittivity (lower velocity) material. The minor back lobes in both the E-plane and H-plane patterns are also reduced as the permittivity of the half-space is increased. The asymmetry in the H-plane minor back lobe is a result of the circle used to calculate the pattern being centred on the transmitter bowtie, i. e., not the centre of the antenna, and the shielding.

Figure 82a and Figure 82b present radiation patterns over the previous lossless half-spaces of $\epsilon_r = 3$ and $\epsilon_r = 9$ respectively, but with the antenna lifted from the subsurface a distance of $h = 0.1\lambda$, where λ is the wavelength in free-space. This is the optimum height for the antenna to be raised above the subsurface to achieve good directivity in the major lobe (Smith, 1984). This increase in directivity is observed for both half-spaces, along with an increase in the size of the minor back lobes. In the case of the higher permittivity half-space ($\epsilon_r = 9$) minor side lobes begin to appear from the major lobe at approximately twice the critical the angle. Figure 83 shows two orientations in 3D of the radiation pattern of Figure 82b.

Figure 84a and Figure 84b present radiation patterns again over lossless half-spaces of $\epsilon_r = 3$ and $\epsilon_r = 9$ respectively, but with the antenna now lifted from the subsurface a distance of $h = 0.2\lambda$. The trend of increased directivity in the major lobe, and increased size of the minor back lobe, is continued. A significant amount of the energy radiated from the antenna is now in the minor back lobe, and raising the antenna further would cause the minor back lobe to become the major lobe in the patterns. This confirms the optimum height of $h = 0.1\lambda$ proposed by Smith (1984).

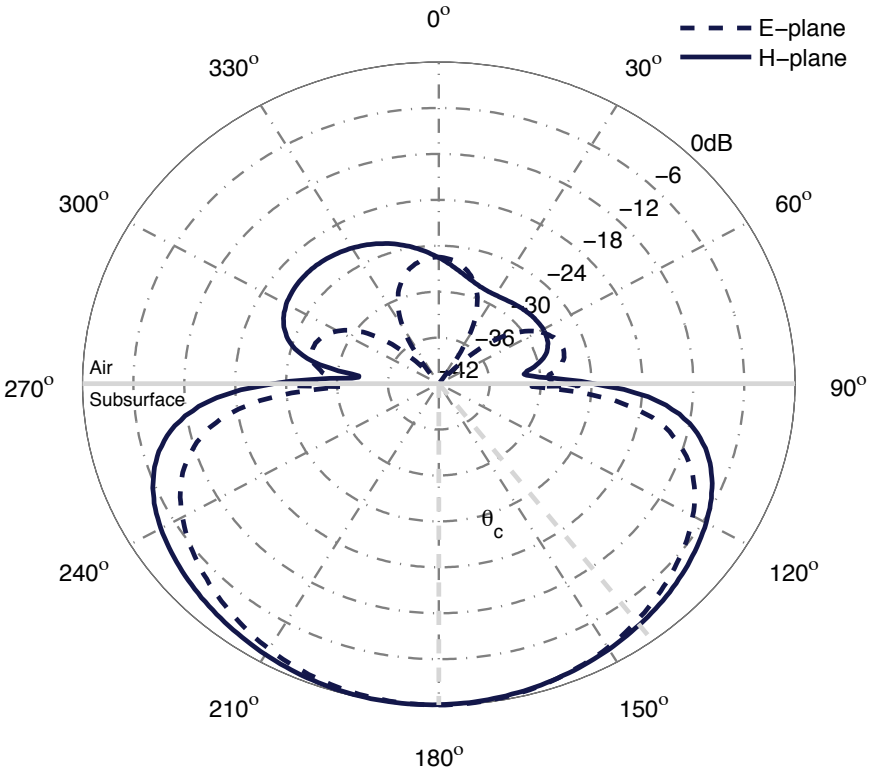

(a) $\epsilon_r = 3$, $\sigma = 0$, $\theta_c = 35°$, $h = 0$

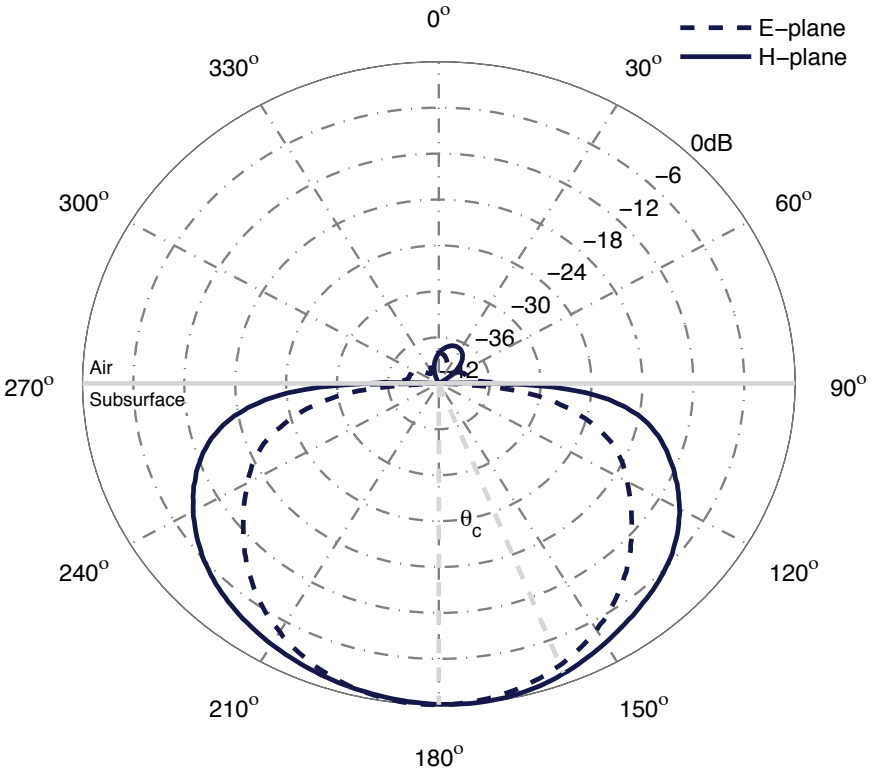

(b) $\epsilon_r = 9$, $\sigma = 0$, $\theta_c = 19°$, $h = 0$

Figure 81: GSSI 1.5 GHz antenna: Radiation patterns over lossless half-spaces

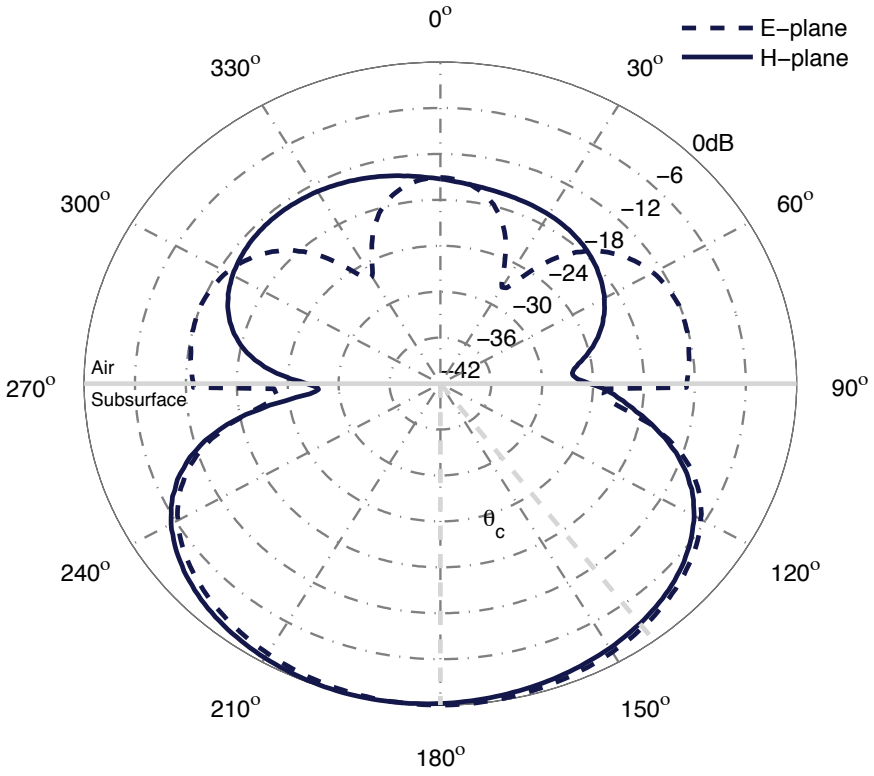

(a) $\epsilon_r = 3$, $\sigma = 0$, $\theta_c = 35°$, $h = 0.1\lambda$

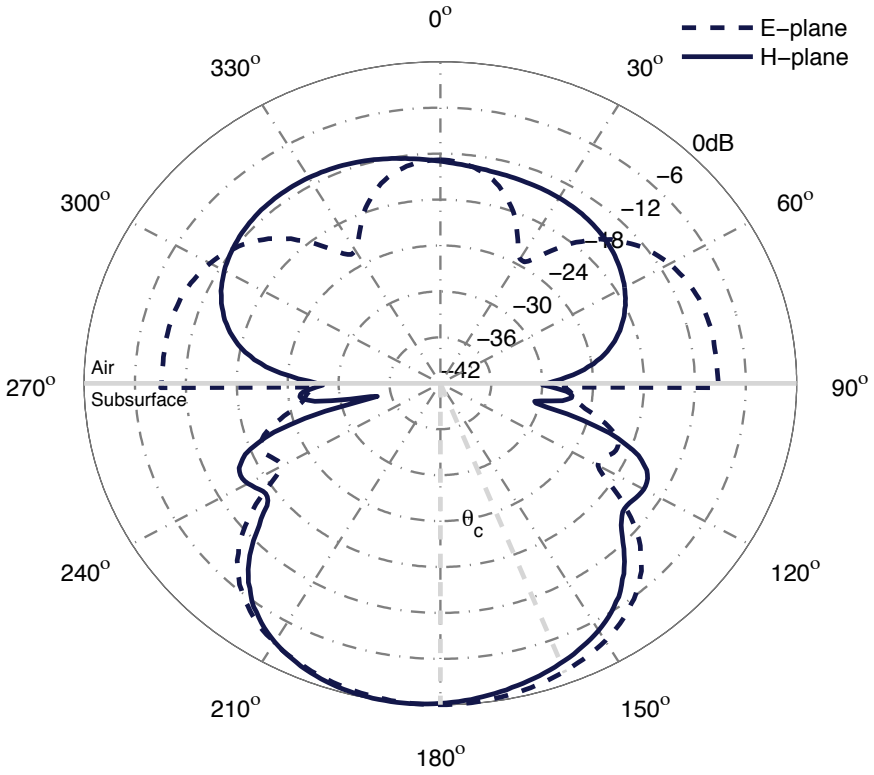

(b) $\epsilon_r = 9$, $\sigma = 0$, $\theta_c = 19°$, $h = 0.1\lambda$

Figure 82: GSSI 1.5 GHz antenna: Radiation patterns over lossless half-spaces with antenna lifted ($h = 0.1\lambda$)

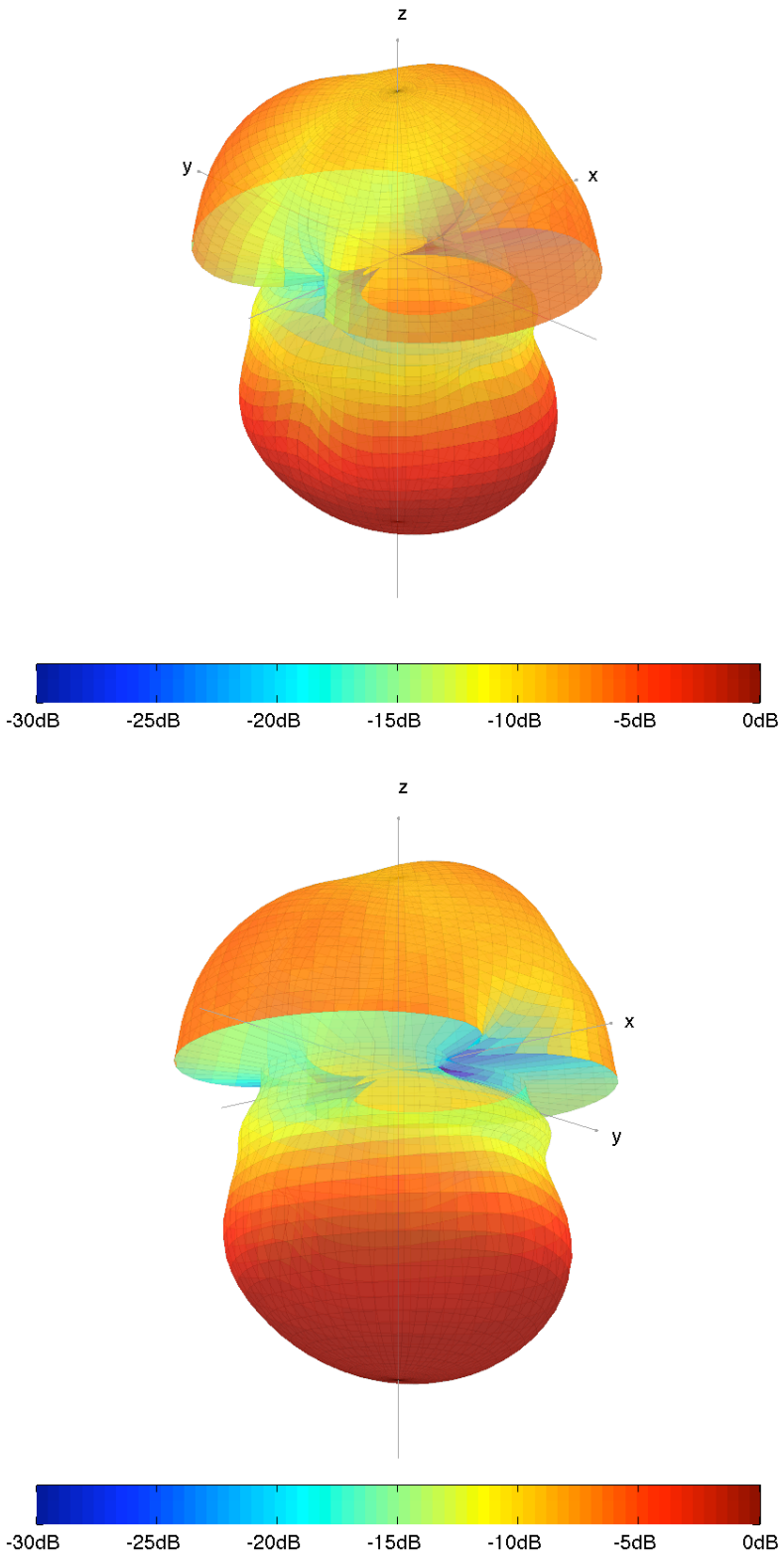

Figure 83: GSSI 1.5 GHz antenna: 3D radiation patterns over a lossless half-space ($\epsilon_r = 9$) with antenna lifted ($h = 0.1\lambda$)

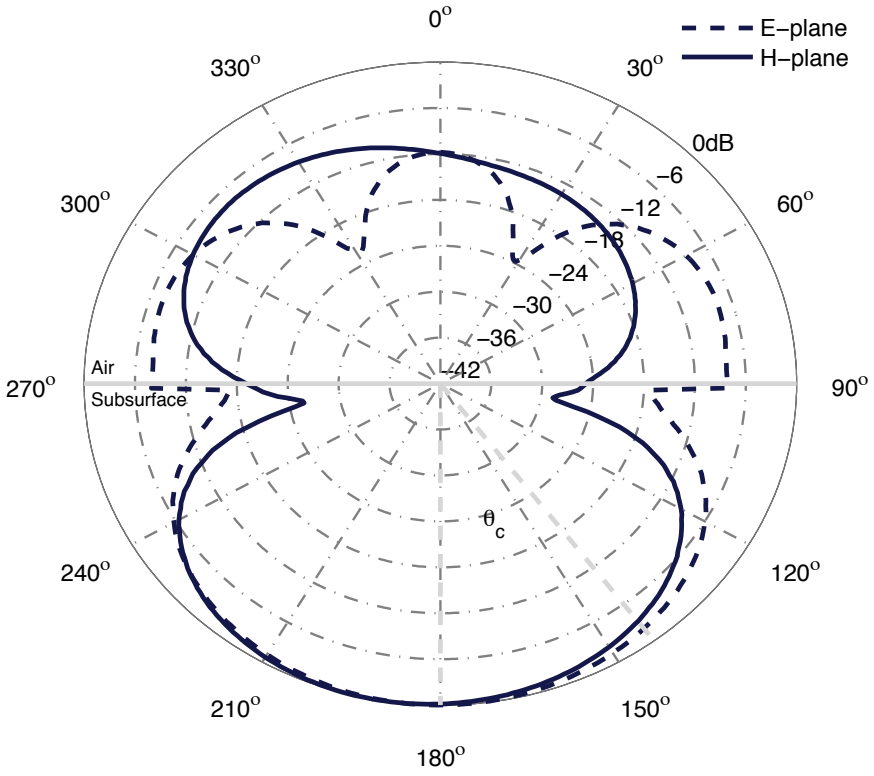

(a) $\epsilon_r = 3$, $\sigma = 0$, $\theta_c = 35°$, $h = 0.2\lambda$

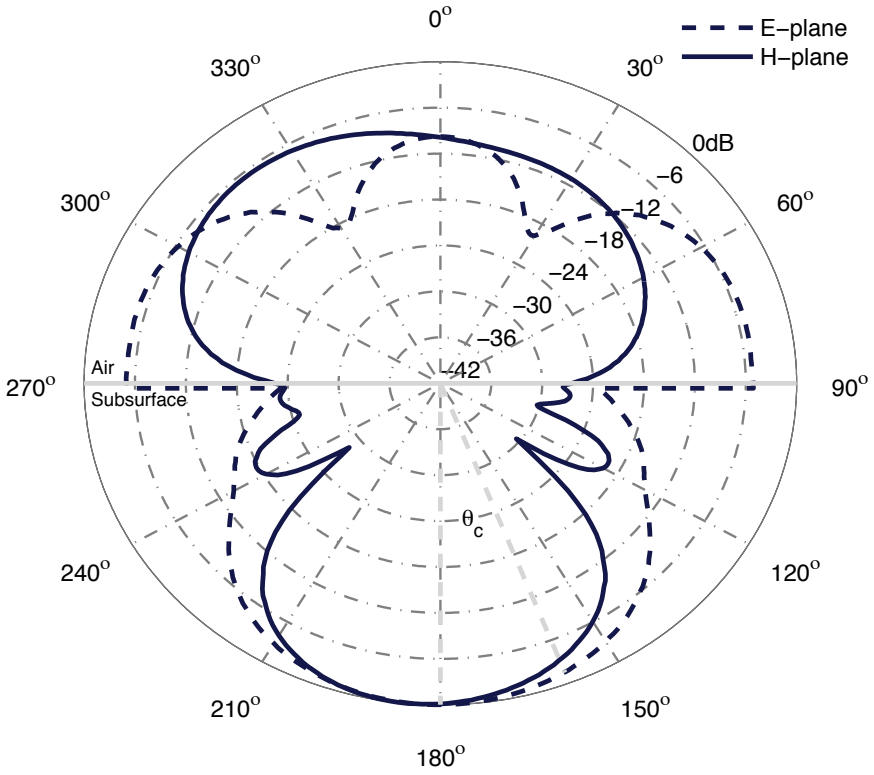

(b) $\epsilon_r = 9$, $\sigma = 0$, $\theta_c = 19°$, $h = 0.2\lambda$

Figure 84: GSSI 1.5 GHz antenna: Radiation patterns over lossless half-spaces with antenna lifted ($h = 0.2\lambda$)

Low-loss half-space

Figure 85a and Figure 85b present the radiation patterns over low-loss half-spaces of $\epsilon_r = 3$ and $\epsilon_r = 9$ respectively, with a conductivity of 100 mS/m. The primary influence of conductivity on the radiation patterns is amplitude decay due to conduction losses in the half-space. This can be clearly seen by comparison with Figure 81a and Figure 81b.

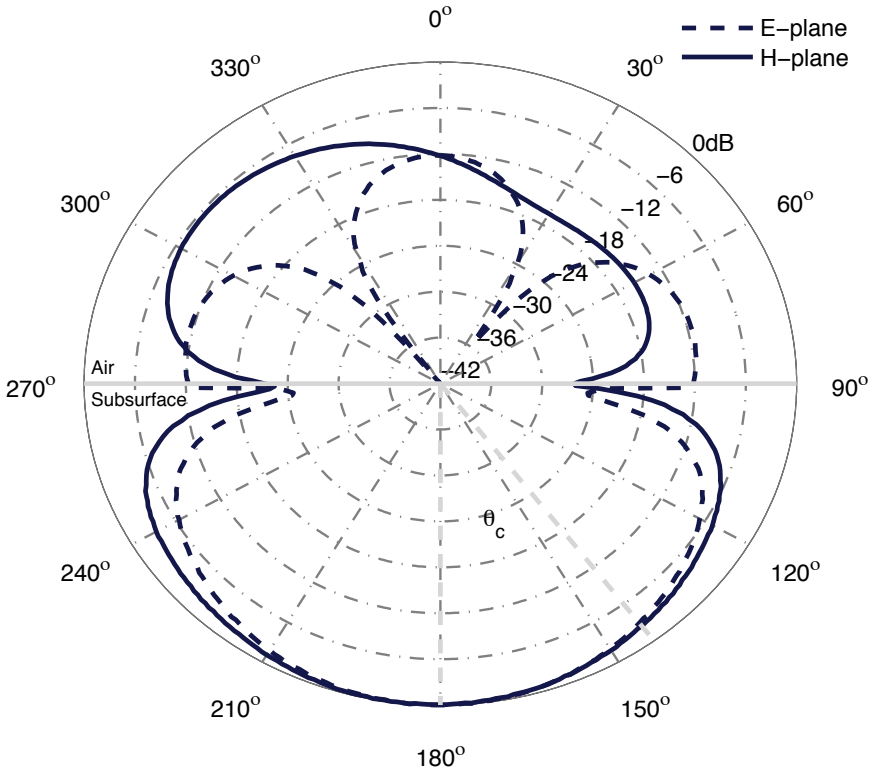

(a) $\epsilon_r = 3$, $\sigma = 100$ mS/m, $\theta_c = 35°$, $h = 0$

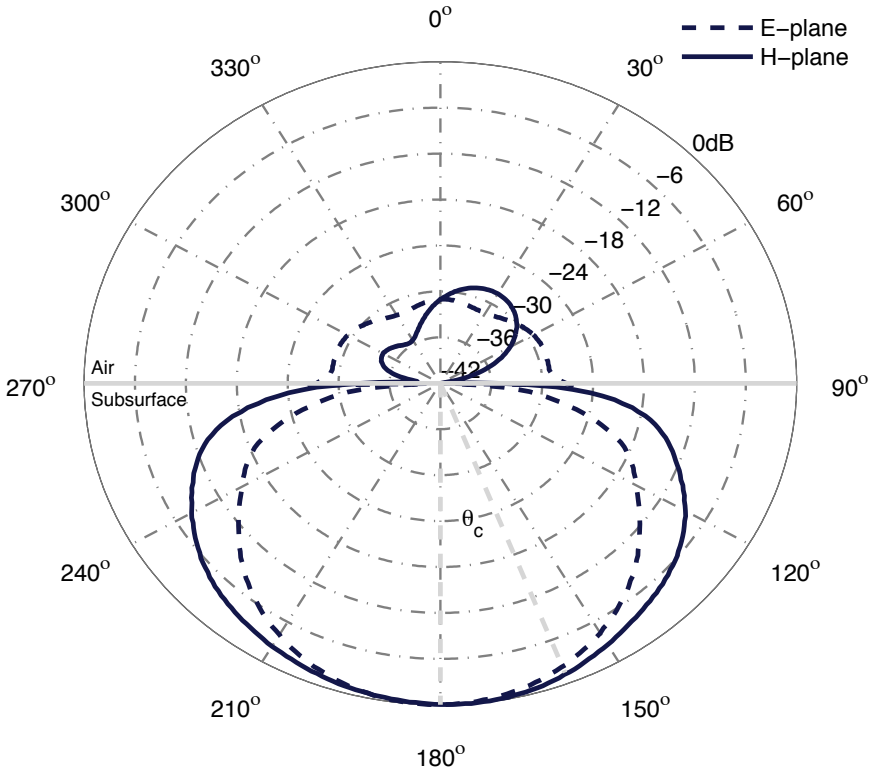

(b) $\epsilon_r = 9$, $\sigma = 100$ mS/m, $\theta_c = 19°$, $h = 0$

Figure 85: GSSI 1.5 GHz antenna: Radiation patterns over low-loss half-spaces

9.2.3 *MALÅ 1.2 GHz antenna radiation patterns*

The same set of patterns that were calculated for the GSSI 1.5 GHz antenna were repeated for the MALÅ 1.2 GHz antenna, which show very similar characteristics.

Free-space

Figure 86 shows a 3D orientation of the radiation pattern of the MALÅ 1.2 GHz antenna in free-space and Figure 87 presents 2D slices. The shapes of the free-space patterns are similar to the GSSI 1.5 GHz antenna except the minor back lobe in the E-plane pattern is much broader and larger.

Lossless half-space

Figure 88a and Figure 88b present radiation patterns over lossless half-spaces of $\epsilon_r = 3$ and $\epsilon_r = 9$ respectively, and also highlight the critical angles. Again, the shapes of the patterns exhibit the same behaviour as those for the GSSI 1.5GHz antenna, except for two notable differences: firstly, the minor back lobe in the E-plane pattern is always broader and larger than the corresponding minor back lobe for the GSSI 1.5 GHz antenna, probably due to a different shielding and absorber configuration in the MALÅ 1.2 GHz antenna; secondly, in Figure 88b side lobes are evident just below the air-subsurface interface that are not present in the corresponding pattern for the GSSI 1.5 GHz antenna.

Figure 89a and Figure 89b present radiation patterns over the previous lossless half-spaces of $\epsilon_r = 3$ and $\epsilon_r = 9$ respectively, but with the antenna lifted from the subsurface a distance of $h = 0.1\lambda$. As with the GSSI 1.5GHz antenna, there is increased directivity in the major lobe, and increased size of the minor back lobe. There are significant side lobes present in the H-plane pattern over the $\epsilon_r = 9$ half-space, creating a trilobate shape. Figure 90 shows two orientations in 3D of the radiation pattern of Figure 89b.

Figure 91a and Figure 91b present radiation patterns again over lossless half-spaces of $\epsilon_r = 3$ and $\epsilon_r = 9$ respectively, but with the antenna now lifted from the subsurface a distance of $h = 0.2\lambda$. Due to the reduced radiation into the half-space, the side lobes that were prominent in the H-plane pattern at $h = 0.1\lambda$ are now reduced, and the minor back lobes have now become major lobes.

Low-loss half-space

Figure 92a and Figure 92b show again conduction losses in the half-spaces.

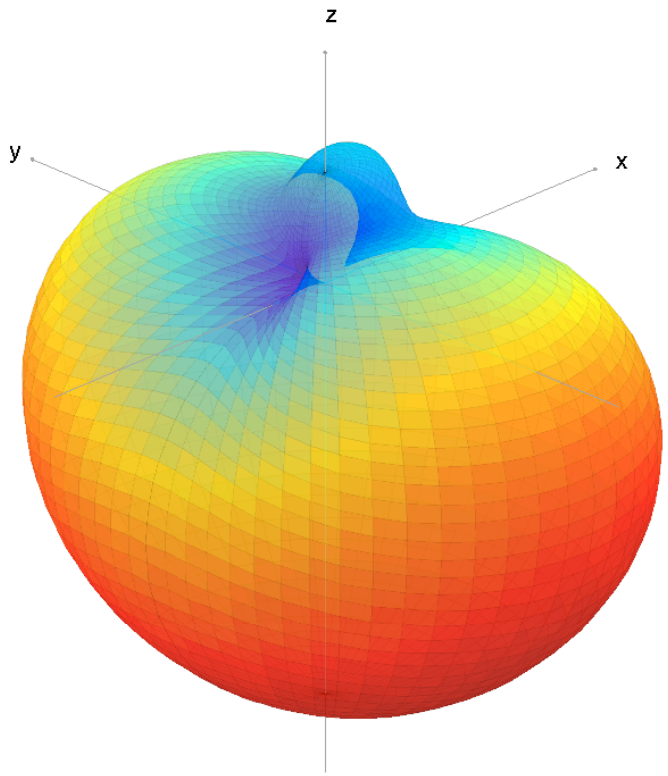

Figure 86: MALÅ 1.2 GHz antenna: 3D radiation pattern in free-space

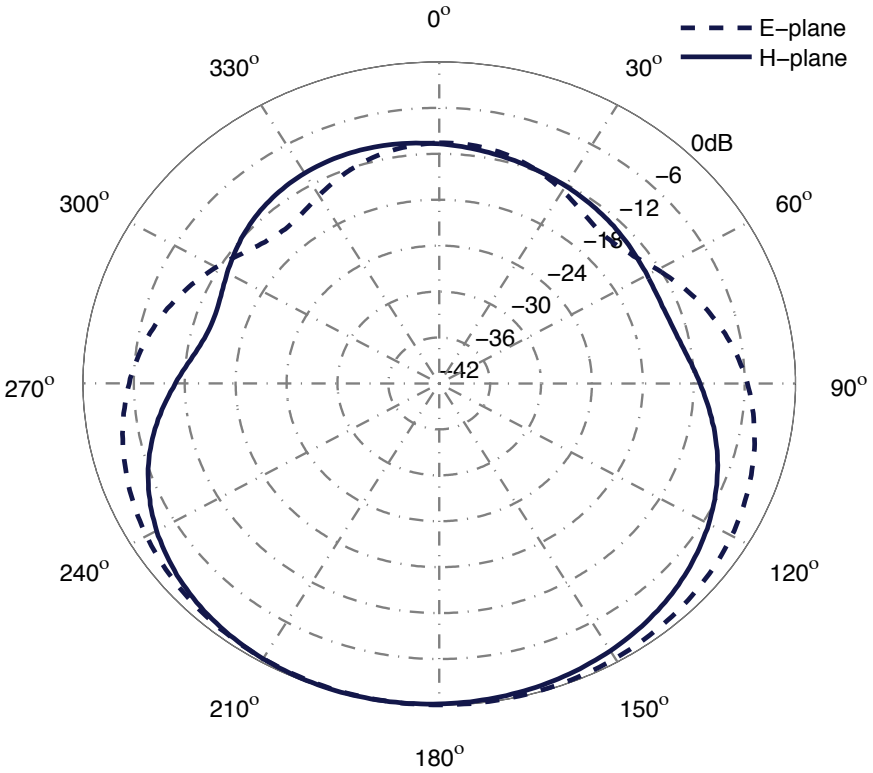

Figure 87: MALÅ 1.2 GHz antenna: Radiation patterns in free-space

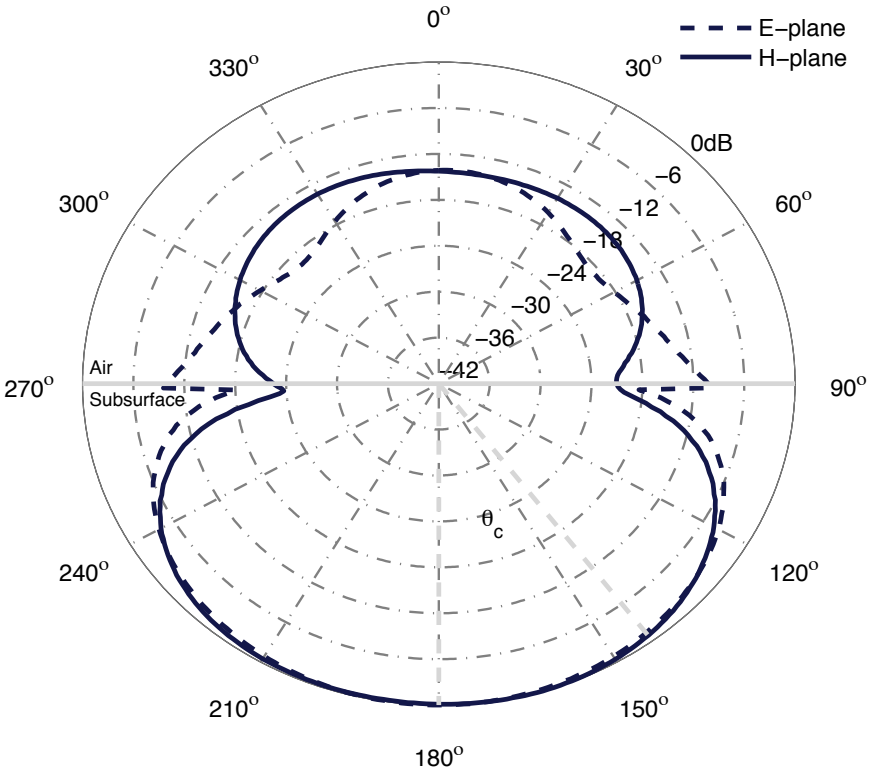

(a) $\epsilon_r = 3$, $\sigma = 0$, $\theta_c = 35°$, $h = 0$

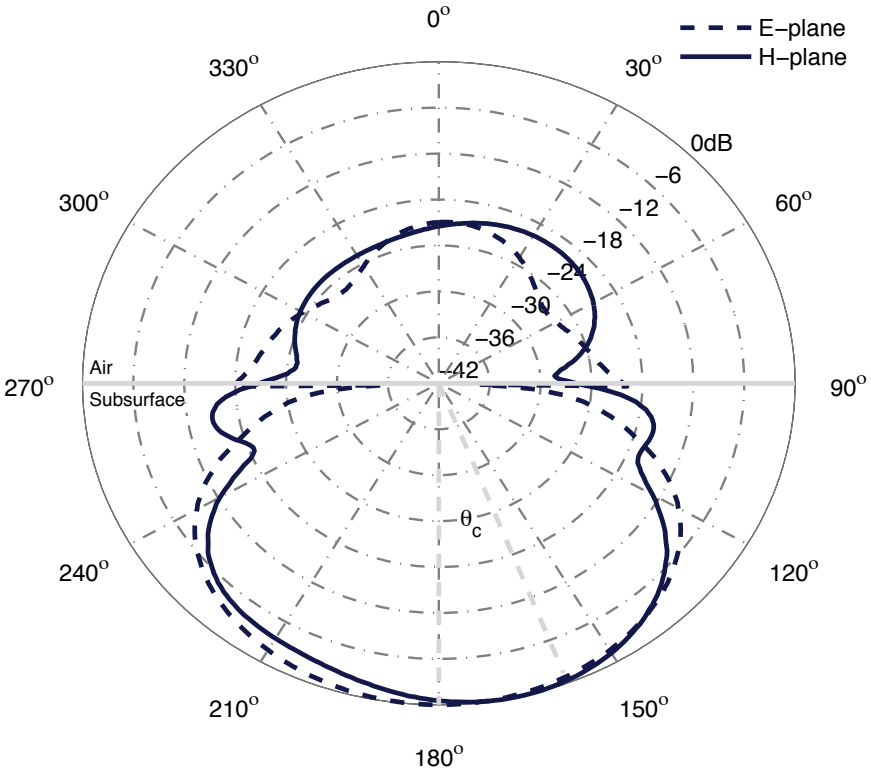

(b) $\epsilon_r = 9$, $\sigma = 0$, $\theta_c = 19°$, $h = 0$

Figure 88: MALÅ 1.2 GHz antenna: Radiation patterns over lossless half-spaces

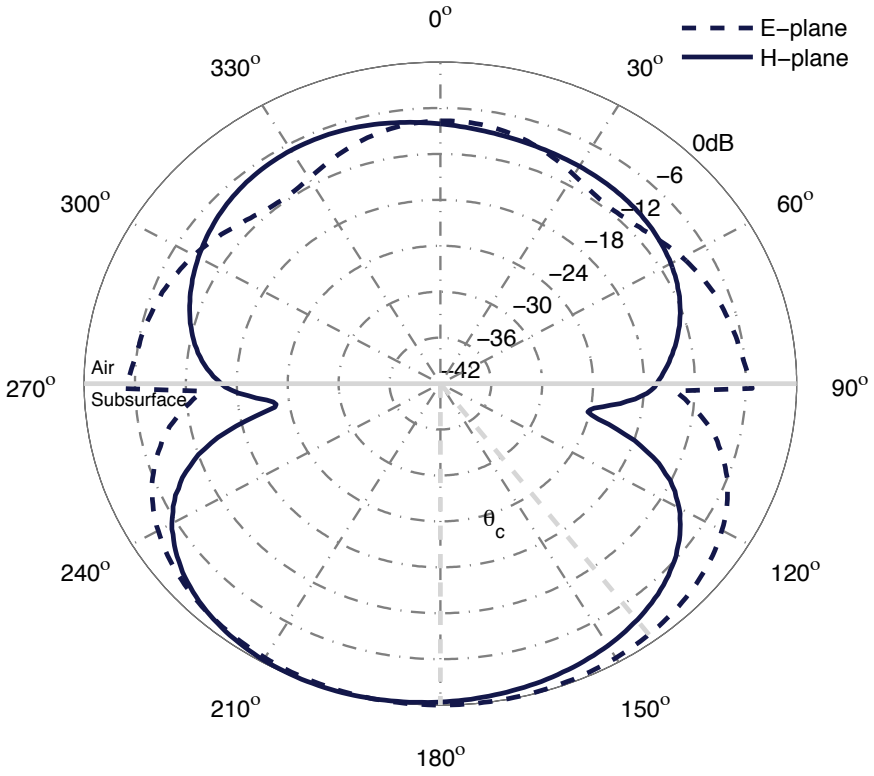

(a) $\epsilon_r = 3$, $\sigma = 0$, $\theta_c = 35°$, $h = 0.1\lambda$

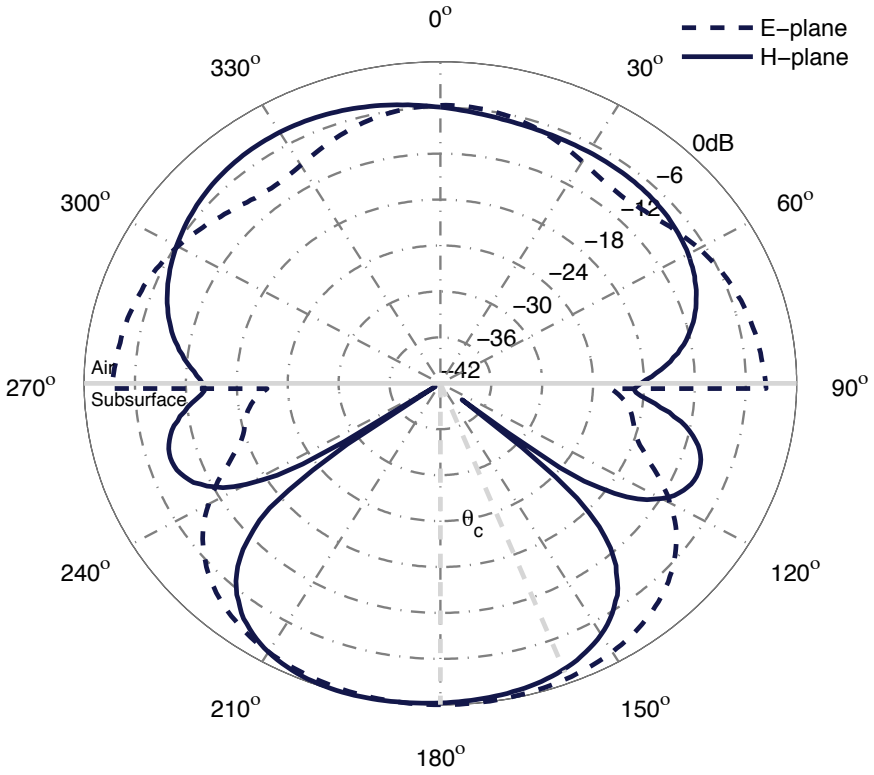

(b) $\epsilon_r = 9$, $\sigma = 0$, $\theta_c = 19°$, $h = 0.1\lambda$

Figure 89: MALÅ 1.2 GHz antenna: Radiation patterns over lossless half-spaces with antenna lifted ($h = 0.1\lambda$)

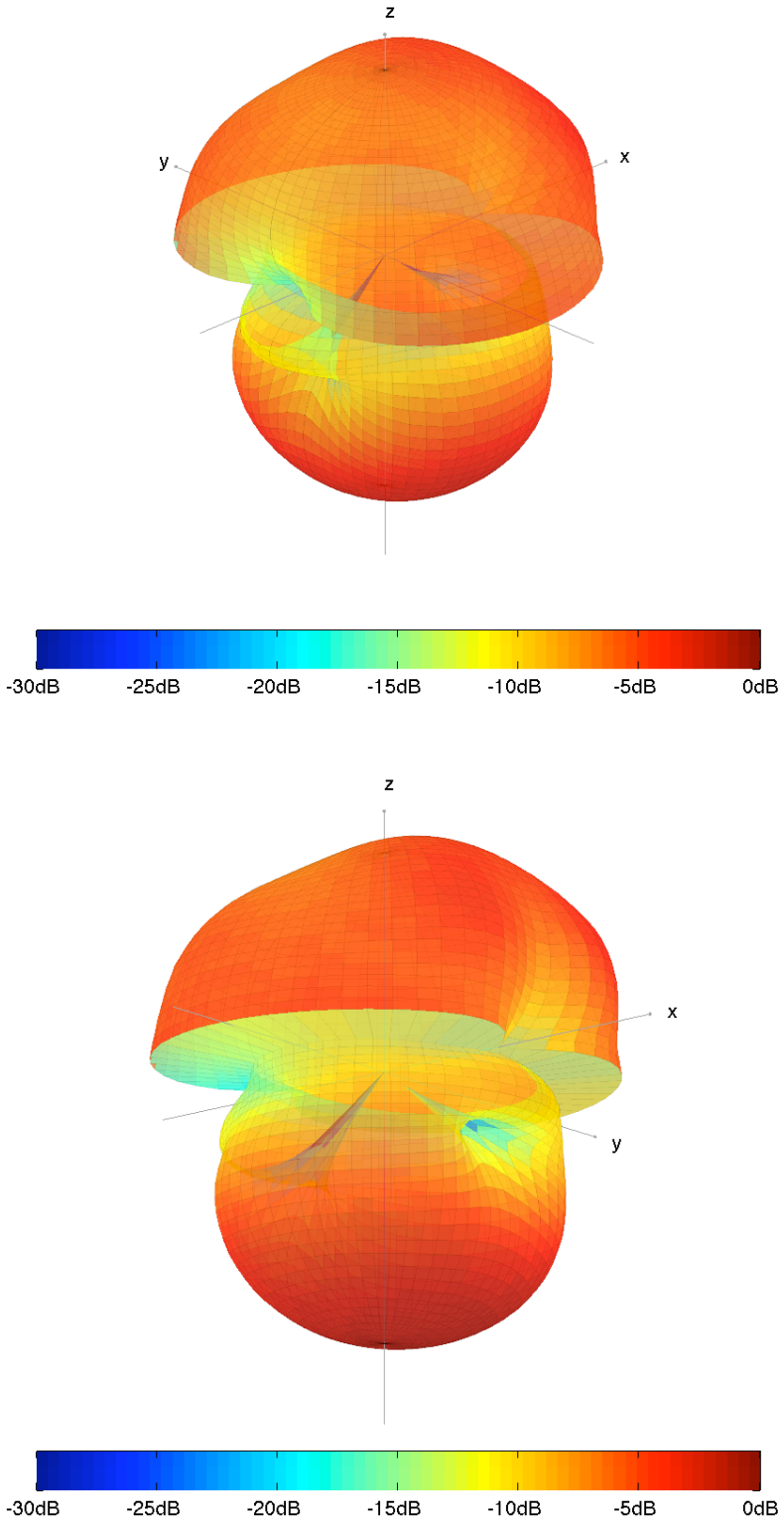

Figure 90: MALÅ 1.2 GHz antenna: 3D radiation patterns over a lossless half-space ($\epsilon_r = 9$) with antenna lifted ($h = 0.1\lambda$)

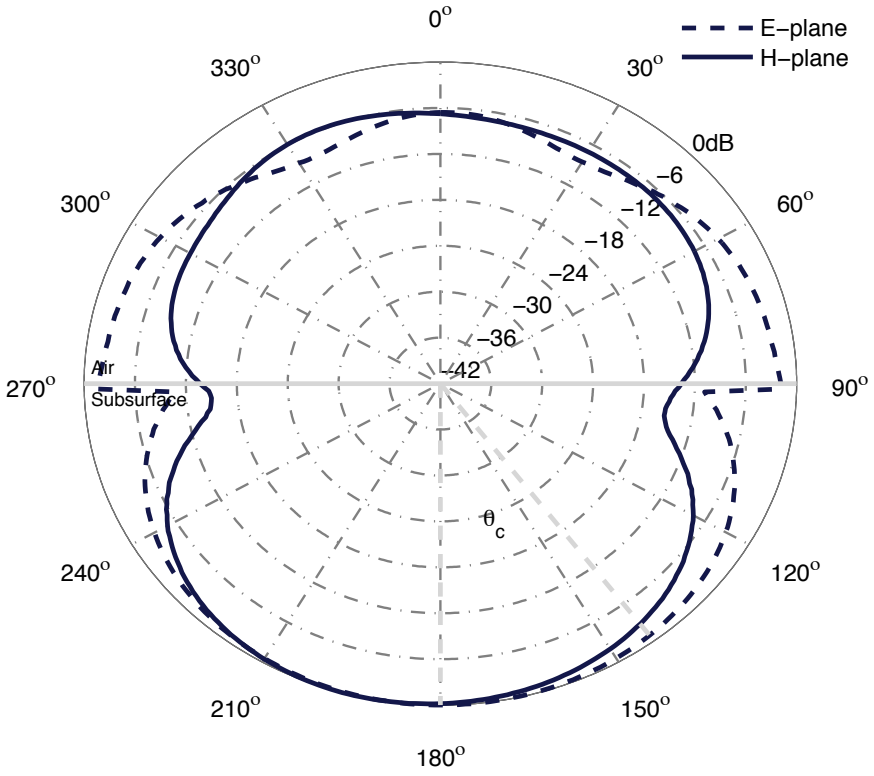

(a) $\epsilon_r = 3$, $\sigma = 0$, $\theta_c = 35°$, $h = 0.2\lambda$

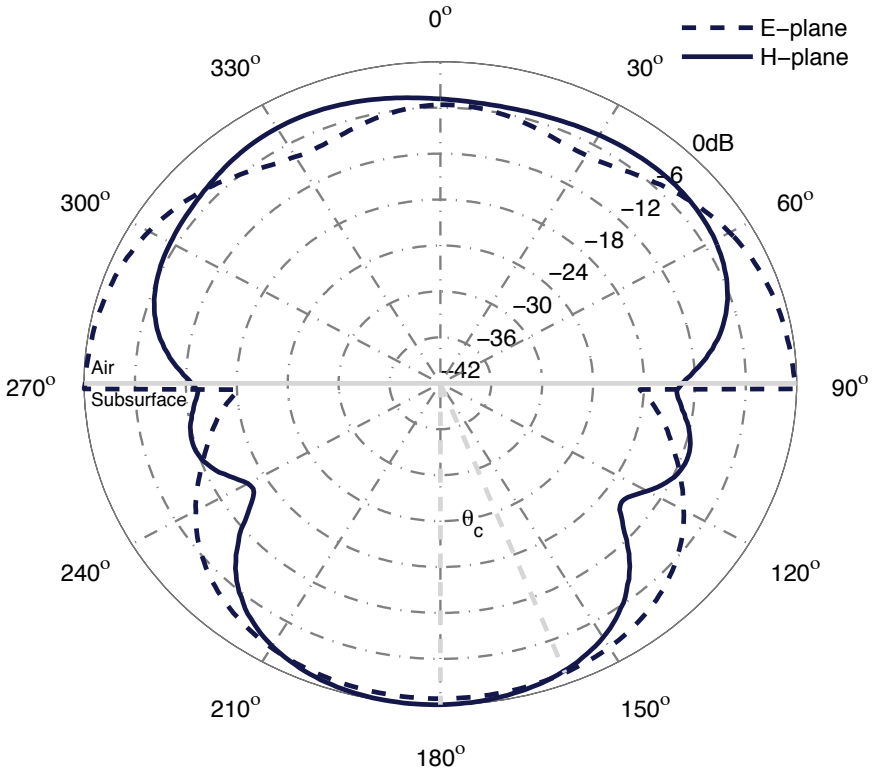

(b) $\epsilon_r = 9$, $\sigma = 0$, $\theta_c = 19°$, $h = 0.2\lambda$

Figure 91: MALÅ 1.2 GHz antenna: Radiation patterns over lossless half-spaces with antenna lifted ($h = 0.2\lambda$)

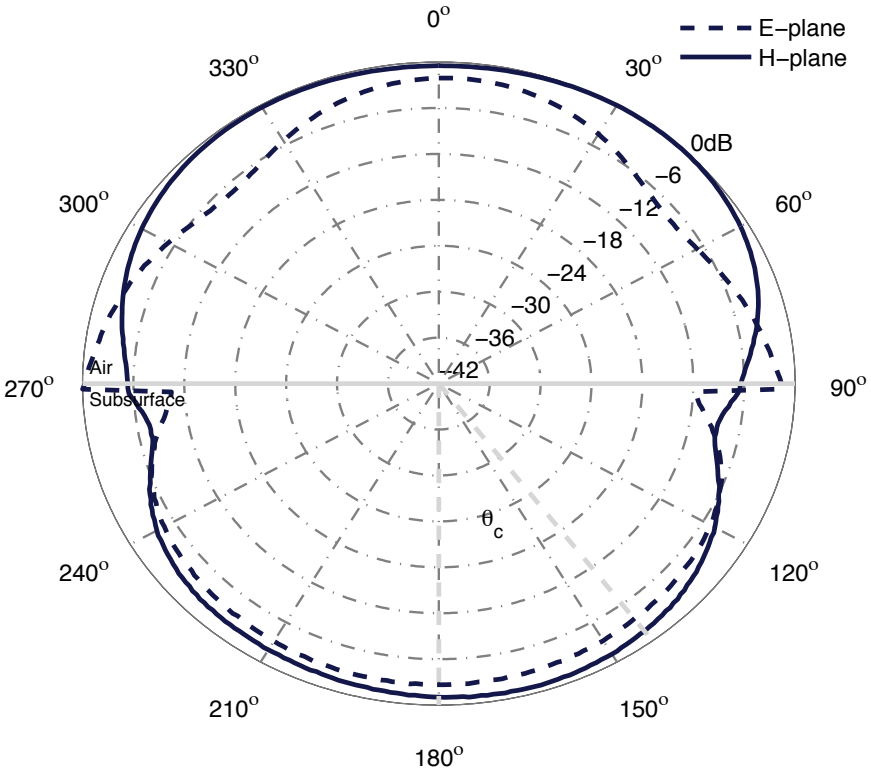

(a) $\epsilon_r = 3$, $\sigma = 100$ mS/m, $\theta_c = 35°$, $h = 0$

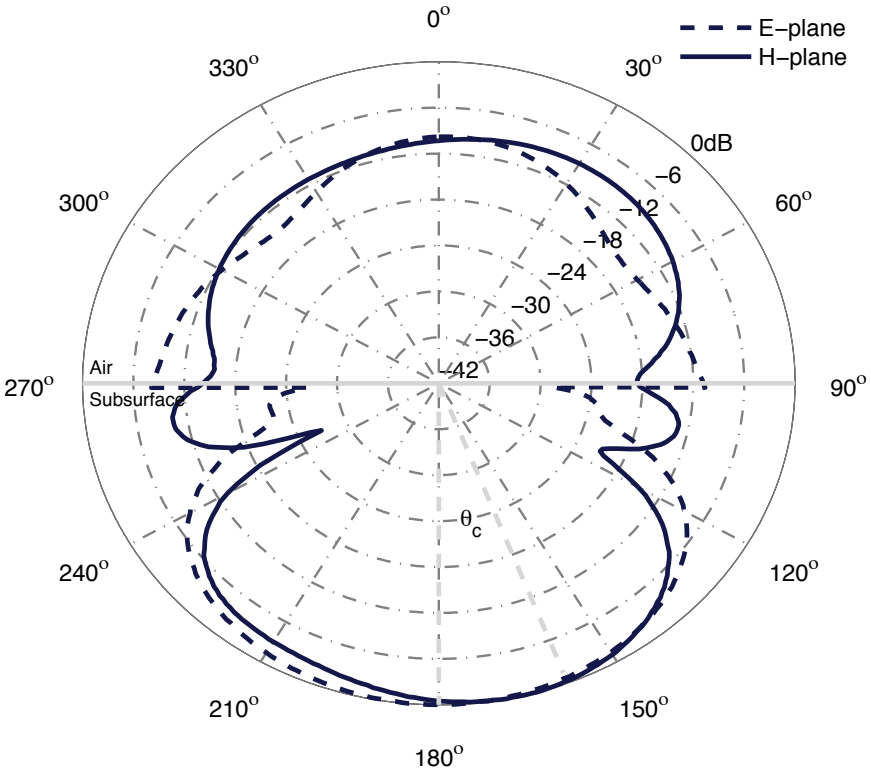

(b) $\epsilon_r = 9$, $\sigma = 100$ mS/m, $\theta_c = 19°$, $h = 0$

Figure 92: MALÅ 1.2 GHz antenna: Radiation patterns over low-loss half-spaces

9.3 SNAPSHOTS FROM THE GSSI 1.5 GHZ ANTENNA

Another method used to study the characteristics of GPR antennas is to analyse time domain snapshots of the currents on the elements of the antenna, and fields propagated by the antenna. This method is demonstrated for the GSSI 1.5 GHz antenna.

9.3.1 *Electric field*

Figure 93 and Figure 94 present snapshots of the magnitude of the electric field (9.6) from the GSSI 1.5 GHz antenna in free-space, and over a lossless half-space ($\epsilon_r = 6$).

$$|\vec{E}| = \sqrt{E_x{}^2 + E_y{}^2 + E_z{}^2} \tag{9.6}$$

The snapshots were recorded at intervals of 0.25 ns for the first 1.25 ns of the time window. Figure 3 in Chapter 2 highlighted the different components of an electromagnetic wave propagating from an antenna into the subsurface. Figure 93 and Figure 94 show the influence that the shape of the shielding, and the absorber in cavities of the antenna, has on the spherical air wave. The reduced velocity in the half-space ($\epsilon_r = 6$) has the effect of delaying the wave propagation and, in addition, making the spherical wave propagating in the ground much more directive.

9.3.2 *Current distribution on transmitter and receiver bowties*

Figure 95 presents snapshots, recorded at intervals of 0.10 ns, that show the conduction current distribution on the transmitter (left) and receiver (right) bowties of the GSSI 1.5 GHz antenna in free-space. The current was calculated by applying Ampere's Law (3.3a) to each magnetic field component, and then obtaining the magnitude by using the current equivalent form of (9.6). The current propagates from the drive-point along the arms of the transmitter towards the open ends of the bowtie, where a rapid deceleration results in radiation. It is evident that there is current present on the shielding separating the transmitter and receiver bowties at 0.55 ns and 0.66 ns, as the pulse is radiated from the transmitter bowtie.

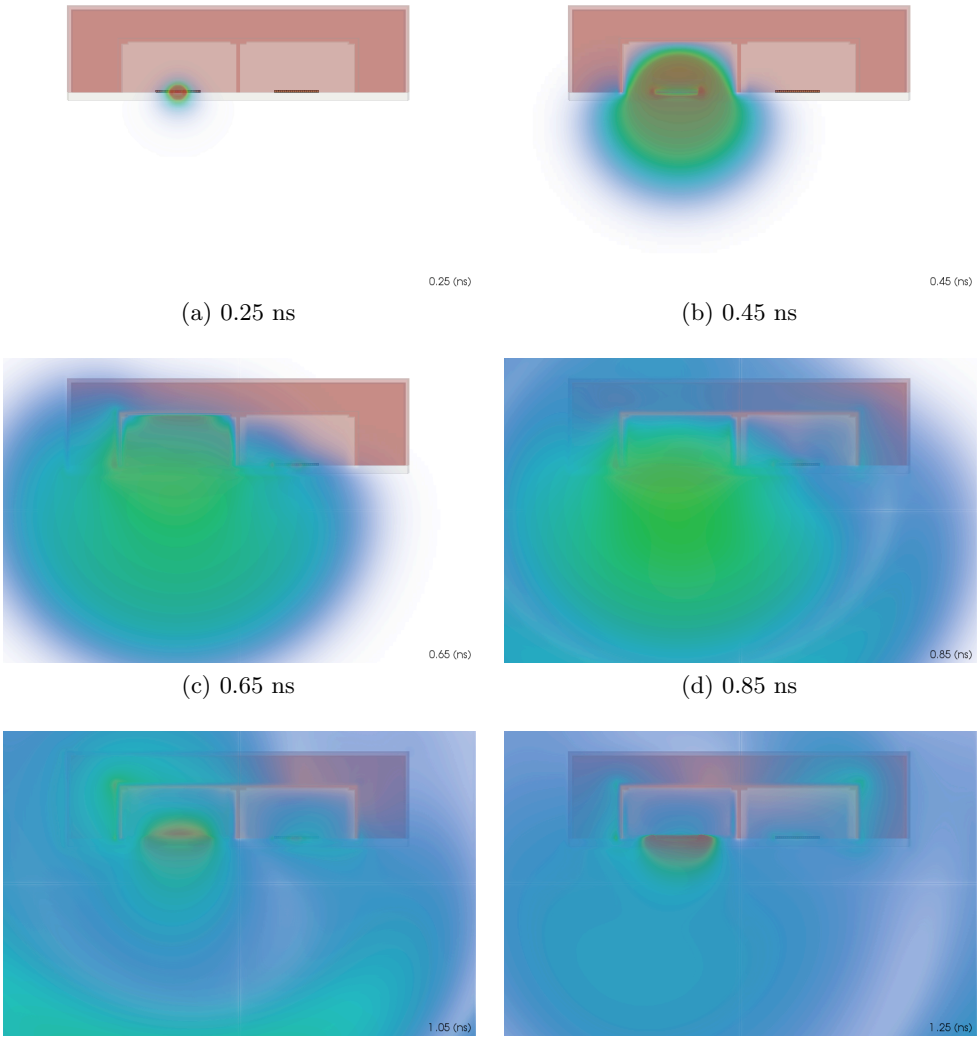

(a) 0.25 ns (b) 0.45 ns

(c) 0.65 ns (d) 0.85 ns

(e) 1.05 ns (f) 1.25 ns

Figure 93: GSSI 1.5 GHz antenna: Snapshots of electric field in free-space

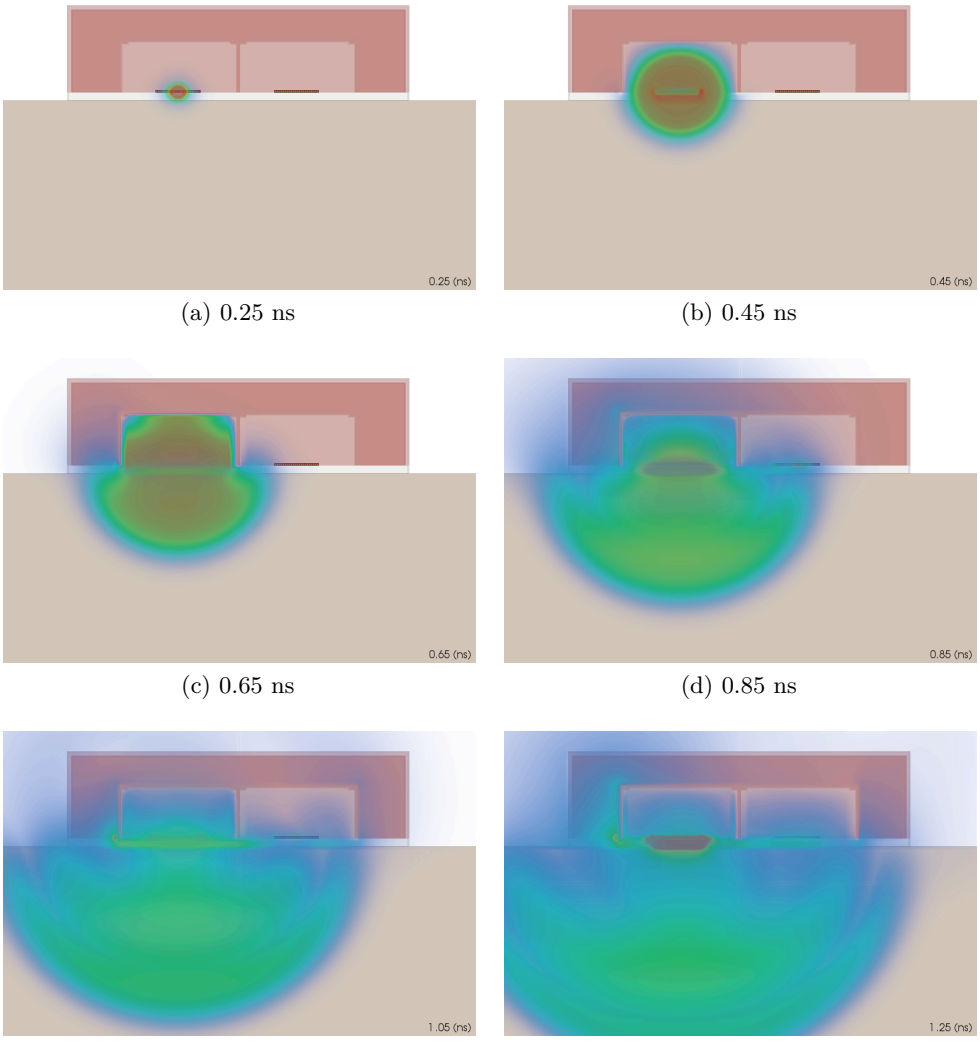

(a) 0.25 ns (b) 0.45 ns

(c) 0.65 ns (d) 0.85 ns

(e) 1.05 ns (f) 1.25 ns

Figure 94: GSSI 1.5 GHz antenna: Snapshots of electric field over lossless half-space ($\epsilon_r = 6$)

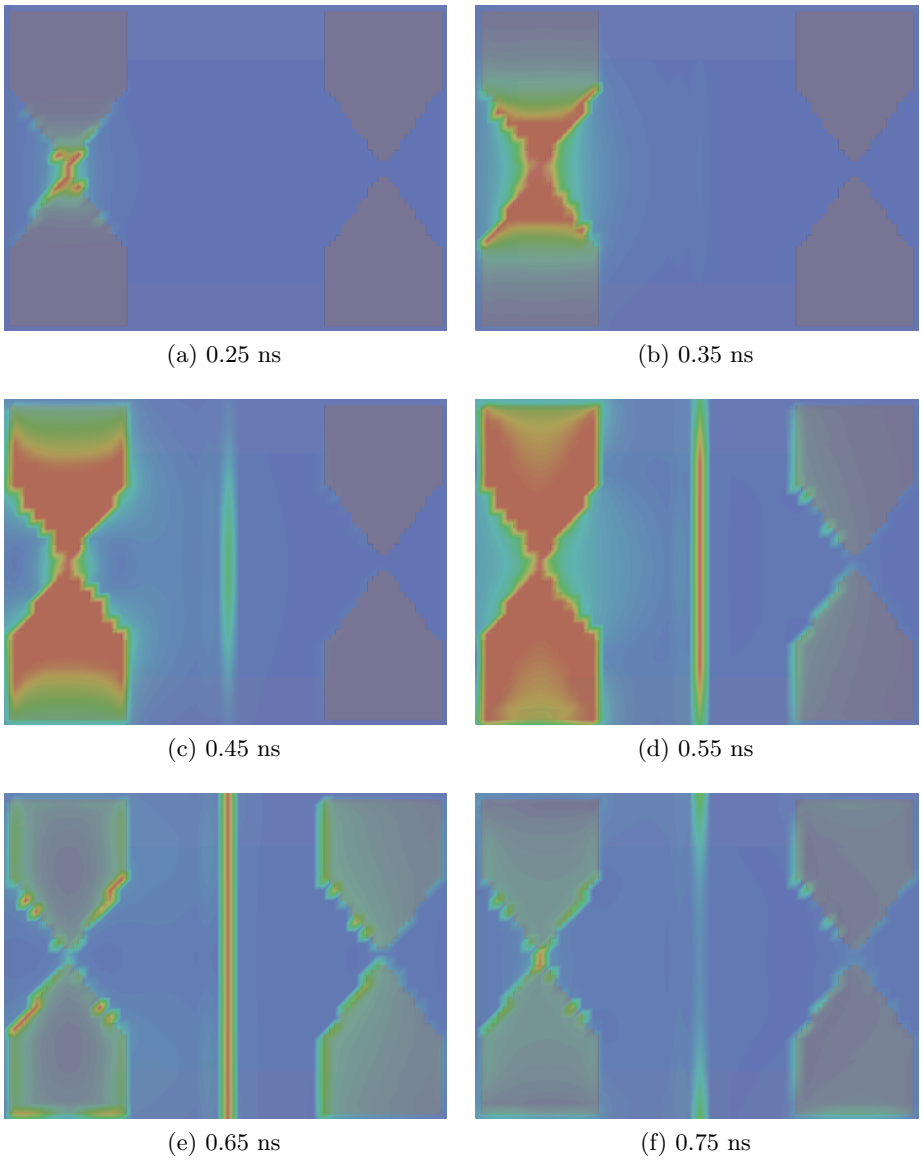

(a) 0.25 ns (b) 0.35 ns

(c) 0.45 ns (d) 0.55 ns

(e) 0.65 ns (f) 0.75 ns

Figure 95: GSSI 1.5 GHz antenna: Snapshots of current distribution on bowties in free-space *left-to-right* transmitter, receiver

9.4 SUMMARY

The aim of this chapter was to utilise the antenna models created, optimised, and comprehensively validated in previous chapters, to investigate the radiation dynamics of the antennas. This was achieved though calculating radiation patterns in free-space, and over lossless and low-loss half-spaces, as well as studying time domain snapshots of the currents and fields of the antennas.

There have been a number of studies using theoretical predictions, numerical solutions, and measured data for the radiation patterns of simple dipole antennas in free-space and over lossless and low-loss half-spaces. However, these studies demonstrated that theoretical far-field predictions could not be applied to the near-field, and that results from simplistic models do not match measured data using real antennas.

Free-space patterns are of limited use for GPR but are shown for the GSSI 1.5 GHz antenna and MALÅ 1.2 GHz antenna to provide a comparison to theoretical predictions of simple antennas. The most significant difference between the real and theoretical free-space patterns was that the E-plane patterns of the real antennas contained a much smaller back lobe due the shielding and absorbers used. Radiation patterns for both antennas over lossless ($\epsilon_r = 3$, $\epsilon_r = 9$) and low-loss ($\epsilon_r = 3$, $\epsilon_r = 9$, with $\sigma = 100$ mS/m) half-spaces were investigated. For GPR, it is the H-plane pattern that is of most interest as it is usually parallel to the survey direction. For both antennas over a lossless half-space, the H-plane pattern remained at a constant amplitude up to the critical angle. The H-plane patterns became more directive as the permittivity of the half-space was increased whilst, at the same time, the size of back lobe decreased. Over low-loss half-spaces, the primary influence of conductivity on the radiation patterns is amplitude decay due to conduction losses which resulted in a larger percentage of energy radiated into the air relative to the subsurface. By raising the antenna from the subsurface, the E- and H-plane major lobes became more directive, but the size of the minor back lobe increased. Raising the antenna beyond the optimum height of $h = 0.1\lambda$ exaggerated these characteristics.

By understanding the radiation dynamics of GPR antennas it is possible to improve survey techniques and hence target detectability, as well as influence future GPR antenna design.

10

CONCLUSIONS AND RECOMMENDATIONS FOR FURTHER RESEARCH

The aim of this chapter is to combine and consolidate the individual summaries presented at the end of each chapter into a coherent set of conclusions for the research. Following the conclusions, recommendations for further research are made.

10.1 CONCLUSIONS

The main objective of this research was to advance the state of computational modelling of GPR by creating models of widely-used commercial GPR antennas. This would enable direct comparisons of real and modelled amplitude and waveshape information from typical GPR targets, and lead to a better understanding and interpretation of real GPR data.

GPR is mainly used in the fields of engineering and geophysics, where the engineering applications typically involve the detection and identification of near-surface targets. Despite sophisticated processing algorithms, the interpretation of GPR data is still application specific and highly dependent on the skill, experience and knowledge of the individual user. This situation is a driving force for the development of accurate numerical models.

The numerical modelling of GPR has grown significantly since the early 1990s, primarily through the accessibility of more powerful computational resources. A GPR forward model can include sub-models of the antennas, the subsurface or structure, and the targets. The transmitter and receiver antennas are critical components to the overall performance of a GPR system. However, most models do not include a realistic antenna sub-model, preferring to use much simpler infinitesimal dipoles as descriptions of the sources. Very few researchers have combined a realistic antenna model with a realistic subsurface model, and where this has been done, it has been with custom-built antennas that are not widely used. Therefore, a need was identified to develop antenna models of realistic, widely-used GPR antennas so that modelled responses could be directly compared with real data.

10.1.1 *Development of computational tools*

Creating models of real GPR antennas required the development of specific software for modelling complex geometries containing fine features.

- The electromagnetic simulation software used was GprMax3D, which is based on the FDTD method and has useful features for antenna modelling, such as GPML boundaries, and user specific source excitation.
- Features were added to GprMax3D to enable the creation of Visualisation Toolkit (VTK) geometry files that could contain different levels of geometry detail from the antenna models.
- The VTK format was used to link GprMax3D to Paraview, a powerful open-source visualisation application. Complex 3D antenna geometries could then be easily visualised and manipulated.
- Scripts were developed to link the software together into a seamless workflow for developing antenna models.
- GprMax3D had been parallelised using OpenMP, and was benchmarked on compute cluster hardware. It was demonstrated that simulation times could be reduced considerably by executing GprMax3D in parallel on multiple CPU cores.

It was shown that the spatial discretisation, staircasing errors, and computational requirements of the antenna models were all closely linked.

- Decreasing the size of the spatial-step (8, 4, 2, 1, 0.5 mm) reduced the errors associated with staircasing approximations.
- However, decreasing the size of the spatial-step also meant the RAM and CPU-time requirements rapidly increased.

A diagonal split-cell local sub-model for PEC surfaces was investigated to potentially further reduce staircasing errors.

- The split-cell model showed marginal improvements in accuracy over standard staircasing for spatial-steps up to 4 mm.
- For spatial-steps larger than 4 mm, the ratio given by (5.4) (Shlager et al., 1994) was not satisfied. In these cases, the diagonal split-cell model was shown to be significantly more accurate than the standard staircasing method.

A spatial-step of 1 mm was chosen for the antenna models, which provided a good compromise between accuracy and computational requirements, and also ensured any numerical dispersion was adequately controlled.

The 3D visualisation of the complex and fine features found in GPR antennas, a key objective for modelling real antennas, has been achieved. In addition, an investigation of the effects of staircasing has shown that for spatial discretisations above 4 mm using a diagonal split-cell, local sub-model provides improved accuracy. Therefore, models using a coarser discretisation (thus reduced computational requirements) and the split-cell model, could achieve similar accuracy to finer models with standard staircasing.

10.1.2 *Development and optimisation of antenna models*

Numerical models of two widely-used, high-frequency GPR antennas—a GSSI 1.5 GHz antenna and a MALÅ 1.2 GHz antenna—were developed. A process was established utilising GprMax3D, ParaView, and MATLAB® to build and test the models. The enclosures of the real antennas were opened so that the fundamental components, geometry, and electrical characteristics could be analysed and used to create the models. The main features in the antenna models were:

- Transmitter and receiver bowties
- Electromagnetic absorber
- Bowtie loading resistors
- Shielding
- Case and skid plate
- Voltage source feed model using Gaussian shaped feed pulse at the manufacturers specified centre frequency

A number of these components had unknown values due to a combination of commercial sensitivity, and a lack of specialist test equipment. These parameters were identified as:

- The centre frequency, f, and shape of the source pulse
- The resistance at the transmitter drive-point, R_{T_x}
- The resistance at the receiver, R_{R_x}

- The permittivity of the electromagnetic absorber, ϵ_r
- The conductivity of the electromagnetic absorber, σ

To establish the accuracy of the models, their crosstalk responses were visually compared to measured crosstalk responses from the real antennas. A sensitivity study of the unknown parameters in the models was carried out to assess the effects of each parameter on the crosstalk responses of the models. The sensitivity study highlighted the permittivity and conductivity of the electromagnetic absorber as two of the most important parameters for controlling the shape (in terms of amplitude and phase) of the crosstalk response of the models.

Significant improvements were made to the antenna models through the optimisation of values of the unknown parameters.

- Taguchi's method (based on OAs) was identified as a global optimisation technique with a good convergence rate that could be used to effectively reduce the number of experiments (models) required to optimise the unknown parameters in the antenna models.
- A fully automated implementation of Taguchi's method was developed using GprMax3D, ParaView, MATLAB® and a compute cluster.
- Optimised values for the unknown parameters yielded excellent matches between the modelled and real crosstalk responses for each antenna. The GSSI antenna model achieved a 98% cross-correlation match and the MALÅ also a 98% match. Both of these results were obtained within 20 iterations of the process, which indicated the method had a good convergence rate.
- Input impedances (self-impedances) of the antenna models were calculated and shown to exhibit flat responses over the bandwidth of operation, typical of broadband antennas.

Detailed models of widely-used GPR antennas have been developed, and optimised values for unknown parameters in the models have been determined. These optimised values may not be the actual values of the real components used by the manufacturers, as there are a number of solutions to this multi-parameter problem. However, the optimised values result in antenna models that have crosstalk responses that are in excellent agreement with the real crosstalk.

10.1.3 *Experimental validation*

A comprehensive validation of the antenna models was carried out for a range of materials and target configurations typically investigated using GPR. A series of O/W emulsions were designed and made to simulate the electrical properties of real materials.

- The two constituents of the emulsions, mineral oil ($\epsilon_r = 2$) and distilled water ($\epsilon_r = 78$), were used along with three emulsions ($\epsilon_r = 10, 19, 32$) to test a range of typical GPR targets using the GSSI 1.5 GHz antenna and MALÅ 1.2 GHz antenna.
- Targets included a range of cylindrical shapes in the form of steel and composite rebars of different diameters (8, 10, 12 mm), and a rectangular metallic box.
- The design theory and the manufacture of the emulsions were successfully verified by comparing the design permittivities to actual measurements made with the GSSI 1.5 GHz antenna.

Models of the experimental configurations were created in GprMax3D utilising Paraview for geometry visualisation.

- The constitutive parameters of each liquid were shown to be critical parameters to correctly input into the models.
- The permittivities of the mineral oil and emulsions were measured, and known to be constant over the bandwidth of interest. The permittivity and conductivity of the distilled water were modelled using the Debye equation.
- It was shown that if only the permittivity of a material is correctly modelled then the time position of wavelets in the modelled response are correct, but the amplitude and some waveshape information are not.
- The real conductivity profile for the emulsions contained a term which increased with the square of the frequency. Capturing this real conductivity behaviour was shown to be very important in order to achieve accurate waveshape and amplitude information in the models.
- The conductivity profile of the emulsions was modelled using the Debye equation with modified $\epsilon'_{r\infty}$ and τ_e parameters. This provided a good match to the real profile over the frequency bandwidth of interest for GPR.

The modelled responses were compared with real data.

- By analysing A-scans of a single target configuration across all the liquids with the GSSI 1.5 GHz antenna it was shown that the modelled responses were in excellent agreement with the real data in terms of the amplitude, phase and shape of the wavelets.
- The importance of including an antenna model in the simulation was highlighted by analysing the responses from models where the antenna was replaced by an infinitesimal dipole source description. In these cases, the simple source models could no longer accurately predict the amplitude or shape of the real responses, especially for low permittivity materials and near-surface targets.
- Responses from the different sizes of steel and composite rebars were analysed and the small differences in the phase and amplitude of the real responses were replicated in the models.
- To get a more general assessment of the accuracy of the models, B-scans of a 12 mm steel rebar and a rectangular metal box were compared with the real data. Not only were the responses from the targets well predicted, but the masking of the signals from the tank base, and the reflections from the corners of the tank were also replicated in the models.

The GSSI 1.5 GHz antenna and MALÅ 1.2 GHz antenna models were shown to accurately predict not only the shape of the real responses but also, crucially, the amplitude information. This provides confidence for their use in more advanced studies. However, inputting accurate permittivity and conductivity parameters into the model was shown to be crucial to achieve realistic waveshape and amplitude information. Models such as the Debye equation with modified $\epsilon'_{r\infty}$ *and* τ_e *parameters can be successfully used to simulate certain real conductivity profiles over the frequency bandwidth of interest for GPR.*

10.1.4 *Radiation dynamics*

The antenna models were utilised to investigate radiation patterns in free-space, and over lossless and low-loss half-spaces, as well as time domain snapshots of currents and fields of the antennas. There have been a number of studies using theoretical predictions, numerical solutions, and measured data of simple dipole antennas in free-space and over lossless and low-loss half-spaces. However, these studies demonstrated that theoretical far-field predictions could not be

applied to the near-field, and that results from simplistic models do not match measured data using real antennas.

- Free-space patterns are of limited use for GPR but provide a comparison to theoretical predictions of simple antennas.
- The most significant difference between the real and theoretical free-space patterns was that the E-plane patterns of the real antennas contained a much smaller minor back lobe due to the shielding and absorbers used.
- Radiation patterns for both antennas over lossless ($\epsilon_r = 3$, $\epsilon_r = 9$) and low-loss ($\epsilon_r = 3$, $\epsilon_r = 9$, with $\sigma = 100$ mS/m) half-spaces were investigated.
- For GPR, it is the H-plane pattern that is of most interest as it is usually parallel to the survey direction.
- For both antennas over a lossless half-space the major lobes in H-plane patterns remained at a constant amplitude up to the critical angle. The major lobes in the H-plane patterns became more directive as the permittivity of the half-space was increased, whilst at the same time the size of the minor back lobes decreased.
- Over low-loss half-spaces, the primary influence of conductivity on the radiation patterns is amplitude decay in the half-space due to conduction losses. The radiation pattern lobes and directivity for low-loss half-spaces are very similar to those for lossless half-spaces. Therefore, radiation patterns in low-loss materials can be calculated using a lossless model.
- By raising the antenna from the subsurface the E- and H-plane major lobes became more directive, but the size of the minor back lobe is increased. Raising the antenna beyond the optimum height of $h = 0.1\lambda$ exaggerated these characteristics.

By understanding the radiation dynamics of GPR antennas it is possible to improve survey techniques and, hence, target detectability, as well as influence future GPR antenna design. Studying radiation patterns in 3D is crucial to attaining this understanding, allowing the visualisation of the detail and spatial position of pattern lobes and shapes.

10.2 RECOMMENDATIONS FOR FURTHER WORK

Opportunities for further research stem from the work presented in this thesis and suggestions are given in the following section. The recommendations are

divided into two parts: development of the antenna models themselves, and problems that the antenna models could be used to investigate.

10.2.1 *Development of the antenna models*

There are two important areas of potential development for the antenna models: the first is to reduce the computational requirements, and the second is to investigate further improvements to the accuracy of the models. The following list presents some research ideas to achieve these objectives.

- *Investigate the shape of the source pulse.* A Gaussian shaped pulse was assumed and used in the models, but this is not necessarily what the GPR manufacturers use. Taguchi's optimisation technique could be used to optimise the source pulse shape. This could potentially improve the accuracy of the models. In a personal communication with van der Kruk (2009) the possibility of using an inversion technique to extract the shape of the pulse was discussed.

- *Discretise the antenna models using a coarser spatial-step.* This is perhaps the most obvious first step to take to reduce computational requirements, but would need to ensure that the accuracy of models was maintained.

- *Employ a sub-gridding technique for the antenna sub-models.* An implementation of the Alternating-Direction Implicit (ADI) method using sub-grids (Diamanti, 2008) for the antenna sub-models would enable the main FDTD grid to use a courser spatial-step. This would considerably reduce RAM requirements, and CPU-time.

- *Investigate simpler equivalent models.* Use source wavelets to represent the behaviour of the real antennas. If achievable, this could considerably reduce computational resources.

10.2.2 *Applications for the antenna models*

There are a great number of areas of research in GPR that the antenna models could be utilised. A selection of interesting problems and questions is presented in the following list.

- *Could the diameter of rebars be determined from amplitude and waveshape information?* The antenna models allow accurate amplitude and waveshape information from targets to be investigated, and this could be more closely linked to the geometry of the targets.

- *How is the centre frequency of GPR antennas effected by real materials with different constitutive parameters?* The centre frequency of an antenna impacts the resolution and, hence, the detectability of targets.
- *The antenna models could provide the basis of forward models for inversion techniques.* A good forward model is an essential element in inversion methods, where geometrical and electrical information is extracted from GPR data.

A

UPDATE EQUATIONS FOR THE FDTD METHOD

Yee's algorithm is applied to the six coupled, scalar partial differential equations of Maxwell's curl equations (3.12) and (3.13). The resulting equations are known as the update equations for the 3D FDTD method.

$$
\begin{aligned}
E_x\Big|^{n+\frac{1}{2}}_{i,j+\frac{1}{2},k+\frac{1}{2}} = &\left(\frac{1-\frac{\sigma_{i,j+\frac{1}{2},k+\frac{1}{2}}\Delta t}{2\epsilon_{i,j+\frac{1}{2},k+\frac{1}{2}}}}{1+\frac{\sigma_{i,j+\frac{1}{2},k+\frac{1}{2}}\Delta t}{2\epsilon_{i,j+\frac{1}{2},k+\frac{1}{2}}}}\right) E_x\Big|^{n-\frac{1}{2}}_{i,j+\frac{1}{2},k+\frac{1}{2}} \\
&+\left(\frac{\frac{\Delta t}{\epsilon_{i,j+\frac{1}{2},k+\frac{1}{2}}}}{1+\frac{\sigma_{i,j+\frac{1}{2},k+\frac{1}{2}}\Delta t}{2\epsilon_{i,j+\frac{1}{2},k+\frac{1}{2}}}}\right)\frac{H_z\Big|^{n}_{i,j+1,k+\frac{1}{2}} - H_z\Big|^{n}_{i,j,k+\frac{1}{2}}}{\Delta y} \\
&-\left(\frac{\frac{\Delta t}{\epsilon_{i,j+\frac{1}{2},k+\frac{1}{2}}}}{1+\frac{\sigma_{i,j+\frac{1}{2},k+\frac{1}{2}}\Delta t}{2\epsilon_{i,j+\frac{1}{2},k+\frac{1}{2}}}}\right)\frac{H_y\Big|^{n}_{i,j+\frac{1}{2},k+1} - H_y\Big|^{n}_{i,j+\frac{1}{2},k}}{\Delta z} \\
&-\left(\frac{\frac{\Delta t}{\epsilon_{i,j+\frac{1}{2},k+\frac{1}{2}}}}{1+\frac{\sigma_{i,j+\frac{1}{2},k+\frac{1}{2}}\Delta t}{2\epsilon_{i,j+\frac{1}{2},k+\frac{1}{2}}}}\right) J_{Sx}\Big|^{n}_{i,j+\frac{1}{2},k+\frac{1}{2}}
\end{aligned}
\tag{A.1}
$$

$$
\begin{aligned}
E_y\Big|^{n+\frac{1}{2}}_{i-\frac{1}{2},j+1,k+\frac{1}{2}} = & \left(\frac{1 - \frac{\sigma_{i-\frac{1}{2},j+1,k+\frac{1}{2}} \Delta t}{2\epsilon_{i-\frac{1}{2},j+1,k+\frac{1}{2}}}}{1 + \frac{\sigma_{i-\frac{1}{2},j+1,k+\frac{1}{2}} \Delta t}{2\epsilon_{i-\frac{1}{2},j+1,k+\frac{1}{2}}}} \right) E_y\Big|^{n-\frac{1}{2}}_{i-\frac{1}{2},j+1,k+\frac{1}{2}} \\
& + \left(\frac{\frac{\Delta t}{\epsilon_{i-\frac{1}{2},j+1,k+\frac{1}{2}}}}{1 + \frac{\sigma_{i-\frac{1}{2},j+1,k+\frac{1}{2}} \Delta t}{2\epsilon_{i-\frac{1}{2},j+1,k+\frac{1}{2}}}} \right) \frac{H_x\Big|^{n}_{i-\frac{1}{2},j+1,k+1} - H_x\Big|^{n}_{i-\frac{1}{2},j+1,k}}{\Delta z} \\
& - \left(\frac{\frac{\Delta t}{\epsilon_{i-\frac{1}{2},j+1,k+\frac{1}{2}}}}{1 + \frac{\sigma_{i-\frac{1}{2},j+1,k+\frac{1}{2}} \Delta t}{2\epsilon_{i-\frac{1}{2},j+1,k+\frac{1}{2}}}} \right) \frac{H_z\Big|^{n}_{i,j+1,k+\frac{1}{2}} - H_z\Big|^{n}_{i-1,j+1,k+\frac{1}{2}}}{\Delta x} \\
& - \left(\frac{\frac{\Delta t}{\epsilon_{i-\frac{1}{2},j+1,k+\frac{1}{2}}}}{1 + \frac{\sigma_{i-\frac{1}{2},j+1,k+\frac{1}{2}} \Delta t}{2\epsilon_{i-\frac{1}{2},j+1,k+\frac{1}{2}}}} \right) J_{Sy}\Big|^{n}_{i-\frac{1}{2},j+1,k+\frac{1}{2}}
\end{aligned}
\tag{A.2}
$$

$$
\begin{aligned}
E_z\Big|^{n+\frac{1}{2}}_{i-\frac{1}{2},j+\frac{1}{2},k+1} = & \left(\frac{1 - \frac{\sigma_{i-\frac{1}{2},j+\frac{1}{2},k+1} \Delta t}{2\epsilon_{i-\frac{1}{2},j+\frac{1}{2},k+1}}}{1 + \frac{\sigma_{i-\frac{1}{2},j+\frac{1}{2},k+1} \Delta t}{2\epsilon_{i-\frac{1}{2},j+\frac{1}{2},k+1}}} \right) E_z\Big|^{n-\frac{1}{2}}_{i-\frac{1}{2},j+\frac{1}{2},k+1} \\
& + \left(\frac{\frac{\Delta t}{\epsilon_{i-\frac{1}{2},j+\frac{1}{2},k+1}}}{1 + \frac{\sigma_{i-\frac{1}{2},j+\frac{1}{2},k+1} \Delta t}{2\epsilon_{i-\frac{1}{2},j+\frac{1}{2},k+1}}} \right) \frac{H_y\Big|^{n}_{i,j+\frac{1}{2},k+1} - H_y\Big|^{n}_{i-1,j+\frac{1}{2},k+1}}{\Delta x} \\
& - \left(\frac{\frac{\Delta t}{\epsilon_{i-\frac{1}{2},j+\frac{1}{2},k+1}}}{1 + \frac{\sigma_{i-\frac{1}{2},j+\frac{1}{2},k+1} \Delta t}{2\epsilon_{i-\frac{1}{2},j+\frac{1}{2},k+1}}} \right) \frac{H_x\Big|^{n}_{i-\frac{1}{2},j+1,k+1} - H_x\Big|^{n}_{i-\frac{1}{2},j,k+1}}{\Delta y} \\
& - \left(\frac{\frac{\Delta t}{\epsilon_{i-\frac{1}{2},j+\frac{1}{2},k+1}}}{1 + \frac{\sigma_{i-\frac{1}{2},j+\frac{1}{2},k+1} \Delta t}{2\epsilon_{i-\frac{1}{2},j+\frac{1}{2},k+1}}} \right) J_{Sz}\Big|^{n}_{i-\frac{1}{2},j+\frac{1}{2},k+1}
\end{aligned}
\tag{A.3}
$$

$$
\begin{aligned}
H_x\Big|^{n+1}_{i-\frac{1}{2},j+1,k+1} = & \left(\frac{1 - \frac{\sigma^*_{i-\frac{1}{2},j+1,k+1}\Delta t}{2\mu_{i-\frac{1}{2},j+1,k+1}}}{1 + \frac{\sigma^*_{i-\frac{1}{2},j+1,k+1}\Delta t}{2\mu_{i-\frac{1}{2},j+1,k+1}}} \right) H_x\Big|^{n}_{i-\frac{1}{2},j+1,k+1} \\
& + \left(\frac{\frac{\Delta t}{\mu_{i-\frac{1}{2},j+1,k+1}}}{1 + \frac{\sigma^*_{i-\frac{1}{2},j+1,k+1}\Delta t}{2\mu_{i-\frac{1}{2},j+1,k+1}}} \right) \frac{E_y\Big|^{n+\frac{1}{2}}_{i-\frac{1}{2},j+1,k+\frac{3}{2}} - E_y\Big|^{n+\frac{1}{2}}_{i-\frac{1}{2},j+1,k+\frac{1}{2}}}{\Delta z} \\
& - \left(\frac{\frac{\Delta t}{\mu_{i-\frac{1}{2},j+1,k+1}}}{1 + \frac{\sigma^*_{i-\frac{1}{2},j+1,k+1}\Delta t}{2\mu_{i-\frac{1}{2},j+1,k+1}}} \right) \frac{E_z\Big|^{n+\frac{1}{2}}_{i-\frac{1}{2},j+\frac{3}{2},k+1} - E_z\Big|^{n+\frac{1}{2}}_{i-\frac{1}{2},j+\frac{1}{2},k+1}}{\Delta y} \\
& - \left(\frac{\frac{\Delta t}{\mu_{i-\frac{1}{2},j+1,k+1}}}{1 + \frac{\sigma^*_{i-\frac{1}{2},j+1,k+1}\Delta t}{2\mu_{i-\frac{1}{2},j+1,k+1}}} \right) M_{Sx}\Big|^{n+\frac{1}{2}}_{i-\frac{1}{2},j+1,k+1}
\end{aligned}
\tag{A.4}
$$

$$
\begin{aligned}
H_y\Big|^{n+1}_{i,j+\frac{1}{2},k+1} = & \left(\frac{1 - \frac{\sigma^*_{i,j+\frac{1}{2},k+1}\Delta t}{2\mu_{i,j+\frac{1}{2},k+1}}}{1 + \frac{\sigma^*_{i,j+\frac{1}{2},k+1}\Delta t}{2\mu_{i,j+\frac{1}{2},k+1}}} \right) H_y\Big|^{n}_{i,j+\frac{1}{2},k+1} \\
& + \left(\frac{\frac{\Delta t}{\mu_{i,j+\frac{1}{2},k+1}}}{1 + \frac{\sigma^*_{i,j+\frac{1}{2},k+1}\Delta t}{2\mu_{i,j+\frac{1}{2},k+1}}} \right) \frac{E_z\Big|^{n+\frac{1}{2}}_{i+\frac{1}{2},j+\frac{1}{2},k+1} - E_z\Big|^{n+\frac{1}{2}}_{i-\frac{1}{2},j+\frac{1}{2},k+1}}{\Delta x} \\
& - \left(\frac{\frac{\Delta t}{\mu_{i,j+\frac{1}{2},k+1}}}{1 + \frac{\sigma^*_{i,j+\frac{1}{2},k+1}\Delta t}{2\mu_{i,j+\frac{1}{2},k+1}}} \right) \frac{E_x\Big|^{n+\frac{1}{2}}_{i,j+\frac{1}{2},k+\frac{3}{2}} - E_x\Big|^{n+\frac{1}{2}}_{i,j+\frac{1}{2},k+\frac{1}{2}}}{\Delta z} \\
& - \left(\frac{\frac{\Delta t}{\mu_{i,j+\frac{1}{2},k+1}}}{1 + \frac{\sigma^*_{i,j+\frac{1}{2},k+1}\Delta t}{2\mu_{i,j+\frac{1}{2},k+1}}} \right) M_{Sy}\Big|^{n+\frac{1}{2}}_{i,j+\frac{1}{2},k+1}
\end{aligned}
\tag{A.5}
$$

$$
\begin{aligned}
H_z\Big|^{n+1}_{i,j+1,k+\frac{1}{2}} = &\left(\frac{1-\frac{\sigma^*_{i,j+1,k+\frac{1}{2}}\Delta t}{2\mu_{i,j+1,k+\frac{1}{2}}}}{1+\frac{\sigma^*_{i,j+1,k+\frac{1}{2}}\Delta t}{2\mu_{i,j+1,k+\frac{1}{2}}}}\right) H_z\Big|^{n}_{i,j+1,k+\frac{1}{2}} \\
&+\left(\frac{\frac{\Delta t}{\mu_{i,j+1,k+\frac{1}{2}}}}{1+\frac{\sigma^*_{i,j+1,k+\frac{1}{2}}\Delta t}{2\mu_{i,j+1,k+\frac{1}{2}}}}\right)\frac{E_x\Big|^{n+\frac{1}{2}}_{i,j+\frac{3}{2},k+\frac{1}{2}} - E_x\Big|^{n+\frac{1}{2}}_{i,j+\frac{1}{2},k+\frac{1}{2}}}{\Delta y} \\
&-\left(\frac{\frac{\Delta t}{\mu_{i,j+1,k+\frac{1}{2}}}}{1+\frac{\sigma^*_{i,j+1,k+\frac{1}{2}}\Delta t}{2\mu_{i,j+1,k+\frac{1}{2}}}}\right)\frac{E_y\Big|^{n+\frac{1}{2}}_{i+\frac{1}{2},j+1,k+\frac{1}{2}} - E_y\Big|^{n+\frac{1}{2}}_{i-\frac{1}{2},j+1,k+\frac{1}{2}}}{\Delta x} \\
&-\left(\frac{\frac{\Delta t}{\mu_{i,j+1,k+\frac{1}{2}}}}{1+\frac{\sigma^*_{i,j+1,k+\frac{1}{2}}\Delta t}{2\mu_{i,j+1,k+\frac{1}{2}}}}\right) M_{Sz}\Big|^{n+\frac{1}{2}}_{i,j+1,k+\frac{1}{2}}
\end{aligned}
\tag{A.6}
$$

B

MATLAB SCRIPTS AND GPRMAX3D INPUT FILES FOR THE ANTENNA MODELS

B.1 MATLAB SCRIPTS TO GENERATE INPUT FILES

B.1.1 *GSSI 1.5 GHz antenna model*

```
function ins_G1500_ant(fid,dx_dy_dz,ant_orig)
% Insert GprMax3D input file description of GSSI 1.5GHz
    antenna
% ant_orig is x,y,z coordinates where antenna should be
    inserted
% Craig Warren, 04/06/2009

global casedims tx

% Antenna material properties
abs_Er=1.58;
abs_cond=0.428;
f=1710E6;
Tx_res=4;
Rx_res=925;

% Antenna geometry
casethick=0.002;
shieldthick=0.002;
pcbthick=0.002;
foamsurroundthick=0.003;
skidthick=0.004;
bowtie_base=0.022;
bowtie_height=0.014;
bowtie_thick=0.001;
if dx_dy_dz > 0.001
    bowtie_thick=dx_dy_dz(1);
end
patch_height=0.015;

tx=[ant_orig(1)+0.114 ant_orig(2)+0.053 ant_orig(3)+
    skidthick];     % Coordinates of transmitter
```

```
sig_rx=(1/Rx_res)*(dx_dy_dz(2)/(dx_dy_dz(1)*dx_dy_dz(3)));

% Material definitions
fprintf(fid,'\n%s\n\n','****** START GSSI 1.5GHz antenna
    model ******');
fprintf(fid,'%s\n','--- Antenna materials ---');
fprintf(fid,'%s%s\n','#medium: ','1.0 0.0 0.0 59.6E6 1.0
    0.0 copper');
fprintf(fid,'%s%s%s%s%s\n','#medium: ',sprintf('%3.1f',
    abs_Er),' 0.0 0.0 ',sprintf('%3.3f',abs_cond),' 1.0 0.0
     absorber');
fprintf(fid,'%s%s\n','#medium: ','3.0 0.0 0.0 0.0 1.0 0.0
    foam_surround');
fprintf(fid,'%s%s\n','#medium: ','3.0 0.0 0.0 0.0 1.0 0.0
    pcb');
fprintf(fid,'%s%s\n','#medium: ','2.35 0.0 0.0 0.0 1.0 0.0
     hdpe');
fprintf(fid,'%s%s\n','#medium: ','2.35 0.0 0.0 0.0 1.0 0.0
     case');
fprintf(fid,'%s%s%s\n','#medium: 3.0 0.0 0.0 ',num2str(
    sig_rx),' 1.0 0.0 res_rx');

% Antenna geometry
fprintf(fid,'\n%s\n','--- Antenna geometry ---');
% Plastic case
fprintf(fid,'%s%s%s%s%s%s%s%s%s%s%s%s%s\n','#box: ',
    num2str(ant_orig(1)),' ',num2str(ant_orig(2)),' ',
    num2str(ant_orig(3)+skidthick),' ', ...
     num2str(ant_orig(1)+casedims(1)),' ',num2str(ant_orig
        (2)+casedims(2)),' ',num2str(ant_orig(3)+skidthick+
        casedims(3)),' case');
fprintf(fid,'%s%s%s%s%s%s%s%s%s%s%s%s%s%s%s%s%s%s%s%s%s\n','#
    geometry_vtk: ',num2str(ant_orig(1)-dx_dy_dz(1)),' ',
    num2str(ant_orig(2)-dx_dy_dz(2)),' ', ...
     num2str(ant_orig(3)-dx_dy_dz(3)),' ',num2str(ant_orig
        (1)+casedims(1)+dx_dy_dz(1)),' ', num2str(ant_orig
        (2)+casedims(2)+dx_dy_dz(2)),' ', ...
     num2str(ant_orig(3)+skidthick+casedims(3)+dx_dy_dz(3))
        ,' ',num2str(dx_dy_dz(1)),' ',num2str(dx_dy_dz(2)),
        ' ',num2str(dx_dy_dz(3)),' G1500_ant n');
fprintf(fid,'%s%s%s%s%s%s%s%s%s%s%s%s\n','#box: ',
    num2str(ant_orig(1)+casethick),' ',num2str(ant_orig(2)+
    casethick),' ',num2str(ant_orig(3)+skidthick), ...
```

```
    ' ',num2str(ant_orig(1)+casedims(1)-casethick),' ',
       num2str(ant_orig(2)+casedims(2)-casethick),' ',
       num2str(ant_orig(3)+skidthick+casedims(3)-casethick
       ), ...
    ' free_space');

% Copper coated PCB enclosure and absorbers
fprintf(fid,'%s%s%s%s%s%s%s%s%s%s%s%s%s\n','#box: ',
   num2str(ant_orig(1)+0.025),' ',num2str(ant_orig(2)+
   casethick),' ',num2str(ant_orig(3)+skidthick), ...
    ' ',num2str(ant_orig(1)+casedims(1)-0.025),' ',num2str
       (ant_orig(2)+casedims(2)-casethick),' ',num2str(
       ant_orig(3)+skidthick+0.027),' pec');
fprintf(fid,'%s%s%s%s%s%s%s%s%s%s%s%s%s\n','#box: ',
   num2str(ant_orig(1)+0.025+shieldthick),' ',num2str(
   ant_orig(2)+casethick+shieldthick),' ', ...
    num2str(ant_orig(3)+skidthick),' ',num2str(ant_orig(1)
       +0.025+shieldthick+0.057),' ',num2str(ant_orig(2)+
       casedims(2)-casethick-shieldthick),' ', ...
    num2str(ant_orig(3)+skidthick+0.027-shieldthick-0.001)
       ,' foam_surround');  % Modelling foam around edge
       of absorber as similar material to pcb
fprintf(fid,'%s%s%s%s%s%s%s%s%s%s%s%s%s\n','#box: ',
   num2str(ant_orig(1)+0.025+shieldthick+foamsurroundthick
   ),' ', ...
    num2str(ant_orig(2)+casethick+shieldthick+
       foamsurroundthick),' ',num2str(ant_orig(3)+
       skidthick),' ',num2str(ant_orig(1)+0.025+
       shieldthick+0.057-foamsurroundthick), ...
    ' ',num2str(ant_orig(2)+casedims(2)-casethick-
       shieldthick-foamsurroundthick),' ',num2str(ant_orig
       (3)+skidthick+0.027-shieldthick),' absorber');
fprintf(fid,'%s%s%s%s%s%s%s%s%s%s%s%s%s\n','#box: ',
   num2str(ant_orig(1)+0.086),' ',num2str(ant_orig(2)+
   casethick+shieldthick),' ', ...
    num2str(ant_orig(3)+skidthick),' ',num2str(ant_orig(1)
       +0.086+0.057),' ',num2str(ant_orig(2)+casedims(2)-
       casethick-shieldthick),' ', ...
    num2str(ant_orig(3)+skidthick+0.027-shieldthick-0.001)
       ,' foam_surround');  % Modelling foam around edge
       of absorber as similar material to pcb
fprintf(fid,'%s%s%s%s%s%s%s%s%s%s%s%s%s\n','#box: ',
   num2str(ant_orig(1)+0.086+foamsurroundthick),' ',
   num2str(ant_orig(2)+casethick+shieldthick+
   foamsurroundthick),' ', ...
```

```
    num2str(ant_orig(3)+skidthick),' ',num2str(ant_orig(1)
        +0.086+0.057-foamsurroundthick),' ',num2str(
        ant_orig(2)+casedims(2)-casethick-shieldthick-
        foamsurroundthick), ...
    ' ',num2str(ant_orig(3)+skidthick+0.027-shieldthick),'
         absorber');

% PCB
fprintf(fid,'%s%s%s%s%s%s%s%s%s%s%s%s\n','#box: ',
   num2str(ant_orig(1)+0.025+shieldthick+foamsurroundthick
   ),' ', ...
    num2str(ant_orig(2)+casethick+shieldthick+
        foamsurroundthick),' ',num2str(ant_orig(3)+
        skidthick),' ',num2str(ant_orig(1)+0.086-
        shieldthick-foamsurroundthick),' ', ...
    num2str(ant_orig(2)+casedims(2)-casethick-shieldthick-
        foamsurroundthick),' ',num2str(ant_orig(3)+
        skidthick+pcbthick),' pcb');
fprintf(fid,'%s%s%s%s%s%s%s%s%s%s%s%s\n','#box: ',
   num2str(ant_orig(1)+0.086+foamsurroundthick),' ',
   num2str(ant_orig(2)+casethick+shieldthick+
   foamsurroundthick), ...
    ' ',num2str(ant_orig(3)+skidthick),' ',num2str(
        ant_orig(1)+0.086+0.057-foamsurroundthick),' ', ...
    num2str(ant_orig(2)+casedims(2)-casethick-shieldthick-
        foamsurroundthick),' ',num2str(ant_orig(3)+
        skidthick+pcbthick),' pcb');

% PCB components
% Bowtie Rx
fprintf(fid,'%s%s%s%s%s%s%s%s%s%s%s%s\n','#box: ',
   num2str(ant_orig(1)+0.044),' ',num2str(ant_orig(2)
   +0.024),' ',num2str(ant_orig(3)+skidthick),' ', ...
    num2str(ant_orig(1)+0.044+bowtie_base),' ',num2str(
        ant_orig(2)+0.024+patch_height),' ',num2str(
        ant_orig(3)+skidthick+bowtie_thick),' copper');
fprintf(fid,'%s%s%s%s%s%s%s%s%s%s%s%s\n','#box: ',
   num2str(ant_orig(1)+0.044),' ',num2str(ant_orig(2)
   +0.068),' ', ...
    num2str(ant_orig(3)+skidthick),' ',num2str(ant_orig(1)
        +0.044+bowtie_base),' ',num2str(ant_orig(2)+0.068+
        patch_height), ...
    ' ',num2str(ant_orig(3)+skidthick+bowtie_thick),'
        copper');
```

```
fprintf(fid,'%s%s%s%s%s%s%s%s%s%s%s%s%s%s%s%s%s%s%s%s%s%s%s%s%s%s\n'
    ,'#wedge: ',num2str(tx(1)-0.059),' ',num2str(tx(2)),' '
    ,num2str(tx(3)),' ', ...
     num2str(tx(1)-0.059-bowtie_base/2),' ',num2str(tx(2)-
        bowtie_height-0.001),' ',num2str(tx(3)),' ',num2str
        (tx(1)-0.059+bowtie_base/2),' ', ...
     num2str(tx(2)-bowtie_height-0.001),' ',num2str(tx(3)),
        ' ',num2str(bowtie_thick),' copper');
fprintf(fid,'%s%s%s%s%s%s%s%s%s%s%s%s%s%s%s%s%s%s%s%s%s%s%s%s%s%s\n'
    ,'#wedge: ',num2str(tx(1)-0.059),' ',num2str(tx(2)
    +0.001),' ',num2str(tx(3)),' ', ...
     num2str(tx(1)-0.059-bowtie_base/2),' ',num2str(tx(2)+
        bowtie_height+0.002),' ',num2str(tx(3)),' ',num2str
        (tx(1)-0.059+bowtie_base/2),' ', ...
     num2str(tx(2)+bowtie_height+0.002),' ',num2str(tx(3)),
        ' ',num2str(bowtie_thick),' copper');

fprintf(fid,'%s%s%s%s%s%s%s%s%s%s%s%s%s\n','#edge: ',
    num2str(tx(1)-0.059),' ',num2str(tx(2)-0.001),' ',
    num2str(tx(3)),' ', ...
     num2str(tx(1)-0.059),' ',num2str(tx(2)),' ',num2str(tx
        (3)),' copper');
fprintf(fid,'%s%s%s%s%s%s%s%s%s%s%s%s%s\n','#edge: ',
    num2str(tx(1)-0.059),' ',num2str(tx(2)+0.001),' ',
    num2str(tx(3)),' ', ...
     num2str(tx(1)-0.059),' ',num2str(tx(2)+0.002),' ',
        num2str(tx(3)),' copper');

% Bowtie Tx
fprintf(fid,'%s%s%s%s%s%s%s%s%s%s%s%s%s\n','#box: ',
    num2str(ant_orig(1)+0.103),' ',num2str(ant_orig(2)
    +0.024),' ',num2str(ant_orig(3)+skidthick),' ', ...
     num2str(ant_orig(1)+0.103+bowtie_base),' ',num2str(
        ant_orig(2)+0.024+patch_height),' ',num2str(
        ant_orig(3)+skidthick+bowtie_thick),' copper');
fprintf(fid,'%s%s%s%s%s%s%s%s%s%s%s%s%s\n','#box: ',
    num2str(ant_orig(1)+0.103),' ',num2str(ant_orig(2)
    +0.068),' ', ...
     num2str(ant_orig(3)+skidthick),' ',num2str(ant_orig(1)
        +0.103+bowtie_base),' ',num2str(ant_orig(2)+0.068+
        patch_height), ...
     ' ',num2str(ant_orig(3)+skidthick+bowtie_thick),'
        copper');
```

```
fprintf(fid,'%s%s%s%s%s%s%s%s%s%s%s%s%s%s%s%s%s%s%s%s%s%s%s\n'
    ,'#wedge: ',num2str(tx(1)),' ',num2str(tx(2)),' ',
    num2str(tx(3)),' ', ...
     num2str(tx(1)-bowtie_base/2),' ',num2str(tx(2)-
        bowtie_height-0.001),' ',num2str(tx(3)),' ',num2str
        (tx(1)+bowtie_base/2),' ', ...
     num2str(tx(2)-bowtie_height-0.001),' ',num2str(tx(3)),
        ' ',num2str(bowtie_thick),' copper');
fprintf(fid,'%s%s%s%s%s%s%s%s%s%s%s%s%s%s%s%s%s%s%s%s%s%s%s\n'
    ,'#wedge: ',num2str(tx(1)),' ',num2str(tx(2)+0.001),' '
    ,num2str(tx(3)),' ', ...
     num2str(tx(1)-bowtie_base/2),' ',num2str(tx(2)+
        bowtie_height+0.002),' ',num2str(tx(3)),' ',num2str
        (tx(1)+bowtie_base/2),' ', ...
     num2str(tx(2)+bowtie_height+0.002),' ',num2str(tx(3)),
        ' ',num2str(bowtie_thick),' copper');

fprintf(fid,'%s%s%s%s%s%s%s%s%s%s%s%s\n','#edge: ',
    num2str(tx(1)),' ',num2str(tx(2)-0.001),' ',num2str(tx
    (3)),' ', ...
     num2str(tx(1)),' ',num2str(tx(2)),' ',num2str(tx(3)),'
         copper');
fprintf(fid,'%s%s%s%s%s%s%s%s%s%s%s%s\n','#edge: ',
    num2str(tx(1)),' ',num2str(tx(2)+0.001),' ',num2str(tx
    (3)),' ', ...
     num2str(tx(1)),' ',num2str(tx(2)+0.002),' ',num2str(tx
        (3)),' copper');

%     % Tx & Rx positioning test
% fprintf(fid,'%s%s%s%s%s%s%s%s%s%s%s%s\n','#edge: ',
    num2str(tx(1)),' ',num2str(tx(2)),' ',num2str(tx(3)),'
    ', ...
%     num2str(tx(1)),' ',num2str(tx(2)+0.001),' ',num2str(
    tx(3)),' pec');
% fprintf(fid,'%s%s%s%s%s%s%s%s%s%s%s%s%s%s%s%s%s%s%s%s%s\n
    ','#geometry_vtk: ',num2str(ant_orig(1)),' ',num2str(
    ant_orig(2)),' ', ...
%     num2str(ant_orig(3)),' ',num2str(ant_orig(1)+
    casedims(1)),' ', num2str(ant_orig(2)+casedims(2)),' ',
     ...
%     num2str(ant_orig(3)+skidthick+pcbthick),' ',num2str(
    dx_dy_dz(1)),' ',num2str(dx_dy_dz(2)),' ',num2str(
    dx_dy_dz(3)),' G1500_ant_bowtie f');

% Skid
```

```
fprintf(fid,'%s%s%s%s%s%s%s%s%s%s%s%s\n','#box: ',
    num2str(ant_orig(1)),' ',num2str(ant_orig(2)),' ',
    num2str(ant_orig(3)),' ',num2str(ant_orig(1)+casedims
    (1)),' ', ...
     num2str(ant_orig(2)+casedims(2)),' ',num2str(ant_orig
         (3)+skidthick),' hdpe');

% Excitation
fprintf(fid,'\n%s','--- Antenna excitation ---');
%     fprintf(fid,'\n%s%s%s%s%s\n','#hertzian_dipole: 1.0
    ',sprintf('%4E',f),' ricker ','Tx_hertz_',num2str(
    file_num_start));
fprintf(fid,'\n%s%s%s%s%s\n','#voltage_source: 1.0 ',
    sprintf('%4E',f),' gaussian ',sprintf('%d',Tx_res),'
    Tx_volt');
fprintf(fid,'%s%s%s%s%s%s%s%s%s%s%s%s%s\n','#edge: ',
    num2str(tx(1)-0.059),' ',num2str(tx(2)),' ',num2str(tx
    (3)),' ', ...
     num2str(tx(1)-0.059),' ',num2str(tx(2)+0.001),' ',
         num2str(tx(3)),' res_rx');

fprintf(fid,'\n%s\n\n','****** END GSSI 1.5GHz antenna
    model ******');
```

B.1.2 *MALÅ 1.2 GHz antenna model*

```
function ins_M1200_ant(fid,dx_dy_dz,ant_orig)
% Insert GprMax3D input file description of Mala 1.2GHz
    antenna
% ant_orig is x,y,z coordinates where antenna should be
    inserted
% Craig Warren, 04/06/2009

global casedims tx

% Antenna material properties
abs_Er=6.49;
abs_cond=0.252;
f=978E6;
Tx_res=1000;
res_rx_line=891;

% Antenna geometry
```

```
casethick=0.002;
cavitydims=[0.062 0.062 0.037];
cavitythick=0.001;
pcbthick=0.002;
polypropylenethick=0.003;
hdpethick=0.003;
skidthick=0.006;
bowtie_height=0.025;
bowtie_thick=0.001;

tx=[ant_orig(1)+0.063 ant_orig(2)+0.052 ant_orig(3)+
    skidthick];     % Coordinates of transmitter

% Antenna material properties - conductivity values for
    resistors
res_tx=470;     % 3 x SMD resistors per transmitter bowtie
     arm
res_tx_cell=res_tx/3;
sig_tx=((1/res_tx_cell)*(dx_dy_dz(2)/(dx_dy_dz(1)*dx_dy_dz
    (3))))/2;     % Divide by 4, as there are 4 parallel
    edges per resistor

res_tx_top_cell=res_tx/4;
sig_tx_top=((1/res_tx_top_cell)*(dx_dy_dz(2)/(dx_dy_dz(1)*
    dx_dy_dz(3))))/2;     % Divide by 4, as there are 4
    parallel edges per resistor

res_rx=150;     % 3 x SMD resistors per receiver arm
res_rx_cell=res_rx/3;
sig_rx=((1/res_rx_cell)*(dx_dy_dz(2)/(dx_dy_dz(1)*dx_dy_dz
    (3))))/2;

res_rx_top_cell=res_rx/4;
sig_rx_top=((1/res_rx_top_cell)*(dx_dy_dz(2)/(dx_dy_dz(1)*
    dx_dy_dz(3))))/2;

sig_rx_line=(1/res_rx_line)*(dx_dy_dz(2)/(dx_dy_dz(1)*
    dx_dy_dz(3)));

% Material definitions
fprintf(fid,'\n%s\n\n','****** START MALA 1.2GHz antenna
    model ******');
fprintf(fid,'%s\n','--- Antenna materials ---');
fprintf(fid,'%s%s\n','#medium: ','1.0 0.0 0.0 59.6E6 1.0
    0.0 copper');
```

```
fprintf(fid,'%s%s%s%s%s\n','#medium: ',sprintf('%3.1f',
    abs_Er),' 0.0 0.0 ',sprintf('%3.3f',abs_cond),' 1.0 0.0
     absorber');
fprintf(fid,'%s%s\n','#medium: ','3.0 0.0 0.0 0.0 1.0 0.0
    pcb');
fprintf(fid,'%s%s\n','#medium: ','2.26 0.0 0.0 0.0 1.0 0.0
     polypropylene');
fprintf(fid,'%s%s\n','#medium: ','2.35 0.0 0.0 0.0 1.0 0.0
     hdpe');
fprintf(fid,'%s%s%s\n','#medium: 3.0 0.0 0.0 ',num2str(
    sig_tx),' 1.0 0.0 res_tx');
fprintf(fid,'%s%s%s\n','#medium: 3.0 0.0 0.0 ',num2str(
    sig_tx_top),' 1.0 0.0 res_tx_top');
fprintf(fid,'%s%s%s\n','#medium: 3.0 0.0 0.0 ',num2str(
    sig_rx),' 1.0 0.0 res_rx');
fprintf(fid,'%s%s%s\n','#medium: 3.0 0.0 0.0 ',num2str(
    sig_rx_top),' 1.0 0.0 res_rx_top');
fprintf(fid,'%s%s%s\n','#medium: 1.0 0.0 0.0 ',num2str(
    sig_rx_line),' 1.0 0.0 res_rx_line');

% Antenna geometry
fprintf(fid,'\n%s\n','--- Antenna geometry ---');
% Shield - Alloy case
fprintf(fid,'%s%s%s%s%s%s%s%s%s%s%s%s%s\n','#box: ',
    num2str(ant_orig(1)),' ',num2str(ant_orig(2)),' ',
    num2str(ant_orig(3)+skidthick),' ', ...
     num2str(ant_orig(1)+casedims(1)),' ',num2str(ant_orig
        (2)+casedims(2)),' ',num2str(ant_orig(3)+casedims
        (3)+skidthick),' pec');
%      fprintf(fid,'%s%s%s%s%s%s%s%s%s%s%s%s%s%s%s%s%s%s%s%
    s%s\n','#geometry_vtk: ',num2str(ant_orig(1)-dx_dy_dz
    (1)),' ',num2str(ant_orig(2)-dx_dy_dz(2)),' ', ...
%         num2str(ant_orig(3)-dx_dy_dz(3)),' ',num2str(
    ant_orig(1)+casedims(1)+dx_dy_dz(1)),' ', num2str(
    ant_orig(2)+casedims(2)+dx_dy_dz(2)),' ', ...
%         num2str(ant_orig(3)+polypropylenethick+hdpethick
    +casedims(3)+dx_dy_dz(3)),' ',num2str(dx_dy_dz(1)),' ',
    num2str(dx_dy_dz(2)),' ',num2str(dx_dy_dz(3)),'
    antenna_',sprintf('%.2i',i),' n');
fprintf(fid,'%s%s%s%s%s%s%s%s%s%s%s%s%s\n','#box: ',
    num2str(ant_orig(1)+0.020),' ',num2str(ant_orig(2)+
    casethick),' ',num2str(ant_orig(3)+skidthick), ...
     ' ',num2str(ant_orig(1)+0.100),' ',num2str(ant_orig(2)
        +casedims(2)-casethick),' ',num2str(ant_orig(3)+
        skidthick+casethick),' free_space');
```

```
fprintf(fid,'%s%s%s%s%s%s%s%s%s%s%s%s\n','#box: ',
    num2str(ant_orig(1)+casethick+0.100),' ',num2str(
    ant_orig(2)+casethick),' ', ...
     num2str(ant_orig(3)+skidthick),' ',num2str(ant_orig(1)
        +casedims(1)-casethick),' ',num2str(ant_orig(2)+
        casedims(2)-casethick),' ', ...
     num2str(ant_orig(3)+skidthick+casethick),' free_space'
        );

% Absorber foam
fprintf(fid,'%s%s%s%s%s%s%s%s%s%s%s%s\n','#box: ',
    num2str(ant_orig(1)+0.020),' ',num2str(ant_orig(2)+
    casethick),' ',num2str(ant_orig(3)+skidthick), ...
     ' ',num2str(ant_orig(1)+0.100),' ',num2str(ant_orig(2)
        +casedims(2)-casethick),' ',num2str(ant_orig(3)+
        skidthick+casedims(3)-casethick),' absorber');
fprintf(fid,'%s%s%s%s%s%s%s%s%s%s%s%s\n','#box: ',
    num2str(ant_orig(1)+casethick+0.100),' ',num2str(
    ant_orig(2)+casethick),' ', ...
     num2str(ant_orig(3)+skidthick),' ',num2str(ant_orig(1)
        +casedims(1)-casethick),' ',num2str(ant_orig(2)+
        casedims(2)-casethick),' ', ...
     num2str(ant_orig(3)+skidthick+casedims(3)-casethick),'
         absorber');

% Shield - Cylinders
fprintf(fid,'%s%s%s%s%s%s%s%s%s%s%s\n','#cylinder: z ',
    num2str(ant_orig(3)+skidthick),' ',num2str(ant_orig(3)+
    skidthick+casedims(3)-casethick),' ', ...
     num2str(ant_orig(1)+0.055),' ',num2str(ant_orig(2)+
        casedims(2)-0.008),' ',num2str(0.008),' pec');
fprintf(fid,'%s%s%s%s%s%s%s%s%s%s%s\n','#cylinder: z ',
    num2str(ant_orig(3)+skidthick),' ',num2str(ant_orig(3)+
    skidthick+casedims(3)-casethick),' ', ...
     num2str(ant_orig(1)+0.055),' ',num2str(ant_orig(2)
        +0.008),' ',num2str(0.008),' pec');
fprintf(fid,'%s%s%s%s%s%s%s%s%s%s%s\n','#cylinder: z ',
    num2str(ant_orig(3)+skidthick),' ',num2str(ant_orig(3)+
    skidthick+casedims(3)-casethick),' ', ...
     num2str(ant_orig(1)+0.147),' ',num2str(ant_orig(2)+
        casedims(2)-0.008),' ',num2str(0.008),' pec');
fprintf(fid,'%s%s%s%s%s%s%s%s%s%s%s\n','#cylinder: z ',
    num2str(ant_orig(3)+skidthick),' ',num2str(ant_orig(3)+
    skidthick+casedims(3)-casethick),' ', ...
```

```
    num2str(ant_orig(1)+0.147),' ',num2str(ant_orig(2)
        +0.008),' ',num2str(0.008),' pec');
fprintf(fid,'%s%s%s%s%s%s%s%s%s%s%s\n','#cylinder: z ',
    num2str(ant_orig(3)+skidthick),' ',num2str(ant_orig(3)+
    skidthick+casedims(3)-casethick),' ', ...
    num2str(ant_orig(1)+0.055),' ',num2str(ant_orig(2)+
        casedims(2)-0.008),' ',num2str(0.007),' free_space'
        );
fprintf(fid,'%s%s%s%s%s%s%s%s%s%s%s\n','#cylinder: z ',
    num2str(ant_orig(3)+skidthick),' ',num2str(ant_orig(3)+
    skidthick+casedims(3)-casethick),' ', ...
    num2str(ant_orig(1)+0.055),' ',num2str(ant_orig(2)
        +0.008),' ',num2str(0.007),' free_space');
fprintf(fid,'%s%s%s%s%s%s%s%s%s%s%s\n','#cylinder: z ',
    num2str(ant_orig(3)+skidthick),' ',num2str(ant_orig(3)+
    skidthick+casedims(3)-casethick),' ', ...
    num2str(ant_orig(1)+0.147),' ',num2str(ant_orig(2)+
        casedims(2)-0.008),' ',num2str(0.007),' free_space'
        );
fprintf(fid,'%s%s%s%s%s%s%s%s%s%s%s\n','#cylinder: z ',
    num2str(ant_orig(3)+skidthick),' ',num2str(ant_orig(3)+
    skidthick+casedims(3)-casethick),' ', ...
    num2str(ant_orig(1)+0.147),' ',num2str(ant_orig(2)
        +0.008),' ',num2str(0.007),' free_space');
fprintf(fid,'%s%s%s%s%s%s%s%s%s%s%s%s\n','#box: ',
    num2str(ant_orig(1)+0.054),' ',num2str(ant_orig(2)+
    casedims(2)-0.016),' ',num2str(ant_orig(3)+skidthick),'
     ', ...
    num2str(ant_orig(1)+0.056),' ',num2str(ant_orig(2)+
        casedims(2)-0.014),' ',num2str(ant_orig(3)+
        skidthick+casedims(3)-casethick),' free_space');
fprintf(fid,'%s%s%s%s%s%s%s%s%s%s%s%s\n','#box: ',
    num2str(ant_orig(1)+0.054),' ',num2str(ant_orig(2)
    +0.014),' ',num2str(ant_orig(3)+skidthick),' ', ...
    num2str(ant_orig(1)+0.056),' ',num2str(ant_orig(2)
        +0.016),' ',num2str(ant_orig(3)+skidthick+casedims
        (3)-casethick),' free_space');
fprintf(fid,'%s%s%s%s%s%s%s%s%s%s%s%s\n','#box: ',
    num2str(ant_orig(1)+0.146),' ',num2str(ant_orig(2)+
    casedims(2)-0.016),' ',num2str(ant_orig(3)+skidthick),'
     ', ...
    num2str(ant_orig(1)+0.148),' ',num2str(ant_orig(2)+
        casedims(2)-0.014),' ',num2str(ant_orig(3)+
        skidthick+casedims(3)-casethick),' free_space');
```

```
fprintf(fid,'%s%s%s%s%s%s%s%s%s%s%s%s\n','#box: ',
    num2str(ant_orig(1)+0.146),' ',num2str(ant_orig(2)
    +0.014),' ',num2str(ant_orig(3)+skidthick),' ', ...
     num2str(ant_orig(1)+0.148),' ',num2str(ant_orig(2)
        +0.016),' ',num2str(ant_orig(3)+skidthick+casedims
        (3)-casethick),' free_space');

% PCB
fprintf(fid,'%s%s%s%s%s%s%s%s%s%s%s%s\n','#box: ',
    num2str(ant_orig(1)+0.020),' ',num2str(ant_orig(2)
    +0.018),' ',num2str(ant_orig(3)+skidthick),' ', ...
     num2str(ant_orig(1)+casedims(1)-casethick),' ',num2str
        (ant_orig(2)+casedims(2)-0.018),' ',num2str(
        ant_orig(3)+skidthick+pcbthick),' pcb');

% Shield - Tx and Rx cavities
fprintf(fid,'%s%s%s%s%s%s%s%s%s%s%s%s\n','#box: ',
    num2str(ant_orig(1)+0.032),' ',num2str(ant_orig(2)
    +0.022),' ',num2str(ant_orig(3)+skidthick),' ', ...
     num2str(ant_orig(1)+0.032+cavitydims(1)),' ',num2str(
        ant_orig(2)+0.022+cavitydims(2)),' ',num2str(
        ant_orig(3)+skidthick+cavitydims(3)),' pec');
fprintf(fid,'%s%s%s%s%s%s%s%s%s%s%s%s\n','#box: ',
    num2str(ant_orig(1)+0.032+cavitythick),' ',num2str(
    ant_orig(2)+0.022+cavitythick),' ', ...
     num2str(ant_orig(3)+skidthick),' ',num2str(ant_orig(1)
        +0.032+cavitydims(1)-cavitythick),' ',num2str(
        ant_orig(2)+0.022+cavitydims(2)-cavitythick),' ',
        ...
     num2str(ant_orig(3)+skidthick+cavitydims(3)),'
        absorber');
fprintf(fid,'%s%s%s%s%s%s%s%s%s%s%s%s\n','#box: ',
    num2str(ant_orig(1)+0.108),' ',num2str(ant_orig(2)
    +0.022),' ',num2str(ant_orig(3)+skidthick), ...
     ' ',num2str(ant_orig(1)+0.108+cavitydims(1)),' ',
        num2str(ant_orig(2)+0.022+cavitydims(2)),' ',
        num2str(ant_orig(3)+skidthick+cavitydims(3)),' pec'
        );
fprintf(fid,'%s%s%s%s%s%s%s%s%s%s%s%s\n','#box: ',
    num2str(ant_orig(1)+0.108+cavitythick),' ',num2str(
    ant_orig(2)+0.022+cavitythick),' ', ...
     num2str(ant_orig(3)+skidthick),' ',num2str(ant_orig(1)
        +0.108+cavitydims(1)-cavitythick),' ',num2str(
        ant_orig(2)+0.022+cavitydims(2)-cavitythick),' ',
        ...
```

```
    num2str(ant_orig(3)+skidthick+cavitydims(3)),'
       free_space');

% Shield - Tx and Rx cavities - joining strips
fprintf(fid,'%s%s%s%s%s%s%s%s%s%s%s%s%s\n','#box: ',
   num2str(ant_orig(1)+0.032+cavitydims(1)),' ',num2str(
   ant_orig(2)+0.022+cavitydims(2)-0.006),' ', ...
    num2str(ant_orig(3)+skidthick+cavitydims(3)-
       cavitythick),' ',num2str(ant_orig(1)+0.108),' ',
       num2str(ant_orig(2)+0.022+cavitydims(2)),' ', ...
    num2str(ant_orig(3)+skidthick++cavitydims(3)),' pec');
fprintf(fid,'%s%s%s%s%s%s%s%s%s%s%s%s%s\n','#box: ',
   num2str(ant_orig(1)+0.032+cavitydims(1)),' ',num2str(
   ant_orig(2)+0.022),' ', ...
    num2str(ant_orig(3)+skidthick+cavitydims(3)-
       cavitythick),' ',num2str(ant_orig(1)+0.108),' ',
       num2str(ant_orig(2)+0.022+0.006),' ', ...
    num2str(ant_orig(3)+skidthick++cavitydims(3)),' pec');

% Shield - Tx and Rx cavities - Vertical PCBs
%     fprintf(fid,'%s%s%s%s%s%s%s%s%s%s%s%s%s\n','#box: ',
   num2str(ant_orig(1)+0.108+0.018),' ',num2str(ant_orig
   (2)+0.022+0.029),' ', ...
%         num2str(ant_orig(3)+skidthick),' ',num2str(
   ant_orig(1)+0.108+0.018+0.024),' ',num2str(ant_orig(2)
   +0.022+0.029+pcbthick),' ', ...
%         num2str(ant_orig(3)+skidthick+cavitydims(3)),'
   pcb');
%     fprintf(fid,'%s%s%s%s%s%s%s%s%s%s%s%s%s\n','#box: ',
   num2str(ant_orig(1)+0.032+0.027),' ',num2str(ant_orig
   (2)+0.022+0.018),' ', ...
%         num2str(ant_orig(3)+skidthick),' ',num2str(
   ant_orig(1)+0.032+0.033),' ',num2str(ant_orig(2)
   +0.022+0.018+0.024),' ', ...
%         num2str(ant_orig(3)+skidthick+cavitydims(3)),'
   pec');

% PCB - replace bits chopped by Tx and Rx cavities
fprintf(fid,'%s%s%s%s%s%s%s%s%s%s%s%s%s\n','#box: ',
   num2str(ant_orig(1)+0.032+cavitythick),' ',num2str(
   ant_orig(2)+0.022+cavitythick),' ', ...
    num2str(ant_orig(3)+skidthick),' ',num2str(ant_orig(1)
       +0.032+cavitydims(1)-cavitythick),' ',num2str(
       ant_orig(2)+0.022+cavitydims(2)-cavitythick),' ',
       ...
```

```
    num2str(ant_orig(3)+skidthick+pcbthick),' pcb');
fprintf(fid,'%s%s%s%s%s%s%s%s%s%s%s%s\n','#box: ',
   num2str(ant_orig(1)+0.108+cavitythick),' ',num2str(
   ant_orig(2)+0.022+cavitythick),' ', ...
    num2str(ant_orig(3)+skidthick),' ',num2str(ant_orig(1)
       +0.108+cavitydims(1)-cavitythick),' ',num2str(
       ant_orig(2)+0.022+cavitydims(2)-cavitythick),' ',
       ...
    num2str(ant_orig(3)+skidthick+pcbthick),' pcb');

% PCB components
% Bowtie Tx - using wedge
fprintf(fid,'%s%s%s%s%s%s%s%s%s%s%s%s%s%s%s%s%s%s%s%s%s%s\n'
   ,'#wedge: ',num2str(tx(1)),' ',num2str(tx(2)-0.001),' '
   ,num2str(tx(3)),' ',num2str(tx(1)-0.026), ...
    ' ',num2str(tx(2)-bowtie_height-0.001),' ',num2str(tx
       (3)),' ',num2str(tx(1)+0.026),' ',num2str(tx(2)-
       bowtie_height-0.001),' ',num2str(tx(3)),' ', ...
    num2str(bowtie_thick),' copper');
fprintf(fid,'%s%s%s%s%s%s%s%s%s%s%s%s%s%s%s%s%s%s%s%s%s%s\n'
   ,'#wedge: ',num2str(tx(1)),' ',num2str(tx(2)+0.002),' '
   ,num2str(tx(3)),' ', ...
    num2str(tx(1)-0.026),' ',num2str(tx(2)+bowtie_height
       +0.002),' ',num2str(tx(3)),' ',num2str(tx(1)+0.026)
       ,' ', ...
    num2str(tx(2)+bowtie_height+0.002),' ',num2str(tx(3)),
       ' ',num2str(bowtie_thick),' copper');
fprintf(fid,'%s%s%s%s%s%s%s%s%s%s%s%s\n','#box: ',
   num2str(tx(1)-0.001),' ',num2str(tx(2)-0.001),' ',
   num2str(tx(3)),' ',num2str(tx(1)+0.001),' ', ...
    num2str(tx(2)),' ',num2str(tx(3)+bowtie_thick),'
       copper');
fprintf(fid,'%s%s%s%s%s%s%s%s%s%s%s%s\n','#box: ',
   num2str(tx(1)-0.001),' ',num2str(tx(2)+0.001),' ',
   num2str(tx(3)),' ',num2str(tx(1)+0.001),' ', ...
    num2str(tx(2)+0.002),' ',num2str(tx(3)+bowtie_thick),'
        copper');

% Bowtie Rx - using wedge
fprintf(fid,'%s%s%s%s%s%s%s%s%s%s%s%s%s%s%s%s%s%s%s%s%s%s\n'
   ,'#wedge: ',num2str(tx(1)+0.076),' ',num2str(tx(2)
   -0.001),' ',num2str(tx(3)),' ', ...
    num2str(tx(1)+0.076-0.026),' ',num2str(tx(2)-
       bowtie_height-0.001),' ',num2str(tx(3)),' ',num2str
       (tx(1)+0.076+0.026),' ', ...
```

```
    num2str(tx(2)-bowtie_height-0.001),' ',num2str(tx(3)),
        ' ',num2str(bowtie_thick),' copper');
fprintf(fid,'%s%s%s%s%s%s%s%s%s%s%s%s%s%s%s%s%s%s%s%s%s%s\n'
   ,'#wedge: ',num2str(tx(1)+0.076),' ',num2str(tx(2)
   +0.002),' ',num2str(tx(3)),' ', ...
    num2str(tx(1)+0.076-0.026),' ',num2str(tx(2)+
        bowtie_height+0.002),' ',num2str(tx(3)),' ',num2str
        (tx(1)+0.076+0.026),' ', ...
    num2str(tx(2)+bowtie_height+0.002),' ',num2str(tx(3)),
        ' ',num2str(bowtie_thick),' copper');
fprintf(fid,'%s%s%s%s%s%s%s%s%s%s%s%s%s\n','#box: ',
   num2str(tx(1)+0.076-0.001),' ',num2str(tx(2)-0.001),' '
   ,num2str(tx(3)),' ',num2str(tx(1)+0.077),' ', ...
    num2str(tx(2)),' ',num2str(tx(3)+bowtie_thick),'
        copper');
fprintf(fid,'%s%s%s%s%s%s%s%s%s%s%s%s%s\n','#box: ',
   num2str(tx(1)+0.076-0.001),' ',num2str(tx(2)+0.001),' '
   ,num2str(tx(3)),' ',num2str(tx(1)+0.077),' ', ...
    num2str(tx(2)+0.002),' ',num2str(tx(3)+bowtie_thick),'
         copper');

% Check tx and rx gaps
%     fprintf(fid,'%s%s%s%s%s%s%s%s%s%s%s%s%s\n','#box: ',
   num2str(tx(1)),' ',num2str(tx(2)),' ',num2str(tx(3)),'
   ',num2str(tx(1)+0.001),' ', ...
%         num2str(tx(2)+0.001),' ',num2str(tx(3)+
   bowtie_thick),' pec');
%     fprintf(fid,'%s%s%s%s%s%s%s%s%s%s%s%s%s\n','#box: ',
   num2str(tx(1)+0.076),' ',num2str(tx(2)),' ',num2str(tx
   (3)),' ',num2str(tx(1)+0.077),' ', ...
%         num2str(tx(2)+0.001),' ',num2str(tx(3)+
   bowtie_thick),' pec');

% Discrete SMD resistors - Tx
fprintf(fid,'%s%s%s%s%s%s%s%s%s%s%s%s%s\n','#edge: ',
   num2str(tx(1)-0.023),' ',num2str(tx(2)-bowtie_height
   -0.004),' ',num2str(tx(3)),' ', ...
    num2str(tx(1)-0.023),' ',num2str(tx(2)-bowtie_height
        -0.001),' ',num2str(tx(3)),' res_tx');
fprintf(fid,'%s%s%s%s%s%s%s%s%s%s%s%s%s\n','#edge: ',
   num2str(tx(1)-0.023+0.001),' ',num2str(tx(2)-
   bowtie_height-0.004),' ',num2str(tx(3)),' ', ...
    num2str(tx(1)-0.023+0.001),' ',num2str(tx(2)-
        bowtie_height-0.001),' ',num2str(tx(3)),' res_tx');
```

```
fprintf(fid,'%s%s%s%s%s%s%s%s%s%s%s%s\n','#edge: ',
    num2str(tx(1)),' ',num2str(tx(2)-bowtie_height-0.004),'
     ',num2str(tx(3)),' ',num2str(tx(1)), ...
     ' ',num2str(tx(2)-bowtie_height-0.001),' ',num2str(tx
        (3)),' res_tx');
fprintf(fid,'%s%s%s%s%s%s%s%s%s%s%s%s\n','#edge: ',
    num2str(tx(1)+0.001),' ',num2str(tx(2)-bowtie_height
    -0.004),' ',num2str(tx(3)),' ', ...
     num2str(tx(1)+0.001),' ',num2str(tx(2)-bowtie_height
        -0.001),' ',num2str(tx(3)),' res_tx');
fprintf(fid,'%s%s%s%s%s%s%s%s%s%s%s%s\n','#edge: ',
    num2str(tx(1)+0.022),' ',num2str(tx(2)-bowtie_height
    -0.004),' ',num2str(tx(3)),' ', ...
     num2str(tx(1)+0.022),' ',num2str(tx(2)-bowtie_height
        -0.001),' ',num2str(tx(3)),' res_tx');
fprintf(fid,'%s%s%s%s%s%s%s%s%s%s%s%s\n','#edge: ',
    num2str(tx(1)+0.022+0.001),' ',num2str(tx(2)-
    bowtie_height-0.004),' ',num2str(tx(3)),' ', ...
     num2str(tx(1)+0.022+0.001),' ',num2str(tx(2)-
        bowtie_height-0.001),' ',num2str(tx(3)),' res_tx');

fprintf(fid,'%s%s%s%s%s%s%s%s%s%s%s%s\n','#edge: ',
    num2str(tx(1)-0.023),' ',num2str(tx(2)+bowtie_height
    +0.002),' ',num2str(tx(3)),' ', ...
     num2str(tx(1)-0.023),' ',num2str(tx(2)+bowtie_height
        +0.006),' ',num2str(tx(3)),' res_tx_top');
fprintf(fid,'%s%s%s%s%s%s%s%s%s%s%s%s\n','#edge: ',
    num2str(tx(1)-0.023+0.001),' ',num2str(tx(2)+
    bowtie_height+0.002),' ',num2str(tx(3)),' ', ...
     num2str(tx(1)-0.023+0.001),' ',num2str(tx(2)+
        bowtie_height+0.006),' ',num2str(tx(3)),'
        res_tx_top');
fprintf(fid,'%s%s%s%s%s%s%s%s%s%s%s%s\n','#edge: ',
    num2str(tx(1)),' ',num2str(tx(2)+bowtie_height+0.002),'
     ',num2str(tx(3)),' ',num2str(tx(1)), ...
     ' ',num2str(tx(2)+bowtie_height+0.006),' ',num2str(tx
        (3)),' res_tx_top');
fprintf(fid,'%s%s%s%s%s%s%s%s%s%s%s%s\n','#edge: ',
    num2str(tx(1)+0.001),' ',num2str(tx(2)+bowtie_height
    +0.002),' ',num2str(tx(3)),' ', ...
     num2str(tx(1)+0.001),' ',num2str(tx(2)+bowtie_height
        +0.006),' ',num2str(tx(3)),' res_tx_top');
fprintf(fid,'%s%s%s%s%s%s%s%s%s%s%s%s\n','#edge: ',
    num2str(tx(1)+0.022),' ',num2str(tx(2)+bowtie_height
    +0.002),' ',num2str(tx(3)),' ', ...
```

```
    num2str(tx(1)+0.022),' ',num2str(tx(2)+bowtie_height
        +0.006),' ',num2str(tx(3)),' res_tx_top');
fprintf(fid,'%s%s%s%s%s%s%s%s%s%s%s%s%s%s\n','#edge: ',
    num2str(tx(1)+0.022+0.001),' ',num2str(tx(2)+
    bowtie_height+0.002),' ',num2str(tx(3)),' ', ...
    num2str(tx(1)+0.022+0.001),' ',num2str(tx(2)+
        bowtie_height+0.006),' ',num2str(tx(3)),'
        res_tx_top');

% Discrete SMD resistors - Rx
fprintf(fid,'%s%s%s%s%s%s%s%s%s%s%s%s%s%s\n','#edge: ',
    num2str(tx(1)+0.076-0.023),' ',num2str(tx(2)-
    bowtie_height-0.004),' ',num2str(tx(3)),' ', ...
    num2str(tx(1)+0.076-0.023),' ',num2str(tx(2)-
        bowtie_height-0.001),' ',num2str(tx(3)),' res_rx');
fprintf(fid,'%s%s%s%s%s%s%s%s%s%s%s%s%s%s\n','#edge: ',
    num2str(tx(1)+0.076-0.023+0.001),' ',num2str(tx(2)-
    bowtie_height-0.004),' ',num2str(tx(3)),' ', ...
    num2str(tx(1)+0.076-0.023+0.001),' ',num2str(tx(2)-
        bowtie_height-0.001),' ',num2str(tx(3)),' res_rx');
fprintf(fid,'%s%s%s%s%s%s%s%s%s%s%s%s%s%s\n','#edge: ',
    num2str(tx(1)+0.076),' ',num2str(tx(2)-bowtie_height
    -0.004),' ',num2str(tx(3)),' ',num2str(tx(1)+0.076),
    ...
    ' ',num2str(tx(2)-bowtie_height-0.001),' ',num2str(tx
        (3)),' res_rx');
fprintf(fid,'%s%s%s%s%s%s%s%s%s%s%s%s%s%s\n','#edge: ',
    num2str(tx(1)+0.076-0.001),' ',num2str(tx(2)-
    bowtie_height-0.004),' ',num2str(tx(3)),' ', ...
    num2str(tx(1)+0.076-0.001),' ',num2str(tx(2)-
        bowtie_height-0.001),' ',num2str(tx(3)),' res_rx');
fprintf(fid,'%s%s%s%s%s%s%s%s%s%s%s%s%s%s\n','#edge: ',
    num2str(tx(1)+0.076+0.023),' ',num2str(tx(2)-
    bowtie_height-0.004),' ',num2str(tx(3)),' ', ...
    num2str(tx(1)+0.076+0.023),' ',num2str(tx(2)-
        bowtie_height-0.001),' ',num2str(tx(3)),' res_rx');
fprintf(fid,'%s%s%s%s%s%s%s%s%s%s%s%s%s%s\n','#edge: ',
    num2str(tx(1)+0.076+0.023-0.001),' ',num2str(tx(2)-
    bowtie_height-0.004),' ',num2str(tx(3)),' ', ...
    num2str(tx(1)+0.076+0.023-0.001),' ',num2str(tx(2)-
        bowtie_height-0.001),' ',num2str(tx(3)),' res_rx');

fprintf(fid,'%s%s%s%s%s%s%s%s%s%s%s%s%s%s\n','#edge: ',
    num2str(tx(1)+0.076-0.023),' ',num2str(tx(2)+
    bowtie_height+0.002),' ',num2str(tx(3)),' ', ...
```

```
    num2str(tx(1)+0.076-0.023),' ',num2str(tx(2)+
        bowtie_height+0.006),' ',num2str(tx(3)),'
        res_rx_top');
fprintf(fid,'%s%s%s%s%s%s%s%s%s%s%s%s%s\n','#edge: ',
    num2str(tx(1)+0.076-0.023+0.001),' ',num2str(tx(2)+
    bowtie_height+0.002),' ',num2str(tx(3)),' ', ...
    num2str(tx(1)+0.076-0.023+0.001),' ',num2str(tx(2)+
        bowtie_height+0.006),' ',num2str(tx(3)),'
        res_rx_top');
fprintf(fid,'%s%s%s%s%s%s%s%s%s%s%s%s%s\n','#edge: ',
    num2str(tx(1)+0.076),' ',num2str(tx(2)+bowtie_height
    +0.002),' ',num2str(tx(3)),' ',num2str(tx(1)+0.076),
    ...
    ' ',num2str(tx(2)+bowtie_height+0.006),' ',num2str(tx
        (3)),' res_rx_top');
fprintf(fid,'%s%s%s%s%s%s%s%s%s%s%s%s%s\n','#edge: ',
    num2str(tx(1)+0.076-0.001),' ',num2str(tx(2)+
    bowtie_height+0.002),' ',num2str(tx(3)),' ', ...
    num2str(tx(1)+0.076-0.001),' ',num2str(tx(2)+
        bowtie_height+0.006),' ',num2str(tx(3)),'
        res_rx_top');
fprintf(fid,'%s%s%s%s%s%s%s%s%s%s%s%s%s\n','#edge: ',
    num2str(tx(1)+0.076+0.023),' ',num2str(tx(2)+
    bowtie_height+0.002),' ',num2str(tx(3)),' ', ...
    num2str(tx(1)+0.076+0.023),' ',num2str(tx(2)+
        bowtie_height+0.006),' ',num2str(tx(3)),'
        res_rx_top');
fprintf(fid,'%s%s%s%s%s%s%s%s%s%s%s%s%s\n','#edge: ',
    num2str(tx(1)+0.076+0.023-0.001),' ',num2str(tx(2)+
    bowtie_height+0.002),' ',num2str(tx(3)),' ', ...
    num2str(tx(1)+0.076+0.023-0.001),' ',num2str(tx(2)+
        bowtie_height+0.006),' ',num2str(tx(3)),'
        res_rx_top');

% Skid
fprintf(fid,'%s%s%s%s%s%s%s%s%s%s%s%s%s\n','#box: ',
    num2str(ant_orig(1)),' ',num2str(ant_orig(2)),' ',
    num2str(ant_orig(3)),' ',num2str(ant_orig(1)+casedims
    (1)),' ', ...
    num2str(ant_orig(2)+casedims(2)),' ',num2str(ant_orig
        (3)+polypropylenethick),' polypropylene');
fprintf(fid,'%s%s%s%s%s%s%s%s%s%s%s%s%s\n','#box: ',
    num2str(ant_orig(1)),' ',num2str(ant_orig(2)),' ',
    num2str(ant_orig(3)+polypropylenethick),' ', ...
```

```
    num2str(ant_orig(1)+casedims(1)),' ',num2str(ant_orig
        (2)+casedims(2)),' ',num2str(ant_orig(3)+
        polypropylenethick+hdpethick),' hdpe');

% Excitation
fprintf(fid,'\n%s','--- Antenna excitation ---');
%     fprintf(fid,'\n%s%s%s%s%s\n','#hertzian_dipole: 1.0
    ',sprintf('%4E',f),' ricker ','Tx_hertz_',num2str(
    file_num_start));
fprintf(fid,'\n%s%s%s%s%s\n','#voltage_source: 1.0 ',
    sprintf('%4E',f),' gaussian ',sprintf('%d',Tx_res),'
    Tx_volt');
fprintf(fid,'%s%s%s%s%s%s%s%s%s%s%s%s\n','#edge: ',
    num2str(tx(1)+0.076),' ',num2str(tx(2)),' ',num2str(tx
    (3)),' ', ...
     num2str(tx(1)+0.076),' ',num2str(tx(2)+0.001),' ',
        num2str(tx(3)),' res_rx');

fprintf(fid,'\n%s\n\n','****** END MALA 1.2GHz antenna
    model ******');
```

B.2 GPRMAX3D INPUT FILES

B.2.1 *GSSI 1.5 GHz antenna model*

```
#title: GSSI 1.5GHz antenna in free space
------
#messages: yes
#abc_type: pml
#pml_layers: 16
#num_of_procs: 6
#nips_number: 40
------
#domain: 0.27 0.207 0.143
#dx_dy_dz: 0.001 0.001 0.001
#time_window: 8e-09
------
#medium: 1.0 0.0 0.0 59.6E6 1.0 0.0 copper
#medium: 1.6 0.0 0.0 0.428 1.0 0.0 absorber
#medium: 3.0 0.0 0.0 0.0 1.0 0.0 pcb
#medium: 2.35 0.0 0.0 0.0 1.0 0.0 hdpe
#medium: 2.35 0.0 0.0 0.0 1.0 0.0 case
#medium: 3.0 0.0 0.0 1.0811 1.0 0.0 res_rx
```

```
------
#box: 0.05 0.05 0.054 0.22 0.157 0.097 case
#box: 0.052 0.052 0.054 0.218 0.155 0.095 free_space
#box: 0.075 0.052 0.054 0.195 0.155 0.081 pec
#box: 0.077 0.054 0.054 0.134 0.153 0.078 pcb
#box: 0.08 0.057 0.054 0.131 0.15 0.079 absorber
#box: 0.136 0.054 0.054 0.193 0.153 0.078 pcb
#box: 0.139 0.057 0.054 0.19 0.15 0.079 absorber
#box: 0.08 0.057 0.054 0.131 0.15 0.056 pcb
#box: 0.139 0.057 0.054 0.19 0.15 0.056 pcb
#box: 0.094 0.074 0.054 0.116 0.089 0.055 copper
#box: 0.094 0.118 0.054 0.116 0.133 0.055 copper
#wedge: 0.105 0.103 0.054 0.094 0.088 0.054 0.116 0.088
   0.054 0.001 copper
#wedge: 0.105 0.104 0.054 0.094 0.119 0.054 0.116 0.119
   0.054 0.001 copper
#edge: 0.105 0.102 0.054 0.105 0.103 0.054 copper
#edge: 0.105 0.104 0.054 0.105 0.105 0.054 copper
#box: 0.153 0.074 0.054 0.175 0.089 0.055 copper
#box: 0.153 0.118 0.054 0.175 0.133 0.055 copper
#wedge: 0.164 0.103 0.054 0.153 0.088 0.054 0.175 0.088
   0.054 0.001 copper
#wedge: 0.164 0.104 0.054 0.153 0.119 0.054 0.175 0.119
   0.054 0.001 copper
#edge: 0.164 0.102 0.054 0.164 0.103 0.054 copper
#edge: 0.164 0.104 0.054 0.164 0.105 0.054 copper
#box: 0.05 0.05 0.05 0.22 0.157 0.054 hdpe
------
#voltage_source: 1.0 1.709628E+09 gaussian 3.611797e+00
   Tx_volt_20
#edge: 0.164 0.103 0.054 0.164 0.104 0.054 res_rx
------
#analysis: 1 GSSI_1500_fs_opt_conf20.out b
#tx: y 0.105 0.103 0.054 Tx_volt_20 0.0 8e-09
#rx: 0.105 0.103 0.054
#rx: 0.164 0.103 0.054
#end_analysis:
```

B.2.2 *MALÅ 1.2 GHz antenna model*

```
#title: Mala 1.2GHz antenna in free space
------
#messages: yes
```

```
#abc_type: pml
#pml_layers: 16
#num_of_procs: 6
#nips_number: 50
#number_of_media: 20
------
#domain: 0.284 0.209 0.14
#dx_dy_dz: 0.001 0.001 0.001
#time_window: 8e-09
------
#medium: 1.0 0.0 0.0 59.6E6 1.0 0.0 copper
#medium: 6.5 0.0 0.0 0.252 1.0 0.0 absorber
#medium: 3.0 0.0 0.0 0.0 1.0 0.0 pcb
#medium: 2.26 0.0 0.0 0.0 1.0 0.0 polypropylene
#medium: 2.35 0.0 0.0 0.0 1.0 0.0 hdpe
#medium: 3.0 0.0 0.0 3.1915 1.0 0.0 res_tx
#medium: 3.0 0.0 0.0 4.2553 1.0 0.0 res_tx_top
#medium: 3.0 0.0 0.0 10 1.0 0.0 res_rx
#medium: 3.0 0.0 0.0 13.3333 1.0 0.0 res_rx_top
#medium: 1.0 0.0 0.0 1.1228 1.0 0.0 res_rx_line
------
#box: 0.05 0.05 0.056 0.234 0.159 0.096 pec
#box: 0.07 0.052 0.056 0.15 0.157 0.058 free_space
#box: 0.152 0.052 0.056 0.232 0.157 0.058 free_space
#box: 0.07 0.052 0.056 0.15 0.157 0.094 absorber
#box: 0.152 0.052 0.056 0.232 0.157 0.094 absorber
#cylinder: z 0.056 0.094 0.105 0.151 0.008 pec
#cylinder: z 0.056 0.094 0.105 0.058 0.008 pec
#cylinder: z 0.056 0.094 0.197 0.151 0.008 pec
#cylinder: z 0.056 0.094 0.197 0.058 0.008 pec
#cylinder: z 0.056 0.094 0.105 0.151 0.007 free_space
#cylinder: z 0.056 0.094 0.105 0.058 0.007 free_space
#cylinder: z 0.056 0.094 0.197 0.151 0.007 free_space
#cylinder: z 0.056 0.094 0.197 0.058 0.007 free_space
#box: 0.104 0.143 0.056 0.106 0.145 0.094 free_space
#box: 0.104 0.064 0.056 0.106 0.066 0.094 free_space
#box: 0.196 0.143 0.056 0.198 0.145 0.094 free_space
#box: 0.196 0.064 0.056 0.198 0.066 0.094 free_space
#box: 0.07 0.068 0.056 0.232 0.141 0.058 pcb
#box: 0.082 0.072 0.056 0.144 0.134 0.093 pec
#box: 0.083 0.073 0.056 0.143 0.133 0.093 absorber
#box: 0.158 0.072 0.056 0.22 0.134 0.093 pec
#box: 0.159 0.073 0.056 0.219 0.133 0.093 free_space
#box: 0.144 0.128 0.092 0.158 0.134 0.093 pec
#box: 0.144 0.072 0.092 0.158 0.078 0.093 pec
```

```
#box: 0.083 0.073 0.056 0.143 0.133 0.058 pcb
#box: 0.159 0.073 0.056 0.219 0.133 0.058 pcb
#wedge: 0.113 0.101 0.056 0.087 0.076 0.056 0.139 0.076
   0.056 0.001 copper
#wedge: 0.113 0.104 0.056 0.087 0.129 0.056 0.139 0.129
   0.056 0.001 copper
#box: 0.112 0.101 0.056 0.114 0.102 0.057 copper
#box: 0.112 0.103 0.056 0.114 0.104 0.057 copper
#wedge: 0.189 0.101 0.056 0.163 0.076 0.056 0.215 0.076
   0.056 0.001 copper
#wedge: 0.189 0.104 0.056 0.163 0.129 0.056 0.215 0.129
   0.056 0.001 copper
#box: 0.188 0.101 0.056 0.19 0.102 0.057 copper
#box: 0.188 0.103 0.056 0.19 0.104 0.057 copper
#edge: 0.09 0.073 0.056 0.09 0.076 0.056 res_tx
#edge: 0.091 0.073 0.056 0.091 0.076 0.056 res_tx
#edge: 0.113 0.073 0.056 0.113 0.076 0.056 res_tx
#edge: 0.114 0.073 0.056 0.114 0.076 0.056 res_tx
#edge: 0.135 0.073 0.056 0.135 0.076 0.056 res_tx
#edge: 0.136 0.073 0.056 0.136 0.076 0.056 res_tx
#edge: 0.09 0.129 0.056 0.09 0.133 0.056 res_tx_top
#edge: 0.091 0.129 0.056 0.091 0.133 0.056 res_tx_top
#edge: 0.113 0.129 0.056 0.113 0.133 0.056 res_tx_top
#edge: 0.114 0.129 0.056 0.114 0.133 0.056 res_tx_top
#edge: 0.135 0.129 0.056 0.135 0.133 0.056 res_tx_top
#edge: 0.136 0.129 0.056 0.136 0.133 0.056 res_tx_top
#edge: 0.166 0.073 0.056 0.166 0.076 0.056 res_rx
#edge: 0.167 0.073 0.056 0.167 0.076 0.056 res_rx
#edge: 0.189 0.073 0.056 0.189 0.076 0.056 res_rx
#edge: 0.188 0.073 0.056 0.188 0.076 0.056 res_rx
#edge: 0.212 0.073 0.056 0.212 0.076 0.056 res_rx
#edge: 0.211 0.073 0.056 0.211 0.076 0.056 res_rx
#edge: 0.166 0.129 0.056 0.166 0.133 0.056 res_rx_top
#edge: 0.167 0.129 0.056 0.167 0.133 0.056 res_rx_top
#edge: 0.189 0.129 0.056 0.189 0.133 0.056 res_rx_top
#edge: 0.188 0.129 0.056 0.188 0.133 0.056 res_rx_top
#edge: 0.212 0.129 0.056 0.212 0.133 0.056 res_rx_top
#edge: 0.211 0.129 0.056 0.211 0.133 0.056 res_rx_top
#box: 0.05 0.05 0.05 0.234 0.159 0.053 polypropylene
#box: 0.05 0.05 0.053 0.234 0.159 0.056 hdpe
------
#voltage_source: 1.0 9.782666E+08 gaussian 1000 Tx_volt_20
#edge: 0.189 0.102 0.056 0.189 0.103 0.056 res_rx_line
------
#analysis: 1 Mala_1200_fs_opt_conf20.out b
```

```
#tx: y 0.113 0.102 0.056 Tx_volt_20 0.0 8e-09
#rx: 0.113 0.102 0.056
#rx: 0.189 0.102 0.056
#end_analysis:
```

C

SHELL SCRIPTS FOR THE TAGUCHI OPTIMISATION PROCESS

C.1 BASH SHELL SCRIPTS

The following scripts were written for a bash shell and the SGE, and were used to run a fully automated Taguchi optimisation process on School of Engineering compute cluster (Duncan, 2008).

C.1.1 *Job controller*

```
#!/bin/bash

# First and last task IDs
# Checks for I_G1500_ENV and sets to 1 if not found (
   should be only 1st iteration)
NUM_EXPS=18
TASK_FIRST_GSSI=$[1+(${I_G1500_ENV:=1}-1)*NUM_EXPS]
TASK_LAST_GSSI=$[$TASK_FIRST_GSSI+NUM_EXPS-1]
export I_G1500_ENV

qsub -t $TASK_FIRST_GSSI-$TASK_LAST_GSSI models_GSSI_1500.
   sh
qsub -hold_jid models_GSSI_1500.sh fitness_GSSI_1500.sh
```

C.1.2 *Parallel model execution*

```
#!/bin/bash
#################################################################
### Specify bash shell:
#$ -S /bin/bash

### Export environmental variables into script:
#$ -V

### Change to current working directory:
#$ -cwd
```

```
### OpenMP parallel environment 6 CPUs:
#$ -pe openmp 6

### Job name:
#$ -N models_GSSI_1500.sh
############################################################

# Run 'opt_stage1' Matlab script to generate experiments
   and write GprMax input files
cd $HOME/MATLAB/GSSI_1500/
/opt/matlab/bin/matlab -nodisplay -nojvm -c 1711
   @mathworksr0 -r "opt_stage1_GSSI_1500;exit"

sleep 10

# Run GprMax3D in parallel
cd $HOME/GprMax-work/GSSI_1500_fs_opt/
$HOME/bin/GprMax3D_omp64_clx GSSI_1500_fs_opt${SGE_TASK_ID
   }.in
```

C.1.3 *Fitness and termination criteria*

```
#!/bin/bash
############################################################
### Specify bash shell:
#$ -S /bin/bash

### Export environmental variables into script:
#$ -V

### Change to current working directory:
#$ -cwd

### OpenMP parallel environment 6 CPUs:
#$ -pe openmp 6

### Job name:
#$ -N fitness_GSSI_1500.sh
############################################################

if ! test -s model_GSSI_1500.sh.e*
then
```

```
        # Remove output and error files from previous
            iteration
        rm -f models_GSSI_1500.sh.*

    # Run 'opt_stage2' Matlab script to calculate fitness
        of each experiment and write confirmation GprMax
        input file
    cd $HOME/MATLAB/GSSI_1500/
    /opt/matlab/bin/matlab -nodisplay -nojvm -c 1711
        @mathworksr0 -r "opt_stage2_GSSI_1500;exit"

    # Run GprMax3D on confirmation experiment
    cd $HOME/GprMax-work/GSSI_1500_fs_opt/
    $HOME/bin/GprMax3D_omp64_clx GSSI_1500_fs_opt_conf${
        I_G1500_ENV}.in

    # Run 'opt_stage3' Matlab script to calculate fitness
        of confirmation experiment and write fitness value
        to file 'fitness'
    cd $HOME/MATLAB/GSSI_1500/
    /opt/matlab/bin/matlab -nodisplay -nojvm -c 1711
        @mathworksr0 -r "opt_stage3_GSSI_1500;exit"

    # If we have not achieved MATCH and not at
        MAX_ITERATIONS then repeat
    MATCH=99
    MAX_ITERATIONS=20

    if [ $(< $HOME/GprMax-work/GSSI_1500_fs_opt/fitness) -
        lt $MATCH ]; then
        if [ $I_G1500_ENV -lt $MAX_ITERATIONS ]; then
            # Resubmit myself.
            export I_G1500_ENV=$[$I_G1500_ENV+1]
            cd $HOME
            master_GSSI_1500
        fi
    fi
fi
```

Altera Corporation (2007). *Stratix II Device Handbook: High-Speed Board Layout Guidelines*. `http://www.altera.com/literature/hb/stx2/stratix2_handbook.pdf`. (Cited on pages xix and 70.)

Anderson, J., Okoniewski, M., and Stuchly, S. (1996). Practical 3-D contour/staircase treatment of metals in FDTD. *IEEE Microwave and Guided Wave Letters*, 6(3):146–148. (Cited on page 41.)

Annan, A. (2002). GPR—History, trends, and future developments. *Subsurface Sensing Technologies and Applications*, 3(4):253–270. (Cited on page 5.)

Annan, A. (2005). *Near-surface geophysics*, chapter 11, pages 357–438. Society of Exploration Geophysicists Tulsa, OK. (Cited on pages 13, 26, and 145.)

Annan, A., Waller, W., Strangway, D., Rossiter, J., Redman, J., and Watts, R. (1975). The electromagnetic response of a low-loss, 2-layer, dielectric earth for horizontal electric dipole excitation. *Geophysics*, 40:285–298. (Cited on page 147.)

Arcone, S. (1995). Numerical studies of the radiation patterns of resistively loaded dipoles. *Journal of Applied Geophysics*, 33:39–52. (Cited on page 147.)

Balanis, C. (1989). *Advanced Engineering Electromagnetics*. Wiley New York. (Cited on pages 7, 10, 11, 29, and 32.)

Balanis, C. (1997). *Antenna Theory: Analysis and Design*. John Wiley and Sons, Inc., 2nd edition. (Cited on pages 45, 69, 80, 143, and 144.)

Becher, P. (1966). *Emulsions: Theory and Practice*. Van Nostrand Reinhold Company. (Cited on pages 110 and 111.)

Benkler, S., Chavannes, N., and Kuster, N. (2006). A new 3-D conformal PEC FDTD scheme with user-defined geometric precision and derived stability criterion. *IEEE Transactions on Antennas and Propagation*, 54(6):1843–1849. (Cited on page 41.)

Beowulf.org (1994). Beowulf.org: The beowulf cluster site. `http://www.beowulf.org/` [Last accessed: June 2009]. (Cited on page 59.)

Berenger, J. (1994). A perfectly matched layer for the absorption of electromagnetic waves. *Journal of Computational Physics*. (Cited on page 42.)

Bergmann, T., Robertsson, J., and Holliger, K. (1998). Finite-difference modeling of electromagnetic wave propagation in dispersive and attenuating media. *Geophysics*, 63:856. (Cited on page 48.)

Birtwisle, A. and Utsi, E. (2008). The use of ground penetrating radar to detect vertical subsurface cracking in airport runways. In *Proceedings of the 12th International Conference on Ground Penetrating Radar*. (Cited on page 19.)

Bondeson, A., Rylander, T., and Ingelström, P. (2005). *Computational electromagnetics*. Springer. (Cited on pages 40 and 41.)

Bourgeois, J. and Smith, G. (1996). A fully three-dimensional simulation of a ground-penetrating radar: Fdtd theory compared with experiment. *IEEE Transactions on Geoscience and Remote Sensing*, 34(1):36–44. (Cited on pages 47 and 124.)

Brown, G. and Woodward, O. (1952). Experimentally determined radiation characteristics of conical and triangular antennas. *RCA rev*, 13(4):425–452. (Cited on pages 46, 48, and 49.)

Buff, P. M. (2006). *Characterization of Propagation on Wires Over Lossy Earth*. PhD thesis, North Carolina State University. (Cited on page 109.)

Bungey, J., Millard, S., and Shaw, M. (1993). Simulation tank to aid interpretation of radar results on concrete. *Magazine of Concrete Research*, 45(164):187–195. (Cited on pages 109 and 114.)

Cangellaris, A. and Wright, D. (1991). Analysis of the numerical error caused by the stair-stepped approximation of a conducting boundary in fdtd simulations of electromagnetic phenomena. *IEEE Transactions on Antennas and Propagation*, 39(10):1518–1525. (Cited on page 41.)

Cassidy, N. (2001). *The application of mathematical modelling in the interpretation of near-surface archaeological ground-penetrating radar*. PhD thesis, Keele University. (Cited on page 48.)

Cassidy, N. (2008). Introduction to gpr. In *Workshop at the 12th International Conference on Ground Penetrating Radar*. (Cited on pages xiv, xix, 10, 14, and 19.)

Charles, A. ., Towers, M., and McCowen, A. (1999). Sensitivity analysis of jaumann absorbers. In *IEE Proceedings - Microwaves, Antennas and Propagation*, volume 146, pages 257–262. (Cited on page 92.)

Chevalier, M., Luebbers, R., and Cable, V. (1997). Fdtd local grid with material traverse. *IEEE Transactions on Antennas and Propagation*, 45(3):411–421. (Cited on pages 41 and 49.)

Chou, T. (1996). Applications of taguchi method for optimized package design. In *Proceedings of the 5th IEEE Topical Meeting on Electrical Performance of Electronic Packaging*, pages 14–17. (Cited on page 92.)

Daniels, D. (2004). *Ground penetrating radar*. The Institution of Electrical Engineers. (Cited on pages 5, 6, 11, and 23.)

Debye, P. (1929). Polare Molekeln. *Leipzig: Hirzel,| c1929*. (Cited on page 33.)

Dey, S. and Mittra, R. (1997). A locally conformal finite-difference time-domain (FDTD) algorithm for modeling three-dimensional perfectly conducting objects. *IEEE Microwave and Guided Wave Letters*, 7(9):273–275. (Cited on page 41.)

Diamanti, N. (2008). *An Efficient Ground-Penetrating Radar Finite-Difference Time-Domain Subgridding Scheme and its Application to the Non-Destructive Testing of Masonry Arch Bridges*. PhD thesis, University of Edinburgh. (Cited on page 180.)

Diamanti, N. and Giannopoulos, A. (2009). Implementation of adi-fdtd subgrids in ground penetrating radar fdtd models. *Journal of Applied Geophysics*, 67(4):309–317. (Cited on page 41.)

Drossaert, F. and Giannopoulos, A. (2007). A nonsplit complex frequency-shifted PML based on recursive integration for FDTD modeling of elastic waves. *Geophysics*, 72. (Cited on page 43.)

Duncan, B. (2008). University of edinburgh, school of engineering, beowulf compute cluster. `http://clx.see.ed.ac.uk` [Last accessed: June 2009]. (Cited on pages 59 and 211.)

El-Said, M. (1956). Geophysical prospection of underground water in the desert by means of electromagnetic interference fringes. *Proceedings of the IRE*, 44(1):24–30. (Cited on page 5.)

Emerson and Cuming (1948). Eccosorb ls - microwave absorber. `http://www.eccosorb.com/asia/english_asia/page/63/eccosorb` [Last accessed: June 2009]. (Cited on pages 70 and 101.)

Encyclopaedia Britannica (2009). A library of orthogonal arrays. `http://www.britannica.com/EBchecked/topic/79080/Brewsters-law` [Last accessed: June 2009]. (Cited on page 12.)

Engheta, N., Papas, C., and Elachi, C. (1982). Radiation patterns of interfacial dipole antennas. *Radio Science*, 17:1557–1566. (Cited on page 147.)

Fang, J. and Wu, Z. (1996). Generalized perfectly matched layer for the absorption of propagating and evanescent waves in lossless and lossy media. *IEEE Transactions on Microwave Theory and Techniques*, 44(12):2216–2222. (Cited on page 49.)

Federal Communications Commission (2002). Revision of part 15 of the commission's rules regarding ultra-wideband transmission systems. `http://www.fcc.gov/Bureaus/Engineering_Technology/Orders/2002/fcc02048.pdf` [Last accessed: June 2009]. (Cited on page 69.)

Galagedara, L., Redman, J., Parkin, G., Annan, A., and Endres, A. (2005). Numerical modeling of GPR to determine the direct ground wave sampling depth. *Vadose Zone Journal*, 4:1096–1106. (Cited on page 53.)

Gedney, S. (1996). An anisotropic PML absorbing media for the FDTD simulation of fields in lossy and dispersive media. *Electromagnetics*, 16(4):399–415. (Cited on page 42.)

Geophysical Survey Systems, Inc. (2001). `http://www.geophysical.com` [Last accessed: June 2009]. (Cited on pages xiv, 16, and 68.)

Giannopoulos, A. (1997). *The investigation of Transmission-Line Matrix and Finite-Difference Time-Domain Methods for the Forward Problem of Ground Probing Radar*. PhD thesis, Department of Electronics, University of York. (Cited on page 45.)

Giannopoulos, A. (2005). *GprMax - FDTD based GPR simulation software*. `http://www.gprmax.org`. (Cited on pages 35 and 53.)

Giannopoulos, A. (2008). An Improved New Implementation of Complex Frequency Shifted PML for the FDTD Method. *IEEE Transactions on Antennas and Propagation*, 56(9):2995–3000. (Cited on page 43.)

Goodwin, R. and Cassidy, N. (2008). Gpr characteristics of magnetite-rich layered igneous bodies. In *Proceedings of the 12th International Conference on Ground Penetrating Radar*. (Cited on page 9.)

Gurel, L. and Oguz, U. (2000). Three-dimensional FDTD modeling of a ground-penetrating radar. *IEEE Transactions on Geoscience and Remote Sensing*, 38(4):1513–1521. (Cited on page 71.)

Hanai, T., Koizumi, N., Sugano, T., and Gotoh, R. (1960). Dielectric properties of emulsions. II. Electrical conductivities of O/W emulsions. *Kolloid-Z.*, 171:20. (Cited on page 15.)

Harrington, R. (1961). *Time-Harmonic Fields*. McGraw-Hill. (Cited on page 47.)

Hedayat, A., Sloane, N., and Stufken, J. (1999). *Orthogonal Arrays: Theory and Applications*. Springer-Verlag. (Cited on pages 92 and 95.)

Hertel, T. and Smith, G. (2003). On the convergence of common fdtd feed models for antennas. *IEEE Transactions on Antennas and Propagation*, pages 1771–1779. (Cited on pages xv, 71, 73, and 74.)

Higdon, R. (1986). Absorbing boundary conditions for difference approximations to the multi-dimensional wave equation. *Mathematics of Computation*, pages 437–459. (Cited on page 42.)

Holland, R. (1993). Pitfalls of staircase meshing. *IEEE Transactions on Electromagnetic Compatibility*, 35(4):434–439. (Cited on page 41.)

Holliger, K., Lampe, B., Meier, U., Lambert, M., and Green, A. (2003). Realistic modeling of surface ground-penetrating radar antenna systems: where do we stand? In *Proceedings of the 2nd International Workshop on Advanced Ground Penetrating Radar*, pages 45–50. (Cited on page 49.)

Huang, Z., Demarest, K., and Plumb, R. (1999). An FDTD/MoM hybrid technique for modeling complex antennas in thepresence of heterogeneous grounds. *IEEE Transactions on Geoscience and Remote Sensing*, 37(6):2692–2698. (Cited on page 47.)

Hwang, G., Hwang, S., Lee, H., Kim, J., Hong, K., and Lee, W. (2005). Application of taguchi method to robust design of acoustic performance in imt-200 mobile phones. *IEEE Transactions on Magnetics*, 41:1900–1903. (Cited on page 92.)

IEEE (1979). IEEE Standard Test Procedures for Antennas. *IEEE Std 149-1979*. (Cited on pages xvii and 144.)

IEEE (1983). IEEE Standard Definitions of Terms for Antennas. *IEEE Std 145-1983*. (Cited on page 143.)

Infrasensec, Inc. (2003). Non-destructive measurement of pavement layer thickness. Technical report, California Department of Transportation. (Cited on pages 109 and 114.)

Jeannin, M., Garambois, S., Grégoire, C., and Jongmans, D. (2006). Multi-configuration GPR measurements for geometric fracture characterization in limestone cliffs (Alps). *Geophysics*, 71:B85. (Cited on page 53.)

Jurgens, T., Taflove, A., Umashankar, K., and Moore, T. (1992). Finite-difference time-domain modeling of curved surfaces. *IEEE Transactions on Antennas and Propagation*, 40(4):357–366. (Cited on page 41.)

King, R. W. (1956). *Theory of Linear Antennas with Charts and Tables for Practical Applications*. Oxford University Press. (Cited on pages 45, 69, and 147.)

Kitware Inc. (2003). *VTK User's Guide - File formats*, 4.2 edition. `http://www.vtk.org/VTK/img/file-formats.pdf`. (Cited on page 57.)

Klysz, G., Ferrieres, X., Balayssac, J., and Laurens, S. (2006). Simulation of direct wave propagation by numerical fdtd for a gpr coupled antenna. *NDT and E International*, 39(4):338–347. (Cited on pages 50 and 147.)

Kraus, J. (1991). *Electromagnetics*. WCB/McGraw-Hill. (Cited on pages 29, 150, and 151.)

Lampe, B. and Holliger, K. (2001). Numerical modeling of a complete ground-penetrating radar system. In *Proceedings of SPIE*, volume 4491, page 99. (Cited on page 49.)

Lampe, B. and Holliger, K. (2005). Resistively loaded antennas for ground-penetrating radar: A modeling approach. *Geophysics*, 70:K23–K32. (Cited on page 49.)

Lampe, B., Holliger, K., and Green, A. (2003). A finite-difference time-domain simulation tool for ground-penetrating radar antennas. *Geophysics*, 68(3):971–987. (Cited on page 49.)

Lawrence Livermore Laboratory (1981). Nec-2. `http://www.nec2.org/` [Last accessed: June 2009]. (Cited on page 47.)

Lee, K.-H., Chen, C.-C., Teixeira, F., and Lee, R. (2004). Modeling and investigation of a geometrically complex uwb gpr antenna using fdtd. *IEEE Transactions on Antennas and Propagation*, 52(8):1983–1991. (Cited on pages 49 and 71.)

Lestari, A., Yarovoy, A., and Ligthart, L. (2004). RC-loaded bow-tie antenna for improved pulse radiation. *IEEE Transactions on Antennas and Propagation*, 52(10):2555–2563. (Cited on page 46.)

Lestari, A., Yarovoy, A., and Ligthart, L. (2005). Adaptive wire bow-tie antenna for GPR applications. *IEEE Transactions on Antennas and Propagation*, 53(5):1745–1754. (Cited on page 46.)

Liao, Z., Wong, H., Yang, B., and Yuan, Y. (1984). A transmitting boundary for transient wave analysis. *Scientia Sinica*, 27(10):1063–1076. (Cited on page 42.)

Liu, L., Su, Y., and Mao, J. (2008). FDTD analysis of ground-penetrating radar antennas with shields and absorbers. *Frontiers of Electrical and Electronic Engineering in China*, 3(1):90–95. (Cited on page 50.)

Lopera, O. and Milisavljevic, N. (2007). Prediction of the effects of soil and target properties on the antipersonnel landmine detection performance of ground-penetrating radar: A Colombian case study. *Journal of Applied Geophysics*, 63(1):13–23. (Cited on page 53.)

MacDonald, A. (1990). A taguchi method for the design of broadband spiral cavity absorbers. In *Proceedings of the Antennas and Propagation Society International Symposium*, volume 3, pages 1180–1183. (Cited on page 92.)

Maloney, J., Smith, G., and Scott, W.R., J. (1989). Accurate computation of the radiation from simple antennas using the finite-difference time-domain method. In *Proceedings of the Antennas and Propagation Society International Symposium*, volume 1, pages 42–45. (Cited on pages 45 and 46.)

Mezzanotte, P., Roselli, L., and Sorrentino, R. (1995). A simple way to model curved metal boundaries in FDTD algorithmavoiding staircase approximation. *IEEE Microwave and Guided Wave Letters*, 5(8):267–269. (Cited on page 41.)

Millard, S., Shaari, A., and Bungey, J. (2002). Field pattern characteristics of gpr antennas. *NDT and E International*, 35(7):473–482. (Cited on page 147.)

Moghaddam, M., Yannakakis, E., Chew, W., and Randall, C. (1991). Modeling of the subsurface interface radar. *Journal of Electromagnetic Waves and Applications*, 5(1):17–39. (Cited on page 45.)

Monorchio, A., Bretones, A., Mittra, R., Manara, G., and Martin, R. (2004). A hybrid time-domain technique that combines the finite element, finite difference and method of moment techniques to solve complex electromagnetic problems. *IEEE Transactions on Antennas and Propagation*, 52(10):2666–2674. (Cited on page 47.)

Nagano, H., Miyano, K., Yamada, T., and Mizushima, I. (2003). Robust selective-epitaxial-growth process for hybrid soi wafer. In *Proceedings of the*

International Symposium on Semiconductor Manufacturing, pages 187–190. (Cited on page 92.)

Nishioka, Y., Maeshima, O., Uno, T., and Adachi, S. (1999). FDTD analysis of resistor-loaded bow-tie antennas covered with ferrite-coated conducting cavity for subsurface radar. *IEEE Transactions on Antennas and Propagation*, 47(6):970–977. (Cited on pages 48 and 71.)

OpenMP.org (2008). `http://openmp.org/wp/` [Last accessed: June 2009]. (Cited on page 55.)

Oristaglio, M. and Hohmann, G. (1984). Diffusion of electromagnetic fields into a two-dimensional earth: A finite-difference approach. *Geophysics*, 49:870. (Cited on page 45.)

Pérez-Gracia, V., Di Capua, D., González-Drigo, R., and Pujades, L. (2009). Laboratory characterization of a GPR antenna for high-resolution testing: Radiation pattern and vertical resolution. *NDT and E International*. (Cited on pages 50 and 147.)

Radzevicius, S., Chen, C., Peters, L., and Daniels, J. (2003). Near-field dipole radiation dynamics through fdtd modeling. *Journal of Applied Geophysics*, 52(2-3):75–91. (Cited on page 150.)

Rao, C. (1946). Hypercubes of strength d leading to confounded designs in factorial experiments. In *Proceedings of the Calcutta Math Society*, volume 38, pages 67–78. (Cited on page 92.)

Rao, C. (1947). Factorial experiments derivable from combinatorial arrangement of arrays. *Journal of the Royal Statistical Society*, 9:128–138. (Cited on page 92.)

Rao, C. (1949). On a class of arrangements. In *Proceedings of the Edinburgh Math Society*, volume 8, pages 119–125. (Cited on page 92.)

Riddle, B., Baker-Jarvis, J., and Krupka, J. (2003). Complex permittivity measurements of common plastics over variable temperatures. *IEEE Transactions on Microwave Theory and Techniques*, 51(3):727–733. (Cited on pages xix and 70.)

Roberts, R. L. and Daniels, J. J. (1997). Modeling near-field gpr in three dimensions using the fdtd method. *Geophysics*, 62(4):1114–1126. (Cited on pages 48 and 71.)

Roden, J. and Gedney, S. (2000). Convolution pml (cpml): An efficient fdtd implementation of the cfs-pml for arbitrary media. *Microwave and Optical Technology Letters*, 27(5). (Cited on page 42.)

Schmid and Partner Engineering AG (SPEAG) (2009). The finite-difference time-domain (fdtd) technique. `http://www.speag.com/simulation/FDTD.php` [Last accessed: June 2009]. (Cited on pages xiv and 36.)

Shlager, K., Smith, G., and Maloney, J. (1994). Optimization of bow-tie antennas for pulse radiation. *IEEE Transactions on Antennas and Propagation*, 42(7):975–982. (Cited on pages xix, 46, 47, 63, 65, 66, and 174.)

Sloane, N. (2009). A library of orthogonal arrays. `http://www.research.att.com/~njas/oadir` [Last accessed: June 2009]. (Cited on page 95.)

Smith, G. (1984). Directive properties of antennas for transmission into a material half-space. *IEEE Transactions on Antennas and Propagation*, 32(3):232–246. (Cited on pages 47, 147, and 153.)

Smith, G. and Scott, W. (1990). The use of emulsions to represent dielectric materials in electromagnetic scale models. *IEEE Transactions on Antennas and Propagation*, 38(3):323–334. (Cited on pages xvi, 109, 110, 113, 114, and 117.)

Soldovieri, F., Hugenschmidt, J., Persico, R., and Leone, G. (2007). A linear inverse scattering algorithm for realistic GPR applications. *Near Surface Geophysics*, 5(1):29–42. (Cited on page 53.)

Taflove, A. and Hagness, S. (2005). *Computational Electrodynamics: The Finite-Difference Time-Domain Method*. Artech House Norwood, MA, 3rd edition. (Cited on pages 29, 34, 37, 40, 42, and 62.)

Taguchi, G., Chowdbury, S., and Wu, Y. (2005). *Taguchi's Quality Engineering Handbook*. John Wiley and Sons, Inc. (Cited on page 92.)

Teixeira, F., Chew, W. C., Straka, M., Oristaglio, M., and Wang, T. (1998). Finite-difference time-domain simulation of ground penetrating radar on dispersive, inhomogeneous, and conductive soils. *IEEE Transactions on Geoscience and Remote Sensing*, 36(6):1928–1937. (Cited on pages 48 and 50.)

Topp, G., Davis, J., and Annan, A. (1980). Electromagnetic determination of soil water content: measurements in coaxial transmission lines. *Water Resources Research*, 16(3). (Cited on page 15.)

Uduwawala, D. and Norgren, M. (2006). An investigation of some geometrical shapes and selection of shielding and lumped resistors of planar dipole antennas for GPR applications using FDTD. *IEEE Transactions on Geoscience and Remote Sensing*, 44(12):3555–3562. (Cited on page 47.)

Uduwawala, D., Norgren, M., Fuks, P., and Gunawardena, A. (2004). A deep parametric study of resistor-loaded bow-tie antennas for ground-penetrating radar applications using fdtd. *IEEE Transactions on Geoscience and Remote Sensing*, 42(4):732–742. (Cited on page 49.)

Uduwawala, D., Norgren, M., Fuks, P., and Gunawardena, A. (2005). A complete FDTD simulation of a real GPR antenna system operating above lossy and dispersive grounds. *Progress In Electromagnetics Research*, pages 209–229. (Cited on page 49.)

Valle, S., Zanzi, L., Sgheiz, M., Lenzi, G., and Friborg, J. (2001). Ground penetrating radar antennas: theoretical and experimental directivity functions. *IEEE Transactions on Geoscience and Remote Sensing*, 39(4):749–759. (Cited on page 150.)

van Coevorden, C., Bretones, A., Pantoja, M., Ruiz, F., Garcia, S., and Martin, R. (2006). GA design of a thin-wire bow-tie antenna for GPR applications. *IEEE Transactions on Geoscience and Remote Sensing*, 44(4):1004–1010. (Cited on page 47.)

van der Kruk, J. (2009). Discussion of determining antenna feed pulse shape and frequency using inversion techniques. Personal communication. (Cited on page 180.)

Wang, H., Liu, Z., Chen, S., and Yang, J. (1999). Application of taguchi method to robust design of bldc motor performance. *IEEE Transactions on Magnetics*, 35(5):3700–3702. (Cited on page 92.)

Weng, W.-C., Yang, F., and Elsherbeni, A. Z. (2007a). *Electromagnetics and Antenna Optimization Using Taguchi's Method*. Morgan and Claypool Publishers. (Cited on pages xix, 92, and 93.)

Weng, W.-C., Yang, F., and Elsherbeni, A. Z. (2007b). Linear antenna array synthesis using taguchi's method: A novel optimization technique in electromagnetics. *IEEE Transactions on Antennas and Propagation*, 55(3):723–730. (Cited on pages xv, 92, and 96.)

Wensink, W., Greeuw, G., Hofman, J., and Deen, J. (1990). Measured underwater near-field E-patterns of a pulsed, horizontal dipole antenna in air:

Comparison with the theory of the continuous wave, infinitesimal electric dipole. *Geophysical Prospecting*, 38(7):805–830. (Cited on pages 48 and 150.)

Wensink, W., Hofman, J., and Deen, J. (1991). Measured reflection strengths of underwater pipes irradiated by a pulsed horizontal dipole in air: Comparison with continuous plane-wave scattering theory. *Geophysical Prospecting*, 39(4):543–566. (Cited on page 48.)

Wharton, R., Hazen, G., Rau, R., and Best, D. (1980). Advancements in electromagnetic propagation logging. *Society of Petroleum Engineering*, 9041. (Cited on page 15.)

Wu, T. and King, R. (1965). The cylindrical antenna with nonreflecting resistive loading. *IEEE Transactions on Antennas and Propagation*, 13(3):369–373. (Cited on pages 47 and 49.)

Yee, K. S. (1966). Numerical solution of inital boundary value problems involving maxwell's equations in isotropic media. *IEEE Transactions on Antennas and Propagation*, 14(3):302–307. (Cited on page 35.)

Yelf, R. (2004). Where is true time zero? In *Proceedings of the 10th International Conference on Ground Penetrating Radar*. (Cited on page 21.)

Yilmaz, O. (2001). *Seismic data analysis*. Society of Exploration Geophysicists Tulsa, Okla. (Cited on pages 19 and 26.)